2022

Optimization and application of a high-performance genetically-encoded fluorescent sensor for membrane voltage imaging

BOSTON UNIVERSITY

COLLEGE OF ENGINEERING

Dissertation

OPTIMIZATION AND APPLICATION OF A HIGH-PERFORMANCE GENETICALLY-ENCODED FLUORESCENT SENSOR FOR MEMBRANE VOLTAGE IMAGING

by

SANAYA NESS SHROFF

B.S., Cornell University, 2016
M.S., Boston University, 2019

Submitted in partial fulfillment of the

requirements for the degree of

Doctor of Philosophy

2022

Approved by

First Reader

Xue Han, Ph.D.
Professor of Biomedical Engineering

Second Reader

John A. White, Ph.D.
Professor and Chair of Biomedical Engineering

Third Reader

Jerome C. Mertz, Ph.D.
Professor of Biomedical Engineering
Professor of Electrical & Computer Engineering
Professor of Physics

Fourth Reader

Michael E. Hasselmo, D.Phil.
William Fairfield Warren Distinguished Professor
Professor of Psychological & Brain Sciences

Fifth Reader

Charles J. Wilson, Ph.D.
Ewing Halsell Distinguished Chair in Biology
Professor of Neuroscience, Developmental, and Regenerative Biology
University of Texas at San Antonio

“May it be a light to you in dark places, when all other lights go out.”
-Galadriel, The Fellowship of the Ring by J.R.R Tolkien

DEDICATION

To Mom, Dad, and Z

For every hug, laugh, and phone call, and for being there always

I could not have done this without you

To Grandma Rati and Grandma Jeroo

And in loving memory of Grandpa Bomi

and Grandpa Polly, who saw me through to the very end

I love you all so much

ACKNOWLEDGMENTS

There are so many people I would like to thank for being there for me on this journey and for helping to make this work possible. First and foremost, to my wonderful family who inspire me to do better every single day: my brother, Zarius, who has grown up way too fast and now helps me more than I help him; my mom, Jasmine, who has been there every step of the way, whether its talking things out on the phone or exercising together on Zoom; and my dad, Ness, who I can always rely on to calm me down, help solve any problem, or make me laugh, and who I admire so much for so many reasons. Words cannot do justice to how much I have relied on you all these past few years (and always) and the never-ending love and support you always show me. I love you all so much. To my Grandpa Bomi who I miss so much for all the laughter and love and happy birthday songs and my Grandma Rati who I love seeing on FaceTime and who never fails to make me smile. To my Grandpa Polly who has always asked after us more than himself and who always makes me laugh, and to my Grandma Jeroo who believes in me and my success always. To my extended family across the country and the world, for your unending love, generosity, and support, even when we don't see each other often. Thank you all.

To my PhD research advisor, Professor Xue Han: thank you for all your support, guidance, mentorship, and encouragement throughout these past 5.5 years. When I reached out to you back in my senior year of college, I didn't know what it would mean to be here 6 years later. You have always believed in me and pushed me to be a better scientist, a deeper thinker, and a more thorough researcher. The level of care you show each and every one of us in the lab has always awed and inspired me, and you are both a personal and

professional inspiration. I am so lucky to have had you as a mentor. Thank you also to my committee members: Department Chair John White, Professor Jerome Mertz, Professor Michael Hasselmo, and Professor Charlie Wilson. I have truly appreciated your guidance and feedback during this time, especially towards the end. Your enthusiasm for research inspires me and I am so grateful to have had your support. I would also be remiss not to thank my wonderful collaborators who played a part in the work presented here: especially Shoshana Das, Jad Noueihed, Dr. Hua-an Tseng, Professor Chris Chen, and Professor John White for their contributions to the work presented in Chapter 2. Shoshana, it was such a joy to work with you every day during that project and I'm so glad we made such a good team — I cherish our friendship so much. Also to Dr. Kiryl Piatkevich, Dr. Seth Bensussen, Dr. Hua-an Tseng, and Professor Ed Boyden for their primary contributions to the work presented in Chapter 3. Seth, Kiryl, and Hua-an, despite all our struggles, it was still so much fun to work alongside you and I learned so much from you all. Finally, to Dr. Eric Lowet, Sudiksha Sridhar, and Professor Howard Gritton, for their contributions to the work presented in Chapter 4. Howard, thank you for being such a fantastic mentor while you were in the lab and for always being there to answer my questions when I needed help or guidance. Eric and Sudi, thank you for helping me get through this project, especially right towards the end, I really appreciate all the hard work you have put in these last few months.

To all the members of the Han Lab, past: Seth, Howard, Kyle, Angela, Marianna, Tina, Sneha, Cyrus, Florence, Mark, Susie, Chengqian, Kimmie, Ali, and Megan and present: Dana, Drew, Rebecca, Hua-an, KK, Eric, Jack, Sudi, Emma, Jenn, Pierre, Athif, Yangyang, Cara, Dana S., Sam, Leo, Mohammed, and Rockwell — thank you for making it so much

fun to come to work every day and for your unwavering friendship. I always know I can count on you all for support and come to you whenever I have questions or need guidance. Special thank you to Seth, who was my main mentor in the lab ever since I first joined grad school and rotated with him. Seth, you taught me basically everything I know and I am so grateful for your guidance, friendship, and for making me feel so welcome from day 1. Also shoutout to all the rotation students, masters students, and undergrads I mentored over the years, whether you ended up joining the lab or not: thank you for your inquisitive questions, curiosity, and hard work — you made me a better mentor and I am so grateful for those opportunities.

Thank you also to the incredible BME department at BU, especially to Christen Bailey and the rest of the BME staff, as well as Department Chair John White. You all made the BME PhD experience so much more enjoyable, manageable, and fun and were our lifesavers more than once. Thank you for your tireless efforts running this department, organizing fun socials and bonding experiences for all of us, and for making sure we always felt supported. I'd also like to thank the staff at CILSE, especially Kevin Gonzales, Joe Walker, and the janitorial staff on the 8th floor. Thank you for making our building such a nice place to work and for always making my day brighter with your hello's and smiles.

A huge thank you to my BME cohort and the rest of the BME PhD students for being such a special group of people – you made the department such a welcoming, exciting place to be for research. I am especially grateful to my cohort mates and friends Megbert, Sandee, and Dana for making these past few years so special, we've had so much fun together and I'm so thankful for your friendship. To all my other amazing friends who have come on

this journey with me: thank you for your unending support, for all the fun hangouts, and for being the lovely people you are. To all the group chats, old and new, for all the hilarity, being there when it counted, and the neverending love, I am so grateful. I especially want to thank my roommates, past and present: Noel, Megan (and of course, Macie the pup!), and Chantal. Thank you for being there for me through it all, for all the cooking adventures, having someone to talk to after hard days or fun ones, for being each other's sounding boards, and for always staying positive even when I couldn't. Also, to my best friend these past 5 years, Arshia, who is always in my corner looking out for me — I love you! Thanks for being the greatest friend I could ask for, your love, support, and friendship have meant the world to me and I cherish so many amazing memories we've made together. To my college best friend, Brittany, who, even if we're miles apart or haven't talked in a while, can pick back up right where we left off. For all the past 10 years we've been friends, study partners, Domino's-ordering buddies, and co-conspirators in all else, I love you. I am also especially grateful to our lifelong family friends, the Daroga family and the Setna family, especially, Saira, for all their love and encouragement throughout the years — even if we don't see each other often, I'm so glad to have you in my life and I feel your unending support always.

I also want to thank the amazing group of women I've had the fortune of working with through GWISE these past several years, especially Dr. Mounika Vutukuru who I served under as Vice-President, Dr. Abby Rendos, who was my own Vice-President, and long-time board member and friend, Dr. Natalie Vaisman. I am so proud of the amazing work we've accomplished together these past 5 years and I know GWISE will continue to make

an impact at BU and beyond. You all inspire me every day and make me confident the future for women in STEM is brighter than ever. Also, thank you to Professor Valerie Williams — Val, you have been such a generous, steadfast friend and an inspiration to me. I'm so grateful I met you through BU fitness and that we've been able to keep each other sane working out together during this pandemic.

Finally, thank you so much to my writing group. You all have been such a huge part of my life this last year and have pushed me to not only get back into creative writing but encouraged me through the process of writing this dissertation. Thank you for staying up with me all the many, many late nights, for the hundreds of writing sprints, challenges, and events, for the watch parties, the general hilarity, and for always making my day just a bit better. Most of all, thank you for your friendship. I am so grateful to have gained so many wonderful friends I never expected through such a wonderful community.

I would also like to acknowledge the funding sources that helped to support this work. I am grateful for funding from the NIH National Institute of General Medical Sciences for the T32 Training Fellowship in Quantitative Biology & Physiology (GM008764) and from the NIH National Institute of Neurological Disorders & Stroke for the F31 Ruth L. Kirschstein National Research Service Award (1 F31 NS115421-01). This work could not have been completed without this generous support.

There are so many people I did not thank here that have made an impact on me in some way, however small, to help me make it through this PhD — I am so grateful for your small kindnesses, your thoughtfulness, and your generosity. To each and every one of you and to all that are mentioned above, thank you.

OPTIMIZATION AND APPLICATION OF A HIGH-PERFORMANCE GENETICALLY-ENCODED FLUORESCENT SENSOR FOR MEMBRANE VOLTAGE IMAGING

SANAYA NESS SHROFF

Boston University College of Engineering, 2022

Major Professor: Xue Han, Ph.D., Professor of Biomedical Engineering

ABSTRACT

The basal ganglia circuit has long been recognized as an important regulator for movement in the brain, with dysfunction of this circuit resulting in motor disorders such as Parkinson's and Huntington's disease. The striatum, the largest nucleus of the basal ganglia, is critical for normal motor control and is implicated in the pathology of various movement disorders. The vast majority (~95%) of striatal neurons are inhibitory spiny projection neurons (SPNs), while the remaining 5% are GABAergic and cholinergic interneurons, thought to modulate striatal function by regulating the output projecting SPNs.

Both striatal SPNs and interneurons are dynamically modulated during movement. In particular, cholinergic interneurons (ChIs) have been shown to promote movement termination by synchronizing SPN activities. ChIs are also thought to contribute to oscillatory dynamics in normal and pathological striatal circuits, with ChI activation resulting in increased beta frequency (~15–30Hz) oscillations in striatal local field potential (LFP) recordings, as well as decreased locomotion akin to deficits observed in Parkinson's disease.

Current techniques, however, fall short of demonstrating how ChIs can coordinate their activity to influence SPNs and subsequent motor output, due to the inability to record both spiking and subthreshold activity from individual cells during movement. Towards this goal, in this dissertation, we first optimize a high-performance genetically-encoded voltage indicator (GEVI) in multiple electrically active systems, including in cardiac cells and tissue, and in both cortical and subcortical brain regions such as the striatum. We demonstrate that this GEVI, Archon1, can detect action potentials in multiple cells simultaneously, with kinetics and sensitivity comparable to the gold standard in the field, patch clamp electrophysiology. Further, its soma-localized variant, SomArchon, can detect both spiking and subthreshold dynamics in awake, behaving animals with high spatiotemporal precision across multiple brain regions. We then apply SomArchon to the striatum to investigate ChIs and SPNs during movement. We reveal that most ChIs and a subset of SPNs exhibit precisely timed spikes coupled to subthreshold voltage oscillations at delta frequency, as well as to higher frequency LFP beta-gamma oscillations, and that these delta-rhythmic neurons are preferentially modulated by changes in movement speed.

Overall, this dissertation develops the use of a high-performance genetically-encoded voltage sensor to probe the electrical activity of excitable cells with high sensitivity and spatiotemporal precision. When applied to the striatum, SomArchon allowed us to reveal critical insight into how delta oscillations, and in particular, ChIs, coordinate both motor activity and broader oscillation patterns in the striatum. Such an understanding could provide valuable insight into the basis of cholinergic signaling in the brain, as well as strategies for intervention in basal ganglia circuit disorders. Additionally, the novel voltage

imaging techniques deployed here could have a broad impact on systems neuroscience, cardiac biology, and the study of other electrically active systems, motivating future voltage imaging analysis of a variety of electrical circuits involved in behavioral and pathological paradigms.

TABLE OF CONTENTS

LIST OF TABLES

LIST OF FIGURES

LIST OF ABBREVIATIONS

1P ..... one-photon microscopy

2D ..... two-dimensional

2P ..... two-photon microscopy

3D ..... three-dimensional

AAV ..... adeno-associated virus

Ace ..... Acetabularia acetabulum rhodopsin

ACh ..... acetylcholine

ACSF ..... artificial cerebrospinal fluid

ANEPPS ..... amino naphthyl ethenyl pyridinium-based dye

ANOVA ..... analysis of variance statistical test

AP ..... anterior-posterior coordinate

APD50 ..... action potential duration at 50% repolarization

APD90 ..... action potential duration at 90% repolarization

APs ..... action potentials

AraC ..... cytosine arabinoside mitotic inhibitor

Arch ..... archaerhodopsin

ASAP ..... accelerated sensor of action potentials

ASAP3-Kv ..... ASAP3-$K_V2.1_{motif}$

ATPase ..... adenosine 5'-triphosphatase

AU or A.U. ..... arbitrary unit

BME ..... biomedical engineering

BOTLab ..... biomedical optical technologies lab at Boston University

BU ..... Boston University

C or °C ..... degrees Celsius

C terminus ..... carboxyl-terminus of a polypeptide amino acid chain

C. elegans ..... Caenorhabditis elegans

CA1 ..... hippocampal cornu ammonis region 1

Ca^{2+} ..... calcium ions

$CaCl_2$ ..... calcium chloride

CAG ..... CMV enhancer chicken β-actin promoter rabbit beta-globin splice acceptor

CaM ..... calcium-sensitive calmodulin domain

ChAT ..... choline acetyltransferase

ChI ..... striatal cholinergic interneuron

CM ..... cardiomyocyte

CMV ..... cytomegalovirus

CoChR ..... *Chloromonas oogama* channelrhodopsin

CPR ..... cardiopulmonary resuscitation

Cre ..... cyclization recombination recombinase

d ..... day(s)

D ..... delta-rhythmic neurons

D-glucose ..... dextrose, D-isomer of glucose

D1 ..... dopamine receptor 1

D2 ..... dopamine receptor 2

DARPP-32 ..... dopamine and cAMP-regulated neuronal phosphoprotein

DCAM .....digital camera

DCIMG ..... digital camera image file

Dept. ..... department

df ..... degrees of freedom

DIV ..... days *in vitro*

DL-lactate .....mixture of D-lactate isoform and L-lactate isoform

DMSO ..... dimethyl sulfoxide

DOF ..... degrees of freedom

DS .....down-sampled

DV ..... dorsoventral coordinate

E ..... embryonic day

EEG ..... electroencephalography

EGTA .....ethylene glycol-bis(β-aminoethyl ether)-*N*,*N*,*N*′,*N*′-tetraacetic acid

EKG ..... electrocardiography

Em .....emission wavelength

EMCCD .....electron multiplying charge coupled device

Eng. ..... engineering

Ephys ..... patch clamp electrophysiology

EPS .....whole heart cardiac electrophysiology study

ER2 .....endoplasmic reticulum export sequence

EU .....European Union

Ex ..... excitation wavelength

F ..... f-value in ANOVA test

FBS ..... fetal bovine serum

FOV ..... field of view

FRET ..... fluorescence resonance energy transfer

FWHM ..... value at full-width half-maximum

GABA ..... gamma-aminobutyric acid

GC ..... number of genome copies

GCaMP ..... genetically-encoded calmodulin green fluorescent fusion protein

GECI ..... genetically encoded calcium indicator

GEVI ..... genetically encoded voltage indicator

GFAP ..... glial fibrillary acidic protein

GFP ..... green fluorescent protein

GPe ..... globus pallidus externa

GPi ..... globus pallidus interna

GWISE ..... Graduate Women in Science & Engineering

GΩ ..... giga (10^9) ohm

HEK ..... human embryonic kidney cells

HEPES ..... 4-(2-hydroxyethyl)-1-piperazineethanesulfonic acid

hERG ..... human *ether-à-go-go*-related gene

hiPSC ..... human induced pluripotent stem cells

hMSC ..... human mesenchymal stem cells

hr ..... hour(s)

HSD ..... honestly significant difference (from Tukey test)

HTML ..... hypertext markup language

Hz ..... hertz

Iba1 ..... ionized calcium binding adaptor molecule 1

I_{change} ..... change in intensity

ID ..... inner diameter

I_{ex} ..... excitation wavelength

IgG ..... immunoglobulin G

ISI ..... inter-spike interval

IUE ..... *in utero* electroporation

JF525F ..... Janelia Fluor® 525 fluorescent dye

K-gluconate ..... potassium gluconate

KA2 ..... kainate receptor subunit 2

KCl ..... potassium chloride

kg ..... kilogram

KGC ..... Golgi export trafficking signal

kHz ..... kilohertz

KOH ..... potassium hydroxide

KS ..... Kolmogorov-Smirnov test

Kv2.1 ..... potassium voltage-gated channel, Shab-related subfamily member 1

Kv2.2 ..... potassium voltage-gated channel, Shab-related subfamily member 2

L2/3 ..... cortex layer 2/3

LED ..... light-emitting diode

LFP ..... local field potential

LP ..... longpass filter

LUT ..... look-up table

M1 ..... muscarinic acetylcholine receptor 1

M13 ..... skeletal muscle myosin light chain kinase peptide

M4 ..... muscarinic acetylcholine receptor 4

Mac ..... *Leptosphaeria maculans* rhodopsin

MEM ..... minimum essential medium

Mg-ATP ..... magnesium adenosine triphosphate

$MgCl_2$ ..... magnesium chloride

ML ..... mediolateral coordinate

ml ..... milliliters

mm ..... millimeter

mM ..... millimolar

mOsm ..... milliosmole

ms ..... millisecond

mTagBFP2 ..... monomeric blue fluorescent protein

MUA ..... multi-unit activity

mV ..... millivolt

mW ..... milliwatt

MYK-461 ..... mavacamten myosin inhibitor

MΩ ..... mega (10^6) ohm

N terminus ..... amino-terminus start of a polypeptide amino acid chain

Na-GTP ..... sodium guanosine-5'-triphosphate

Na_2ATP ..... adenosine triphosphate disodium salt

Na_3GTP ..... guanosine-5'-triphosphate trisodium salt

NaCl ..... sodium chloride

NaH_2PO_4 ..... monosodium dihydrogen phosphate

$NaHCO_3$ ..... sodium bicarbonate

NaOH ..... sodium hydroxide

$Na_v1.2$ ..... voltage-gated sodium channel type II

NBQX ..... 2,3-dioxo-6-nitro-7-sulfamoyl-benzo[f]quinoxaline

ND ..... non-delta rhythmic neurons

nd ..... not determined

Nif ..... Nifedipine

NIH ..... National Institutes of Health

nm ..... nanometer

nM ..... nanomolar

NRT ..... National Science Foundation research traineeship

NSD ..... no spikes detected

NSF ..... national science foundation

OCT ..... optimal cutting temperature compound

OD ..... outer diameter

optopatch..... dual optogenetics and voltage imaging

p ..... probability value

p-value ..... probability value

P# ..... postnatal day #

P2A ..... self-cleaving peptide 2A

paQuasAr3-s ..... paQuasAr3-PP-mCitrine-$K_V2.1_{motif}$-ER2

PBS ..... phosphate buffered saline

PGH ..... Pittsburgh series dyes

PGP1 ..... Harvard University Personal Genome Project

pH ..... potential of hydrogen

PhD ..... doctorate of philosophy

PLS ..... phase locking strength

PLV ..... phase locking value

Prof. ..... professor

PV ..... parvalbumin-expressing neurons

PVP ..... polyvinylpyrrolidone

QBP ..... quantitative biology & physiology

Quasar3-s ..... QuasAr3-PP-mCitrine-$K_V2.1_{motif}$-ER2

rAAV2 ..... recombinant adeno-associated virus vector, serotype 2

rAAV8 ..... recombinant adeno-associated virus vector, serotype 8

ROI ..... region of interest

ROS ..... reactive oxygen species

RPMI ..... Rosewall Park Memorial Institute medium

Rs ..... series resistance

s ..... seconds

SBR ..... signal to baseline ratio

sCMOS ..... scientific complementary metal-oxide-semiconductor

SD ..... standard deviation

SEM ..... standard error of the mean

SmT ..... smoothed trace

SNPc ..... substantia nigra pars compacta

SNR ..... signal to noise ratio

SomArchon ..... soma-targeted Archon1

SPN ..... striatal spiny projection neuron

SR ..... sustained release

SST ..... somatostatin-expressing neurons

ST ..... soma-targeted

std ..... standard deviation

STN ..... subthalamic nucleus

syn ..... synapsin promoter

TAN ..... tonically active neuron

tdT ..... tdTomato fluorescent protein

TRB ..... translational research in biomaterials

t_{rise} ..... rise time

trisGTP PVP..... tris buffered 5'-guanosine triphosphate

TTL ..... transistor-transistor logic

US ..... United States

UV ..... ultraviolet

V ..... volts

ViRMEn..... virtual reality MATLAB engine

Vm ..... subthreshold membrane voltage

V_{mo} ..... optically recorded membrane voltage

Voltron-ST ..... Ace2N-HaloTag-KGC-ER2-$K_V2.1_{motif}$

VSD ..... voltage-sensitive dye

VSFP ..... voltage-sensitive fluorescent protein

WPRE ..... woodchuck posttranscriptional regulatory element

zval ..... Wilcoxon rank sum z-statistic

Δ ..... change

$\Delta F/F$ ..... change of fluorescence divided by mean baseline fluorescence

λ_{em} ..... emission wavelength

λ_{ex} ..... excitation wavelength

μm ..... micrometer

μM ..... micromolar

μTUG ..... polydimethylsiloxane micro-fabricated tissue gauges

χ^2 ..... Pearson's chi-squared statistic

1 INTRODUCTION

1.1 Motivation & Significance

Motor disorders present a large public health burden and are one of the major causes of chronic disability in older adults, with nearly 30% of those between the ages of 50–89 displaying symptoms indicative of movement disorders[1]. A 2011 study of 31 countries, including the US, Canada, and the EU, projected that the prevalence of many of the most common motor disorders, most of which have no cure, would nearly double by the year 2050 (**Figure 1.1**)[2]. In addition to the impact on quality of life for patients and their families, the economic burden on individuals and on the healthcare system is profound. In 2010, the US economic burden of Parkinson's disease alone, the second most common motor disorder, was $14.4B and is projected to increase to greater than $24B by 2050[3].

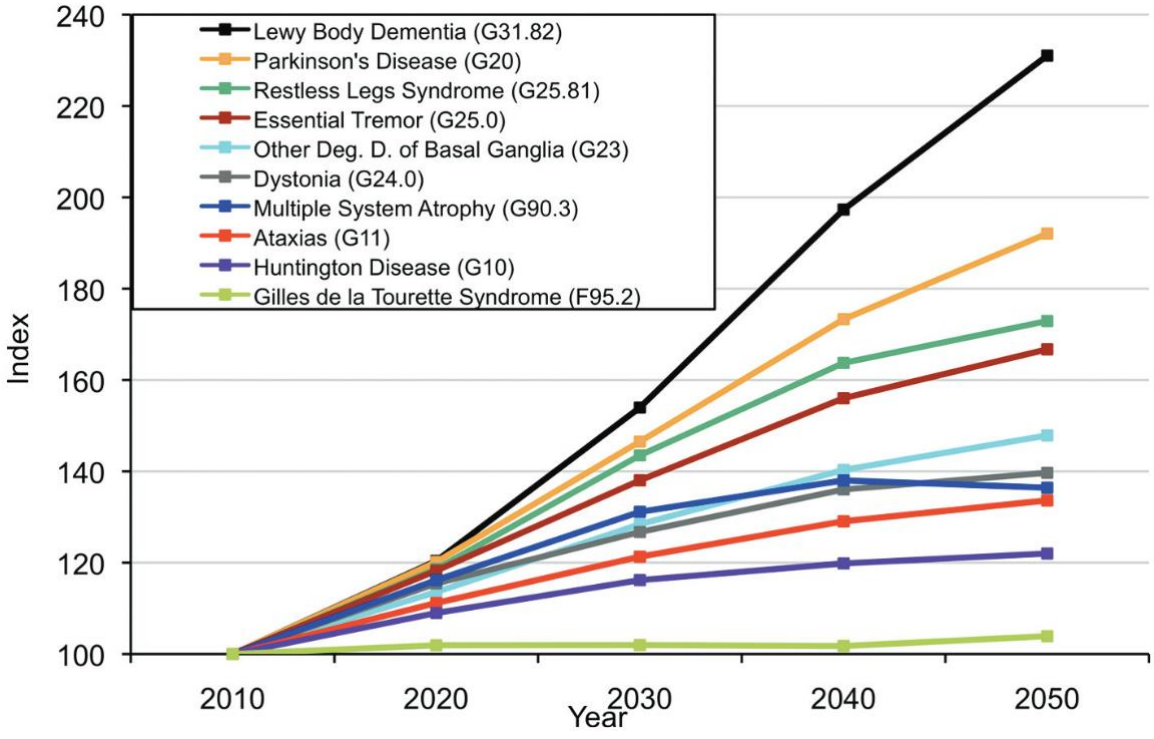

Figure 1.1. Projected prevalence over time of major motor disorders in 31 major countries (US, Canada, EU27, Norway, Switzerland). Adapted from Bach et. al. 2011[2].

Because the underlying neural circuit pathology is poorly understood, most currently available treatment options focus on symptom management, rather than targeting the root cause of disease[4–13]. This may lead to eventual resistance to therapies such as dopamine replacement or electrical stimulation[14–18], leaving patients with few options. There is thus an unmet need to better understand the underlying causes of such pathology, as well as healthy movement circuitry, in order to best develop targeted therapeutics for positive, long-term patient outcomes.

1.2 The basal ganglia circuit

The basal ganglia circuit has long been recognized as an important regulator of movement in the brain[19,20] with dysfunction of this circuit thought to be critical for the development of motor disorders such as Parkinson's and Huntington's disease[21,22]. The circuit consists of a feedforward loop where the motor cortex provides excitatory input to deep brain structures by way of the striatum, a relay station which incorporates dopaminergic activation by the substantia nigra, before feeding to the thalamus and back to the cortex[23,24]. The canonical two pathway model describes a direct or "GO" pathway which promotes movement, via disinhibition of the thalamus and activation of the motor cortex, and an indirect or "NO-GO" pathway that suppresses movement through the inhibition of the thalamus and cortex[25–28]. The striatum, as the largest nucleus of the basal ganglia, and integrator of various sources of input, plays a critical role in the execution or suppression of motor plans, although its exact mechanism of action is less well understood[29,30].

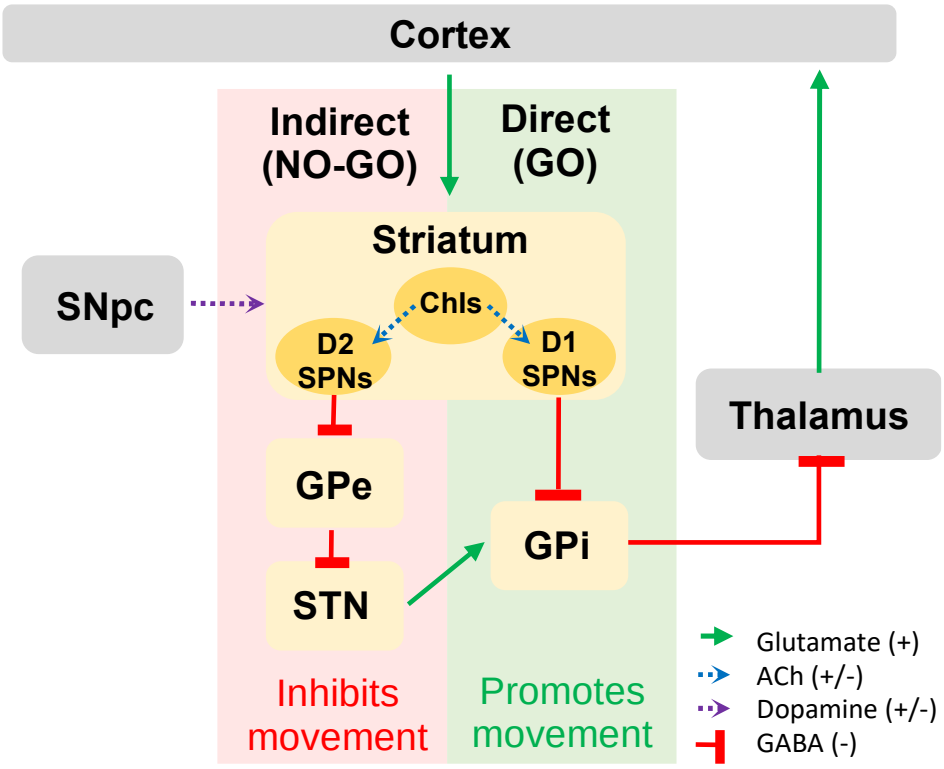

Figure 1.2. Basal ganglia circuit and the canonical two pathway model. In basal ganglia circuit disorders, such as Parkinson's disease, an imbalance in the indirect and direct pathways leads to motor dysfunction. GPe and GPi: globus pallidus externa and interna, respectively; STN: subthalamic nucleus; SNPc: substantia nigra pars compacta. ChIs: striatal cholinergic interneurons; D1 and D2 SPNs: dopamine receptor 1 and 2 striatal spiny projection neurons, respectively; Green arrows are excitatory (representing neurotransmitter glutamate), red are inhibitory (representing neurotransmitter GABA), while blue and purple are neuromodulatory, representing acetylcholine (ACh) and dopamine, respectively.

1.2.1 The dorsal striatum

The striatum is often divided into dorsal and ventral structural subregions, due to its discretized function. While the ventral striatum is associated with the limbic system and plays a critical role in reward pathways[31–34], the dorsal striatum is thought to be critical for motor control and has been implicated in the pathology of various movement disorders[19–22]. The dorsal striatum receives input primarily from three major sources: the cortex

(primarily motor and sensory cortices), the thalamus, and the substantia nigra[35,36]. Inputs from the cortices are mostly excitatory, modulated by the excitatory neurotransmitter glutamate. The substantia nigra pars compacta (SNpc), a specific region within the substantia nigra, sends dopaminergic projections to the striatum which alternatively activate or inhibit neurons, depending on dopamine receptor expression[37]. Death of these SNpc dopaminergic neurons cause dysregulation of movement and eventually result in motor dysfunction disorders, such as Parkinson's disease[38–41].

1.2.1.1 Spiny projection neurons and the two pathway model

The vast majority (~95%) of striatal neurons are inhibitory spiny projection neurons (SPNs), which project out of the striatum and are often classified into two groups based on their dopamine receptor expression[42,43]. The canonical two pathway model of the basal ganglia circuit suggests that SPNs expressing dopamine D1 receptors (D1-SPNs) form the direct pathway, promoting movement, while SPNs expressing dopamine D2 receptors (D2-SPNs) form the indirect pathway, inhibiting movement (**Figure 1.2**). However, recent calcium imaging studies have shown that both D1- and D2-SPNs are active during movement[44–46], suggesting that these two pathways may not be as segregated as previously thought. In addition, though SPNs exhibit very low, near zero, basal firing rates and little rhythmicity in resting states, during movement, SPNs can support high instantaneous firing rates[47,48] and be driven to oscillate[49–54]. Thus, it remains unclear how individual SPNs are modulated during movement, and whether different SPN populations are recruited at various phases of a movement bout.

1.2.1.2 Cholinergic interneurons and movement

The remaining 5% of striatal neurons are interneurons that are thought to modulate striatal output through inhibitory neurotransmitters such as GABA, or neuromodulators such as acetylcholine (ACh)[55–57]. Cholinergic interneurons (ChIs), are of particular interest because they are the main source of ACh in the striatum, where ACh is especially concentrated[58,59] and though they make up a small percentage of striatal neurons, their large, dense, and extensive arborizations reach across the striatum[58,60]. ChIs are thought to be tonically active neurons, with firing rates of 3–12Hz[58,61]. While ChIs in the ventral striatum have been extensively studied, demonstrating stereotypic pausing of tonic firing in relation to reward[31,58], recent electrophysiology studies in the dorsal striatum have found that ChIs modulate their spiking during movement[62,63]. More recently, calcium imaging studies have reported that dorsal striatum ChIs are both positively and negatively modulated at various phases of movement bouts[59,64]. Together, these results highlight the involvement of dorsal striatal ChIs in regulating movement, though it remains largely unclear how ChIs coordinate their activities to impact movement.

1.2.1.3 Relationship between SPNs and ChIs

The canonical two-pathway model (**Figure 1.2**) proposes that ChIs regulate both classes of SPNs via metabotropic ACh receptors. Recent work has demonstrated that stimulation of ChIs decreases movement speed and increases SPN co-activity[59,65] and in some cases results in motor deficits akin to those observed in Parkinson's disease in otherwise healthy mice[65–67]. Furthermore, activation of ChIs has been shown to increase

beta frequency oscillations (~15–30Hz) in the striatal local field potential (LFP), a bulk measure of local neuron activity. Beta oscillations are a known hallmark of motor disorders such as Parkinson's disease[66,68–75] and have also been observed transiently in functional motor behavior and planning[48,76–79].

1.3 Hypothesis

Based on these observations, we hypothesized that a relationship exists between ChIs, beta oscillations, and SPNs to mediate motor control. However, the source of these LFP oscillations and how ChIs particularly coordinate SPN activity remains unclear. Because action potentials are transient and sparse, LFP oscillations may be dominated by summated synaptic currents rather than spiking activity alone. Under this framework, synchronized oscillatory synaptic inputs to neurons could thus produce subthreshold membrane potential oscillations in individual neurons, which could organize spike timing[80–83].

To investigate how ChIs modulate SPNs during movement and how both groups relate to bulk LFP oscillations, we must thus observe the individual spiking and subthreshold dynamics of striatal neurons, while simultaneously recording LFP. Until recently, however, finding tools to monitor such dynamics in awake, behaving animals was extremely challenging. This dissertation aims to fill this gap by optimizing a novel genetically-encoded voltage sensor to enable detection of spiking and subthreshold dynamics with single cell-, single spike-precision to further investigate the above described striatal

circuitry in mice during movement.

1.4 Tools for monitoring electrical activity

1.4.1 Electrophysiology techniques

For the past 60 years, electrophysiology recording techniques have been the gold standard for measuring membrane voltage and have revealed important insights into the spiking and oscillation dynamics of electrically active systems, such as neurons and cardiac cells[84–94]. Most electrophysiology methods benefit from extremely high temporal resolution, with typical recording sampling rates at 10–40kHz (kilohertz). However, each technique has a uniquely narrow spatial precision that restricts its applicability to specific types of studies.

1.4.1.1 Intracellular & patch clamp recordings

Intracellular electrophysiology is an extremely precise, yet invasive technique that involves inserting a microelectrode (typically a glass pipette) into a cell to monitor electrical potential across the membrane[95]. Similarly, whole cell patch clamp techniques access the cell interior through a small opening on the membrane, while holding current or voltage constant and measuring the voltage changes or current flow, respectively[96]. Both techniques can be used to measure electrical activity, such as spiking and subthreshold dynamics of individual cells or synaptic potentials[95–97]. However, these methods are limited by the integrity of the pipette-membrane seal and are extremely difficult to perform in more

than one cell at a time. This restricts the duration and type of experiments able to be performed: first, because low throughput methods are insufficient for studies looking to investigate animal behavior or pathology which may involve large populations of cells, and second because, especially in awake animals, but even in anesthetized ones, animal movement presents a large problem to the stability of the electrode seal. Additionally, without the inclusion of secondary markers to label specific cell types, the genetic identity of cells is unknown, which may be critical information necessary for certain experiments. Thus, spike features or morphology have often been used to classify cells, and some of these features have been attributed to certain genetic identities (e.g. ChIs often display tonic firing rates[58,61] and thus tonically-active neurons (TANs) are often considered putative ChIs). Finally, due to the invasiveness of the procedure, many cells die once the electrode is removed, which presents difficulty for longitudinal studies or experiments where it is necessary to monitor the same cells at multiple time points. Recent advances in automated patch clamping techniques have made these extracellular recording techniques more accessible to end users and have even made it possible to extract genetic information for analysis of cell type, but it still remains difficult to monitor more than a few cells simultaneously in live mice and this low-throughput nature makes it challenging to adapt to various behavioral conditions[86,98,99] (see **Table 1.1**).

1.4.1.2 Extracellular electrophysiology techniques

Extracellular electrophysiology is a less spatially precise electrophysiology method that places an electrode into the brain or other electrically-active region of interest and

monitors the field activity generated in the region. Single-unit recordings (SUA) use small microelectrodes with tip sizes around 1μm, which subsequently capture the activity around one cell[100–102]. Increasing the size of the electrode allows multiple cells to be recorded and is often called multi-unit activity (MUA). If the recording field is relatively small and spatially arrayed microelectrodes are used, it is possible to predict how each cell may be contributing to the overall recorded electrical activity. However, as electrode sizes increase, the spatial arrangement of cells in an activity field may become unclear. When a single large electrode is used to measure the collective activity of a population of cells, this is called local field potential (LFP). MUA and LFP recordings are particularly useful when attempting to record from larger populations of cells in awake, behaving animals[103–106] as the recording apparatus does not require a tight seal or as precise positioning as do intracellular or patch clamp techniques. In addition to losing spatial precision, extracellular recording techniques have no way of determining cell identity as they are not sampling from inside the neuron (see **Table 1.1**). Despite these disadvantages, LFP recordings have revealed important insights into how oscillation dynamics of populations of neurons relate to behavior and pathology and have been an important clinical biomarker in human studies[68,107–112]. As LFPs have been hypothesized to be dominated by aggregated subthreshold activity of single neurons, in this work, it will be important to simultaneously record LFPs alongside single neuron activity to best understand the multi-spatial-scale dynamics of the dorsal striatum.

Table 1.1. Comparison of various tools for measurement of electrical activity.

		Electrophysiology		Dye-based Imaging		Genetically Encoded Sensors	
		Patch Clamp/SUA	MUA/LFP	Calcium Dyes	VSDs	Calcium Imaging	Voltage Imaging
Spatial Scale	Sub Cellular Activity	✓	X	X	X	✓	✓
	Single Cell Precision	✓	X	✓	✓	✓	✓
	Population Dynamics	X	✓	✓	✓	✓	✓
Temporal Scale	Individual Spikes	✓	X	X	✓	X	✓
	Subthreshold Dynamics	✓	X	X	?	X	✓
Experimental	Cell-Type Specificity	X	X	X	X	✓	✓
	During Behavior/State Modulation	?	✓	?	?	✓	✓

1.4.2 Calcium indicators

Intracellular calcium release, triggered by action potentials (APs), has long been used as a proxy for membrane voltage changes to study electrically active systems. In both neurons and cardiac cells, an influx of calcium accompanies action potential termination as it reaches a synapse or gap junction[113–118]. Calcium indicators are typically fluorescent molecules that change their fluorescence intensity in response to calcium concentration or binding events. Most indicators can be broken into two main types: chemical indicators (i.e., calcium-sensitive dyes) or fluorophore protein-based genetically encoded calcium indicators (GECIs), the most commonly used of which is GCaMP.

1.4.2.1 Calcium-sensitive dyes

Many calcium-sensitive dyes, such as the commonly used fura-2 or fluo series (fluo-3, fluo-4, etc), are chemical chelators that bind calcium ions (Ca^{2+}) with high

affinity[119]. When Ca^{2+} ions bind, this triggers a spectral frequency shift or increase in fluorescence which can be recorded by a camera, typically with around 30Hz sampling frequency. The largest disadvantage of calcium indicators is this time resolution. Although calcium indicators have a broad range of spatial resolution, able to monitor population dynamics of many cells simultaneously while retaining both single cell precision and the spatial arrangement of cells, they suffer from poor temporal resolution. While action potentials occur on the scale of milliseconds and have event rates ranging from 0.5–200Hz, calcium events occur on the scale of tens of milliseconds or longer[120–127]. In addition, calcium is an important secondary messenger in several signaling pathways and the uptake of intracellular calcium may not always be associated with action potentials or other electrical activity[128–133].

Dyes as a vehicle also pose other problems. Due to the chemical nature of the reagent, they must be reapplied often, as cells metabolize or dye washes out into solution. In addition to being tedious, this can restrict long term studies, and continuous reapplication of a chelating agent may be toxic to cell health[134–137]. Few studies have been able to use calcium-sensitive dyes *in vivo*, with many requiring intricate delivery systems to ensure adequate imaging conditions[138,139]. Furthermore, dyes ubiquitously label all cells to which they are applied and cannot be used to target specific subpopulations. It is possible to label specific cell subunits, such as the mitochondria, by permeabilizing cell membranes[140] or using dyes that tend to aggregate in specific organelles[141], however this is not as efficient as genetically targeting an indicator to a specific cell type or location (see **Table 1.1**).

1.4.2.2 GCaMP

Genetically-encoded indicators, such as GCaMP, aim to solve some of the drawbacks of dye-based measurement techniques, by expressing a calcium-sensitive fluorescent protein directly in the cells of interest. GCaMP, first developed in 2001, is a synthetic protein composed of a circularly permuted green fluorescent protein (GFP), a Ca^{2+}-sensitive calmodulin domain (CaM), and the M13 peptide from the myosin light chain kinase[142]. When calcium levels are low and the CaM domain remains unbound, the GFP remains in a protonated form and fluoresces minimally. However, in the presence of Ca^{2+} ions, the bound CaM domain undergoes a conformational change, protecting the GFP from protonation and allowing it to fluoresce. The genetically-targeted nature of GCaMP allows it to be applied easily to multiple spatial scales (e.g. subcellular, single cell, populations) and behavioral paradigms (e.g. to genetically label specific cell types or subcellular structures, for *in vivo* behavior experiments, within drug-induced pathological models) simultaneously (**Table 1.1**). As a result, GCaMP has become widely used for large-scale population imaging of neural activity[143–147], cardiac activity[148–150], as well as for other Ca^{2+}-dependent processes[151–155]. However, while calcium imaging studies have yielded important insights into population dynamics in a broad range of behavioral and pathological paradigms, as previously mentioned, calcium sensors do not have the time resolution to report individual spikes or subthreshold activity, which may be altered in biological, pharmacological or pathological states[156–167].

1.4.3 Optical voltage imaging

Due to the desire to measure membrane voltage changes directly, with both high temporal and spatial resolution, there has been a recent push to develop optical methods of tracking membrane voltage. Optical voltage sensors, like calcium indicators, can also be used across multiple spatial scales, but they have the benefit of directly measuring membrane voltage with single-spike precision and potentially even capturing subthreshold dynamics (see **Table 1.1**). Voltage indicators can also be categorized into voltage-sensitive dyes and genetically-encoded voltage indicators (GEVIs), as well as a third hybrid group, termed "chemigenetic" sensors, which integrate both genetically-encoded and chemical dye elements. Several GEVIs are still under development and thus far, there is no one superior sensor.

1.4.3.1 Voltage-sensitive dyes

Most voltage-sensitive dyes (VSDs) consist of a hydrophobic membrane-binding group, a hydrophilic head group to orient the dye with the electric field, and an intervening chromophore which, when excited by changes in the electric field, undergoes a spectral shift measured as fluorescence[168,169]. Recent attempts to study cardiac membrane potential have made use of VSDs such as the ANEPPS series or the PGH series[135,170–174]. Although many of these VSDs have the time resolution necessary to capture AP dynamics of cardiac cells, they often suffer from poor signal-to-noise ratio (SNR) and membrane localization, and are often cytotoxic[135,175]. In addition, by nature, similar to calcium dyes, VSDs are transient and must be reapplied to samples which hinders long term studies, and they lack the ability to label specific subpopulations without the addition of other chemical agents[176].

While a few studies have deployed VSDs *in vivo*[177,178] or demonstrated their ability to monitor subthreshold oscillations[179,180], it is unclear given their experimental limitations and poor sensitivity that VSDs would be suitable for precise spatiotemporal imaging in behaving animals.

1.4.3.2 Genetically-encoded voltage indicators

Similarly to calcium indicators, the disadvantages of VSDs gave rise for the need to develop effective genetically-encoded voltage indicators (GEVIs). The development of new GEVIs has opened the possibility for imaging population activity with high temporal and spatial precision. The majority of GEVIs fall into two categories: those with voltage-sensitive domains (VSDs) and those derived from rhodopsin proteins. Near-infrared GEVIs derived from rhodopsins offer high temporal fidelity, and are compatible with optogenetics[181–183], whereas green fluorescent GEVIs derived from voltage sensing domains of phosphatases or opsins are often slower and brighter[184–189]. Translating these sensors into awake, behaving animals has been challenging however, because poor membrane localization, photostability, and sensitivity of previous molecules has resulted in poor signal-to-noise ratio (SNR) *in vivo*. Prior to the work described in this dissertation, only Ace2N and paQuasAr3-s had been used to optically report voltage dynamics in a living mouse brain, reporting the activities from up to four cells in one field of view (FOV) in awake mice[97,188].

1.4.3.2.1 First generation GEVIs

GEVIs with VSDs such as ArcLight, Mermaid, ASAP1, or the VSFP series have been successfully applied to study cardiac cells, arrhythmias and neurons, as well as aid in cellular phenotyping, but they lack the time resolution, sensitivity, or SNR to capture voltage dynamics under various conditions[162,185,190–195]. ArcLight, for example, has slow kinetics which hinders its ability to capture the characteristic upstroke morphology of cardiac APs and any perturbations to this upstroke such as those caused by diseases or drugs[162,196–198]. In contrast, VSFP3.1 has relatively fast kinetics (activation time ~ 1.3ms) but displays fluorescence changes of only 0.5% per 100mV, which impedes monitoring of subthreshold fluctuations and contributes to a very low SNR[149,199]. Many of these VSD-based GEVIs thus suffer from this dichotomy between superior kinetics and sensitivity.

Rhodopsin-based sensors, such as Arch, Quasar1/2, MacQ, or Ace2N use their innate voltage-sensitive fluorescence or biophysics such as fluorescence resonance energy transfer (FRET) to optically report voltage dynamics[181,186,187,200]. Although these sensors often display faster kinetics than their VSD-based counterparts, they still suffer from low brightness, sensitivity, and signal-to-noise, hindering their ability to be applied *in vivo*[181,182,184–187,189,201]. See Section 3.4 and Figure 3.6 for a detailed discussion and comparison of next-generation GEVIs such as ASAP3, Quasar3, paQuasar3, and Voltron.

1.4.3.2.2 Archon1

Recently, Piatkevich et. al. developed a high-performance GEVI called Archon1, a far-red fluorescent plasma transmembrane protein evolved from the Arch3

archaerhodopsin, with fluorescence emission linearly dependent on membrane voltage[183]. Archon1 exhibits high temporal resolution, sensitivity, and brightness under simple one-photon widefield microscopy which enabled imaging of neural activity in mouse cortical brain slices, whole zebrafish, and *C. elegans*[183]. Archon1's fast kinetics and linear fluorescence-voltage relationship resulted in fluorescence traces which closely matched simultaneously recorded electrophysiology. Since Archon1 does not need chemical cofactors, the sensor showed no phototoxicity and retained photostability for up to 800 seconds in cultured mouse neurons[183]. In addition, Archon1 demonstrated excellent membrane localization and did not alter membrane resistance, capacitance, or resting potential as compared to non-expressing cells. Its far-red excitation is also compatible with blue-light driven optogenetics enabling all-optical electrophysiology[183,202]. These features of Archon1, along with its easily adaptable one-photon widefield imaging setup, make it an ideal GEVI candidate to deploy in other electrically-dependent systems.

1.5 Overview

1.5.1 *Voltage imaging of cardiac cells and tissue using Archon1*

In this dissertation, I first demonstrate the applicability of Archon1 as a high-performance GEVI by deploying it in cardiac cells and tissue[203]. When expressed in cardiomyocytes, Archon1 demonstrated fast kinetics comparable to patch-clamp electrophysiology, and SNR significantly greater than the leading VSD used in the field. With Archon1, we were able to detect drug-induced changes in action potential waveforms and monitor voltage dynamics across multiple cells simultaneously in 3D cardiac tissues.

This study also helped us to optimize voltage imaging systems with improved sensitivity in order to measure individual neuron voltage dynamics in the mouse brain, enabling the other studies discussed in this dissertation, as well as future investigations into neural circuitry.

1.5.2 Development of a soma-targeted GEVI for imaging in multiple brain regions

Next, I describe how we developed a soma-targeted version of Archon1, termed SomArchon, which allowed us to conduct *in vivo* population voltage imaging in multiple cortical and subcortical brain regions of awake, behaving mice using conventional, widefield microscopy[202]. SomArchon had comparable kinetics, SNR, and sensitivity to its predecessor Archon1 and outperformed many other next-generation soma-targeted voltage sensors. We also demonstrated SomArchon's compatibility with blue-light optogenetics and were able to detect spiking and subthreshold activity in multiple neurons simultaneously, while recording LFPs. Most importantly to this work, SomArchon was able to detect voltage dynamics, both spiking and subthreshold, from individual striatal neurons, while mice ran on a spherical treadmill. In addition to aiding our work henceforth, SomArchon has already been deployed in other studies[204,205] and we expect that the novel voltage imaging techniques described here could have a broad impact on systems neuroscience, motivating future voltage imaging analysis of a variety of neural circuits involved in behavior and pathology.

1.5.3 Using SomArchon to investigate striatal circuits during movement

Finally, I describe how we deployed SomArchon in the dorsal striatum to investigate striatal ChI and SPN activity during movement, and their relationship to LFP dynamics. We found that most ChIs and a subset of SPNs exhibited spike bursts locked to delta frequency oscillations, and that these delta-related spikes organized higher frequency oscillations, such as beta oscillations, in both Vm and LFP. In addition, during movement, these neurons appeared time-locked to transitions in movement speed, and ChI spiking, in particular, was associated with increases in LFP delta and gamma oscillations during high movement, suggesting a unique role of ChIs in neural synchronization during locomotion. Finally, we corroborated existing studies that linked beta power to immobility, as LFP beta power decreased during high movement around SPN spikes. Together, these results demonstrate that the Vm and spiking dynamics of individual neurons in the nucleated striatum can support oscillation network features that are prominent in cortical-basal ganglia circuits during locomotion and that delta oscillations in particular play a prominent role in supporting striatal participation in cross-region computation via network level synchronization.

2 VOLTAGE IMAGING OF CARDIAC CELLS AND TISSUE USING THE GENETICALLY-ENCODED VOLTAGE SENSOR ARCHON1

2.1 Citation

The work described in this chapter has been published at iScience[203]. **Shroff SN***, Das SL*, Tseng HA, et al. Voltage Imaging of Cardiac Cells and Tissue Using the Genetically Encoded Voltage Sensor Archon1. ***iScience***. 2020; **23**(4):100974. doi:10.1016/j.isci.2020.100974.

2.2 Summary

Precise measurement of action potentials (APs) is needed to observe electrical activity and cellular communication within cardiac tissue. Voltage-sensitive dyes (VSDs) are traditionally used to measure cardiac APs, however they require acute chemical addition that prevents chronic imaging. Genetically encoded voltage indicators (GEVIs) enable long-term studies of APs without the need of chemical additions, but current GEVIs used in cardiac tissue exhibit poor kinetics and/or low signal-to-noise (SNR). Here, we demonstrate the use of Archon1, a recently developed GEVI, in hiPSC-derived cardiomyocytes (CMs). When expressed in CMs, Archon1 demonstrated fast kinetics comparable to patch-clamp electrophysiology, and high SNR significantly greater than the VSD Di-8-ANEPPS. Additionally, Archon1 enabled monitoring of APs across multiple cells simultaneously in 3D cardiac tissues. These results highlight Archon1's capability to investigate the electrical activity of CMs in a variety of applications, and its potential to

probe functionally-complex *in vitro* models, as well as *in vivo* systems.

2.3 Introduction

The measurement of electrical potential and conduction in the heart are important for understanding how electrical signals propagate through cardiac tissue in both healthy and diseased conditions. Although numerous methods exist for monitoring whole-heart voltage (EKG, EPS, etc.), few techniques examine the properties at the individual cell level within cardiac tissue. Intracellular calcium release, triggered by action potentials (APs), has long been used to study mechanisms such as excitation-contraction coupling, and as a proximal measurement for signal propagation[148,151–153]. However, calcium does not provide insight into membrane voltage dynamics and individual AP waveforms, which may be altered in biological, pharmacological, or pathological states[156–164]. Recent attempts to study cardiac membrane potential have made use of voltage-sensitive dyes (VSDs) such as the ANEPPS series or the PGH series[135,170–174]. Although many of these VSDs have the time resolution necessary to capture AP dynamics of cardiac cells, they often suffer from poor signal-to-noise ratio (SNR) and membrane localization, and are often cytotoxic[135,175]. In addition, by nature, VSDs are transient and must be reapplied to samples, which hinders long term studies and they also lack the ability to label specific cell subpopulations.

Genetically encoded voltage indicators (GEVIs), which have been successfully utilized in a similarly electrically-excitable cell population, neurons[97,181–189,206–208], have recently been deployed in cardiac tissue to overcome the shortcomings of VSDs[162,175,209]. Although

GEVIs such as ArcLight, Mermaid, or the VSFP series have been successfully applied to study arrhythmias, as well as aid in cellular phenotyping, these GEVIs lack the time resolution, sensitivity, and SNR to capture voltage dynamics under various conditions[162,190–193]. For example, ArcLight, a commonly used GEVI, has slow kinetics which hinders its ability to capture the characteristic upstroke morphology of cardiac APs and any perturbations to this upstroke such as those caused by diseases or drugs[162,196–198]. In contrast, the GEVI VSFP3.1 has relatively fast kinetics (activation time ~ 1.3ms) but displays fluorescence changes of only 0.5% per 100mV which impedes monitoring of subthreshold fluctuations and contributes to a very low SNR[149,199]. Many of these GEVIs thus suffer from this dichotomy between superior kinetics and sensitivity.

Recently, Piatkevich et al. developed a high-performance GEVI called Archon1, a far-red fluorescent plasma transmembrane protein evolved from the Arch3 opsin, with fluorescence emission linearly dependent on membrane voltage[183]. Archon1 exhibits high temporal resolution, sensitivity, and brightness under simple one-photon widefield microscopy which enabled imaging of neural activity in mouse cortical brain slices, whole zebrafish, and *C. elegans*[183]. Archon1's fast kinetics and linear fluorescence-voltage relationship resulted in fluorescence traces which closely matched simultaneously recorded electrophysiology. Since Archon1 does not need chemical cofactors, the sensor showed no phototoxicity and retained photostability for up to 800 seconds in cultured mouse neurons[183]. In addition, Archon1 demonstrated excellent membrane localization and did not alter membrane resistance, capacitance, or resting potential as compared to non-

expressing cells. Its far-red excitation is also compatible with blue-light driven optogenetics enabling all-optical electrophysiology[183,202]. These features of Archon1, along with its easily adaptable one-photon widefield imaging setup, make it an ideal GEVI candidate to deploy in other electrically-dependent systems. Here, we demonstrate Archon1's utility for monitoring cardiac APs in both 2D cell culture and 3D tissue environments under a variety of biologically-relevant conditions (**Figure 2.1**).

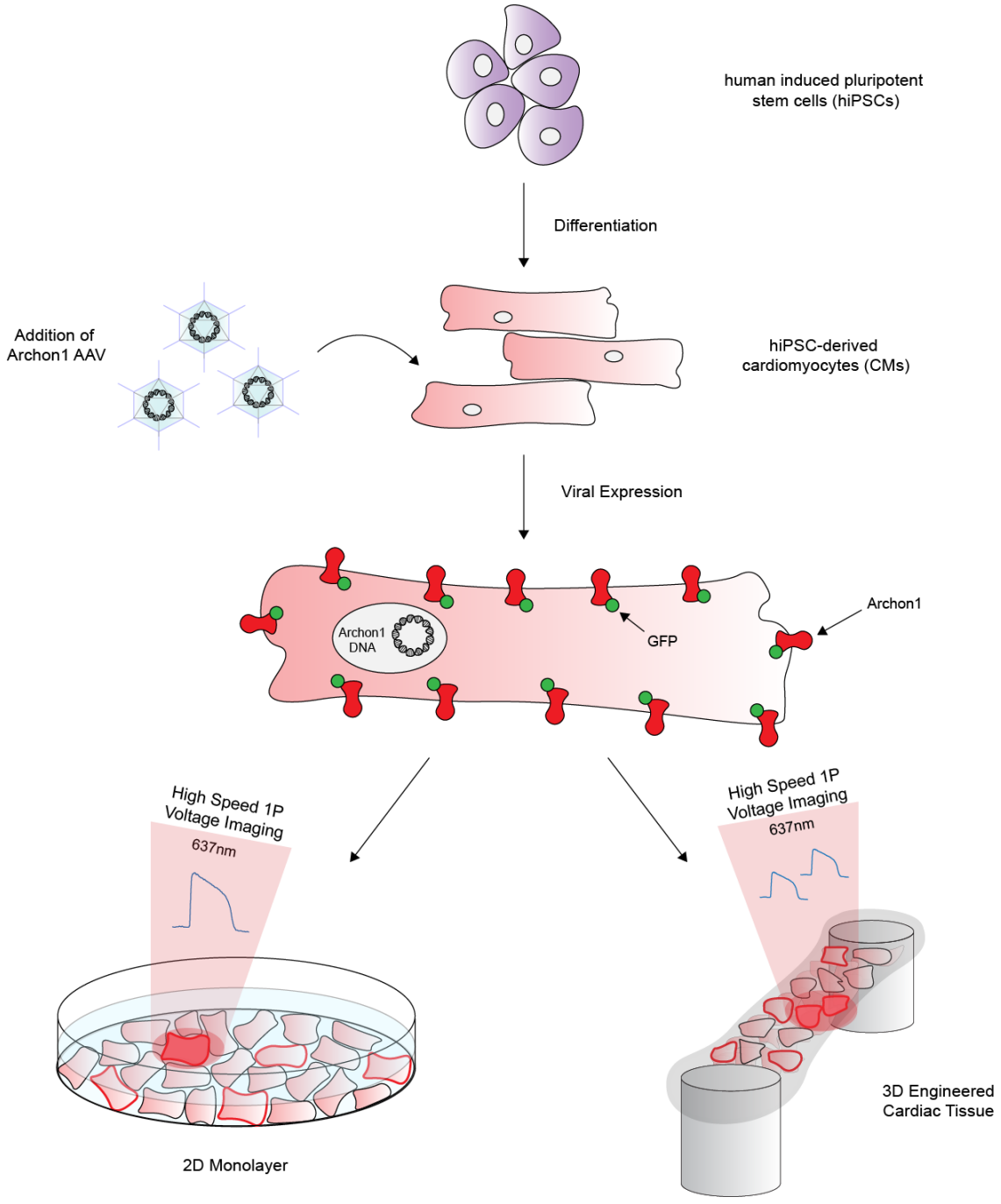

Figure 2.1. Diagram describing transduction of Archon1 AAV into hiPSC-derived cardiomyocytes (CMs) for high-speed one photon voltage imaging in 2D cultures and 3D engineered cardiac tissues.

2.4 Characterization of Archon1 in iPSC-derived cardiomyocytes

Archon1 was expressed in 2D monolayers of human induced pluripotent stem cell (iPSC)-derived cardiomyocytes (CMs) using both Cre-dependent CAG-Archon1-KGC-EGFP-ER2 (Archon1) and CMV-Cre AAVs (**Figure 2.2A**) 5–7 days after spontaneous beating was observed. CM membrane potential was recorded optically at 100Hz using a scientific cMOS camera (l_{ex}=637nm). Archon1 fluorescence changes exhibited typical cardiac AP waveforms with clearly identifiable phases (**Figure 2.2B,C;** i: resting potential, ii: peak depolarization, iii: end of repolarization). Changes in intensity were not due to motion from cellular contraction as indicated by lack of fluorescence changes in the GFP channel, as compared to the Archon1 channel (see **Videos S1&S2** from Shroff et al. 2020[203]). In order to quantify AP duration, we calculated rise time (t_{rise}; defined by 10% to 90% of the valley-to-peak duration), APD50 (AP duration at 50% repolarization), and APD90 (AP duration at 90% repolarization) (**Figure 2.2D,** see **Methods**). Without electrical stimulation, APD90 values ranged from 345–1210ms (n = 31 cells, 880±218ms, mean±standard deviation, **Figure 2.2C right**). We then evoked APs by electrically pacing CMs at 0.5 Hz, 1Hz, and 2 Hz, and found that Archon1 fluorescence faithfully followed electrical stimulation (**Figure 2.2E**; respective APD90 distributions, **Figure 2.2F**). Together, these results demonstrate that Archon1 can robustly capture AP dynamics and waveform morphology, and this capability is maintained at higher frequencies.

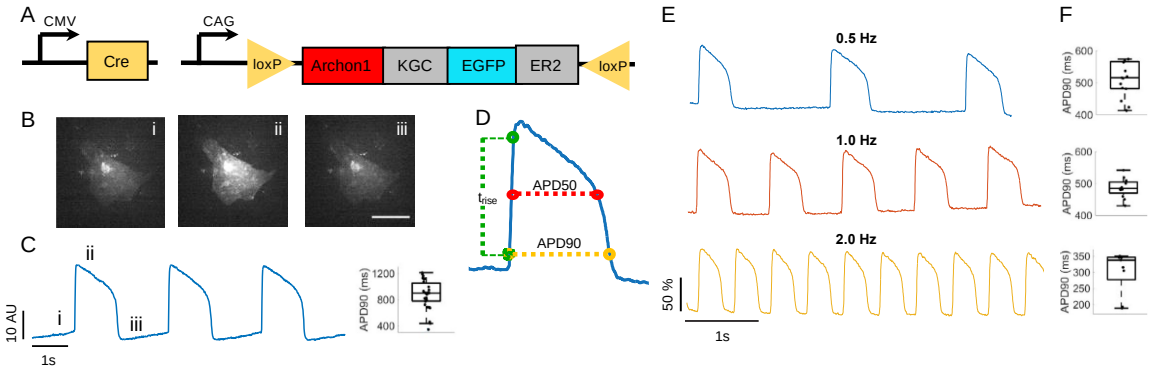

Figure 2.2. Demonstration of Archon1 for monitoring action potentials of iPSC-derived cardiomyocytes. (A) Diagrams of cre-recombinase AAV system used to infect CMs with Archon1. KGC: linker, ER2: ER export trafficking sequence. **(B)** Single frame images of CM expressing Archon1 at different phases of an AP as shown in **C**. Scale bar, 50 μm. **(C)** *Left*, optically recorded raw voltage trace for cell shown in **B**. *Right*, quantification of APD90, as defined in **D**, per voltage trace for unpaced CMs (n= 31 cells). **(D)** An example AP waveform with APD90, APD50, and rise time (t_{rise}) defined. **(E)** Representative normalized fluorescence voltage traces from CM electrically paced at 0.5 Hz (blue), 1 Hz (orange), and 2 Hz (yellow). **(F)** Corresponding APD90 box plot for each pacing shown in **E** (from n = 15, 12, 9, cells, respectively). Box plots represent 25th to 75th percentiles, with whiskers extending 1.5x the interquartile range, horizontal line represents median, each dot represents data from a single cell. All optical traces obtained at image acquisition rate of 100Hz.

To quantify Archon1 performance, we conducted patch-clamp electrophysiology while simultaneously optically recording Archon1 fluorescence of CMs. We found that membrane voltage recorded via Archon1 fluorescence matched well with that recorded via electrophysiology (representative overlay in **Figure 2.4A**). Archon1 fluorescence was linearly correlated with electrically recorded membrane potential (**Figure 2.4B**; example corresponding to **Figure 2.4A;** Least Squares Regression Line: $y = 0.009x – 0.584$; $R^2 = 0.996$) for all simultaneously recorded cells (n = 4 cells, **Figure 2.4C;** Least Squares Regression Line: $y = 0.926x – 0.048$; $R^2 = 0.989$). In addition, Archon1 expression did not alter CM properties such as resting membrane potential, beat amplitude, membrane resistance, rise time, APD90, and beat period (**Figure 2.3,** see statistics in **Table 2.1**).

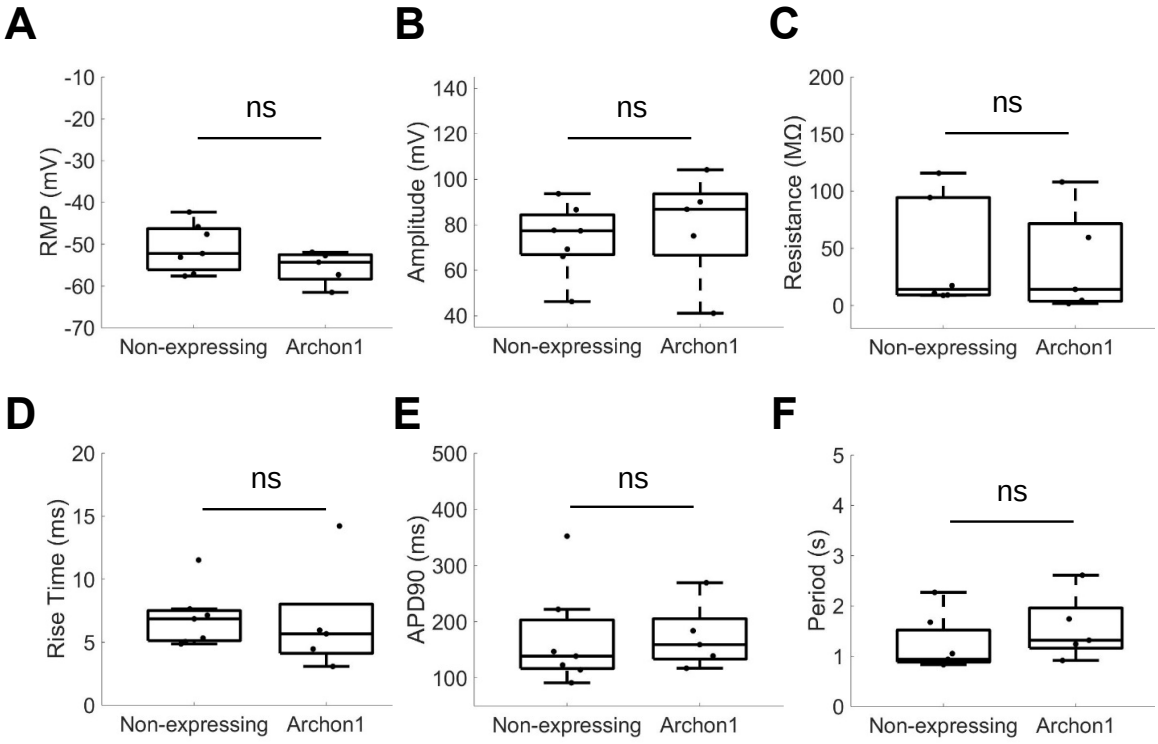

Figure 2.3. Quantification of electrophysiological properties of non-expressing CMs compared to Archon1-expressing CMs. Related to **Figure 2.4**. **(A)** Resting membrane potential (RMP, n = 7, 5 cells, respectively), ns, $p > 0.05$ in two-tailed t-test. **(B)** Action potential amplitude (n = 7, 5 cells, respectively), ns, $p > 0.05$ in two-tailed t-test. **(C)** Resistance (n = 6, 5 cells, respectively), ns, $p > 0.05$ in two-tailed t-test. **(D)** Rise time (n = 7, 5 cells, respectively), ns, $p > 0.05$ in two-tailed t-test. **(E)** APD90 (n = 7, 5 cells, respectively), ns, $p > 0.05$ in two-tailed t-test. **(F)** Beat period (n = 7, 5 cells, respectively), ns, $p > 0.05$ in two-tailed t-test. See full statistics in **Table 2.1**. Box plots represent 25th to 75th percentiles, with whiskers extending 1.5x the interquartile range, horizontal line represents median, each dot represents data from a single cell.

Table 2.1. Two tailed student t-test for Figure 2.3 comparing electrophysiological properties of Archon1-expressing vs. non-expressing cardiomyocytes.

Property	**p value**
Resting Membrane Potential	0.146
Amplitude	0.628
Resistance	0.861
Rise Time	0.905
APD90	0.934
Period	0.343

To further characterize the performance of Archon1, rise times were calculated across all CMs recorded with electrophysiology and Archon1 (n = 17 cells for electrophysiology, 67

cells for Archon1; **Figure 2.4D**). The rise time of Archon1 (29.8±13.2ms, mean±standard deviation) was slightly longer than that of electrophysiology (15.9±5.6ms, mean±standard deviation; Ephys ↔ Archon1: p=5.8E-05; two-tailed student t-test; **Table 2.2**). To examine how these kinetic measures are influenced by the difference in data acquisition rates — 10–20kHz for electrophysiology vs. 100Hz for Archon1 — we down-sampled the same electrophysiology data to 100Hz to match the optical imaging frame rate. We obtained a rise time of 23.3±9.4ms (mean±standard deviation) for down-sampled electrophysiology traces, which was no longer significantly different from Archon1 (p=0.06, two-tailed student t-test; **Figure 2.4D**).

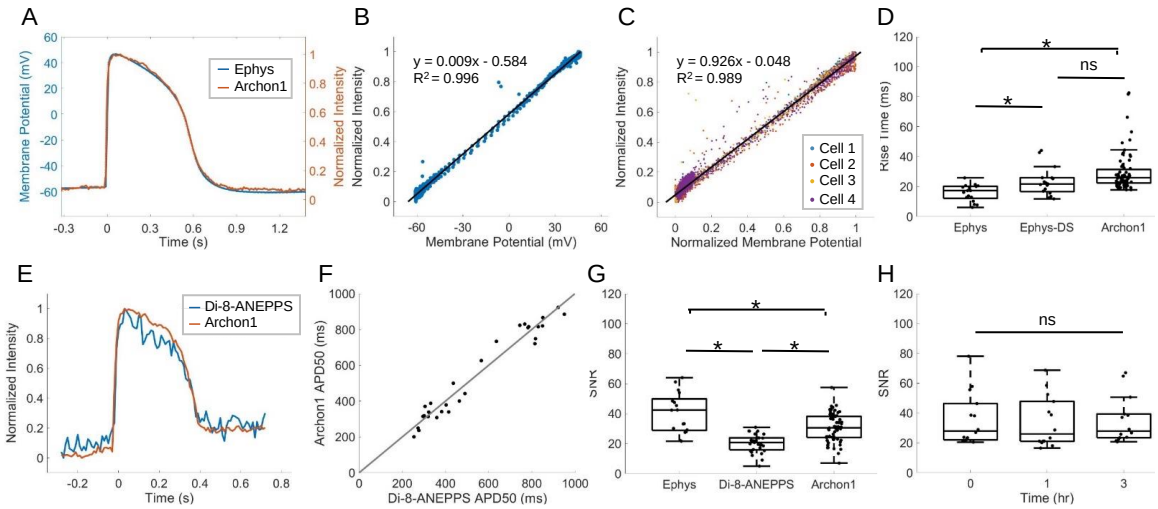

Figure 2.4. Characterization of Archon1 in iPSC-derived cardiomyocyte monolayers. (A) Representative overlay of single AP waveform simultaneously measured using patch-clamp electrophysiology (blue) and Archon1 fluorescence (orange). **(B)** Normalized intensity Archon1 fluorescence trace vs. membrane potential recorded via electrophysiology for cell simultaneously recorded in **A**. Trendline equation and R^2 value shown on chart. **(C)** Normalized intensity Archon1 fluorescence traces vs. normalized membrane potential from all simultaneously recorded cells (n = 4). Trendline equation and R^2 value shown on chart. **(D)** Quantification of rise time, as defined in **Figure 2.2D**, per cell for patch-clamp electrophysiology (*Ephys*; acquired at 10-20kHz), down-sampled electrophysiology (*Ephys-DS*; same electrophysiology data down-sampled to 100Hz to match the acquisition rate of Archon1) and Archon1 (*Archon1;* acquired at 100Hz) from n = 17, 17, and 67, cells, respectively. *: $p < 0.05$ in two-tailed student t-test, ns: $p > 0.05$ in two-tailed t-test. **(E)** Representative overlay of single AP waveform measured with Di-8-ANEPPS (blue) vs. Archon1 (orange). **(F)** APD50 values per cell for Archon1 vs. Di-8-ANEPPS. Trendline equation

and R^2 value shown on chart. **(G)** Quantification of SNR (defined in **Methods**) per cell for patch-clamp electrophysiology, Di-8-ANEPPS, and Archon1 (from n = 17, 29, 67, cells, respectively). *, $p < 0.05$ in two-tailed student t-test. **(H)** Quantification of SNR per cell recorded repeatedly with Archon1 at t = 0, 1hr, and 3hrs (n = 14 cells). ns: $p > 0.05$ in two-tailed t-test. See **Figure 2.5A–C** for optical traces of representative cell. Box plots displayed as described in **Figure 2.2**. For full statistics see **Table 2.2**. All optical traces obtained at image acquisition rate of 100Hz; patch clamp electrophysiology acquisition rate, 10-20kHz.

We also compared Archon1 with a widely used red membrane-targeted voltage dye, Di-8-ANEPPS (I_{ex}=470nm; **Figure 2.4E**). APD90 values were also compared per cell between Di-8-ANEPPS and Archon1, and showed a nearly 1:1 correlation (Least Squares Regression Line: $y = 1.001x - 0.003$, $R^2 = 0.954$; **Figure 2.4F;** n = 29 cells). To compare performances across electrophysiology, Di-8-ANEPPS, and Archon1, we calculated the corresponding SNR (defined as the valley-to-peak amplitude divided by the standard deviation of the noise) for each method (n = 17, 29, 67 cells, respectively; **Figure 2.4G**). SNR was significantly different between all groups, with Archon1's SNR (Archon1: 30.7±9.3, mean±standard deviation) significantly higher than that of Di-8-ANEPPS (Di-8-ANEPPS: 20.2±6.1, mean±standard deviation; Archon1 ↔ Di-8-ANEPPS: p=4.87E-08; two-tailed student t-test), but significantly lower than that of electrophysiology (Ephys: 40.36±13.5, mean±standard deviation; Ephys ↔ Archon1: p = 8.3E-04, two-tailed student t-test; **Table 2.2**). Together, these results demonstrate that Archon1 voltage imaging exhibited comparable kinetics to that achieved via patch-clamp electrophysiology, and SNR significantly better than the VSD Di-8-ANEPPS.

Table 2.2. Two tailed student t-test for Figure 2.4D,G between rise time or SNR of CMs recorded with patch-clamp electrophysiology, Di-8-ANEPPS, or Archon1.

	Comparison	p value
Rise Time	ephys ↔ down-sampled ephys	8.86E-03
	ephys ↔ Archon1	5.83E-05
	down-sampled ephys ↔ Archon1	0.0584
SNR	ephys ↔ Di-8-ANEPPS	1.35E-08
	Di-8-ANEPPS ↔ Archon1	2.91E-07
	ephys ↔ Archon1	8.31E-04

Because Archon1 is genetically encoded and optical voltage imaging does not incur mechanical damage to the cell membrane, as with electrophysiology, Archon1 should allow repeated imaging of the same cells. To demonstrate Archon1's robustness over time, CMs expressing Archon1 were imaged repeatedly at three time points: (t = 0, 1, and 3 hrs) (n =14 cells, **Figure 2.4H**, example in **Figure 2.5A–C**). Over repeated recordings, SNR remained constant (36.0±17.7, 34.1±17.1, 35.1±15.6 mean±standard deviation for t = 0,1,3 hrs respectively; $p = 0.96$, repeated measures one-way ANOVA; **Table 2.3**). We also found that Archon1 was highly photostable over 5 minutes of continuous imaging with SNR remaining stable across the recording (**Figure 2.5D–F**; SNR: 24.67±0.659, 24.72±0.475, 24.56±0.816, mean±standard deviation, for t = 0–20s, 100–120s, 280–300s, respectively; $p = 0.73$, repeated measures one-way ANOVA; full statistics in **Table 2.4**). Further, CMs expressing Archon1 retained expression months post-infection (see Shroff et. al. 2020[203] for video of Archon1-expressing CM at day 62 after infection). Archon1 is thus capable of monitoring CM APs over extended periods of time, with high fidelity as compared to currently available methods, in cultured 2D monolayers.

Table 2.3. Repeated measures one-way ANOVA for Figure 2.4H of SNR per cell recorded repeatedly at t = 0, 1, 3 hours.

Mauchly's Test of Sphericity for SNR

Within Subjects Effect	Mauchly's W	Approx. Chi-Square	df	Sig.
Time	0.683	4.568	2	0.102*

*Sphericity can be assumed

Repeated Measures ANOVA: Tests of Within-Subjects Effects

Source	Assumption	Type III Sum of Squares	df	Mean Square	F	Sig.	Partial Eta Squared
Time	Sphericity Assumed	23.928	2	11.964	0.201	0.819	0.015

Table 2.4. One-way ANOVA for Figure 2.5D–F of SNR per waveform of cell recorded for 5 minutes

Groups	Count	Sum	Average	Variance
0 to 20s	18	444.1389	24.67438	0.434717
100 to 120s	18	445.103	24.72794	0.226051
last 20s	18	442.0286	24.55714	0.665828

Source of Variation	SS	df	MS	F	P-value	F crit
Between Groups	0.274723	2	0.137361	0.310633	0.73436	3.178799
Within Groups	22.55213	51	0.442199			
Total	22.82686	53				

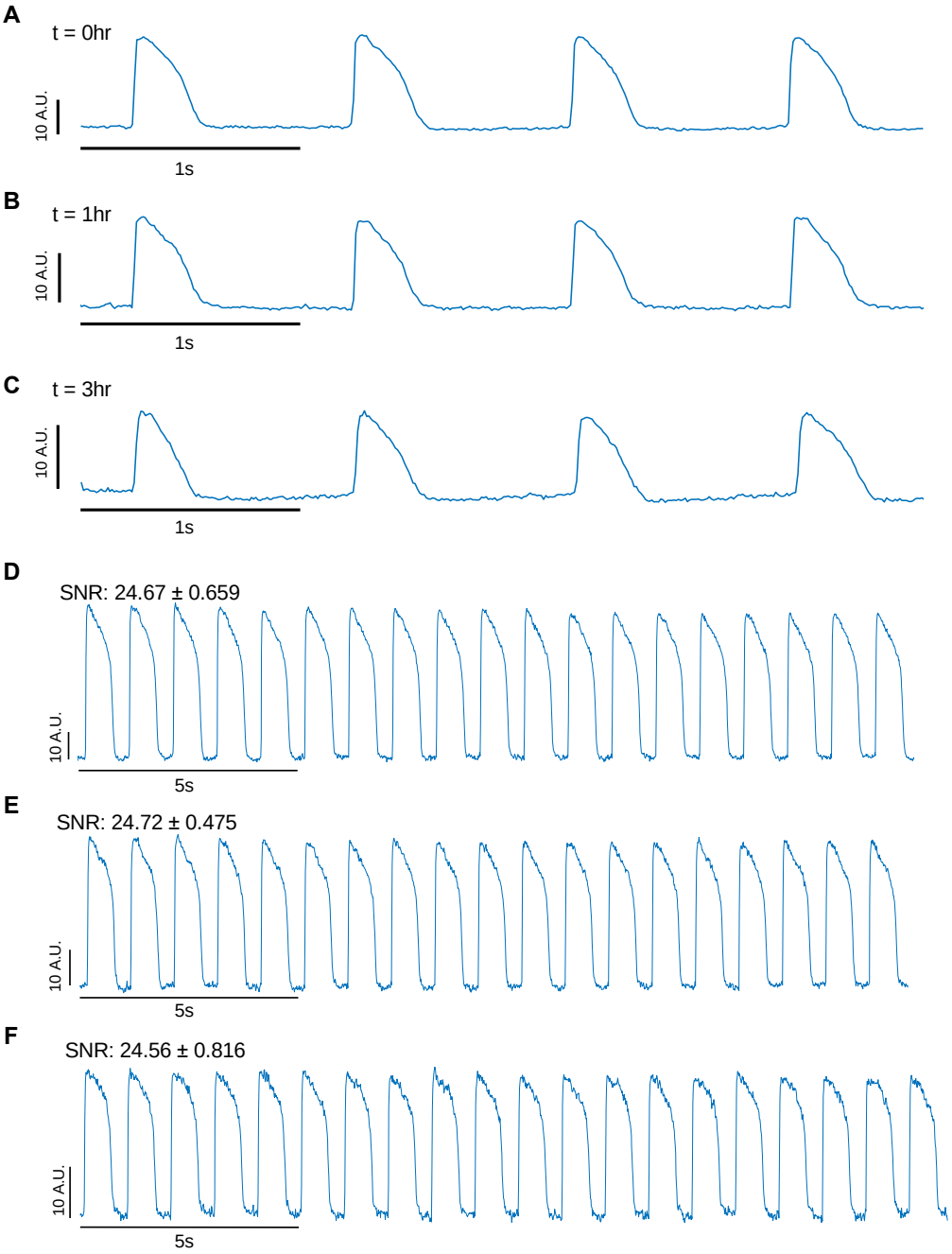

Figure 2.5. Archon1 allows for robust measurement of action potentials under repeated and long-duration imaging. Related to **Figure 2.4H**. **(A–C)** Representative optical voltage trace for an example CM recorded repeatedly at **(A)** t = 0hr, **(B)** t = 1hr, **(C)** t = 3hr. Electrically paced at 1Hz. Quantification of SNR for all repeatedly recorded cells in **Figure 2.4H**. **(D–F)** Archon1 optical voltage trace for CM recorded for 5 minutes continuously, electrically paced at 1Hz. **(D)** 0–20s; SNR: 24.67±0.659, mean±standard deviation, **(E)** 100–120s; SNR: 24.72 ±0.475, mean±standard deviation, **(F)** 280–300s; SNR: 24.56 ±0.816, mean±standard deviation. $p = 0.734$, one-way ANOVA. For full statistics see **Table 2.4**. All optical traces obtained at acquisition rate of 100Hz.

2.5 Archon1 can reliably detect pharmacologically-induced changes in AP waveforms

To examine the sensitivity of Archon1 to detect changes in AP waveforms, we recorded Archon1-expressing CMs upon the application of two well characterized ion channel inhibitors, E-4031 and Nifedipine. E-4031 is a hERG K+ ion channel inhibitor that prolongs the refractory period of the cardiac AP[157,159]. Nifedipine, on the other hand, is a Ca2+ ion channel inhibitor which shortens the AP plateau and overall AP duration and is commonly used to treat hypertension and angina[160]. Archon1 fluorescence was imaged from the same cells before and after inhibitor treatment. Treated groups were compared to a DMSO control group (**Figure 2.6A**). E-4031 treatment of 2D monolayers at increasing concentrations (3nM, 10nM, 30nM) showed concentration-dependent prolongation of APs. (**Figure 2.6B**). We compared the mean APD90 before and after E-4031 treatment for all concentrations and observed increasing %ΔAPD90 with increasing E-4031 concentration (mean±standard deviation, n=10; 3nM: 25.2±12.2%, 10nM: 43.2±8.9%, 30nM: 55.2±8.1%; full statistics in **Table 2.5**) in comparison to the %ΔAPD90 of the DMSO control (n=10, 1.7%±3.6%), consistent with previous studies[157,173,210–212] (**Figure 2.6D**). Nifedipine treatment of 2D monolayers at increasing concentrations (10nM, 30nM, 100nM) also showed the expected concentration-dependent shortening of AP length (**Figure 2.6C**). Comparison of the mean APD50 before and after treatments for all three concentrations showed an inverse relationship between %ΔAPD50 and Nifedipine concentration (n=10; 10nM: -7.3±2.0%, 30nM: -11.4±1.9%, 100nM: -25.0±4.4%, n=10), compared to the DMSO control (n=10, 1.9±4.3%) (**Figure 2.6E; Table 2.6**), consistent

with previous studies which have performed similar measurements[173,210,212,213]. Thus, Archon1 is capable of capturing changes in AP waveform morphology in 2D monolayers.

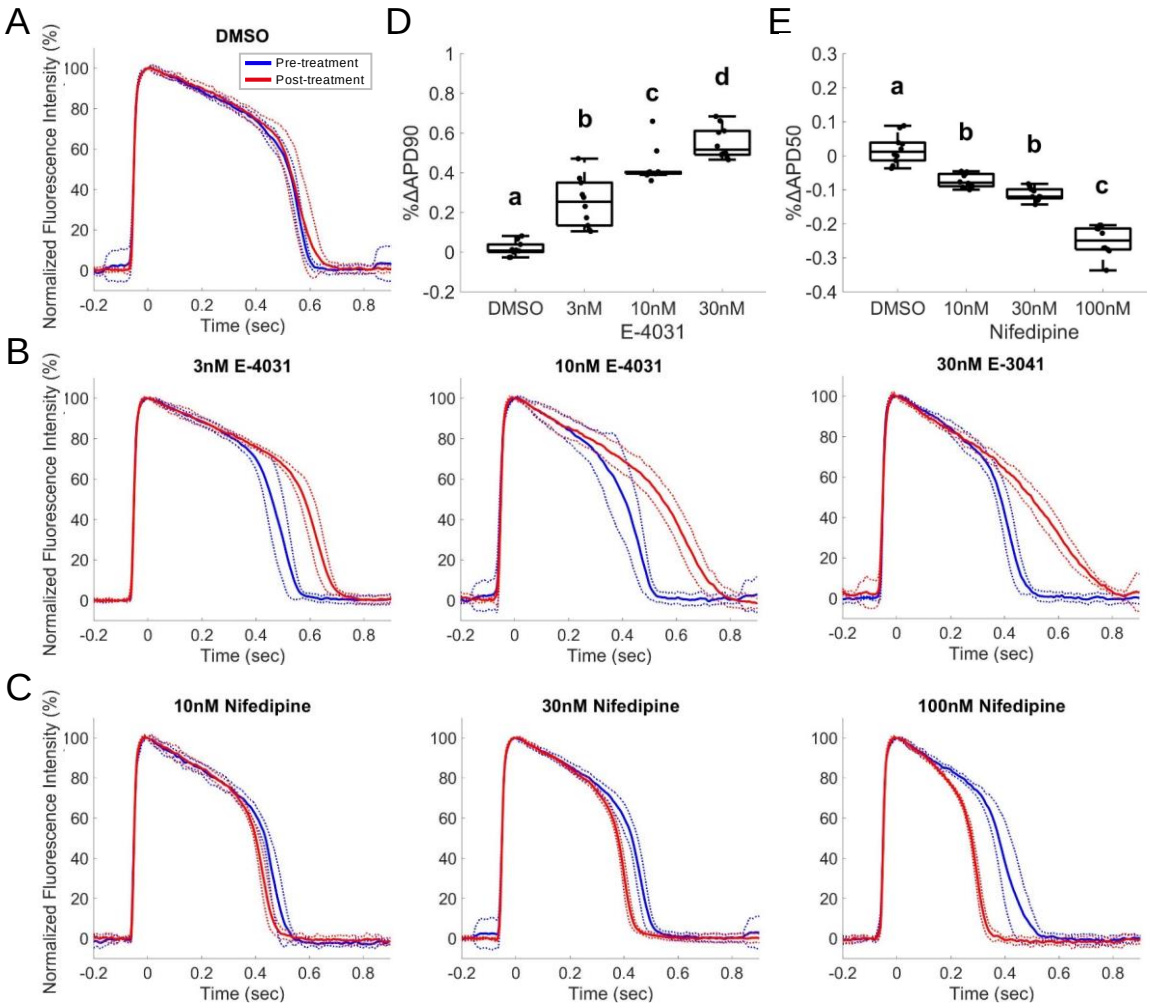

Figure 2.6. Archon1 can reliably detect changes in AP waveforms induced by K+ and Ca2+ ion channel inhibitors: E-4031 (K^+ Channel Blocker) and Nifedipine (Nif; Ca^{2+} Channel Blocker) compared to DMSO control; electrically paced at 1Hz. **(A)** Average normalized Archon1 fluorescence intensity traces for DMSO control (n = 10 cells), **(B)** E-4031 (10nM, 30nM, 100nM; n = 10 cells, and **(C)** Nifedipine (30nM, 100nM, 300nM; n = 10 cells) before (blue) and after (red) drugs, SD (dotted lines). **(D)** %ΔAPD90 for E-4031 APs from pre-drug condition **(E)** %ΔAPD50 for Nifedipine APs from pre-drug condition where *a*, *b*, *c*, and *d* represent different statistical groups (all pairs Tukey HSD test). For full statistics see **Table 2.5** and **Table 2.6**. Box plots displayed as described in **Figure 2.2**. All optical traces obtained at image acquisition rate of 100Hz.

Table 2.5. All pairs Tukey HSD test for Figure 2.6D between %ΔAPD90 of CMs exposed to 0 (DMSO), 3, 10, 30 nM E-4031.

E-4031 (nM)	0	3	10	30
0	-0.10548	0.12918	0.30957	0.43012
3	0.12918	-0.10548	0.07491	0.19546
10	0.30957	0.07491	-0.10548	0.01507
30	0.43012	0.19546	0.01507	-0.10548

Group 1	Group 2	Difference	Std Err Diff	Lower CL	Upper CL	p value
0 nM	3 nM	0.2346604	0.0391640	0.1291829	0.3401378	<.0001
0 nM	10 nM	0.4150448	0.0391640	0.3095673	0.5205222	<.0001
0 nM	30 nM	0.5355928	0.0391640	0.4301154	0.6410703	<.0001
3 nM	10 nM	0.1803844	0.0391640	0.0749070	0.2858619	0.0003
3 nM	30 nM	0.3009325	0.0391640	0.1954550	0.4064099	<.0001
10 nM	30 nM	0.1205480	0.0391640	0.0150706	0.2260255	0.0198

Table 2.6. All pairs Tukey HSD test for Figure 2.6E between %ΔAPD50 of CMs exposed to 0 (DMSO), 10, 30, 100 nM Nifedipine.

Nifedipine (nM)	0	10	30	100
0	-0.04047	0.05134	0.09180	0.22796
10	0.05134	-0.04047	-0.00001	0.13615
30	0.09180	-0.00001	-0.04047	0.09569
100	0.22796	0.13615	0.09569	-0.04047

Group1	Group2	Difference	Std Err Dif	Lower CL	Upper CL	p value
0 nM	10 nM	0.0918113	0.0150277	0.051338	0.1322844	<.0001
0 nM	30 nM	0.1322704	0.0150277	0.091797	0.1727435	<.0001
0 nM	100 nM	0.2684331	0.0150277	0.227960	0.3089062	<.0001
10 nM	30 nM	0.0404590	0.0150277	-0.000014	0.0809321	0.0501
10 nM	100 nM	0.1766218	0.0150277	0.136149	0.2170949	<.0001
30 nM	100 nM	0.1361627	0.0150277	0.095690	0.1766358	<.0001

2.6 Archon1 enables monitoring of action potentials within cardiac tissues

Engineered cardiac tissues can provide an optical, structural, and functional context which is more similar to *in vivo* tissue. The use of engineered cardiac tissues, particularly with iPSC-derived CMs, has been shown to increase both the structural and functional maturity of CMs, providing better models compared to more simple 2D monolayer

systems[214-217]. To demonstrate Archon1's ability to measure the APs of single cells embedded within a tissue, we constructed engineered cardiac tissues containing Archon1-expressing CMs alongside a stromal cell population (**Figure 2.7A left**; see **Methods**). The same Cre-recombinase system (**Figure 2.2A**) was used for controlled stochastic labeling of CMs to enable optical isolation of individual cells within the engineered tissues. Single CMs expressing Archon1 within the tissues were optically identified via EGFP fluorescence and their APs recorded in the far-red Archon1 fluorescence channel (**Figure 2.7A right**, **Figure 2.7B**).

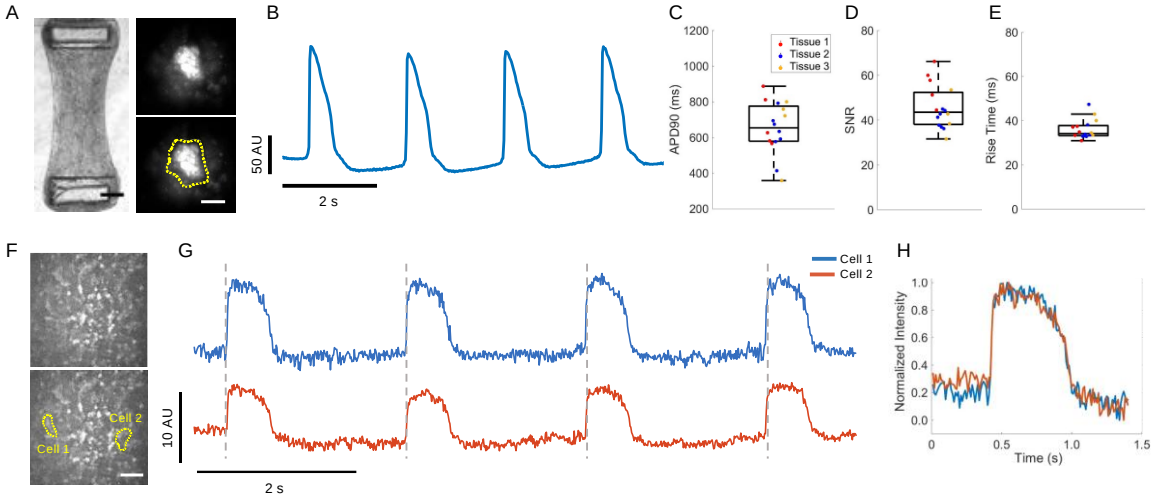

Figure 2.7. Archon1 enables monitoring of APs in µTUG hMSC-cardiomyocyte tissues. (A) Brightfield image of µTUG fibroblast-CM tissues (*left*). Scale bar, 250µm. See **Video S5**[203]. Maximum-minus-minimum projection image of CM within µTUG tissue expressing Archon1 (*top right*), with corresponding ROI overlaid (*bottom right*). Scale bar, 20µm. **(B)** Optically recorded voltage trace for the cell shown in **A**. Image acquisition rate, 50Hz. **(C)** Quantification of APD90 for CMs within tissues (n = 5, 7, 4, cells for Tissue 1 (red), 2 (blue), 3 (yellow), respectively). **(D)** Quantification of SNR for CMs within tissues (n = 5, 7, 4, cells for Tissue 1 (red), 2 (blue), 3 (yellow), respectively). Tissues are colored as in **C**. **(E)** Quantification of rise time for CMs within tissues (n = 5, 7, 4, cells for Tissue 1 (red), 2 (blue), 3 (yellow), respectively). Tissues are colored as in **C**. Box plots displayed as described in **Figure 2.2**, image acquisition rate: 50Hz. **(F)** Max projection image of µTUG tissue (*top*), with cells expressing Archon1 identified in yellow (*bottom*). Scale bar, 50 µm. **(G)** Corresponding optically recorded voltage traces for cells identified in **F**, with gray dashed vertical lines demonstrating AP synchrony. Image acquisition rate, 100Hz. **(H)** Overlay of representative normalized AP from two traces shown in **G** highlighting waveform consistency.

Across 3 unpaced tissues, APD90 ranged from 360–890 ms (mean±standard deviation: 655±143ms; range: 530ms), with cells from individual tissues more closely clustered (range: 321, 379, 442ms and n = 5, 7, 4 cells for Tissue 1, 2, 3, respectively; **Figure 2.7C**) demonstrating expected within-tissue homogeneity compared to between-tissue heterogeneity. The SNR and rise time across the three tissues (mean±standard deviation: 45.7±9.6, and 35ms±4.3 ms, for SNR and rise time, respectively; **Figure 2.7D,E**) were comparable to those of 2D monolayers (**Figure 2.4D,G**), demonstrating that Archon1 is as capable of measuring high fidelity APs in complex 3D environments, and highlighting its potential for use in future *in vivo* studies.

In order to investigate how CMs interact and synchronize in the tissue, we simultaneously recorded two cells in the same field of view in an unpaced tissue (**Figure 2.7F,G**). MYK-461, a cardiac-specific myosin ATPase inhibitor was used to prevent tissue contraction and associated movement related optical artifacts[218]. We found that the two cells' APs were highly synchronized (**Figure 2.7G**, gray lines), suggesting that they are likely electrically coupled within the tissue, even in the absence of externally-applied electrical pacing. In addition, by overlaying normalized single AP waveforms from these two cells, we found that the AP waveform morphology was largely similar, further highlighting their intercellular synchrony (**Figure 2.7H**). The ability to simultaneously record APs from multiple CMs with single-cell precision enables the monitoring of intercellular conductance and/or whole tissue synchrony. Such measurements, when combined with high speed and ultra-large field of view imaging, could enable future studies to examine

how individual cell APs contribute to population dynamics in complex 3D environments and *in vivo* systems.

2.7 Discussion

Here, we demonstrate the use of a high-performance GEVI, Archon1, to monitor cardiac action potentials in iPSC-derived cardiomyocytes in 2D monolayers and engineered 3D tissues. Our results demonstrate that Archon1 is capable of robustly reporting AP dynamics under a variety of conditions, including when exposed to electrical pacing and ion channel inhibitors, and has comparable sensitivity and time resolution to patch-clamp electrophysiology—the technically challenging but current gold standard in the field for measuring membrane potential. In addition, Archon1 outperformed the commonly used VSD, Di-8-ANEPPS, in SNR. In contrast to VSDs, Archon1 is fully genetically encoded, which enabled long-term studies and has the potential for cell-type specific labelling in *in vivo* models. Furthermore, the Cre-recombinase system used here enabled optical isolation of CMs within a complex 3D tissue environment, which can be easily translatable to imaging of whole heart slices or cardiac tissue in Cre-transgenic animals. Finally, Archon1 is capable of reporting membrane potential of multiple cells simultaneously, including in 3D tissue environments. This enables population studies, while retaining single-cell precision, allowing measurement of conduction velocity and AP propagation, as well as intercellular phase-locking or phase delay. Future studies could examine changes in individual cell voltage dynamics or intercellular propagation around and distal from injury or diseased sites within tissues.

Although we did not take advantage of this utility here, as Archon1 is a far-red indicator, it is compatible with blue light-driven optogenetic molecules such as channelrhodopsins[202]. These molecules could be paired to provide simultaneous control and monitoring of cardiac membrane potential. Similarly, Archon1 can be used together with the genetically encoded calcium indicator, GCaMP6, for simultaneous, multicolor imaging of voltage and calcium dynamics[156,219]. This could enable studies of diseases like Timothy syndrome or heart failure which affect both voltage dynamics and calcium handling[220–223]. Furthermore, the far-red spectrum of Archon1 enables deeper penetration into tissues than those operating at shorter wavelengths, facilitating future *in vivo* applications.

The genetically encoded nature of Archon1 makes it a useful tool for longer duration studies of disease mechanisms, such as detecting arrhythmias, which are known to affect AP waveforms or for phenotyping atrial, ventricular, or nodal cells based on waveform morphology[156,162,163]. In particular, Archon1 could be used to follow their development through differentiation, maturation, etc., or during disease progression[156,162]. In addition, while we currently transduce CMs with AAVs expressing Archon1, lentiviral particles could be used to create stable cell lines expressing Archon1 for characterization through iPSC-differentiation, development, or integration into living tissue.

Finally, Archon1's capability to monitor CMs in both 2D and 3D environments could assist in the development and evaluation of more functionally mature, biologically-relevant engineered cardiac tissues.

2.7.1 Limitations of Study

Photobleaching is often a concern for all optical imaging techniques that deploy fluorescent indicators. However, under 5 minutes of continuous imaging, Archon1 demonstrated robust monitoring of membrane voltage with no change in SNR, which we expect could extend to tens of minutes. For experiments requiring hours of continuous monitoring, periodic imaging of short durations may be necessary. As GEVIs are engineered to become more sensitive, less light illumination power will be needed to achieve the same SNR and longer imaging studies could be conducted.

In addition, due to current limitations in camera speed, in order to capture an entire CM (typically ~50–100μm across) within the field of view, the acquisition rate must be limited to ~100Hz. We have previously shown that Archon1 and its variants can follow millisecond time scale events, such as neuron APs, with high temporal precision at acquisition rates up to 1kHz[183,202]. As camera technology continues to improve, we hope to be able to conduct such high-speed imaging of larger fields of view containing populations of CMs. Like all non-ratiometric GEVIs or VSDs, Archon1 does not report absolute values of membrane potential, and SNR may vary due to GEVIs expression levels across individual cells. However, relative membrane potential is still valuable for comparing AP dynamics between different biological states.

In conclusion, Archon1, with its the diverse functionality and its simple one-photon widefield imaging setup, can be easily adapted for investigating a variety of paradigms in

cardiac biology and relevant pathology.

2.8 Methods

2.8.1 Cell Source Details

iPSC cells I.D. Personal Genome Project (PGP1) were isolated from male, 53 years of age, fibroblasts. hMSCs were isolated from purchased Human Bone Marrow Mononuclear Cells (Lonza), from a male, 39.

2.8.2 Cell Preparation and Culture

iPSCs were screened for copy number variants and virtual karyotyping using Illumina HumanOmniExpress-12v1 arrays. iPSCs were maintained in complete mTeSR1 medium (Stem Cell) and differentiated in monolayers into CMs using RPMI 1640 Medium, GlutaMAX (Gibco) supplemented with B-27 Supplement, minus insulin (Gibco). CHIR99021 (12μM, Tocris) was added on Day 1 of differentiation to activate Wnt pathway, and IWP4 (5μM, Tocris) was added for Days 3 and 4 to inhibit Wnt pathway. Cells were switched to RPMI 1640 Medium, GlutaMAX containing standard B-27 Supplement (Gibco) on Day 10. Once spontaneous beating was observed, CMs were metabolically selected using glucose free, RPMI 1640 Medium (Gibco) supplemented with 4mM of DL-lactate (Sigma) for two days. Following selection, CMs were maintained in RPMI 1640, GlutaMAX supplemented with B-27 Supplement. hMSCs were maintained in DMEM, low glucose medium (Gibco) with 10% Fetal Bovine Serum (Sigma) and 1%

Penicillin-Streptomycin (Gibco) and used from passage 6–9. All cells were kept at 37°C with 5.0% CO_2.

2.8.3 Cardiomyocyte Transduction

CMs were replated onto Fibronectin, human (Corning) coated plates. 24 hours after replating, CAG-FLEX-Archon1-KGC-EGFP-ER2 rAAV2 (Archon1) (MOI: 2000–3000) and CMV-Cre AAV9 (Addgene) (MOI: 4000–6000) were added. After 2 days, viruses were washed out and CMs were maintained in RPMI 1640 supplemented with B27. Experiments were performed between days 7 and 14 post-transduction.

2.8.4 Engineered Cardiac Tissue Seeding

Engineered cardiac tissues were prepared as previously described[224]. Briefly, Polydimethylsiloxane micro-fabricated tissue gauges (μTUGs) were prepared by molding from SU-8 masters. μTUG devices were UV light sterilized then treated with 0.05% Pluronic F127 (Sigma) for 30 minutes to prevent cell and extracellular adhesion. CMs and hMSCs were dissociated and suspended together (8.4% CMs expressing Archon1, 75.6% non-expressing CMs, 16% hMSCs, total 1.2 million cells/ml) in a hydrogel consisting of 2.25mg/ml Collagen I, Rat Tail (Corning) and 0.5mg/ml human plasma fibrinogen (Sigma). The cell suspension was centrifuged into device microwells and excess was removed by dewetting. Hydrogels were polymerized at 37°C for 20 minutes and tissues were maintained in DMEM (Corning) 10% Fetal Bovine Serum (Sigma), 1% Penicillin-

Streptomycin (Gibco), GlutaMAX Supplement (Gibco), MEM Non-Essential Amino Acid Solution (Gibco). Tissues were imaged on Day 6–9 post-seeding. 5μM MYK-461 (Cayman Chemical) was used to inhibit CM contraction during multi-cell imaging.

2.8.5 Electrophysiology

Two-photon microscopy was used for visually guided patch clamp recordings of CMs. CMs were visualized using the EGFP fluorescent marker bound to Archon1, and the electrode pipette was visualized by adding the orange fluorescent dye Alexa Fluor 568 hydrazide (Thermo Fisher Scientific) to the intracellular electrode solution (50μM). Imaging was performed using a two-photon microscope (Thorlabs) equipped with a 20X, NA 1.0 (Olympus) objective lens. A mode-locked Ti:Sapphire laser (Chameleon Ultra II; Coherent) set to a wavelength of 900 nm was used to excite both the Alexa Fluor 568 and EGFP. Fluorescence was detected using two photo-multiplier tubes (Hamamatsu) equipped with 525/25nm and 607/35nm filters to separate emission from EGFP and Alexa Fluor 568, respectively.

Electrical recordings acquired simultaneously with optical recordings used the same imaging setup described in detail in **Section 2.8.8** for the visualization of the patching process. The electrode pipette was visualized by adding the green fluorescent dye Alexa Fluor 488 hydrazide (Thermo Fisher Scientific) to the intracellular electrode solution (50μM). The electrode was placed in the on-cell configuration using 470 nm LED excitation, before switching to the far-red imaging of Archon1 and proceeding with the

electrical recordings.

To verify that Archon1 does not alter CMs electrically, cells expressing Archon1 and non-expressing control cells were patched within the same monolayer. Differential interference contrast (DIC) microscopy (Olympus BX51W1) was used for visualizing the CMs and patch pipettes. CMs expressing Archon1 were identified using the EGFP tag.

CM monolayers on coverslips were immersed in the bath solution (140mM NaCl, 5.4mM KCl, 1mM $MgCl_2$, 10mM D-glucose, 1.8mM $CaCl_2$, 10mM HEPES; pH 7.4 with NaOH)[225]. A silver-chloride wire placed inside the bath was used as the ground electrode. Intracellular membrane voltage recordings were carried out using patch clamp electrodes with resistance values between 8 MΩ and 12 MΩ. Electrodes were pulled using a horizontal puller (Sutter Instruments) using filamented, thin-wall glass (Sutter Instruments) and filled with the intracellular solution (120mM potassium D-gluconate, 15mM KCl, 4mM Na_2ATP, 2mM trisGTP, 4mM ditrisphosphocreatine, 10mM EGTA, 1mM $CaCl_2$, 10mM HEPES)[225]. Electrodes were lowered into the bath approximately 200 µm above the coverslip surface using a micromanipulator (Sutter Instruments) and then slowly lowered to a cell. A small amount of positive pressure was used to push away debris and prevent clogging of the pipette tip. A 10 mV voltage step was used to measure seal resistance and the capacitance associated with the glass electrode. Upon seal formation (>1GΩ) in the on-cell (i.e., cell-attached) configuration, capacitance compensation was used to eliminate the pipette capacitance. Small amounts of transient negative pressure were used to break the

seal and establish whole cell recordings. The membrane voltage was recorded in current clamp with full bridge balance compensation and no injected current. Trace signals were amplified and low-pass filtered at 10 kHz before being digitized at 20 kHz. All electrophysiology was carried out using a Multiclamp 700B (Molecular Devices) and a Digidata 1440A (Molecular Devices).

2.8.6 Di-8-ANEPPS

Di-8-ANEPPS (Santa Cruz) was dissolved in Dimethyl Sulfoxide (DMSO, Thermo Fisher). CMs transduced with Archon1 were incubated with 10μM Di-8-ANEPPS, RPMI 1640, no phenol red medium (Gibco)and 0.05% F127 Pluronics for 15 minutes. After incubation, samples were washed 3x with RPMI 1640, no phenol red medium before imaging. Imaging was done both with spontaneously beating and electrically paced (0.5–3Hz) cells. Cells with Di-8-ANEPPS were imaged using a 470 nm LED (ThorLabs Inc., M470L3) with a 570 nm LP dichroic (Olympus, OCT49005BX3) and a 620/60 nm (Olympus, OCT49005BX3 bandpass emission filter.

2.8.7 Ion Channel Inhibitors

E-4031 dihydrochloride (Abcam) and Nifedipine (Abcam) were dissolved in DMSO at 50mM and 100mM, respectively. Drug solutions were made by diluting stock solutions with RPMI, no phenol red medium to 20x the final drug treatment concentration. For all samples, 10 cells were imaged prior to drug treatment. Then, concentrated drug solution

was added to samples to make final concentrations of 10nM, 30nM, and 100nM for E-4031 and 30nM, 100nM, and 300nM for Nifedipine. DMSO concentrations for all samples were 0.0003% or less. DMSO control was performed using 0.0003% DMSO. Samples were incubated at 37°C for 20 minutes with drug, and the 10 same cells were imaged. All cells were electrically paced at 1Hz.

2.8.8 Microscopy

All optical recordings were acquired using a conventional one-photon widefield fluorescence microscope equipped with an ORCA Flash 4.0 V3 Digital CMOS camera (Hamamatsu Photonics K.K., C13440-20CU) or Hamamatsu ORCA Fusion Digital CMOS camera (Hamamatsu Photonics K.K., C14440-20UP), 10x NA0.3 CFI Plan Fluorite water immersion objective (Nikon), and 40x NA0.8 CFI APO NIR water immersion objective (Nikon). Archon1's green GFP fluorescence was imaged using a 470 nm LED (ThorLabs Inc., M470L3) with 470/25 nm bandpass excitation filter, 495 nm dichroic, and a 525/50 nm bandpass emission filter (Olympus, OCT49002BX3). Archon1's far-red fluorescence was imaged using a 140 mW 637 nm laser (Coherent Obis 637-140X), 635 nm laser dichroic filter, and a 664 nm long pass emission filter (Olympus, OCT49006BX3) with 1x1 or 2x2 binning. Optical recordings were acquired at 50 or 100 Hz with HCImage Live (Hamamatsu Photonics K.K.). HC Image Live data were stored as multi-TIFF files and further analyzed offline in Fiji/ImageJ and MATLAB (MathWorks Inc.). Samples were maintained at 37°C throughout imaging using a heated stage. Samples were paced using an Ionoptix C-Pace EM using carbon electrodes made from carbon rods (Ladd Research)

attached to platinum wires (Sigma) submerged in medium. Pacing was performed at 20V, with a 10ms duration, at indicated frequencies.

2.8.9 ROI identification

Images were imported into Fiji/ImageJ and ROIs were manually segmented by examining each time-series to identify areas with clear cell borders. Voltage traces for each ROI were extracted in Fiji/ImageJ and used for subsequent analyses.

2.8.10 Voltage trace processing

Before analysis, we pre-processed the fluorescence traces per the following: Di-8-ANEPPS traces were first inverted by multiplying -1 so that increases of membrane potential corresponded to increases in the trace value. The traces were then detrended using the MATLAB function "detrend" and rescaled so that the maximum intensity equaled 100 while the minimum intensity equaled zero. After rescaling, the Archon1 and Di-8-ANEPPS traces were resampled at 20kHz to match the sampling rate of electrophysiological recordings.

2.8.11 Rise time calculation

To calculate rise time, we first identified the peaks and valleys of each waveform. The peaks of each waveform were identified using the MATLAB function "findpeaks", and the valleys were defined as the first data point before the peak with a negative slope and

rescaled intensity value less than 50. To ensure that we captured the whole waveform, we excluded any peak that occurred within the first 0.5 seconds or within the last 1.5 seconds of recording. The rise time was defined as the duration between the take off point (10% above the valley) to 90% of the peak.

2.8.12 APD90 and APD50 calculation

To obtain the ADP90 for each waveform, we first calculated a threshold at 10% of the amplitude (the intensity difference between the peak and its prior valley) above the valley. We then identified two time points: the time point right before the intensity increased over the threshold during the rising phase, and the time point right after the intensity decreased below the threshold during the falling phase. The ADP90 was defined as the duration between these two time points. A similar calculation was conducted for determination of APD50 values, except with a threshold set at 50% of the amplitude above the valley.

2.8.13 Signal to noise ratio (SNR) calculation

To calculate the SNR, we divided the amplitude of each waveform (signal) by the noise, which we defined as the standard deviation of the 10 Hz high-pass-filtered trace.

3 DEVELOPMENT OF A NOVEL SOMA-TARGETED VOLTAGE INDICATOR FOR POPULATION IMAGING OF NEURAL ACTIVITY IN AWAKE BEHAVING MICE

3.1 Citation & Contribution

The work described in this chapter has been published at Nature[202]. Piatkevich, KD*, Bensussen, S*, Tseng, H-A.*, **Shroff, SN**, *et al.* Population imaging of neural activity in awake behaving mice. *Nature* **574,** 413–417 (2019). https://doi.org/10.1038/s41586-019-1641-1.

My contribution to this work was second to the three co-first authors, however, it still constitutes an important part of my thesis work. Along with the first authors, I designed and performed all *in vivo* experiments and interpreted and analyzed all *in vivo* data. Along with Dr. Bensussen and Dr. Gritton, I performed all mouse surgeries for these *in vivo* experiments. Finally, along with the first authors and co-corresponding authors, I wrote and edited the manuscript and subsequent revisions based on peer review. Full author contributions are listed online[202].

3.2 Summary

A longstanding goal in neuroscience has been to image membrane voltage across a population of individual neurons in an awake, behaving mammal. Here, we report a genetically encoded fluorescent voltage indicator, SomArchon, which exhibits millisecond response times and compatibility with optogenetic control, and which increases the

sensitivity, signal-to-noise ratio, and number of neurons observable, by several-fold over previously published reagents[97,181,185,186,188,206,208,226]. Under conventional one-photon microscopy, SomArchon enables population analysis of approximately a dozen neurons at once, in multiple brain regions: cortex, hippocampus, and striatum, of head-fixed, awake, behaving mice. Using SomArchon, we detected both positive and negative responses of striatal neurons during movement, previously reported by electrophysiology but not easily detected using modern calcium imaging techniques[59,227,228], highlighting the power of voltage imaging to reveal bidirectional modulation. We also examined how spikes relate to subthreshold theta oscillations of individual hippocampal neurons, with SomArchon reporting that individual neurons' spikes are more phase locked to their own subthreshold theta oscillations than to local field potential theta oscillations. Thus, SomArchon reports both spikes and subthreshold voltage dynamics in awake, behaving mice.

3.3 Introduction

Traditional electrophysiological techniques are able to record electrical activity in the brains of awake animals with high temporal precision at various spatial scales, ranging from single cell activity to merged population activity[85,89,95,102,103,105,106,229]. These methods, such as whole-cell patch clamp, local field potential recordings, or electroencephalography (EEG), however, lack the ability to observe the activity of populations with single cell resolution, which is often desired for many *in vivo* neuroscience applications. Alternatively, the genetically encoded calcium sensor, GCaMP, alleviates some of these spatial limitations by allowing optical tracking of neural activity in hundreds of individual

cells simultaneously[143–146]. Yet calcium only serves as an indirect measure of neural activity, and GCaMP signals often do not promptly reflect individual action potentials or subthreshold voltage dynamics, due to its slower temporal resolution than electrophysiology.

Due to the desire to be able to image population neural activity with high temporal precision and sensitivity, much recent interest has focused on the development of genetically-encoded voltage indicators (GEVIs). Near-infrared genetically encoded voltage indicators (GEVIs) derived from rhodopsins offer high temporal fidelity, and are compatible with optogenetics[181–183], whereas green fluorescent GEVIs derived from voltage sensing domains of phosphatases or opsins are often slower and brighter[184–189]. Translating these into the living mouse brain has been challenging, because poor membrane localization, photostability, and sensitivity of previous molecules has resulted in poor signal-to-noise ratio (SNR) *in vivo*. Prior to the start of this project, only Ace2N had been used to optically report voltage dynamics in multiple single cells in a living mouse brain, reporting only a single example of the activities from just two cells in one field of view[188].

Recently, Piatkevich et al. developed a robotic directed evolution approach that could perform multidimensional optimization of fluorescent voltage indicators along the axes of photostability, sensitivity, and membrane localization, resulting in the rhodopsin-based voltage sensor Archon1 (the focus of Chapter 2), which performed well in the *C. elegans* nervous system, larval zebrafish brain, and in mouse brain slice[183]. Here, we report a

variant we call SomArchon, which exhibits improved SNR sufficient to achieve a key milestone: the ability to routinely report activity of a dozen neurons at once, in multiple brain regions of awake behaving mice, using inexpensive and simple conventional one-photon microscopes. To synthesize SomArchon we built on prior work targeting opsins to neural somata[230–233]: we conducted a screen for peptides to localize Archon1 to the soma membrane, causing increased signal and reduced background (by eliminating neuropil signals from axons and dendrites that obscure the signal from the soma; **Figure 3.1**). The impact was significant, resulting in improvements in sensitivity, SNR, and the number of neurons imageable by manyfold in each case, over prior published reagents. Taking advantage of this improved SNR, we were able to use simple one-photon fluorescence optics to perform wide-field voltage imaging in multiple cortical (visual and motor cortex) and subcortical (hippocampus and striatum) brain regions in awake, attentive, and/or behaving mice. We were able to detect neurons in the striatum whose activities were negatively modulated by movement, previously reported by electrophysiology but not easily detected using modern calcium imaging techniques[44,46,234], and highlighting the complexity of how the striatum encodes voluntary movement. We were also able to measure the phase of spiking relative to intracellular theta oscillations in hippocampal CA1 neurons, confirming earlier experimental results using *in vivo* patch clamp techniques, and further extending these studies by examining how the spiking output of nearby neurons varied despite highly coherent intracellular subthreshold oscillations.

3.4 Development and evaluation of a soma-targeted GEVI

To improve SNR in the dense, living mammalian brain, we conducted a screen for peptides to localize Archon1 to the soma[230–233], so that neuropil contamination could be reduced (**Figure 3.1**). We chose amino acid sequences that have been shown to target microbial opsins, popular for optogenetic control of neural activity, to the cell bodies of neurons. We chose six such localization motifs and fused them with Archon1 for further validation (see **Table 6.13)** for the design of the fusion constructs and the full amino acid sequences of the selected motifs). The selected motifs were fragments of the N-terminus of the kainate receptor subunit KA2 (*ref*[232]), a 222-amino-acid intracellular loop between transmembrane domains I and II of the $Na_V1.2$ sodium channel[235], a 27-amino-acid segment within the intracellular loop between transmembrane domains II and III of the $Na_V1.6$ sodium channel[235–237], a 65-amino-acid segment at the C terminus of the $K_V2.1$ potassium channel[230], and the membrane-binding domain of the adaptor protein ankyrinG[238].

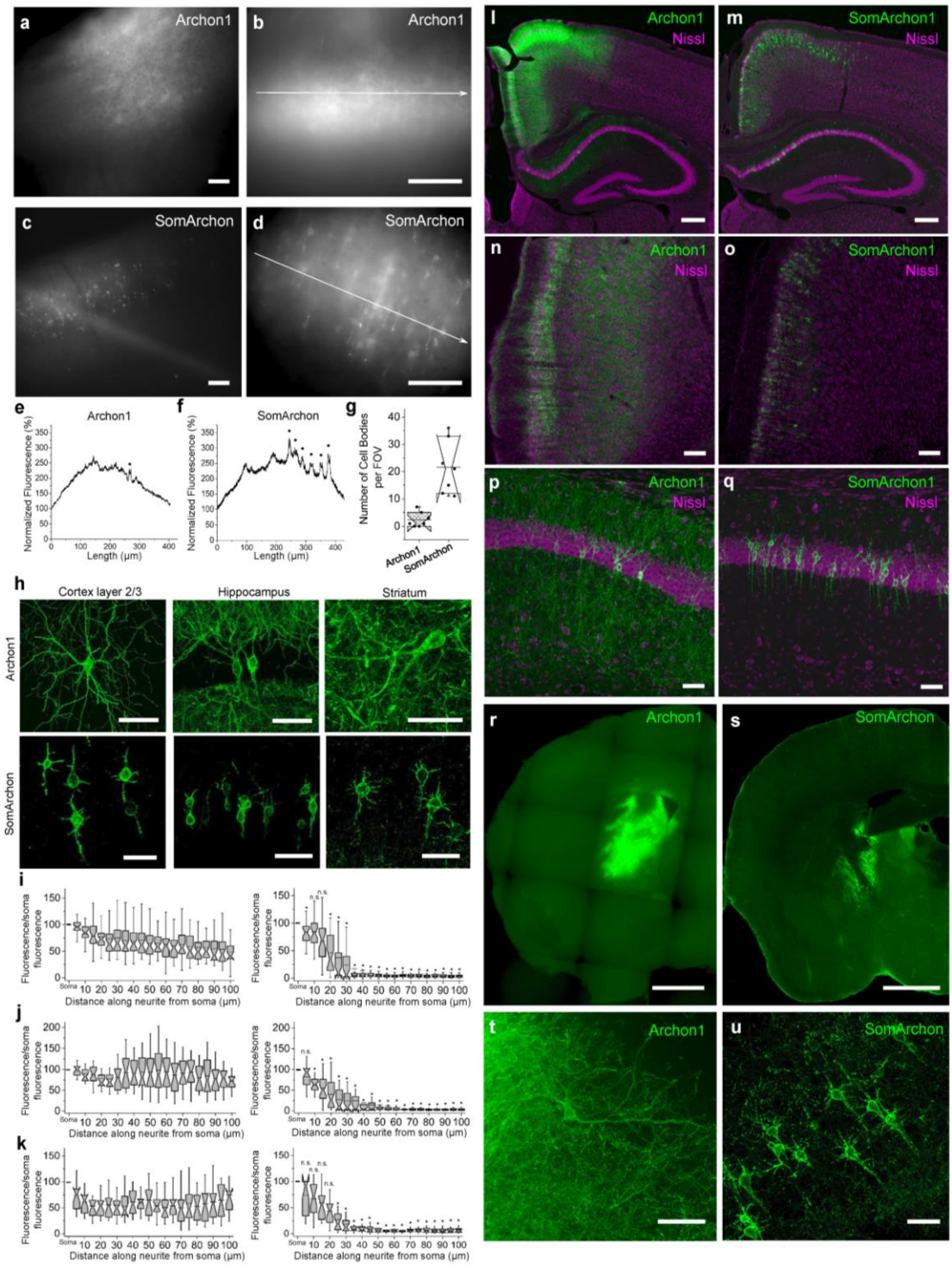

Figure 3.1. Expression of Archon1 and SomArchon in mouse brain. (a,b) Representative Archon1- and **(c,d)** SomArchon-expressing mouse brain slices (CAG promoter, via IUE) imaged with a wide-field microscope with (**a,c**) 10x and **(b,d)** 40x objective lenses (from n = 7 slices from 2 mice each). **(e,f)** Normalized EGFP fluorescence along white arrows shown in b and d. Black

dots correspond to resolvable cells. (**g**) Number of resolvable cells per field of view (FOV) for Archon1- and SomArchon-expressing brain slices (2.4 ± 2.5 and 22 ± 9 neurons per FOV (350×415 μm^2) for Archon1 and SomArchon respectively; mean ± standard deviation; n = 7 slices from 2 mice each; boxplots as in Fig. 1). Further confocal analysis with larger FOVs of 500×500×50 μm^3 revealed that SomArchon can resolve ~15 times more neurons in the cortex than Archon1 (n = 4, 8, 9, 11, 11, 18, and 20 neurons from 7 slices for Archon1, versus n = 180, 187, and 137 neurons from 3 slices for SomArchon). **(h)** Representative confocal images of neurons in cortex layer 2/3 (*left*), hippocampus (*middle*), and striatum (*right*) expressing Archon1 (*top*) and SomArchon (*bottom*). **(i–k)** EGFP fluorescence along a neurite, normalized to soma, for Archon1- (*left*) and SomArchon- (*right*) expressing neurons in **(i)** cortex layer 2/3 (n = 39 and 37 neurites from 10 cells from 2 mice each), **(j)** hippocampus (n = 20 and 34 neurites from 9 and 17 cells from 2 mice each), and **(k)** striatum (n = 17 and 20 neurites from 7 cells from 2 mice each). Box plots as in **Figure 3.2**. n.s.: not significant; *: $p < 0.002$ compared to Archon1 at corresponding position away from the soma; two-sample Kolmogorov-Smirnov test, see **Table 6.1**. **(l–u)** Representative confocal fluorescence images of Archon *(left column*) and SomArchon-expressing slices (*right column*) via **(l–q)** IUE or **(r–u)** AAV injection (green: EGFP; magenta: Nissl staining) in **(n,o)** cortex layer 2/3 (n = 8 slices from 2 mice), **(p,q)** hippocampus (n = 8 slices from 2 mice), and **(t,u)** striatum (n = 6 slices from 2 mice). Scale bars: 100 μm, **a–d**; 50 μm, **h,n–q,t,u**; 250 μm, **l,m,r,s**.

Additionally, we tested other ankyrinG domains, such as the spectrin-binding domain (AnkSB-motif), the tail domain (AnkTail-motif), the COOH-terminal domain (AnkCt-motif), and the serine-rich domain (AnkSR-motif), that were shown to be sufficient to restrict GFP localization to cell bodies and axon proximal segments[239]. Screening constructs in primary cultured mouse neurons with wide-field fluorescence microscopy, we found that 4 out of 12 constructs showed fluorescence changes during spontaneous neuronal activity (**Table 6.13**). The Archon1-KGC-EGFP-K_V2.1-motif-ER2 fusion protein, which we call SomArchon (**Figure 3.2a**) exhibited the highest ΔF/F during 100-mV voltage steps (**Figure 3.2g**) and appeared to have good soma localization **(Figure 3.1h–k**).

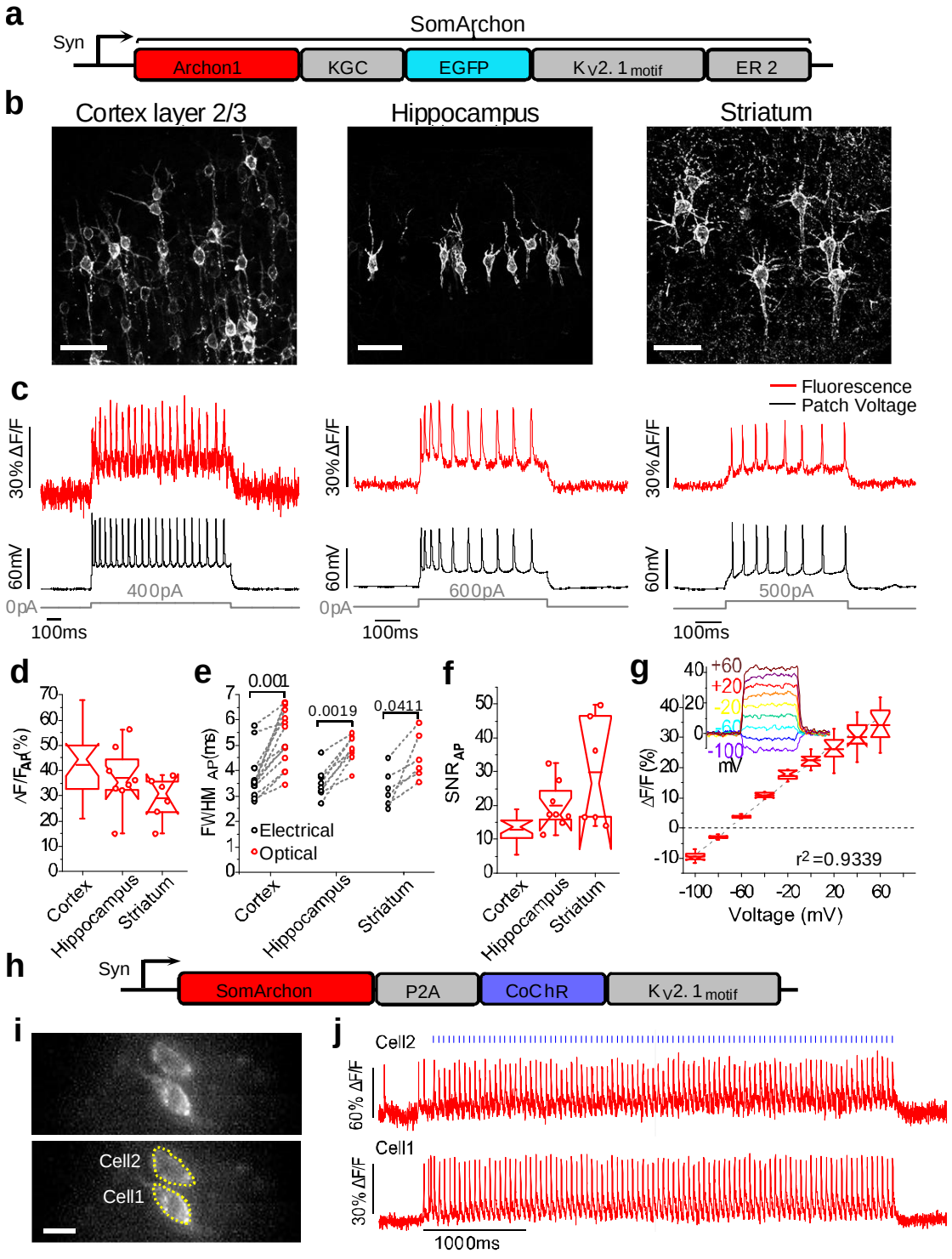

Figure 3.2. SomArchon enables high fidelity voltage imaging in brain slices. (a) Diagram of the SomArchon construct. **(b)** Confocal images of SomArchon expressing neurons in cortex layer 2/3 (*left*), hippocampus (*middle*), and striatum (*right*). λ_{ex}=488nm laser, λ_{em}=525/50 nm (representative images selected from 8, 10, and 6 slices from 2 mice each, respectively). Scale bars,

50 μm. **(c)** Single-trial SomArchon fluorescence (red), and concurrently recorded membrane voltage via whole-cell patch-clamp (black), during current injection (gray) evoked action potentials (APs); λ_{ex}=637nm laser at 0.8, 1.5, and 1.5 W/mm^2 for cortex, hippocampus, and striatum, respectively. **(d)** ΔF/F per AP across recordings exemplified in **c** (representative traces selected from n=18, 8, and 6 neurons from 5, 2, and 2 mice, respectively). Box plots (25th and 75th percentiles with notch being the median; whiskers extend 1.5x the interquartile range from the 25th and 75th percentiles; middle horizontal line, mean; individual data points shown as open circles when n < 9). **(e)** Electrical and optical AP waveform full-width-at-half-maximum (FWHM; dashed lines connect same neurons) across recordings exemplified in **c** (*p*-values are from two-sided Wilcoxon rank sum test, see **Table 6.2**). **(f)** SNR per AP across recordings exemplified in **c**. **(g)** Population fluorescence of SomArchon in response to voltage steps in voltage-clamp mode, normalized to the fluorescence at -70 mV (optical recordings for a representative neuron shown in inset) recorded in cortex (n=12 neurons from 2 mice). **(h)** Diagram of SomArchon-P2A-CoChR-$K_V2.1_{motif}$. **(i)** Fluorescence image of neurons in hippocampal slice, expressing SomArchon-P2A-CoChR-$K_V2.1_{motif}$ (*top*) with two cells identified (*bottom*); λ_{ex}=637 nm, exposure time 1.3 ms (selected from n=3 slices from 2 mice). Scale bar, 25 μm. **(j)** Representative single-trial optical voltage traces from cells shown in **i** with blue light stimulation (2 ms pulse at 20 Hz). Acquisition rate: 777 Hz.

SomArchon fluorescently reported action potentials in mouse brain slice after *in utero* electroporation (IUE) into cortex and hippocampus, and after adeno-associated virus (AAV)-mediated expression in cortex, striatum, and thalamus (**Figure 3.3**). SomArchon was localized primarily to the membrane within 30–45 μm from the cell body in the cortex, striatum, and hippocampus (**Figure 3.2b; Figure 3.1h–k**).

We evaluated the performance of SomArchon in multiple regions of the mouse brain via simultaneous patch clamp electrophysiology and one-photon imaging in brain slice (**Figure 3.2c**). The voltage sensitivity of SomArchon obtained was ΔF/F of 42 ± 12%, 37 ± 11%, and 26 ± 7% (mean ± standard deviation throughout) per action potential for cortex layer 2/3, hippocampus, and striatum, respectively (**Figure 3.2d**; imaging conditions described in the caption; n = 18, 8, 6 neurons from 5, 2, 2 mice for cortex layer 2/3, hippocampus, and striatum, respectively). This represents an improvement over the parent,

Archon1, of ~2-fold in sensitivity, likely because of decreased background neuropil fluorescence (compared to the mouse cortex brain slice data of Piatkevich *et al.* 2018[183]).

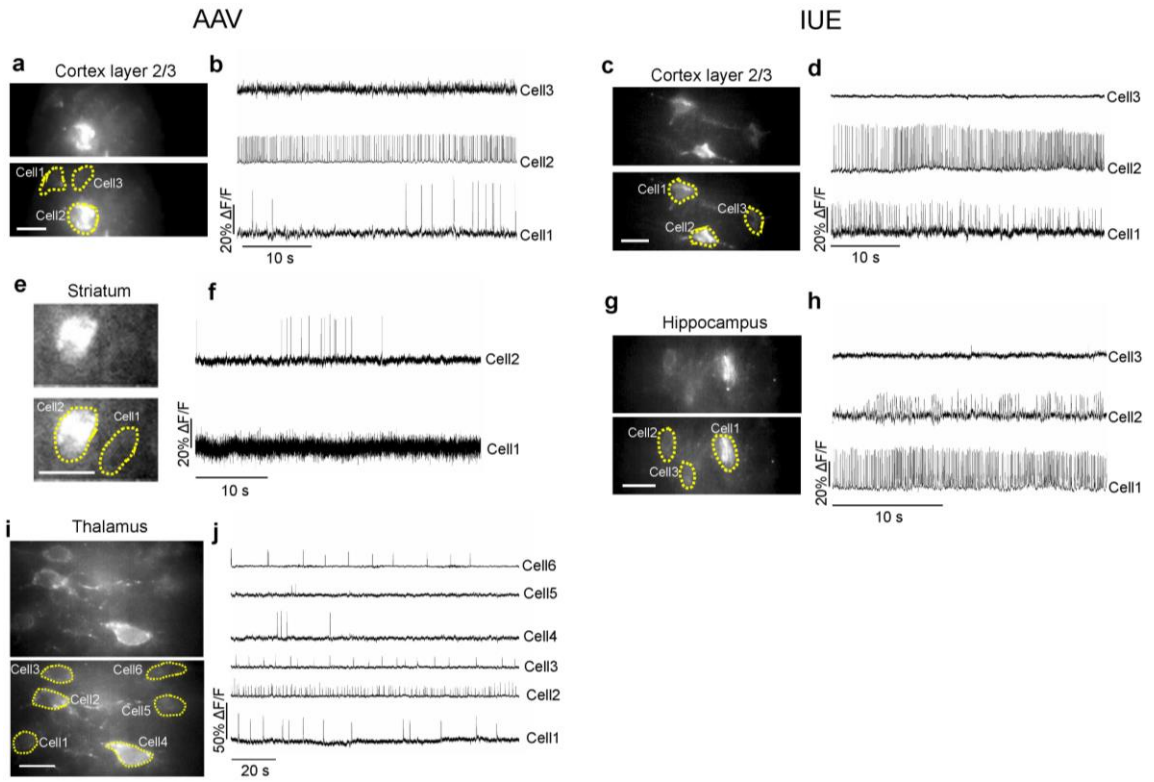

Figure 3.3. Voltage imaging using SomArchon in mouse brain slices. (a–d) Representative fluorescence wide-field images of cortex layer 2/3 neurons expressing SomArchon via **(a)** AAV transduction or **(c)** IUE with selected ROIs (bottom), and (**b,d**) corresponding fluorescence traces (n = 6 and 13 slices from 2 and 4 mice for AAV transduction and IUE, respectively). Acquisition rate: 632 Hz, **b**; 440Hz, **d**. **(e)** Representative fluorescence wide-field images of striatal neurons expressing SomArchon via AAV transduction (*top*) with selected ROIs (*bottom*), and **(f)** corresponding fluorescence traces (n = 8 slices from 2 mice). Acquisition rate: 733 Hz. **(g)** Representative fluorescence wide-field images of hippocampal neurons expressing SomArchon via IUE (*top*) with selected ROIs (*bottom*), and **(h)** corresponding fluorescence traces (n = 8 slices from 2 mice). Acquisition rate: 333 Hz. **(i)** Fluorescence wide-field images of thalamus neurons expressing SomArchon (*top*) via AAV transduction with selected ROIs (*bottom*), and **(j)** corresponding fluorescence traces (n = 5 slices from 2 mice). Acquisition rate: 333 Hz. Scale bars, 25 µm.

SomArchon fluorescence followed high-speed changes in voltage during single action potentials, with fluorescence waveforms being only slightly broader than electrically-

recorded action potential waveforms (**Figure 3.2e**, n = 14, 8, and 6 neurons from 5, 2, and 2 mice for cortex layer 2/3, hippocampus, and striatum, respectively; **Table 6.2**). During action potentials, SomArchon fluorescence changes exhibited SNRs (defined as the maximum fluorescence change observed during an action potential divided by the standard deviation of the baseline) of 13 ± 4, 20 ± 6, and 27 ± 13 per action potential, in the cortex, hippocampus, and striatum, respectively (**Figure 3.2f**; imaging conditions described in the caption; n = 18, 8, 6 neurons from 5, 2, 2 mice for cortex layer 2/3, hippocampus, and striatum, respectively). In summary, SomArchon exhibited about two-fold greater sensitivity (**Figure 3.2c** and **d**), and comparable kinetics (**Figure 3.2e**) and signal to noise ratio (**Figure 3.2f**, SNR, defined as the maximum fluorescence change observed during an action potential divided by the standard deviation of the baseline) to our previously published values for Archon1[183]. SomArchon also shows a linear relationship to membrane voltage (**Figure 3.2g)**, which allows fluorescence readout to be easily extrapolated to relative voltage changes. In addition, expression of SomArchon did not alter membrane properties or resting potential in mouse brain slices, induce gliosis, or mediate light-induced phototoxicity (**Figure 3.4, Figure 3.5**).

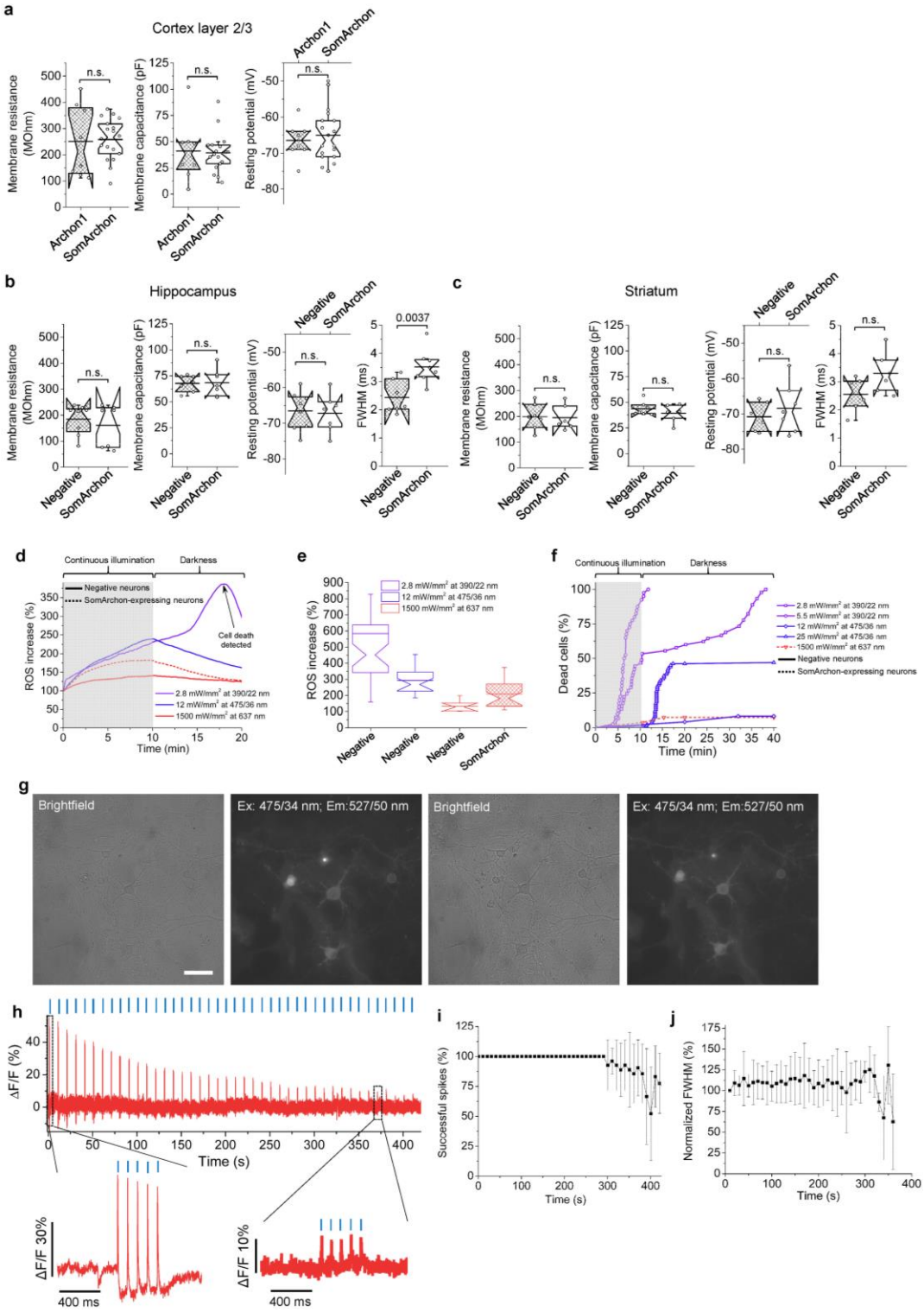

Figure 3.4. SomArchon expression and voltage imaging do not alter membrane properties or cause phototoxicity. (**a**) Membrane properties of Archon1- (hashed boxes) and SomArchon-expressing (open boxes) neurons in cortex layer 2/3 brain slices (p=0.8026, 0.8895, 0.8236, two-

sided Wilcoxon Rank Sum test, comparing Archon1 versus SomArchon, for resistance, capacitance, and resting potential respectively; n = 8 and 18 cells from 1 and 2 mice for Archon1 and SomArchon). (**b**) Similar to **a**, but in hippocampus (p=0.6294, 0.9720, 0.8880, 0.0037, two-side Wilcoxon Rank Sum test, comparing negative versus SomArchon for resistance, capacitance, resting potential, FWHM, n = 8 and 7 cells from 2 mice each for negative and SomArchon for resistance and resting potential comparison; n = 7 and 7 cells from 2 mice each for negative and SomArchon for capacitance comparison. FWHM: p=0.0037, n = 7 and 8 cells from from 2 mice each for negative and SomArchon for FWHM comparison). (**c**) Similar to **a**, but in striatum (p=0.7380, 0.8357, 0.7751, 0.0931, two-sided Wilcoxon Rank Sum test, comparing negative and SomArchon, for resistance, capacitance, resting potential and FWHM; n = 7 and 6 cells from 2 mice each for negative and SomArchon for resistance and capacitance comparisons; n = 6 and 7 cells from 2 mice each for negative and SomArchon for resting potential comparison; n = 6 and 6 cells from 2 mice each for negative and SomArchon for FWHM comparisons). (**d**) Changes of relative reactive oxygen species (ROS) concentration (normalized to that before illumination) over time in negative (solid line) and SomArchon-expressing (dashed line) cultured mouse neurons under various illumination protocols. (**e**) Maximal increase in ROS concentration during continuous illumination for conditions performed in **d** (n = 45, 24, and 8 negative neurons from 2, 2, and 1 cultures for 390/22 nm, 475/36 nm, and 637 nm illumination, respectively; n = 24 SomArchon-expressing neurons for 637 nm illumination from 1 culture). (**f**) Cell death for negative (solid line) and SomArchon-expressing (dashed line) cultured neurons at DIV 14–18 under various illumination protocols. (n=45, 35, 91, 40, and 27 neurons from 2, 1, 2, 1, and 1 cultures respectively for 390/22 nm at 2.8 mW/mm^2, 390/22 nm at 5.5 mW/mm^2, 475/36 nm at 12 mW/mm^2, 475/36 nm at 25 mW/mm^2, and 637 nm at 1500 mW/mm^2 illumination). (**g**) Bright-field and fluorescence images of representative neurons expressing SomArchon before and after 10 min of continuous 637nm laser illumination at 1500 mW/mm^2, followed by 10 min in darkness (93% of imaged cells did not exhibit noticeable changes in morphology; n = 27 cells from 1 culture; non-illuminated cells did not show any changes in morphology; n = 10 cells from 1 culture). Scale bar, 50μm. (**h**) Representative SomArchon fluorescence trace from neuron co-expressing SomArchon and CoChR-$K_v2.1_{motif}$. (**i**) Normalized spike rates (to initial value) elicited by blue light illumination dropped after 300 s of continuous recording, due to decrease in spike amplitude as a result of photobleaching (n = 10 neurons from 1 culture; plotted as mean ± standard deviation). (**j**) Normalized (to initial value) full width half maximum (FWHM) of spikes elicited by continuous light exposure as in **h**. Box plots displayed as in **Figure 3.2**. Full statistics in **Table 6.3**, **Table 6.4**, **Table 6.5**, and **Table 6.6**.

We performed a side-by-side comparison of SomArchon with soma-localized versions of several next-generation voltage sensors, specifically QuasAr3[97], paQuasAr3[97], ASAP3[226], and Voltron$_{525}$[206], in mouse cortical brain slice, focusing on layer 2/3 neurons, under identical expression conditions (**Table 6.14**). The spectrally similar sensors QuasAr3, paQuasAr3, and SomArchon were recorded under identical imaging conditions

(1.5W/mm^2), during co-expressed blue-light driven CoChR-mediated action potentials. ASAP3 and Voltron were recorded with filter sets used in their respective preprints[206,226], under similar excitation intensities used in the Voltron pre-print[206] (25–29 mW/mm^2), during action potentials evoked upon application of 4-aminopyridine.

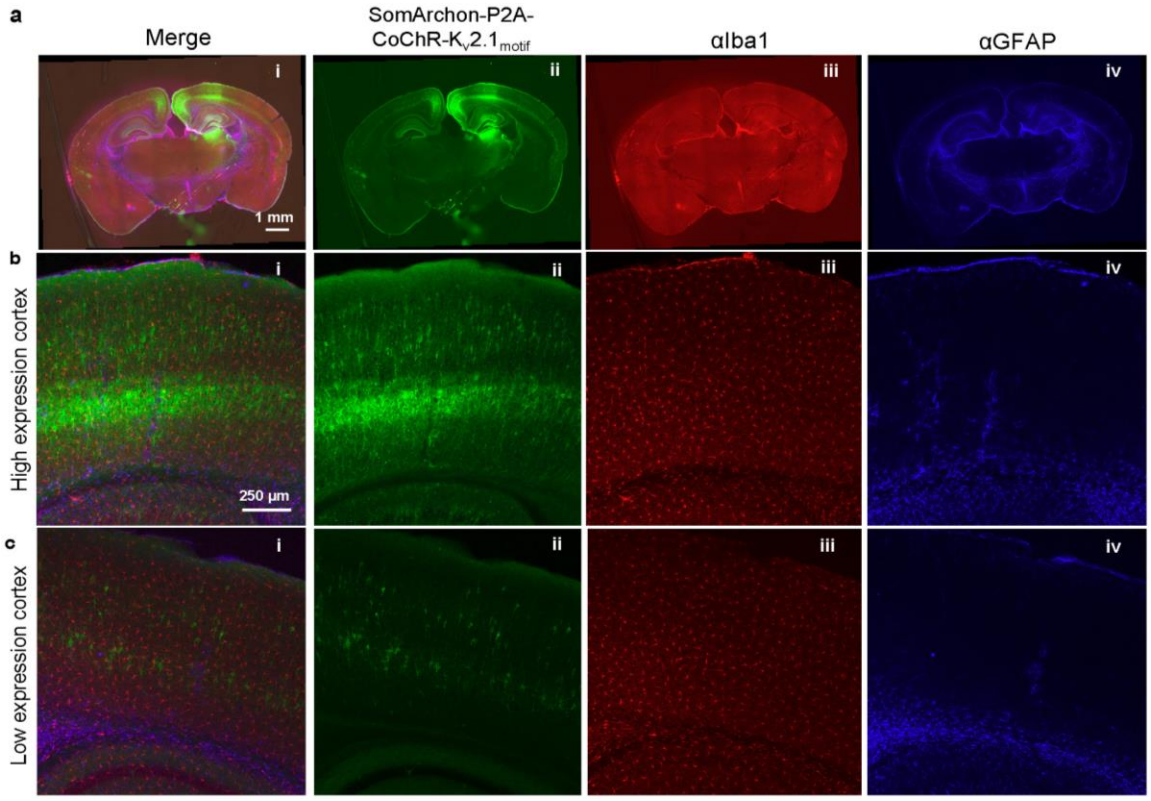

Figure 3.5. **SomArchon expression *in vivo* does not cause gliosis.** SomArchon was expressed in the cortex by AAV2.9-Syn-SomArchon-P2A-CoChR-$K_V2.1_{motif}$ injection into P0 Swiss Webster mice. Brain tissues were analyzed 63 days post viral injection. (i) Merged fluorescence images from 50 μm-thick coronal sections were visualized via (ii) EGFP fluorescence of SomArchon, (iii) anti-Iba1 immunofluorescence, and (iv) anti-GFAP immunofluorescence (n = 4 slices from 2 mice). (**a**) Expression throughout coronal section. (**b**) Zoomed-in view on the virally injected area (high expression cortex). (**c**) Zoomed-in view on the non-injected contralateral hemisphere (low expression cortex). GFAP and Iba1, commonly used glial and microglial markers, showed similar appearance on the virally injected hemisphere versus the non-injected hemisphere, suggesting that expression of SomArchon did not cause gliosis. Scale bars: 1 mm, **a**; and 250 µm, **b**,**c**.

Under these conditions, SomArchon exhibited the highest ΔF/F and SNR per action potential (**Figure 3.6**); in addition, SomArchon exhibited values higher than those previously reported for Ace2N-mNeon[188], ASAP1[185], MacQ-mCitrine[186], and QuasAr2[208] (see **Table 6.14** for details). SomArchon also showed higher photostability than soma localized versions of ASAP3 and Voltron$_{525}$ under comparable imaging conditions in cultured neurons (**Figure 3.6e**).

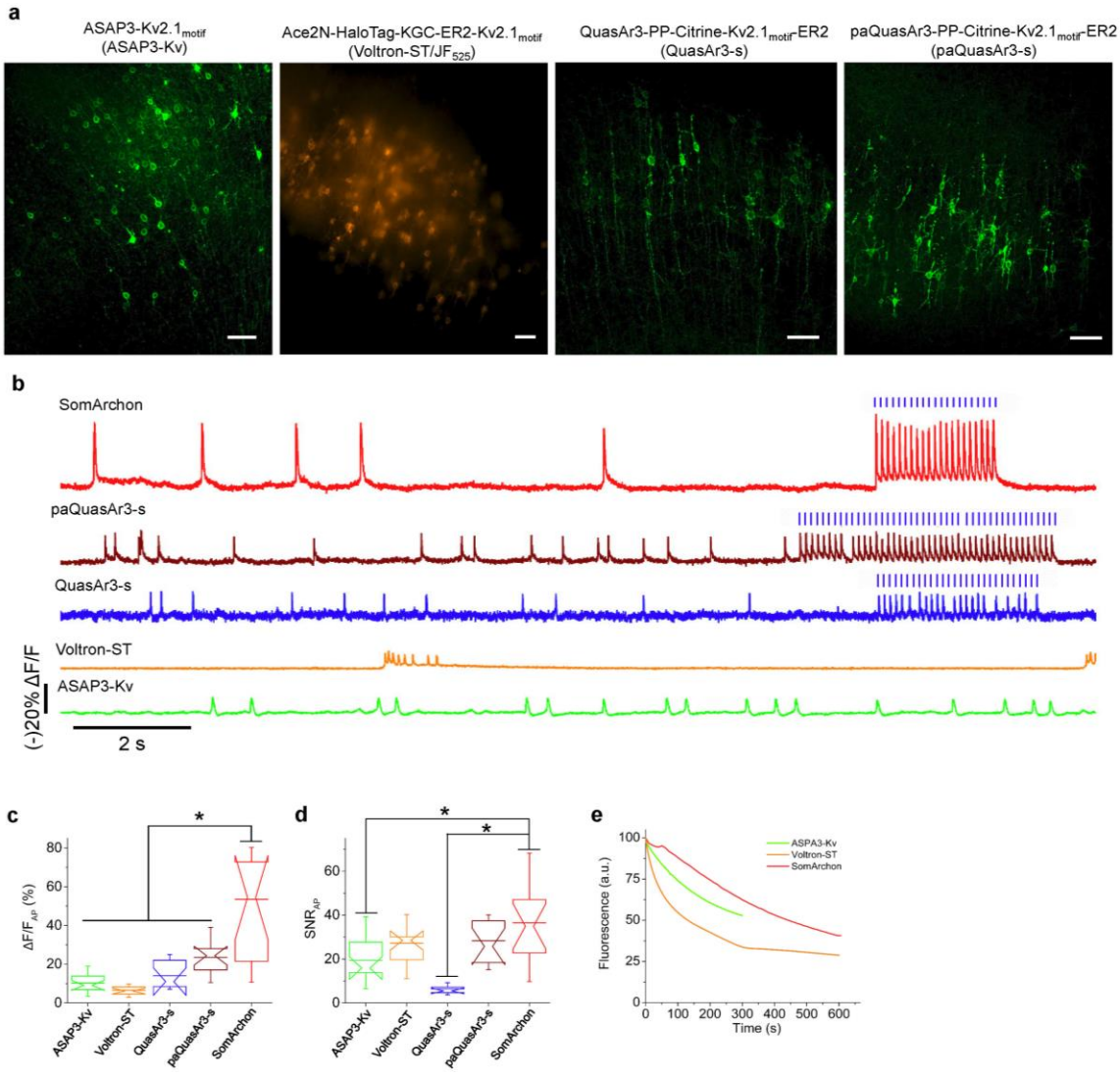

Figure 3.6. Side-by-side comparison of next-generation voltage indicators in mouse brain slices. (a) Representative fluorescence images of mouse cortex layer 2/3 neurons expressing

ASAP3-$K_V2.1_{motif}$ (ASAP3-Kv), Ace2N-HaloTag-KGC-ER2-$K_V2.1_{motif}$ (Voltron-ST), QuasAr3-PP-mCitrine-$K_V2.1_{motif}$-ER2 (QuasAr3-s), and paQuasAr3-PP-mCitrine-$K_V2.1_{motif}$-ER2 (paQuasAr3-s). ASAP3-Kv, QuasAr3-s and paQuasAr3-s were visualized via cpGFP, mCitrine, and mCitrine fluorescence respectively, using laser excitation at 488 nm and emission at 525/50 nm under a confocal microscope. Voltron-ST was visualized via JF525 fluorescence using LED excitation at 510/25 nm and emission at 545/40 nm under a wide-field microscope. Scale bar, 50µm. **(b)** Single-trial optical recordings of ASAP3-Kv (green) and Voltron-ST/JF525 (orange) fluorescence responses during 4-aminopyridine evoked neuronal activity, and QuasAr3-s (blue), paQuasAr3-s (brown), and SomArchon (red) fluorescence responses during CoChR-mTagBFP2-$K_V2.2_{motif}$ evoked neuronal activity. Acquisition rate ~500 Hz. Blue light pulses (470/20nm, 2ms per pulse, 10Hz), shown as vertical blue bars, were used to activate CoChR to evoke spiking. **(c,d)** Quantification of **(c)** ΔF/F and **(d)** signal-to-noise ratio (SNR) per AP across all recordings (n = 18, 14, 9, 13, and 14 neurons from 1, 2, 2, 2, and 2 mice for ASAP3-Kv, Voltron-ST/JF525, QuasAr3-s, paQuasAr3-s, and SomArchon, respectively). Box plots displayed as in **Figure 3.2**. (*$p < 0.01$, Wilcoxon rank sum test; see **Table 6.7** and **Table 6.8** for statistics) **(e)** Photobleaching curves of ASAP3-Kv, Voltron-ST/JF525, and SomArchon under continuous illumination (n=11, 8, and 17 neurons from 1 culture, respectively).

3.5 SomArchon enables *in vivo* voltage imaging with single cell, single spike precision using conventional wide-field microscopy

Having established the improved performance of SomArchon over prior molecules in terms of sensitivity and SNR, we next sought to quantify whether this was reflected in improved ability to observe neuronal activity *in vivo*. We targeted multiple brain regions with AAV containing SomArchon under the synapsin promoter, including the motor cortex, visual cortex, striatum, and hippocampus. Mice were head-fixed and awake while under a simple, conventional wide-field one-photon microscope (**Figure 3.7a**). We first identified virally-transfected cells with a low magnification (10x) objective lens in the green channel, as SomArchon includes a GFP tag (**Figure 3.7b**), and then performed voltage imaging of near-infrared fluorescence of SomArchon using laser excitation light at 637 nm, with a 20x objective lens at ~1.6 W/mm^2 (75mW), a 40x objective lens at ~4 W/mm^2 (75mW), or a 16x objective lens at 1.6 W/mm^2 (95mW).

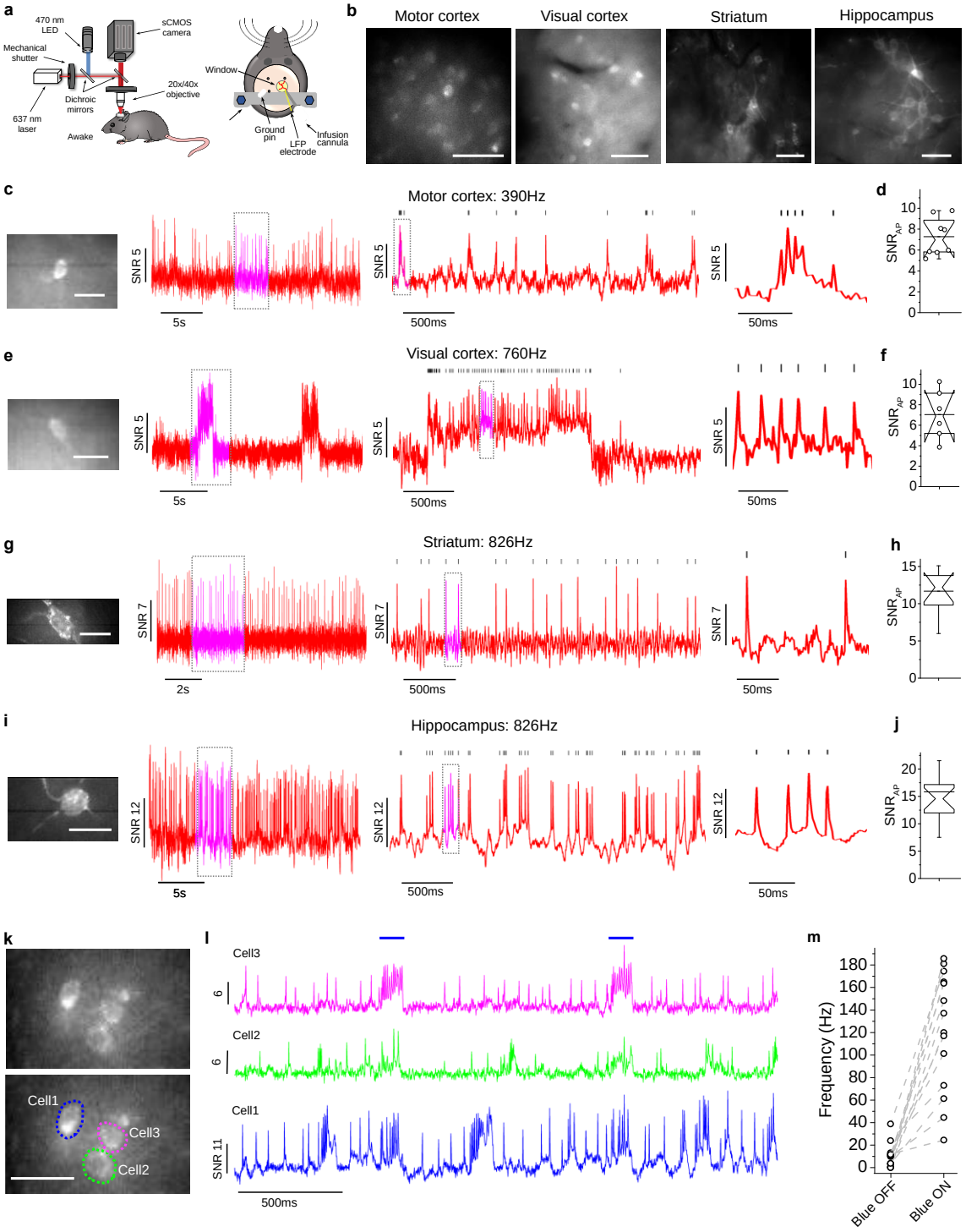

Figure 3.7. SomArchon enables single cell voltage imaging in multiple brain regions of awake mice, using a simple wide-field imaging setup. (a) Experimental setup: awake mice were head-fixed under a wide-field microscope (*left*); diagram of surgical window implant coupled with an infusion cannula and an LFP recording electrode (*right*). **(b)** Representative SomArchon-

expressing neurons visualized via EGFP fluorescence in motor cortex, visual cortex, striatum, and hippocampus (λ_{ex}=470/25 nm LED, λ_{em}=525/50 nm). Scale bars, 50μm. **(c, e, g, i)** Voltage imaging in **(c)** motor cortex, **(e)** visual cortex, **(g)** striatum, and **(i)** hippocampus. SomArchon fluorescence image of the cell *in vivo* (*left*) and optical voltage trace acquired from the cell (*right*; dashed boxes indicate time intervals shown at successively expanded time scales; vertical bars indicate peaks of action potentials identified by a custom spike-sorting algorithm); λ_{ex}=637 nm laser, at 1.6 W/mm^2 for visual cortex and motor cortex, 4 W/mm^2 for striatum and hippocampus, λ_{em}=664LP). Scale bars, 25μm. **(d, f, h, j)** Quantification of SNR per action potential for **(d)** motor cortex, **(f)** visual cortex, **(h)** striatum, and **(j)** hippocampus. Box plots are displayed as described in **Figure 3.2**. In **b–j**, representative images and traces were selected from, and statistics performed on, n = 8, 6, 10, and 17 cells from 3, 2, 3, and 4 mice respectively. **(k)** Fluorescence image of selected FOV showing hippocampal neurons expressing SomArchon-P2A-CoChR-$K_V2.1_{motif}$ (*top*) with neurons identified (*bottom*); λ_{ex}=637 nm, exposure time 1.2 ms. Scale bar, 20μm. **(i)** Representative single-trial optical voltage traces from cells shown in **k** with blue light stimulation (100 ms pulse). Image acquisition rate: 826 Hz. **(m)** Firing rate changes during blue light off versus blue light on conditions in individual neurons. In **k–m**, representative image selected from, and statistics performed on, n = 14 cells from 2 mice.

Optical voltage recordings of awake, head-fixed mice with an acquisition rate of 390–910 Hz using an sCMOS camera consistently detected individual spikes, as well as bursts of spikes, in single cells across all four brain regions (**Figure 3.7).** SomArchon baseline fluorescence levels were sufficient to resolve individual cells in the near-infrared voltage channel (**Figure 3.7c,e,g,i**), with single cell bodies resolvable at depths up to 180 μm below the imaging chamber surface, and with most cells imaged at depths of 50–150 μm for cortex and hippocampus, and 20–150 μm for striatum. The SNR per action potential ranged from ~7 to ~16 across the brain regions examined (**Figure 3.7d,f,h,j**). No other paper reported SNR values per action potential in living mouse brain, so we cannot directly compare our molecule to others in this regard. We were also able to resolve short segments of proximal dendrites next to the soma, and detected voltage fluctuation patterns that sometimes differed from those in the soma (**Figure 3.8c–f**), providing evidence that SomArchon could be used for sub-cellular imaging if targeting strategies were refined to specific cell compartments.

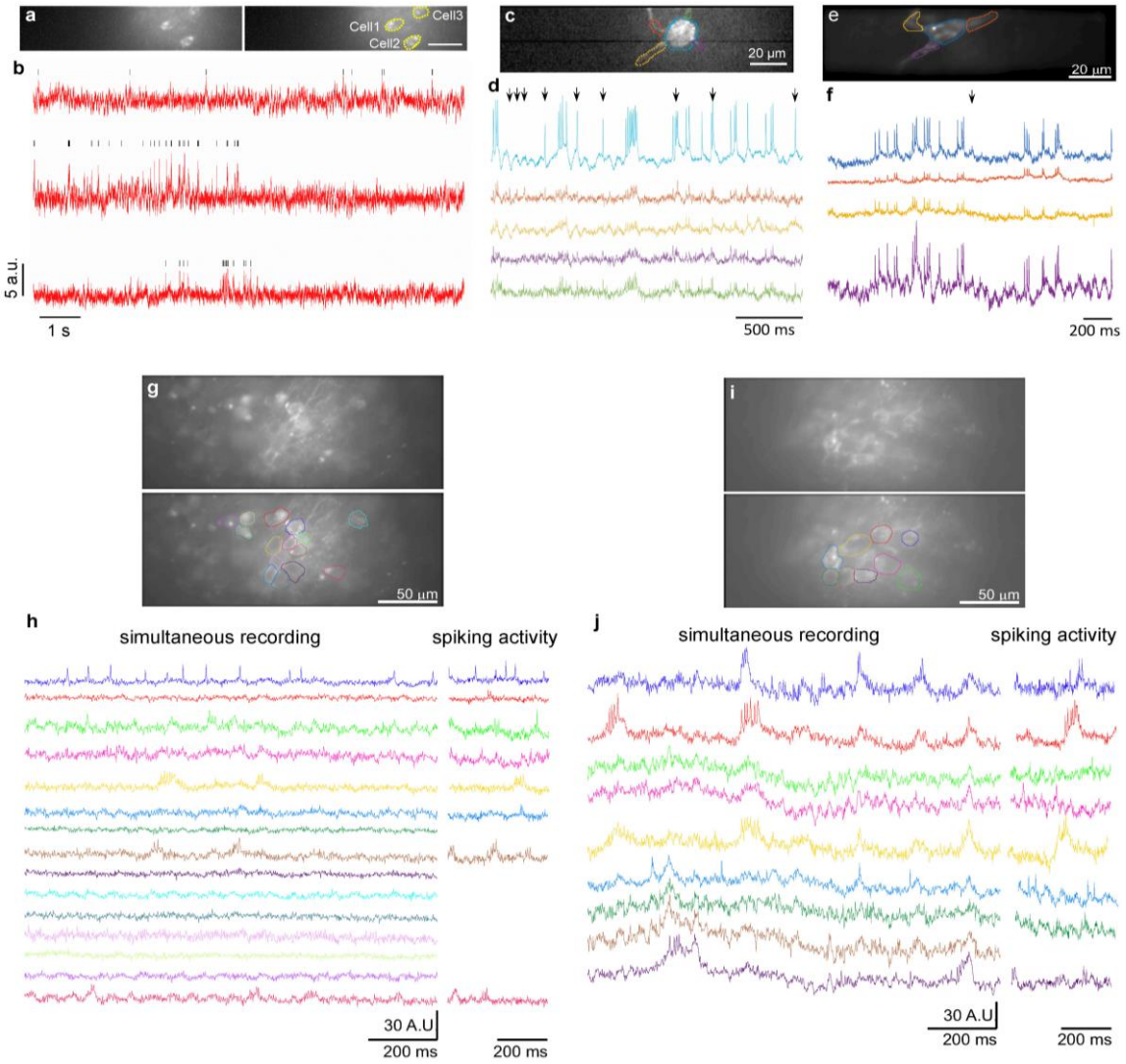

Figure 3.8. SomArchon enables both local dendritic and population imaging of neurons in multiple brain regions *in vivo*. (**a**) Fluorescence images of selected FOV in motor cortex (*left*) with selected ROIs corresponding to somas of three neurons (*right*) (n = 1 FOV from 1 mouse). Scale bar, 50 μm. (**b**) Representative fluorescence traces from **a** with detected spikes (black ticks). (**c**) Fluorescence image of a hippocampal neuron expressing SomArchon with ROIs selected at the soma and on four proximal dendrites (n = 1 neuron from 1 mouse). Scale bar, 20 μm. (**d**) Optical voltage traces from the selected ROIs shown in **c**. (**e**) Fluorescence image of a striatal neuron expressing SomArchon with ROIs selected at the soma and on three proximal dendrites (n = 1 neuron from 1 mouse). Scale bar, 20 μm. (**f**) Optical voltage traces from the selected ROIs shown in **e**. Black arrows highlight example instances when dendritic voltages visibly differed from those on the soma. (**g–k**) *In vivo* population voltage imaging in the hippocampus CA1 region (n = 14 FOVs from 3 mice). (**g**,**i**) Average intensity projection image for each FOV (*top*), and with identified ROIs (*bottom*). (**h**,**j**) Optical voltage traces for each neuron shown in **g,i**, respectively, with colors matching corresponding ROI colors. Shown are 1.2 seconds of simultaneously recorded voltage for all neurons (*left*), and a zoomed-in period with prominent spikes (*right*). Image acquisition rate for all recordings: 826 Hz.

3.6 All-optical electrophysiology *in vivo* using SomArchon in combination with a blue-light activated channelrhodopsin

The use of microbial rhodopsins has become widespread in neuroscience as a method for activating and silencing neuronal activity of genetically targeted cell populations[240]. Some high-performance channelrhodopsins are activated with blue light, and thus, could in principle be spectrally combined with near-infrared fluorescence indicators such as SomArchon for *in vivo* neural activation and voltage imaging. As we previously demonstrated that Archon1 exhibits no crosstalk under continuous or pulsed blue illumination[183], we used a bicistronic expression system, SomArchon-P2A-CoChR-K_V2.1 ("Optopatch") to co-express SomArchon and the high-performance channelrhodopsin CoChR[241] in the same cell via a P2A cleavage sequence (**Figure 3.2h**). Illuminating transduced cells in brain tissue with 2 ms blue light pulses at 10 and 20 Hz reliably evoked single action potentials, (n = 8 neurons from 2 mice; **Figure 3.2i,j**). We further expressed SomArchon-P2A-CoChR-K_V2.1 via AAV injection in the hippocampus of the mouse brain, and optogenetically evoked neural activity in awake mice while simultaneously imaging membrane voltage of the same cells (**Figure 3.7k**). Blue light stimulation for durations of 100 ms reliably evoked spiking, as imaged in populations of neurons within the same field of view (**Figure 3.7l),** and across different fields of view (**Figure 3.7m,** n = 14 neurons, from 7 recording sessions from 2 mice). This demonstrates that Optopatch can be used as an all-in-one tool for simultaneous optical control and voltage imaging recording in the same construct, which could be useful for a variety of neuroscience applications.

3.7 *In vivo* single cell, single spike optical voltage imaging from striatal neurons during locomotion

Electrophysiology has demonstrated that many striatal neurons increase their firing rate responses during movement[228,242], while others decrease their responses[227,228]. While electrophysiology recordings largely discard spatial information regarding the relative location of the neurons being observed, recent calcium imaging studies have revealed that spatially clustered striatal neurons are activated by similar aspects of movement[59]. These calcium imaging studies focused on the increases in activity during movement as decreases in activity are harder to observe with calcium imaging. We performed voltage imaging while mice ran on a spherical treadmill (**Figure 3.10a**), identifying cell bodies and spikes from cells in the striatum (**Figure 3.10b–d**), and aligned spiking activity to movement (**Figure 3.10d**).

a

	Firing Rate (Hz)	Area (um²)	ISI (mean+/- SD)
Cell 1	2	187.59	403.8+/-881.5
Cell 2	1.6686	144.073	530.2+/-953.4
Cell 3	2.7771	172.803	300.4+/-542.4
Cell 4	2.9167	175.338	273.3+/-509.6
Cell 5	7.933	175.76	124.4+/-198.3
Cell 6	13.2778	89.993	71.3+/-88.6
Cell 7	15.1389	69.29	64.8+/-87.6
Cell 8	11.7222	86.612	83.7+/-98.9
Cell 9	29.95	131.82	33.2+/-39.8
Cell 10	2.0167	117.455	462.6+/-586.2
Cell 11	2.7667	149.143	351.2+/-470.7
Cell 12	5.4271	361.66	182.4+/-133.1
Cell 13	14.3626	181.253	69.1+/-96.8
Cell 14	23.1753	191.393	43.0+/-44.0

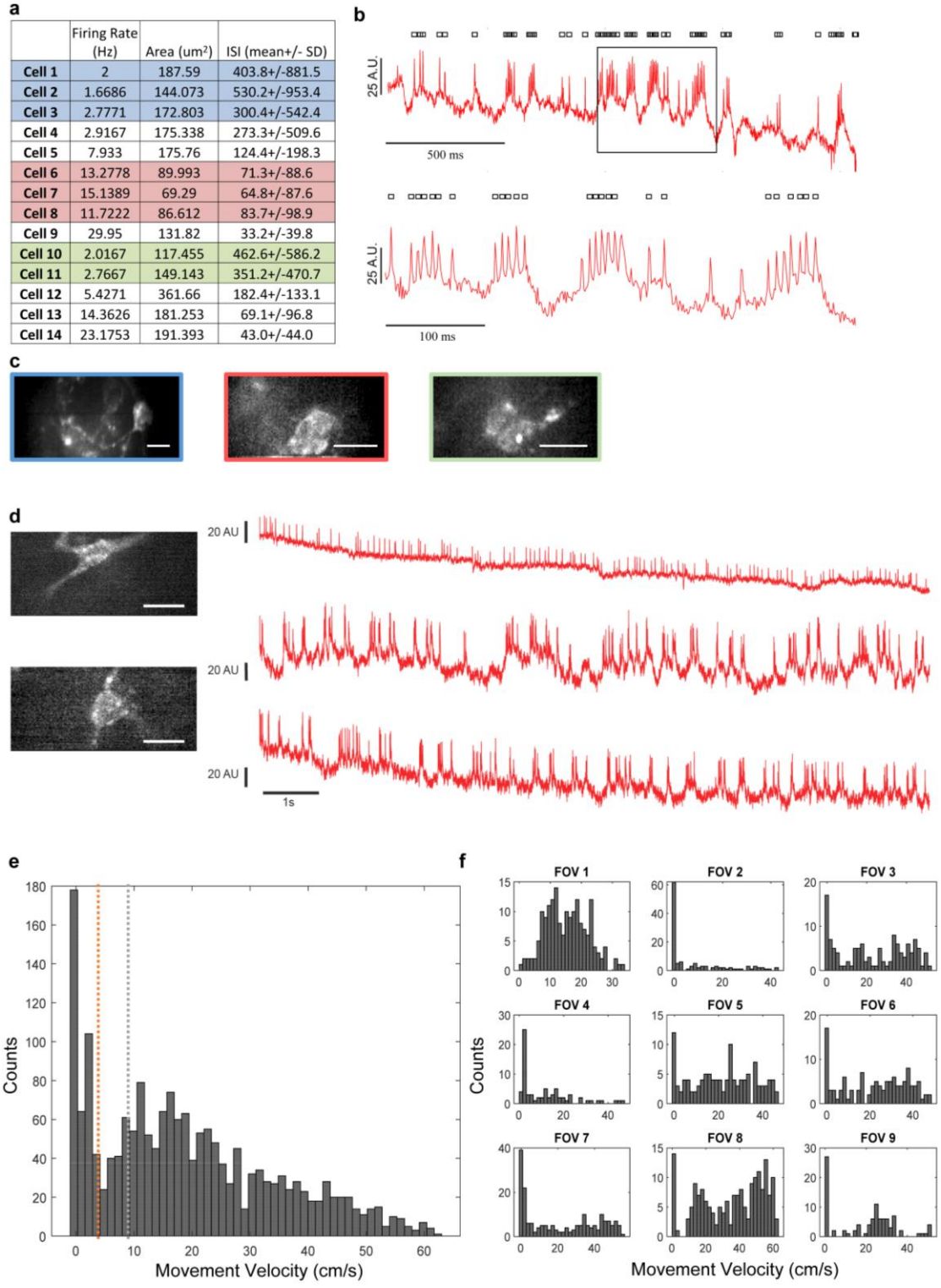

Figure 3.9. Properties of striatal neurons and movement thresholds. (a) Average firing rate, size, and inter-spike interval (ISI) for the 14 neurons recorded in 9 FOVs in 2 mice. Cells simultaneously recorded in the same FOV are color-coded (blue, red, green). Cells in rows with a

white background were recorded individually. **(b)** Selected trace from Cell 9 exhibiting spike bursting (*top*), and a zoomed view of the boxed region (*bottom*). A.U.: arbitrary unit. Identified spikes are indicated by the black dots on top of the trace. **(c)** Single frame images for FOVs with multiple neurons. Each FOV is color-coded to match **a**. Scale bars, 20μm. **(d)** Representative optical traces of two striatal cholinergic interneurons from Cre-dependent SomArchon-expressing in a ChAT-Cre mouse (*left*, scale bar, 20μm), recorded in 3 sessions, while mouse was awake, head-fixed and navigating a spherical treadmill (n = 2 neurons from 1 mouse). Two bottom traces are from the same neuron, *left bottom*. Image acquisition rate, 826 Hz. **(e)** Histogram of instantaneous movement speeds for all FOVs shown in **Figure 3.10** (9 FOVs in 2 mice). Instantaneous movement speed was calculated as average speed during each 0.5-second time interval. Red line, threshold for low movement speed identification; green line, threshold for high movement speed identification. **(f)** Histogram of instantaneous movement speed for individual FOVs analyzed.

Some neurons exhibited firing patterns known to occur in striatal fast spiking interneurons[243] or cholinergic interneurons[244] (**Figure 3.9a–d)**. We found that 4 of the 14 neurons were positively modulated by movement speed, and 2 were negatively modulated by movement speed (**Figure 3.10e,f, Figure 3.9e,f;** statistics in **Table 6.9**). Furthermore, adjacent neurons did not respond to movement speed in identical ways. For example, in two recordings with three neurons each, we found that one of the three neurons was positively modulated by movement speed whereas the other two were not (**Figure 3.10f, Figure 3.9a,c;** see Cells 1, 2, 3, and Cells 6, 7, 8; and **Table 6.9**). Thus, SomArchon can readily detect decreases in striatal neuron spiking during movement, and help disambiguate activity changes amongst spatially clustered striatal neurons.

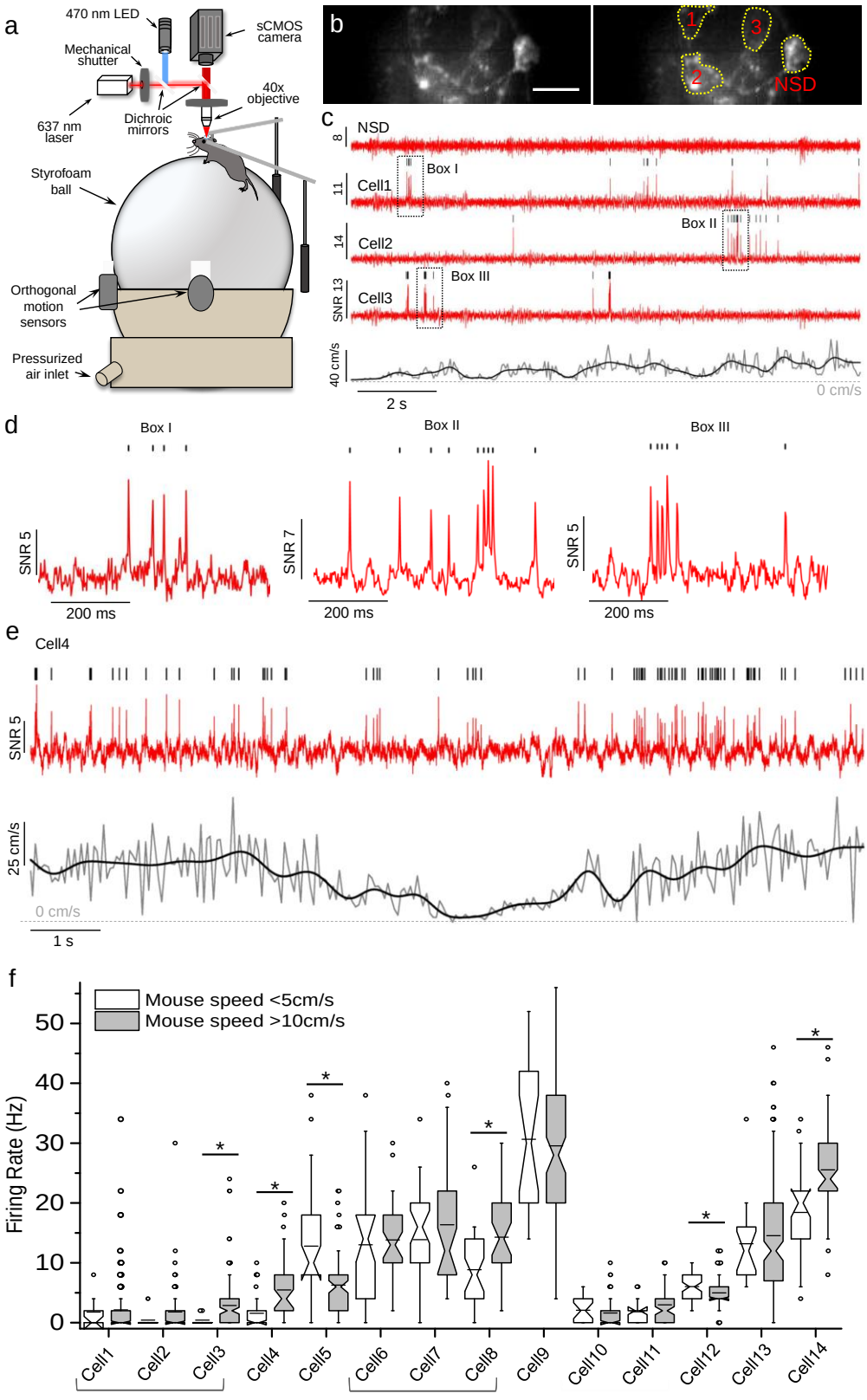
a
470 nm LED
sCMOS camera
Mechanical shutter
40x objective
637 nm laser
Dichroic mirrors
Styrofoam ball
Orthogonal motion sensors
Pressurized air inlet
b
1
2
3
NSD
c
NSD
Box I
Cell1
Box II
Cell2
Box III
Cell3
SNR 13
40 cm/s
0 cm/s
2 s
d
Box I
Box II
Box III
SNR 5
SNR 7
SNR 5
200 ms
200 ms
200 ms
e
Cell4
SNR 5
25 cm/s
0 cm/s
1 s
f
Mouse speed <5cm/s
Mouse speed >10cm/s
Firing Rate (Hz)
0
10
20
30
40
50
Cell1
Cell2
Cell3
Cell4
Cell5
Cell6
Cell7
Cell8
Cell9
Cell10
Cell11
Cell12
Cell13
Cell14

Figure 3.10. Voltage imaging of striatal neurons during locomotion. (**a**) Schematic representation of the experimental setup, similar to that in **Figure 3.7a**, but with mice positioned on a spherical treadmill. Imaging was performed with a 40x objective lens. (**b**) SomArchon fluorescence image of striatal cells (*left*), with identified ROIs corresponding to somas (*right*), λ_{ex}=637 nm, exposure time 1.2 ms (representative image selected from n = 9 FOV from 2 mice). Scale bar, 20μm. NSD: no spikes detected. (**c**) Optical voltage traces acquired from cells shown in **b**, and corresponding mouse movement speed (black: low pass filtered at 1.5 Hz; gray: raw data; representative traces selected from n = 2 FOVs from one mouse). Image acquisition rate, 826 Hz. (**d**) Zoomed-in views of the three periods indicated by black boxes shown in **c**. (**e**) Optical voltage trace (red) for a neuron modulated by movement speed and corresponding movement speed (black) (representative trace selected from n = 14 neurons from 2 mice). (**f**) Firing rates of individual striatal neurons, during periods with low (open box) versus high (gray) movement speed (n = 14 neurons from 2 mice, brackets indicate neurons from the same FOV). *, p<0.05, two-sided Wilcoxon rank sum test. Box plots are displayed as described in **Figure 3.2**. Full statistics in **Table 6.9**.

3.8 Simultaneous recordings of intracellular membrane voltage and local field potentials (LFPs) revealed distinct phase relationships between spikes and theta oscillations in the hippocampus

We performed wide-field voltage imaging with SomArchon in hippocampal CA1 neurons in awake, head-fixed mice, while simultaneously recording LFPs. CA1 neurons exhibited average firing rates ranging from 3.3 to 18.0 Hz (7.92±3.55 Hz, mean± standard deviation, n = 16 neurons, from 7 recording sessions from 4 mice), consistent with previous electrophysiology recordings[245,246]. *In vivo* patch clamp recordings have shown stronger phase-locking of a CA1 neuron's spikes to its own intracellular theta frequency (4–10Hz) oscillations, than to the across-neuron averaged LFP theta oscillations[245,247]. We found that 6 of the 16 neurons had spikes phase-locked to both intracellular and LFP theta oscillations (example in **Figure 3.11a**), and 9 were phase locked only to intracellular theta oscillations, but not to LFP theta oscillations (example in **Figure 3.11b).** As a population**,** neurons exhibited stronger phase locking to intracellular theta oscillations than to LFP theta oscillations (**Figure 3.11c,d**). SomArchon thus supports the analysis of subthreshold

intracellular oscillations, although interpretation of these measurements must take into account background fluorescence, which in densely labelled tissue may result in crosstalk that affects correlations.

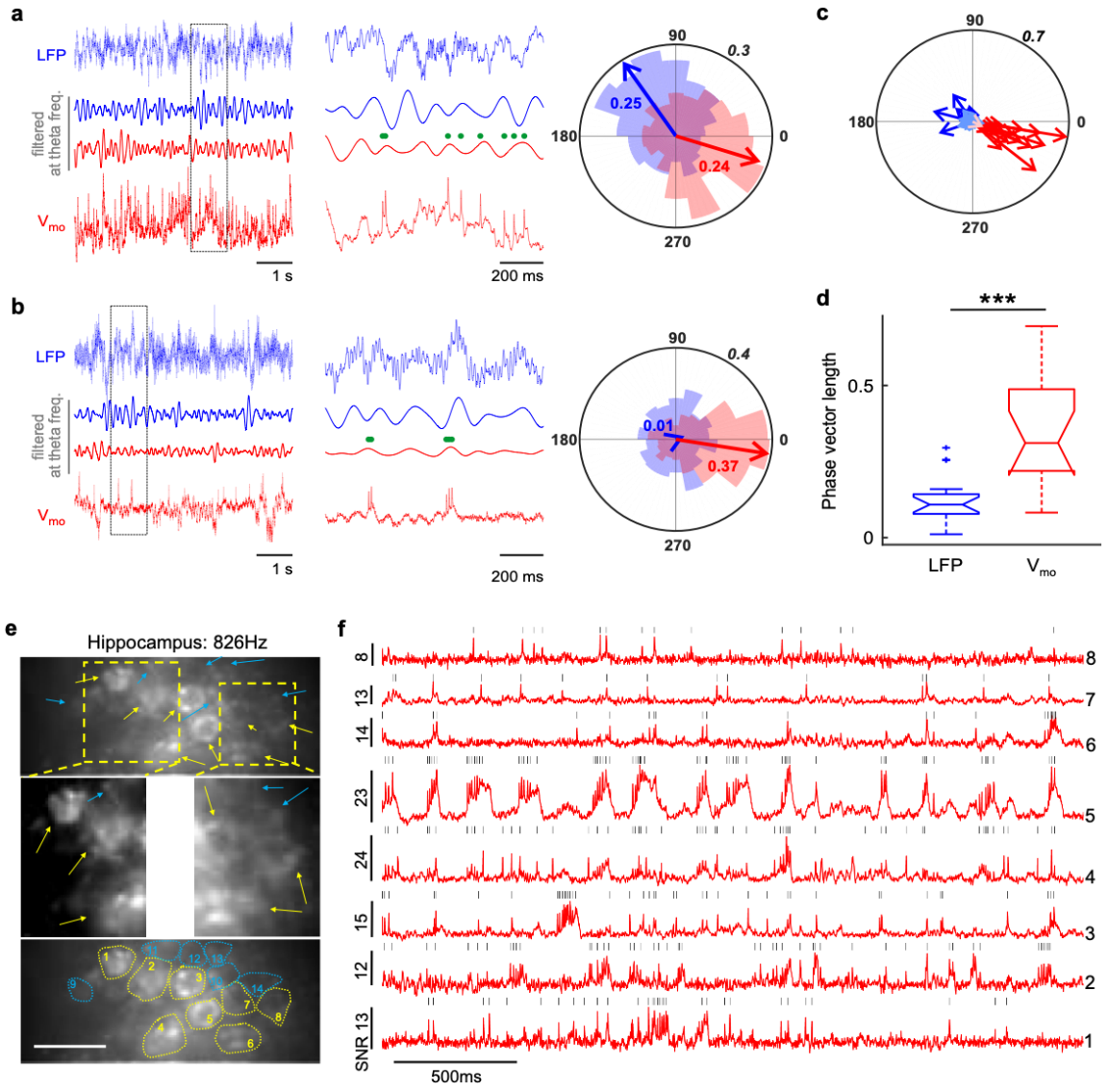

Figure 3.11. Population voltage imaging of spikes and subthreshold voltage activities in CA1 neurons. (**a**) A neuron with spikes phase-locked to theta oscillations of local field potentials (LFPs, blue) and optically-recorded membrane voltage (V_{mo}, red). (*Left*) Raw LFPs, *top*, and V_{mo}, *bottom*, and theta frequency filtered traces, *middle*. (*Center*) Zoomed-in view of the boxed period on the *left*. Theta oscillation peaks are indicated by blue and red vertical lines, and spikes by green dots. (*Right*) Probability distribution of spikes to theta oscillation phases of LFP (blue) and V_{mo} (red). Arrows indicate the average phase vector (with vector length indicated). Outer circle number indicates probability. (Example is selected from n = 16 neurons in 7 FOVs from 4 mice) (**b**) As in

(**a**), but for an example neuron phase locked to V_{mo} theta oscillations, but not to LFP theta oscillations. (**c**) Population spike-phase vectors to theta oscillations of LFP (blue and light blue) and V_{mo} (red and pink). Each vector represents the average vector from one neuron (blue and red: $p<0.05$; light blue and pink: not significant; χ^2 test, spike-phase distribution of each neuron against uniform distribution; n = 198–1077 spikes per neuron; 16 neurons in 7 FOVs from 4 mice). (**d**) Population spike-phase relationship. (***, $p = 5.0 \times 10^{-5}$, two-tailed paired Student's t-test, n = 16 neurons in 7 FOVs from 4 mice). Box plots (25th and 75th percentiles with notch being the median; whiskers extend to all data points not considered outliers; + are outliers. (**e**) SomArchon fluorescence images of CA1 neurons (*left*), with ROIs overlaid (*right*) (n = 14 FOV from 3 mice). Example spiking cells are indicated by yellow arrows whose optical voltage traces are shown in (**f**); blue arrows indicate neurons not active during the period shown; λ_{ex}=637 nm laser at 1.5 W/mm^2. Scale bar, 20 μm. Full statistics in **Table 6.10**.

3.9 SomArchon retains stable fluorescence intensity and signal-to-noise ratio (SNR) *in vivo* during behavioral experiments

We evaluated SomArchon photostability *in vivo*, and found a slight decrease in intensity in both the striatum and the hippocampus over time, but the SNR remained largely stable in both brain regions (**Figure 3.12**). In the hippocampus, firing rates remained constant over time, and we were able to continuously image for up to 80 seconds with minimal changes in SNR (**Figure 3.12i–m**). This lack of toxicity is consistent with our results from cultured neurons (**Figure 3.4**).

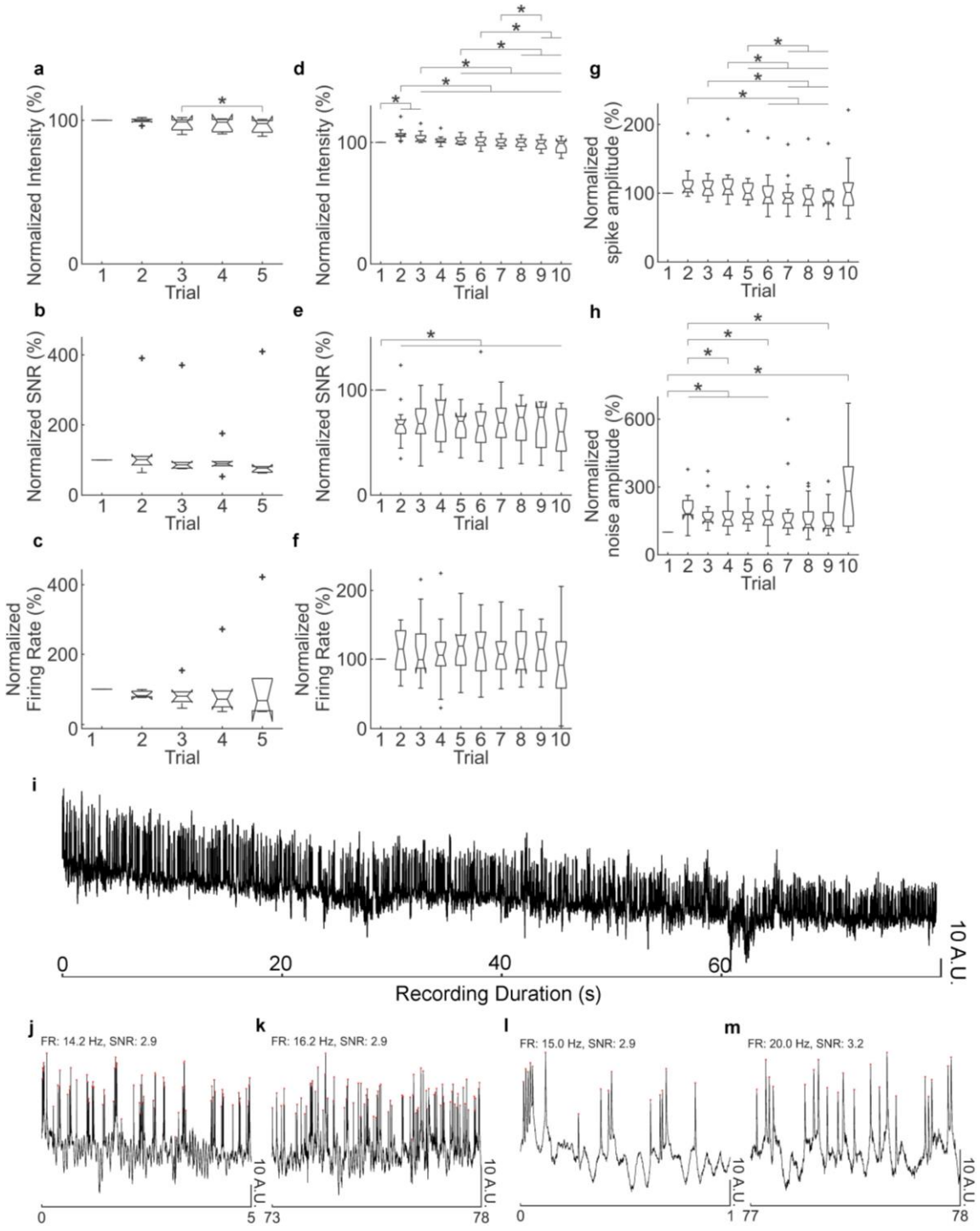

Figure 3.12. ***In vivo*** **SomArchon performance over time in the striatum and hippocampus of awake mice. (a–h)** Average fluorescence intensity, SNR per spike, and firing rates of neurons in the striatum and hippocampus of awake mice, over multiple trials. **(a–c)** In each striatal recording session, we performed 5 trials, each 12 seconds long, with inter-trial intervals of 30–60 seconds. **(a)** Average fluorescence intensity decreased slightly, while **(b)** spike SNR and **(c)** firing rates

remained constant throughout the recording session (repeated measures ANOVA, n = 6 neurons in 5 FOVs from one mouse). **(d–h)** In each hippocampal recording session, we performed 10 trials, each 6 seconds long, with inter-trial intervals of 20–30 seconds. **(d)** Average fluorescence intensity showed a slight but significant decrease across trials. **(e)** SNR decreased between the 1st and 2nd trials but not afterwards, and **(f)** the firing rate remained constant. **(g)** Spike amplitude fluctuated randomly over trials, and **(h)** there was a significant increase in baseline noise between the 1st and 2nd trials (repeated measures ANOVA; *: $p<0.05$, post-hoc test: Tukey's HSD test, n = 16 neurons in 7 FOVs from 4 mice, see **Tables 6.11**). Measurements were normalized to the first trial for each neuron. All box plots displayed are as in **Figure 3.11**. **(i–m)** A representative continuous optical trace of a hippocampal neuron over 80 seconds in an awake, head-fixed mouse, with zoomed-in view **(j–m)** at the beginning and end of the recording highlighting comparable firing rates and SNRs (n = 16 neurons in 7 FOVs from 4 mice).

3.10 Population imaging of hippocampal neuron spiking dynamics *in vivo*.

Due to the high performance and soma-targeted nature of SomArchon, we were able to routinely image multiple neurons at once in both cortical and subcortical brain regions (**Figure 3.7k,l, Figure 3.10b,c, Figure 3.8a,b**). In the hippocampus, using a 20x objective lens, we were able to record from 14 neurons at once, 8 of which were spiking (**Figure 3.11e,f**). In addition, using a 16x objective lens, we routinely recorded from approximately a dozen cells at once (n = 13.1±3.5 neurons per FOV, mean±standard deviation, from 13 recording sessions in 2 awake mice). Of the 170 manually identified neurons, 107 (63%) spiked during the recording periods (duration: 13.5–27 seconds; **Table 6.15** and examples in **Figure 3.8g–j**). The ability to simultaneously record from multiple neurons allowed us to examine correlation and coherence of subthreshold activities between neuron pairs, though background fluorescence crosstalk between nearby neurons will need to be considered when interpreting pairwise correlation/coherence measurements (see **3.11, Figure 3.13e–h, Figure 3.14).**

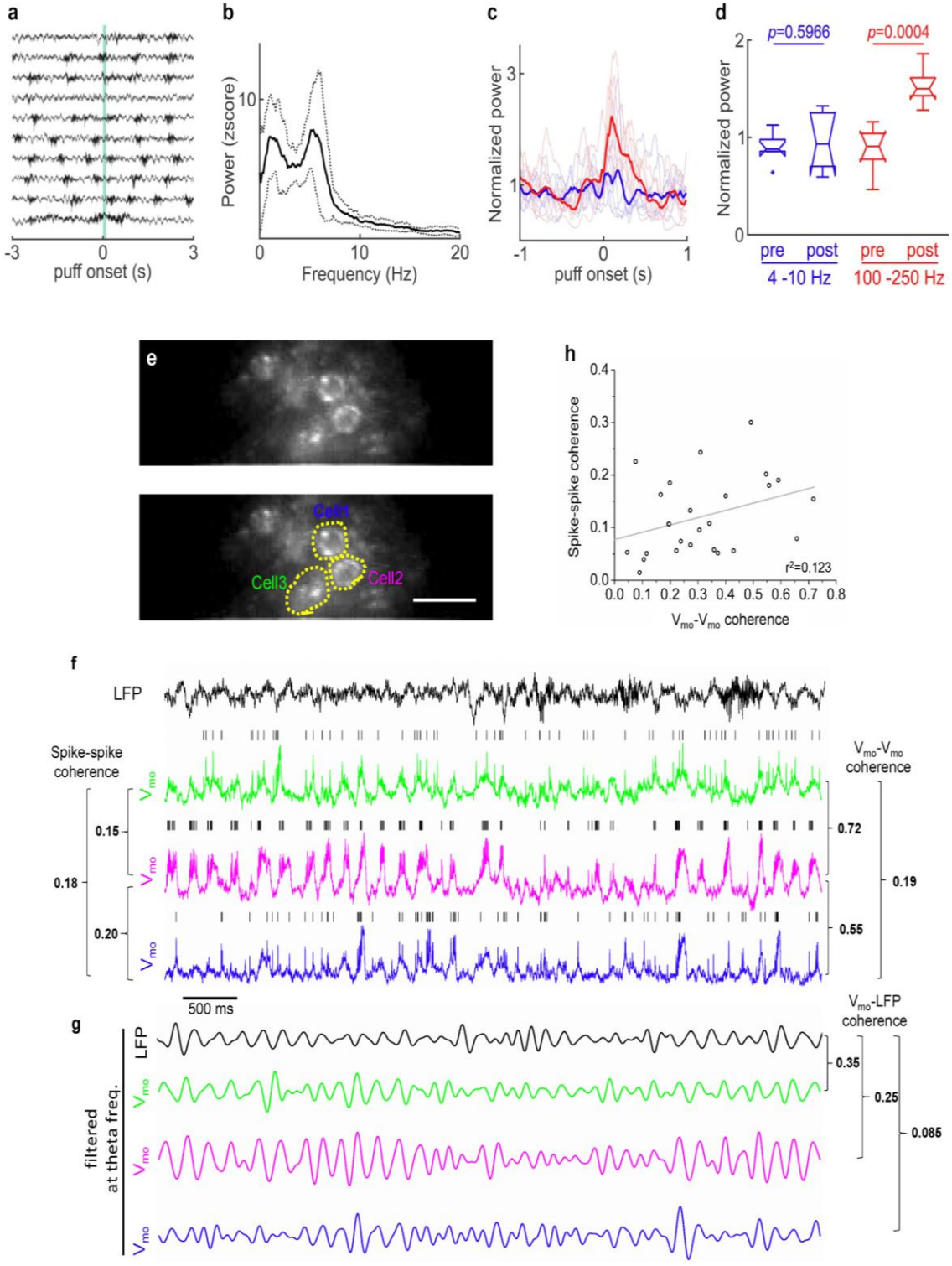

Figure 3.13. LFP and subthreshold membrane voltage oscillation analysis in the hippocampus. (**a**) Example hippocampal LFP recordings from a session with 10 trials, aligned to the onset of an air puff (green shading) directed to one eye in awake headfixed mice. (**b**) LFP power

spectrum shows strong theta oscillations. Plotted are mean±standard deviation, n=10 trials in 1 session. (**c**) Oscillation power at high frequencies (100–250 Hz, red) and at theta frequencies (blue), aligned to puff onset. Each thin line represents an individual recording session, and the thick lines denote means (n = 7 sessions in 4 mice). (**d**) Eye puff evoked a significant increase in LFP power at high frequency, but not at theta frequency (theta frequency: p = 0.5966, high frequency: p = 0.0004, two-tailed paired Student's t-test, n=7 sessions in 4 mice). Box plots are as in **Figure 3.11.** (**e**) Fluorescence image of a representative FOV (*top*) with selected ROIs (*bottom*). (**f**) Membrane voltage recorded optically (V_{mo}) from neurons identified in **e**, and simultaneously recorded LFPs. Black vertical ticks above V_{mos} denote spikes. Spike-spike coherence values between neurons are shown at the *left* and V_{mo}-V_{mo} theta coherence values are shown at the *right*. (**g**) Theta frequency-filtered LFPs and V_{mos} for the four traces shown in **f**. V_{mo}-LFP coherence values are shown to the right. (**h**) Scatter plot of V_{mo}-V_{mo} theta frequency coherence and spike-spike coherence from all neuron pairs, fitted with a linear regression (n=25 pairs, p=0.08, t-statistic, r^2=0.12).

3.11 SomArchon allows detection of subthreshold activity in hippocampal neurons *in vivo*

The hippocampus has typically been regarded as having little topographical organization[248,249], although some evidence has suggested a degree of spatial clustering[250,251]. Recently, based upon multi-neuron automated patch clamp data[252], we hypothesized that even when nearby neurons in the awake mouse hippocampus exhibit highly coordinated subthreshold activities, they might generate extremely divergent spiking outputs that are sensitive to transient and stochastic intracellular membrane voltage fluctuations. Since we were unable to analyze more than one cell in the hippocampus at a time over an extended period of time in awake mice, even with automated patch clamp, we were previously unable to test this hypothesis.

SomArchon allowed us to record from a population of neurons simultaneously (**Figure 3.11e,f**), and thus we could examine the extent to which subthreshold oscillations are coordinated across neural populations to regulate spiking. Accordingly, we calculated the

coherence, both at the spiking level and at the subthreshold intracellular oscillation level, to determine whether nearby neurons exhibited similar subthreshold intracellular oscillations and how coordinated subthreshold activities impact spiking with a focus on theta frequencies that are prevalent in the hippocampus (**Figure 3.11a–d, Figure 3.13**). The coherence between two nearby neurons' intracellular subthreshold oscillations was not constant, but fluctuated over time (coefficient of variation, 0.39±0.12, mean±standard deviation) and was significantly different from a stable coherence value (one sample t-test, $p<0.001$), revealing temporally dynamic input structures.

To further explore how intracellular subthreshold oscillations may relate to the across-neuron averaged LFP signals, we examined the coherence between intracellular subthreshold theta oscillations recorded in two neurons, versus the coherence between one neuron and the simultaneously recorded LFP theta oscillations. While simultaneously recorded neurons exhibited a wide range of coherence to LFP oscillations (**Figure 3.13f,g**), at a population level, adjacent neurons showed greater intracellular oscillation coherence amongst themselves than with LFPs (V_{mo}-V_{mo} coherence=0.32±0.13, V_{mo}-LFP coherence=0.10±0.05, mean±standard deviation, two-sided Wilcoxon rank sum test, p=0.0008, n = 9 sessions). These results highlight that among the diverse current sources that contribute to the spatiotemporally integrated LFP signals, some may exhibit a greater role in synchronizing post-synaptic responses measured as V_{mo} by SomArchon.

In 9 hippocampal recording sessions where we recorded multiple neurons, we found that

across the 25 neuron pairs simultaneously imaged (n = 25 neurons, from 9 recording sessions from 4 mice), spike-spike coherence showed no linear relationship with subthreshold intracellular oscillation coherence at theta frequency (**Figure 3.13h,** n = 25 pairs, linear regression, $p = 0.083$, $r^2 = 0.12$). The lack of correlation between intracellular oscillations and their spike timing is consistent with the idea that nearby neurons may receive vast common synchronized inputs, where a small number of selective inputs may have an outsized role in governing spiking output, at least in the awake-at-rest state investigated here.

To quantify the impact of background fluorescence on creating shared fluorescence crosstalk across neurons, we identified the immediate surrounding background in a donut-shaped area around each neuron (for details, see **Methods**). We did not detect any significant decrease in coherence and correlation measures over distance between neuron pairs or between their background donut pairs, within our imaging FOVs with a size of ~80–100 μm in diameter (**Figure 3.14**). We further calculated the correlation and coherence between each neuron's V_{mo} and its surrounding background fluorescence, and found that V_{mos} exhibited low coherence and low correlation with its background donut fluorescence (coherence at theta: 0.33±0.16, coherence at gamma: 0.34±0.17, Pearson correlation coefficient: 0.27±0.16; mean±standard deviation, n=24 neuron/donut pairs). These results suggest that while wide-field imaging background fluorescence may create shared background fluorescence signal crosstalk between neuron pairs, the observed V_{mo}-V_{mo} coherence cannot be not fully contributed by crosstalk.

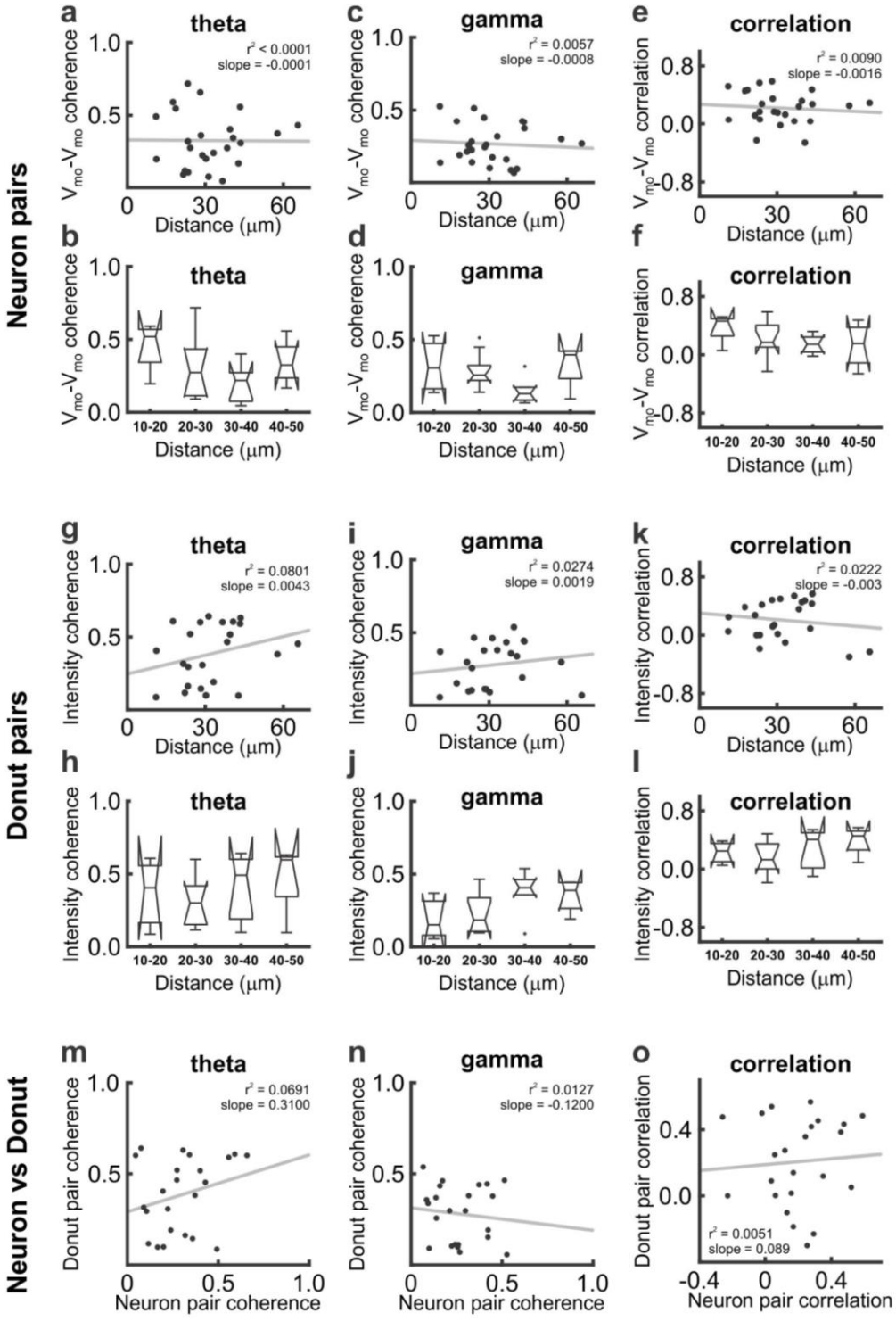

Figure 3.14. Pair-wise coherence and correlation measures over spatial distance. To investigate the potential of background fluorescence signals under wide-field imaging to produce shared crosstalk signals on neuron pairs, we examined the relationship of various coherence and correlation measures between neurons and background fluorescence over spatial distance. (**a**–**b**)

Pair-wise coherence at theta frequencies between neurons. V_{mo}-V_{mo} coherence did not decrease significantly with spatial distance. (**a**, n=25 pairs analyzed with spatial distance of 11–66 μm, center to center; **b**, n=23 pairs within 50 μm of each other, F=1.44, p=0.26, one-way ANOVA). (**c,d**) Pair-wise V_{mo}-V_{mo} coherence at gamma frequencies (30–50 Hz) was not dependent on spatial distance (**c**, n = 25 pairs); **d**, n = 23 pairs within 50 μm of each other, F=2.10, p=0.13, one-way ANOVA). **(e**,**f)** Pair-wise correlation between neurons did not decrease significantly with spatial distance (**e**, n=25 pairs; **f**, n=23 pairs within 50 μm, F=1.00, p=0.42, one-way ANOVA). (**g–l**) Same analysis as in **a–f** performed in background donut ROIs surrounding each neuron (for donut definition see Methods). Similar to results from neuron pairs, we found that theta frequency coherence between background donut ROIs was not dependent on spatial distance (**g**, n=23 pairs; **h**, n=21 pairs, F=0.65, p=0.59, one-way ANOVA), nor was gamma frequency coherence (**l**, n=23 pairs; **j**, n=21 pairs, F=1.93, p=0.16, one-way ANOVA), nor was the correlation coefficient (**k**, n=23 pairs; **l**, n=21 pairs, F=1.02, p=0.41, one-way ANOVA). (**m–o**) The coherence between neurons and their corresponding donuts were not correlated, at theta frequency (**m**) or at gamma frequency (**n**), or for the Pearson correlation coefficients (**o**). All box plots displayed are as in **Figure 3.11.** Full statistics in **Tables 6.12**.

3.12 Discussion

Compared to existing GEVIs, SomArchon achieves a severalfold improvement in the number of cells simultaneously imaged, while being fully genetically encoded and using inexpensive one-photon microscopy. The previously published record for fully genetically encoded voltage imaging was 4 spiking cells recorded simultaneously in an awake behaving mouse, but requires a specialty imaging setup that combines two-photon structural imaging to support patterned single-photon excitation illumination targeting individual cell bodies, as well as the blue light-gated molecule paQuasAr3 that is incompatible with commonly used pulsed blue light optogenetic modulation[97]. ASAP3 has been used to image three dendrites at once, with 2-photon microscopy, but this approach can only be used to record single cells at the fast rates typical for voltage imaging[226]. The hybrid GEVI sensor Voltron enables imaging of 46 neurons[206], but requires the addition of chemicals delivered to the living brain that complicate *in vivo* mammalian use, is not compatible with optogenetics, and exhibits lower dynamic range than SomArchon (**Figure**

3.6). Voltron, ASAP3, and Ace2N-mNeon all exhibit crosstalk with rhodopsins hampering their use with optogenetic actuators. Voltage imaging with SomArchon, as well as QuasAr3, is mainly limited by the high power and illumination spot of the 637 nm excitation laser; however, our data suggest that high powered 637 nm excitation does not induce more phototoxicity than with common, lower-powered 470 nm excitation (**Figure 3.4**).

3.13 Conclusion

In conclusion, SomArchon is fully genetically encoded, compatible with conventional easily accessible one-photon widefield fluorescence microscopes, fully compatible with blue light-driven optogenetics, and enables routine imaging of a dozen neurons in a single FOV. We anticipate that the practicality of SomArchon will enable its rapid deployment into a diversity of contexts in neuroscience. As camera performance improves in years to come, and as further evolution of GEVIs continues, we anticipate that perhaps dozens to hundreds of neurons will be imageable with simple one-photon optics in the near future.

3.14 Methods

3.14.1 Molecular Cloning

To screen candidates for the soma-localized Archon1 voltage sensor in primary hippocampal neurons, DNA encoding candidate localization motifs were synthesized *de novo* with mammalian codon optimization and subcloned with Archon1 (GenBank ID

MG250280.1) and EGFP genes into the pAAV-CAG vector to obtain the final constructs described in **Table 6.13** (gene synthesis and subcloning were performed by Epoch Life Science Inc.). For *in vivo* expression in the mouse brain via *in utero* electroporation (IUE), the Archon1-KGC-EGFP-$K_V2.1_{motif}$-ER2, QuasAr3-PP-Citrine-$K_V2.1_{motif}$-ER2 (QuasAr3-s), paQuasAr3-PP-Citrine-$K_V2.1_{motif}$-ER2 (paQuasAr3-s) and CoChR-mTagBFP2-$K_V2.2_{motif}$-ER2 genes were subcloned into the pCAG-WPRE vector. The QuasAr3-PP-Citrine-K_V2.1-ER2 and paQuasAr3-PP-Citrine-K_V2.1-ER2 genes were synthesized de novo (GenScript Biotech Corp.) based on sequences reported in the original preprint[253]. The CoChR-mTagBFP2-$K_V2.2_{motif}$-ER2 gene was assembled by Epoch Life Science Inc. using pAAV-Syn-CoChR-GFP (Addgene plasmid #59070) and pBAD-mTagBFP2 (Addgene plasmid #34632) as the source of the CoChR and mTagBFP2 genes, respectively; the K_V2.2 motifs were synthesized *de novo* with mammalian codon optimization (Epoch Life Science Inc.). The pAAV-Syn-Archon1-KGC-EGFP-$K_V2.1_{motif}$-P2A-CoChR-$K_V2.1_{motif}$ plasmid was also cloned by Epoch Life Science Inc. We used the Kv2.1motif fused to CoChR for the following reason: in our original paper on soma-targeted CoChR[232], we used the KA2 sequence, which worked best with CoChR-GFP, but in this paper we used fluorophore-free CoChR, which did not express well with KA2, and rather worked better with K_V2.1; we also sometimes used the corresponding sequence from K_V2.2 as described in the text. Plasmid amplification was performed using Stellar (Clontech Laboratories Inc.) or NEB10-beta (New England BioLabs Inc.) chemically competent *E. coli* cells. Small-scale isolation of plasmid DNA was performed with Mini-Prep kits (Qiagen); large-scale DNA plasmid purification was done with GenElute HP

Endotoxin-Free Plasmid Maxiprep Kits (Sigma-Aldrich Corp.). The ASAP3-Kv and Voltron-ST genes were synthesized *de novo* by GenScript, based on the sequences reported in the corresponding pre-prints[206,226], and cloned into pCAG-WPRE vector.

3.14.1.1 Amino acid sequences

Linker:

GGSGGTGGSGGT

KA2(1–150)

MPAELLLLLIVAFANPSCQVLSSLRMAAILDDQTVCGRGERLALALAREQINGIIE
VPAKARVEVDIFELQRDSQYETTDTMCQILPKGVVSVLGPSSSPASASTVSHICGE
KEIPHIKVGPEETPRLQYLRFASVSLYPSNEDVSLAVS

KA2(1–100)

MPAELLLLLIVAFANPSCQVLSSLRMAAILDDQTVCGRGERLALALAREQINGIIE
VPAKARVEVDIFELQRDSQYETTDTMCQILPKGVVSVLGPSSSP

KGC:

KSRITSEGEYIPLDQIDINV

ER2:

FCYENEV

Nav1.2(II–III):

SSFSSDNLAATDDDNEMNNLQIAVGRMQKGIDFVKRKIREFIQKAFVRKQKALD

EIKPLEDLNNKKDSCISNHTTIEIGKDLNYLKDGNGTTSGIGSSVEKYVVDESDYM

SFINNPSLTVTVPIALGESDFENLNTEEFSSESDMEESKEKLNATSSSEGSTVDIGA

PAEGEQPEAEPEESLEPEACFTEDCVRKFKCCQISIEEGKGKLWWNLRKTCYKIS

Nav1.6(II–III)

TVRVPIAVGESDFENLNTEDVSSESDP

Kv2.1-motif:

QSQPILNTKEMAPQSKPPEELEMSSMPSPVAPLPARTEGVIDMRSMSSIDSFISCAT

DFPEATRF

AnkMB(270)-motif (270-kDa AnkyrinG (1–837aa)):

MAHAASQLKKNRDLEINAEEETEKKKKHRKRSRDRKKKSDANASYLRAARAG

HLEKALDYIKNGVDVNICNQNGLNALHLASKEGHVEVVSELLQREANVDAATK

KGNTALHIASLAGQAEVVKVLVTNGANVNAQSQNGFTPLYMAAQENHLEVVRF

LLDNGASQSLATEDGFTPLAVALQQGHDQVVSLLLENDTKGKVRLPALHIAARK

DDTKAAALLLQNDTNADIESKMVVNRATESGFTSLHIAAHYGNINVATLLLNRA

AAVDFTARNDITPLHVASKRGNANMVKLLLDRGAKIDAKTRDGLTPLHCGARS

GHEQVVEMLLDRAAPILSKTKNGLSPLHMATQGDHLNCVQLLLQHNVPVDDVT

NDYLTALHVAAHCGHYKVAKVLLDKKANPNAKALNGFTPLHIACKKNRIRVME

LLLKHGASIQAVTESGLTPIHVAAFMGHVNIVSQLMHHGASPNTTNVRGETALH

MAARSGQAEVVRYLVQDGAQVEAKAKDDQTPLHISARLGKADIVQQLLQQGAS

PNAATTSGYTPLHLSAREGHEDVAAFLLDHGASLSITTKKGFTPLHVAAKYGKLE

VASLLLQKSASPDAAGKSGLTPLHVAAHYDNQKVALLLLDQGASPHAAAKNGY

TPLHIAAKKNQMDIATSLLEYGADANAVTRQGIASVHLAAQEGHVDMVSLLLSR

NANVNLSNKSGLTPLHLAAQEDRVNVAEVLVNQGAHVDAQTKMGYTPLHVGC

HYGNIKIVNFLLQHSAKVNAKTKNGYTPLHQAAQQGHTHIINVLLQNNASPNEL

TVNGNTALAIARRLGYISVVDTLKVVTEEIMTTTTIT

AnkMB(490)-motif (490-kDa AnkyrinG (1–800aa))

MAHAASQLKKNRDLEINAEEETEKKRKHRKRSRDRKKKSDANASYLRAARAGH

LEKALDYIKNGVDVNICNQNGLNALHLASKEGHVEVVSELLQREANVDAATKK

GNTALHIASLAGQAEVVKVLVTNGANVNAQSQNGFTPLYMAAQENHLEVVRFL

LDNGASQSLATEDGFTPLAVALQQGHDQVVSLLLENDTKGKVRLPALHIAARKD

DTKAAALLLQNDTNADVESKSGFTPLHIAAHYGNINVATLLLNRAAAVDFTARN

DITPLHVASKRGNANMVKLLLDRGAKIDAKTRDGLTPLHCGARSGHEQVVEML

LDRSAPILSKTKNGLSPLHMATQGDHLNCVQLLLQHNVPVDDVTNDYLTALHV

AAHCGHYKVAKVLLDKKASPNAKALNGFTPLHIACKKNRIRVMELLLKHGASIQ

AVTESGLTPIHVAAFMGHVNIVSQLMHHGASPNTTNVRGETALHMAARSGQAE

VVRYLVQDGAQVEAKAKDDQTPLHISARLGKADIVQQLLQQGASPNAATTSGY

TPLHLAAREGHEDVAAFLLDHGASLSITTKKGFTPLHVAAKYGKLEVASLLLQK

SASPDAAGKSGLTPLHVAAHYDNQKVALLLLDQGASPHAAAKNGYTPLHIAAK

KNQMDIATSLLEYGADANAVTRQGIASVHLAAQEGHVDMVSLLLSRNANVNLS

NKSGLTPLHLAAQEDRVNVAEVLVNQGAHVDAQTKMGYTPLHVGCHYGNIKIV

NFLLQHSAKVNAKTKNGYTALHQAAQQGHTHIINVLLQNNASPNELTVNGNTA

L

AnkSB-motif (270-kDa AnkyrinG (801–1521aa)):

AIARRLGYISVVDTLKVVTEEIMTTTTITEKHKMNVPETMNEVLDMSDDEVRKA

SAPEKLSDGEYISDGEEGEDAITGDTDKYLGPQDLKELGDDSLPAEGYVGFSLGA

RSASLRSFSSDRSYTLNRSSYARDSMMIEELLVPSKEQHLTFTREFDSDSLRHYSW

AADTLDNVNLVSSPVHSGFLVSFMVDARGGSMRGSRHHGMRIIIPPRKCTAPTRI

TCRLVKRHKLANPPPMVEGEGLASRLVEMGPAGAQFLGPVIVEIPHFGSMRGKE

RELIVLRSENGETWKEHQFDSKNEDLAELLNGMDEELDSPEELGTKRICRIITKDF

PQYFAVVSRIKQESNQIGPEGGILSSTTVPLVQASFPEGALTKRIRVGLQAQPVPEE

TVKKILGNKATFSPIVTVEPRRRKFHKPITMTIPVPPPSGEGVSNGYKGDATPNLR

LLCSITGGTSPAQWEDITGTTPLTFIKDCVSFTTNVSARFWLADCHQVLETVGLAS

QLYRELICVPYMAKFVVFAKTNDPVESSLRCFCMTDDRVDKTLEQQENFEEVAR

SKDIEVLEGKPIYVDCYGNLAPLTKGGQQLVFNFYSFKENRLPFSIKIRDTSQEPC

GRLSFLKEPKTTKGLPQTAVCNLNITLPAHKKETESDQDDAEKADRRQSFASLAL

RKRYSYLTEPSMKTVERSSGTARSLPTTYSHKPFFSTRPYQSWTTAPITVPGPAKS

GSLSSSPSNTPSA

AnkCt-motif (270-kDa AnkyrinG (2334–2622aa))

RTDIRMAIVADHLGLSWTELARELNFSVDEINQIRVENPNSLISQSFMLLKKWVT
RDGKNATTDALTSVLTKINRIDIVTLLEGPIFDYGNISGTRSFADENNVFHDPVDG
WQNETPSGSLESPAQARRLTGGLLDRLDDSSDQARDSITSYLTGEPGKIEANGNH
TAEVIPEAKAKPYFPESQNDIGKQSIKENLKPKTHGCGRTEEPVSPLTAYQKSLEE
TSKLVIEDAPKPCVPVGMKKMTRTTADGKARLNLQEEEGSTRSEPKQGEGYKV
KTKKEIRNVEKKTH

AnkSR-motif (270-kDa AnkyrinG (1534–1933aa))

SPLKSIWSVSTPSPIKSTLGASTTSSVKSISDVASPIRSFRTVSSPIKTVVSPSPYNPQ
VASGTLGRVPTITEATPIKGLAPNSTFSSRTSPVTTAGSLLERSSITMTPPASPKSNI
TMYSSSLPFKSIITSATPLISSPLKSVVSPTKSAADVISTAKATMASSLSSPLKQMSG
HAEVALVNGSVSPLKYPSSSALINGCKATATLQDKISTATNAVSSVVSAASDTVE
KALSTTTAMPFSPLRSYVSAAPSAFQSLRTPSASALYTSLGSSIAATTSSVTSSIITV
PVYSVVNVLPEPALKKLPDSNSFTKSAAALLSPIKTLTTETRPQPHFNRTSSPVKSS
LFLASSALKPSVPSSLSSSQEILKDVAEMKEDLMRMTAILQTDVPEEKPFQTDLP

AnkTail-motif (270-kDa AnkyrinG (1934–2333aa)):

REGRIDDEEPFKIVEKVKEDLVKVSEILKKDVCVESKGPPKSPKSDKGHSPEDDW
TEFSSEEIREARQAAASHAPSLPERVHGKANLTRVIDYLTNDIGSSSLTNLKYKFE

EAKKDGEERQKRILKPAMALQEHKLKMPPASMRPSTSEKELCKMADSFFGADAI
LESPDDFSQHDQDKSPLSDSGFETRSEKTPSAPQSAESTGPKPLFHEVPIPPVITETR
TEVVHVIRSYEPSSGEIPQSQPEDPVSPKPSPTFMELEPKPTTSSIKEKVKAFQMKA
SSEEEDHSRVLSKGMRVKEETHITTTTRMVYHSPPGGECASERIEETMSVHDIMK
AFQSGRDPSKELAGLFEHKSAMSPDVAKSAAETSAQHAEKDSQMKPKLERIIEV
HIEKGPQSPCE

3.14.2 Neuronal culture and transfection

All mouse procedures were performed in accordance with the National Institute of Health Guide for Laboratory Animals and approved by the Massachusetts Institute of Technology Institutional Animal Care and Use and Biosafety Committees. For dissociated hippocampal mouse neuron culture preparation, postnatal day 0 or 1 Swiss Webster mice without regard to sex (Taconic Biosciences Inc., Albany, NY) were used as previously described[183]. Briefly, dissected hippocampal tissue was digested with 50 units of papain (Worthington Biochemical Corporation) for 6-8 min at 37 °C, and the digestion was stopped by incubating with ovomucoid trypsin inhibitor (Worthington Biochemical Corporation) for 4 min at 37 °C. Tissue was then gently dissociated with Pasteur pipettes, and dissociated neurons were plated at a density of 20,000–30,000 per glass coverslip coated with Matrigel (BD Biosciences). Neurons were seeded in 100 µL plating medium containing MEM (Life Technologies Corp.), glucose (33 mM, Sigma), transferrin (0.01%, Sigma), Hepes (10mM, Sigma), Glutagro (2 mM, Corning), Insulin (0.13%, Millipore), B27 supplement (2%, Gibco), and heat inactivated FBS (7.5%, Corning). After cell adhesion, additional plating

medium was added. AraC (0.002 mM, Sigma) was added when glia density was 50–70% of confluence. Neurons were grown at 37°C and 5% CO2 in a humidified atmosphere.

For *in vitro* screening of candidate soma-localized Archon1 sensors, primary hippocampal neuron cultures were transfected with 500 ng of plasmid DNA per well with a commercial calcium phosphate transfection kit (Life Technologies Corp.) after 4 days *in vitro* (DIV), as previously described. After 30–60 min of DNA-calcium phosphate precipitate incubation with cultured neurons at 37°C, neurons were washed twice with acidic MEM buffer (pH 6.7–6.8) to remove residual calcium phosphate particles and returned to the original plating media. All measurements on cultured neurons were taken between days in vitro (DIV) 14 and DIV 18 (~9–14 d post transfection) to allow for sodium channel maturation (and thus spiking). No all-trans-retinal was supplemented for any cultured neuron recordings.

3.14.3 Electrophysiology and fluorescence microscopy in cultured primary hippocampal neurons

Whole-cell patch clamp recordings of cultured neurons for **Table 6.13** were acquired via an Axopatch 700B amplifier (Molecular Devices LLC) and Digidata 1440 digitizer (Molecular Devices LLC). Neurons were patched between DIV14 and DIV18 and were bathed in Tyrode's solution (125mM NaCl, 2mM KCl, 3mM CaCl2, 1mM MgCl2, 10mM HEPES, 30mM glucose, pH 7.3 (NaOH adjusted)) at 32 °C during measurements. Synaptic blockers (NBQX, 10µM; d(–)-2-amino-5-phosphonovaleric acid, 25 µM; gabazine, 20µM;

Tocris) were added to the extracellular solution for single-cell electrophysiology. Borosilicate glass pipettes with an outer diameter of 1mm and a wall thickness of 0.2mm were pulled to produce electrodes with resistance of 3–10 MΩ and were filled with an internal solution containing 135mM potassium gluconate, 8mM NaCl, 10mM HEPES, 4mM Mg-ATP, 0.4mM Na-GTP, 0.6mM MgCl2, 0.1mM CaCl2, pH 7.25 (KOH adjusted) at 295mOsm. Measurements from primary neuron cultures were performed on the electrophysiology setup described above. Patch-clamp data was acquired only if the resting potential was below -45mV and access resistance was <25 MΩ. Access resistance was compensated at 30–70%. Fluorescence imaging was performed on an inverted fluorescence microscope (Nikon Ti), equipped with a red laser (637 nm, 100 mW, Coherent, OBIS 637LX, Pigtailed) expanded by a beam expander (Thorlabs Inc) and focused onto the back focal plane of a 40×NA 1.15 objective lens (Nikon Corp.).

Two-photon imaging of SomArchon expressing neurons was performed using an Olympus FVMPE-RS equipped with two lasers for fluorescence excitation. An InSight X3 laser (Spectra-Physics) tuned to 1150 nm at 50% transmissivity was used to excite SomArchon, and a MaiTai HP Ti:Sapphire laser (Spectra-Physics) tuned to 920 nm at 15% transmissivity was used to excite EGFP. The laser beams were focused by a 25× 1.05 NA water-immersion objective lens (Olympus). SomArchon emission was separated using a 590 nm dichroic mirror and imaged with 660–750 nm and 495–540 nm filters for near-infrared and green fluorescence, respectively, and signals were collected onto separate photomultiplier tubes. Imaging was performed at 2.0 μs/pixel sampling speed with one-

way galvano scanning.

3.14.4 Phototoxicity and photobleaching measurements in cultured neurons

For phototoxicity and photostability measurements, primary mouse neuron cultures, prepared as described above, were imaged using an inverted Eclipse Ti-E microscope (Nikon) equipped with a sCMOS camera (OrcaFlash4.2, Hamamatsu), LED light source (Spectra, Lumencor), a 637 nm Laser (637 LX, OBIS) focused on the back focal plane of a 40× NA 1.15 water immersion objective lens (Nikon), and a Polygon400 Multi-wavelength Patterned Illuminator (Mightex) with a 470 nm LED (ThorLabs). To express SomArchon, neurons were infected with AAV2-CaMKII-SomArchon or AAV2-Syn-SomArchon-P2A-CoChR-$K_V2.1_{motif}$ at DIV 5. To express ASAP3-Kv and Voltron-ST, neurons were transfected with the pCAG-ASAP3-Kv-WPRE and pCAG-Voltron-ST-WPRE plasmids, respectively, using the calcium phosphate method described above. For imaging of Voltron-expressing neurons, the cells were incubated with JF525 at final concentration 1.25 μM for 60 min at 37ºC (application of higher concentration of JF525 resulted in significant internalization of the dye with 40 min of incubation at 37ºC thus completely preventing functional imaging due to high background fluorescence). After incubation, the cells were washed 3 times with fresh plating media for 3 h to removed unbound dye. The ROS measurements were performed using CellROX Orange dye (Invitrogen) according to the manufacturer's protocol. Briefly, neurons were incubated with the CellROX Orange reagent at a final concentration of 5 μM for 30 minutes at 37°C in darkness, and then washed once with fresh plating media prior to imaging. Right before

imaging, cells were supplemented with the NucGreen Dead 488 reagent for detection of plasma membrane integrity, which we used to indicate cell death. Cells that showed >10 times increase in green fluorescence in the nucleus over background fluorescence levels were considered dead. Neurons were imaged between DIV 14 and DIV 18 in the plating media at 22^{o}C. CellROX Orange fluorescence was acquired using 510/25 nm excitation at 0.8 mW/mm^2 and 545/40 nm emission. NucGreen fluorescence was acquired using 475/36 nm excitation at 3.5 mW/mm^2 and 527/50 nm emission.

3.14.5 In utero electroporation, AAV injection, and acute brain slice preparation

For IUE, embryonic day (E) 15.5 timed-pregnant female Swiss Webster (Taconic Biosciences Inc., Albany, NY) mice were deeply anesthetized with 2% isoflurane. Uterine horns were exposed and periodically rinsed with warm sterile PBS. Plasmid DNA (1–2 μg total at a final concentration of ~2–3 μg/μL diluted in sterile PBS) was injected into the lateral ventricle of one cerebral hemisphere of an embryo. Five voltage pulses (50V, 50ms duration, 1Hz) were delivered using 5mm round plate electrodes (ECM™ 830 electroporator, Harvard Apparatus), placing the anode or cathode on the top of the skull to target the cortex or hippocampus, respectively. Electroporated embryos were placed back into the dam, and allowed to mature to delivery. Brain slices were prepared from electroporated mice without regard to sex at P12-P22.

The electroporated mice were anaesthetized by isoflurane inhalation, decapitated, and cerebral hemispheres were quickly removed and placed in cold choline-based cutting

solution consisting of (in mM): 110 choline chloride, 25 NaHCO3, 2.5 KCl, 7 MgCl2, 0.5 CaCl2, 1.25 NaH2PO4, 25 glucose, 11.6 ascorbic acid, and 3.1 pyruvic acid (339-341 mOsm/kg; pH 7.75 adjusted with NaOH) for 2 min, then blocked and transferred into a slicing chamber containing ice-cold choline-based cutting solution. For mice electroporated with Voltron-ST, 50 µL of JF525 dye (Janelia Farm; 12.5 nM of JF525 in 10µL of DMSO mixed with 10 µL Pluronic F-127 (20% w/v in DMSO; Invitrogen) and 30 µL of sterile PBS) was injected into the retro-orbital sinus one day before slicing. Coronal slices (300 µm thick) were cut with a Compresstome VF-300 slicing machine, then transferred to a holding chamber with artificial cerebrospinal fluid (ACSF) containing (in mM) 125 NaCl, 2.5 KCl, 25 NaHCO3, 2 CaCl2, 1 MgCl2, 1.25 NaH2PO4 and 11 glucose (300-310 mOsm/kg; pH 7.35 adjusted with NaOH), and recovered for 10 min at 34 °C, followed by another 30 min at room temperature. Slices were subsequently maintained at room temperature (22^{o}C) until use. Both cutting solution and ACSF were constantly bubbled with 95% O2 and 5% CO2.

For AAV injection, 21-day-old C57BL/6J mice were anesthetized with isoflurane and placed in a small animal stereotaxic apparatus (David Kopf Instruments, CA, USA). Animals were injected with a volume of 200 nl rAAV8-Syn-Archon1-KGC-EGFP-Kv2.1motif-ER2 using a Nanoject (Drummond Scientific Co Inc, Broomall, PA) via glass pipettes with 20–30 µm diameter tips in the striatum: anteroposterior (AP) 1.2, mediolateral (ML) 2.1, dorsoventral (DV) 3.2. Brain slices were then prepared from these AAV-injected mice at postnatal day 30–35. Mice were deeply anesthetized with isoflurane and perfused

transcardially using cold saline containing (in mM): 194 sucrose, 30 NaCl, 4.5 KCl, 1.2 NaH_2PO_4, 0.2 $CaCl_2$, 2 $MgCl_2$, 26 $NaHCO_3$, and 10 D-(+)-glucose saturated with 95% O_2 and 5% CO_2, pH=7.4 adjusted with NaOH, 320–340 mOsm/L. Coronal slices (250–300 μm thick) were cut using a slicer (VT1200 S, Leica Microsystems, USA) and then incubated for 10-15 min in a holding chamber (BSK4, Scientific System Design Inc., USA) at 32°C with regular ACSF containing (in mM): 136 NaCl, 3.5 KCl, 1 $MgCl_2$, 2.5 $CaCl_2$, 26 $NaHCO_3$ and 11 glucose saturated with 95% O_2 and 5% CO_2, followed by at least one hour recovery at room temperature (21–25°C) before recording.

3.14.6 Concurrent electrophysiology and fluorescence imaging in acute brain slice

For recording in **Figure 3.2** and **Figure 3.4a–c**, individual slices were transferred to a recording chamber mounted on an upright microscope (Olympus BX51WI, see below) and continuously superfused (2–3 mL/min) with carbogenated ACSF at room temperature. Whole cell patch-clamp recordings were performed with borosilicate glass pipettes (KG33, King Precision Glass Inc.) heat polished to obtain direct current resistances of ~4–6 MΩ. For cortex recordings, pipettes were filled with an internal solution containing in mM: 120 K-Gluconate, 2 MgCl2, 10 HEPES, 0.5 EGTA, 0.2 Na2ATP, and 0.2 Na3GTP. For hippocampus and striatum recordings, pipettes were filled with an internal solution containing in mM: 131 K-Gluconate, 17.5 KCl, 9 NaCl, 1 MgCl2, 10 HEPES, 1.1 EGTA, 2 Na2ATP, and 0.2 Na3GTP. Voltage clamp recordings were made with a microelectrode amplifier (Multiclamp 700B, Molecular Devices LLC). Cell membrane potential was held at -60 mV, unless specified otherwise. Signals were low-pass filtered at 2 kHz and sampled

at 10–20 kHz with a Digidata 1440A (Molecular Devices LLC), and data were stored on a computer for subsequent off-line analysis. Cells in which the series resistance (Rs, typically 8–12 MΩ) changed by >20% were excluded from subsequent data analysis. In addition, cells with Rs more than 25 MΩ at any time during the recordings were discarded. In some cases, conventional characterization of neurons was made in both voltage and current clamp configurations. Positive neurons were identified for recordings on the basis of EGFP expression visualized with a microscope equipped with a standard GFP filter (BX-51WI, Olympus Corp.). Optical voltage recordings were taken through a 40x water immersion objective (Olympus LUMFL N 40x/0.8W). Fluorescence was excited using a fiber-coupled 637 nm red laser (140mW, Coherent Obis 637-140 LX), and the emission was filtered through a 664 long pass filter. Images were collected on an EMCCD camera (Andor iXON Ultra 888) or sCMOS camera (Andor Zyla4.2 Plus Andor) in a reduced pixel window to enable acquisition at ~1kHz. Each trial was about 30 seconds in duration. Of the 18 cortical neurons reported in **Figure 3.2**, four neurons were not analyzed for **Figure 3.2e** because the electrophysiology files were inadvertently not saved, owing to manual save process clunkiness.

For optical recordings in **Figure 3.2i,j**, **Figure 3.1a–g, Figure 3.3,** and **Figure 3.6**, acute brain slices were transferred to a recording chamber mounted on an inverted Eclipse Ti-E (Nikon) equipped with a CMOS camera (Zyla5.5, Andor), LEDs (Spectra, Lumencor), a 637nm Laser (637 LX, OBIS) focused on the back focal plane of a 40×NA 1.15 objective (Nikon), and a Polygon400 Multiwavelength Patterned Illuminator (Mightex) with 470 nm

LED (ThorLabs), and continuously superfused (2–3 mL/min) with carbogenated ACSF at room temperature. Positive cells were imaged under 0.8 or 1.5 W/mm^2 (55 mW) excitation light power at 637 nm from the laser. 4-aminopyridine at a final concentration of 1 mM was added to induce neuronal activity for experiments in **Figure 3.3c,d,g,h,** and **Figure 3.6**. For **Figure 3.2i,j** and **Figure 3.6**, cells were illuminated with 2 ms blue light pulses at light power in the range from 0.1 to 1.0 mW/mm^2.

3.14.7 Mouse surgery

All *in vivo* mouse procedures were performed in accordance with the National Institute of Health Guide for Laboratory Animals and approved by the Boston University Institutional Animal Care and Use and Biosafety Committees.

3.14.7.1 Viral injections

All AAV was produced by the University of North Carolina Chapel Hill Vector Core. Adult female C57BL/6 mice (Charles River Laboratories, Inc.) or Chat-Cre mice (Chat-cre;129S6-Chattm2(cre)Lowl/J, the Jackson Laboratory), 8-12 weeks at the time of surgery, were used for all experiments. AAV-Syn-SomArchon (5.9e12 genome copies (GC)/ml) or AAV-syn-SomArchon-P2A-CoChR-Kv2.1 (2.19e13 GC/ml) was injected into the motor cortex (AP: +1.5, ML: +/-1.5, DV: -0.3, 0.5uL virus), visual cortex (AP: -3.6, ML: +/-2.5, DV: -0.3, 0.5uL virus), hippocampus (AP:-2.0, ML:+1.4, DV:-1.6, 1uL virus) or striatum (AP:+0.8, ML:-1.8, DV:-2.1, 1uL virus). Viral injections occurred at 50-

100nL/min (ten minutes total) using a 10uL syringe (NANOFIL, World Precision Instruments LLC) fitted with a 33-gauge needle (World Precision Instruments LLC, NF33BL) and controlled by a microinfusion pump (World Precision Instruments LLC, UltraMicroPump3–4). The syringe was left in place for an additional 10 minutes following injection to facilitate viral spread. About one week following the viral injection, mice underwent a second surgery to implant the cranial window for *in vivo* imaging.

3.14.7.2 Cortical image window implantation

The imaging window consisted of a stainless-steel cannula (OD: 3.17mm, ID: 2.36mm, 1mm height, AmazonSupply, B004TUE45E) fitted with a circular coverslip (#0, OD: 3mm, Deckgläser Cover Glasses, Warner Instruments LLC, 64-0726 (CS-3R-0)) adhered using a UV curable glue (Norland Products Inc., Norland Optical Adhesive 60, P/N 6001). A craniotomy of ~3mm in diameter was created, with the dura left intact, over the motor cortex (centered at AP: +1.5, ML: +/-1.75) or visual cortex (AP: -3.6, ML: +/- 2.15). The imaging window was positioned over the cortex so that it was flush with the dura surface. Kwik sil adhesive (World Precision Instruments LLC, KWIK-SIL) was applied around the edges of the imaging window to hold the imaging window in place and to prevent any dental cement from touching the brain. Three small screws (J.I. Morris Co., F000CE094) were screwed into the skull to further anchor the imaging window to the skull. Dental cement was then gently applied to affix the imaging window to the exposed skull, and to mount an aluminum headbar posterior to the imaging window. See **Figure 3.15a,b** for window placement.

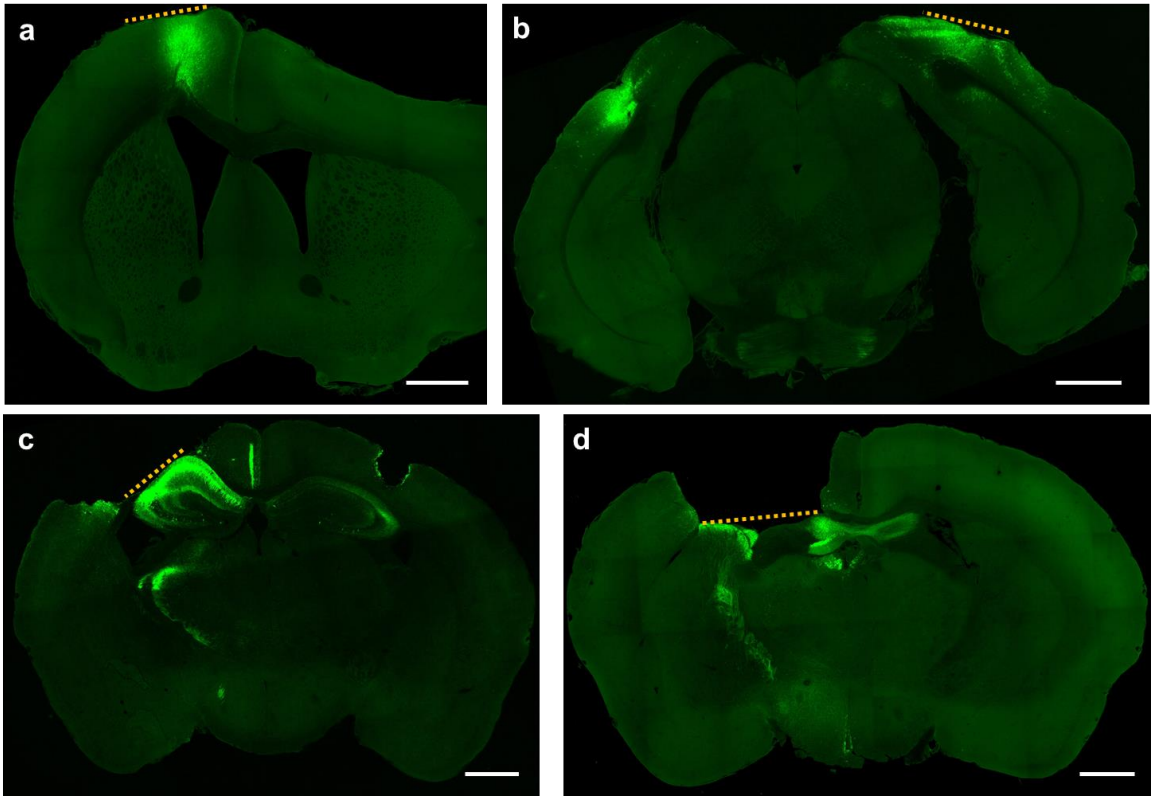

Figure 3.15. Fluorescence images of mouse brain sections prepared after *in vivo* imaging. Fluorescence images of brain slices expressing SomArchon in (**a**) motor cortex (a representative slice selected from n = 12 slices from 2 mice), (**b**) visual cortex (a representative slice selected from n = 12 slices from 2 mice), (**c**) hippocampus (a representative slice selected from n = 24 slices from 4 mice), and (**d**) striatum (a representative slice selected from n =12 slices from 2 mice). Dotted line indicates the position of optical imaging window used for *in vivo* imaging. Scale bars, 1 mm.

3.14.7.3 Subcortical image window implantation

Hippocampal and striatal window surgeries were performed similar to those described previously[59,254]. For each imaging window, a virus/drug infusion cannula (26G, PlasticsOne Inc., C135GS-4/SPC) was attached to a stainless-steel imaging cannula (OD: 3.17mm, ID: 2.36mm, 1 or 2mm height, AmazonSupply, B004TUE45E). The bottom of the infusion cannula was flush with the base of the stainless-steel cannula, and a circular coverslip (#0, OD: 3mm, Deckgläser Cover Glasses, Warner Instruments Inc., 64-0726

(CS-3R-0)) was adhered using a UV curable glue (Norland Products Inc., Norland Optical Adhesive 60, P/N 6001). An additional insulated stainless-steel wire (Diameter: 130µm, PlasticsOne Inc., 005SW-30S, 7N003736501F) was glued to the viral/drug infusion cannula with super glue (Henkel Corp., Loctite 414 and Loctite 713) and protruded from the bottom of the infusion cannula and imaging window by about 200µm for LFP recordings.

A craniotomy ~3mm in diameter was made over the hippocampus CA1 region (AP: -2.0, ML: +2.0) or the striatum (AP: +0.8, ML: -1.8). A small notch was made on the posterior edge of the craniotomy to accommodate the infusion cannula and LFP recording electrode. The overlying cortex was gently aspirated using the corpus callosum as a landmark. The corpus callosum was then carefully thinned in order to expose the hippocampus CA1 region or the dorsal striatum. The imaging window was positioned in the craniotomy, and Kwik sil adhesive (World Precision Instruments LLC, KWIK-SIL) was applied around the edges of the imaging window to hold it in place and to prevent any dental cement from touching the brain. Three small screws (J.I. Morris Co., F000CE094) were screwed into the skull to further anchor the imaging window to the skull, and a small ground pin was inserted into the posterior part of the brain near the lambda suture as a ground reference for LFP recordings. Dental cement was then gently applied to affix the imaging window to the exposed skull, and to mount an aluminum headbar posterior to the imaging window. See **Figure 3.15c,d** for window placement.

In mice that did not receive a virus injection prior to window implantation, 1uL of AAV-syn-SomArchon (5.9e12 GC/ml) or 1uL of AAV-syn-SomArchon-P2A-CoChR-Kv2.1 (2.19e13 GC/ml), or 1µL of AAV-CAG-FLEX-SomArchon (6.3e12 GC/ml) was injected through the virus/drug infusion cannula at 100nL/min through an internal infusion cannula (33G, PlasticsOne Inc., C315IS-4/SPC) connected to a microinfusion pump (World Precision Instruments LLC, UltraMicroPump3-4), one week after the window implantation surgery. The internal infusion cannula was left in place for 10 minutes following injection to facilitate viral spread. Mice were awake and head-fixed throughout the injection period.

All mice were treated with buprenex for 48 hours following surgery and single-housed to prevent any damage to the headbar or window implant.

3.14.8 In vivo imaging in the live mouse brain

All optical recordings were acquired on a conventional one-photon fluorescence microscope equipped with an ORCA Flash 4.0 V3 Digital CMOS camera (Hamamatsu Photonics K.K., C13440-20CU) or Hamamatsu ORCA Fusion Digital CMOS camera (Hamamatsu Photonics K.K., C14440-20UP), 10x NA0.25 LMPlanFI air objective (Olympus Corp.), 40x NA0.8 LUMPlanFI/IR water immersion objective (Olympus Corp.), 20x NA1.0 XLUMPlanFL N water immersion objective (Olympus Corp.), 16x NA0.8 CFI LWD Plan Fluorite water immersion objective (Nikon), 470 nm LED (ThorLabs Inc., M470L3), 140 mW 637 nm red laser (Coherent Obis 637-140X), a green filter set with a 470/25 nm bandpass excitation filter, a 495 nm dichroic, and a 525/50 nm bandpass

emission filter, and a near infrared filter set with a 635 nm laser dichroic filter and a 664 nm long pass emission filter. The near-infrared laser illuminated a circular area of ~60–80 µm, ~80–140 µm, and ~100–200 µm in diameter in brain tissue, with FOV height (limited by camera acquisition rate) 40–60 µm, 80–100 µm, and 100–120 µm under 40x, 20x, and 16x objective lenses, respectively, and a mechanical shutter (Newport Corporation, model 76995) was positioned in the laser path to control the timing of illumination over the imaging window. Optical recordings were acquired at 390-900 Hz with HCImage Live (Hamamatsu Photonics K.K.) or NIS Elements (Nikon) software. HC Image Live data were stored as DCAM image files (DCIMG), and further analyzed offline in Fiji/ImageJ and MATLAB (MathWorks Inc.). NIS Elements data were stored as .nd2 files and further analyzed offline using the NIS Elements software.

The GFP signal of SomArchon was acquired in the green channel (λ_{ex}=470 nm) at 1024x1024 pixels with 2x2 binning to show cell structure and distribution. Optical voltage recordings were imaged in the near infrared channel (λ_{ex}=637 nm) with 2x2 or 4x4 binning. OmniPlex system (PLEXON Inc.) was used to synchronize data acquisition from different systems. In all experiments, the OmniPlex system recorded the start of image acquisition from the sCMOS camera, the acquisition time of each frame, and other experiment-dependent signals described below.

3.14.8.1 Optical imaging of spontaneous neural activity

All *in vivo* optical imaging of spontaneous neural activity was performed when mice were awake and head fixed in a custom holder that allowed for attachment of the headplate at the anterior end. Animals were covered with an elastic wrap to prevent upward movement. Spontaneous neural activity recordings lasted continuously up to 30,000 frames (~36 seconds).

3.14.8.2 Eye puff

During some *in vivo* hippocampal imaging recordings, an eye puff was applied to evoke high frequency local field potential responses in the hippocampus (**Figure 3.13a–d**). The mice were head fixed in a custom holder that allowed for attachment of the headplate at the anterior end, and they were covered with an elastic wrap to prevent upward movement. Each experimental session consisted of 20–30 trials, with each trial lasting for 5000 frames (~6 seconds). Three seconds after the start of image acquisition, the sCMOS camera sent a TTL pulse to a function generator (Agilent Technologies, model 33210A), which triggered a 100ms long air puff. The air puff was 5–10 psi, and administered via a 0.5mm cannula placed 2–3cm away from the mouse's eye. The puff TTL pulses were also recorded with the OmniPlex system (PLEXON Inc.). Eye movement was monitored using a USB webcam (Logitech, Carl Zeiss Tessar 2.0/3.7 2MP Autofocus).

3.14.8.3 Optogenetic blue light stimulation

All *in vivo* optopatch (i.e., optogenetics plus voltage imaging) experiments were performed when mice were awake and head fixed in a custom holder that allowed for attachment of the headplate at the anterior end. Animals were covered with an elastic wrap to prevent upward movement. A 470nm LED (ThorLabs Inc., M470L3) was coupled to a Polygon400 Multiwavelength Patterned Illuminator (Mightex), and the blue light was focused through the objective lens to illuminate the center of the FOV. At the onset of imaging, the sCMOS camera sent a TTL pulse to trigger Axon CNS (Molecular Devices LLC, Digidata 1440A) which controlled the 470 nm LED (ThorLabs). Each trial lasted 1.1 second and consisted of a single 100 ms long blue light pulse, 500 ms after trial onset. Each recording session consisted of 10 trials with increasing blue light power from 0.1 to 1 mW/mm^2, with a step of ~ 0.1 mW/mm^2 per trial. The OmniPlex system (PLEXON Inc.) recorded the timing of TTL pulses used to trigger the Axon CNS.

3.14.8.4 Head-fixed voluntary movement experiments

All voluntary movement experiments were performed while awake, head-fixed mice were freely navigating a spherical treadmill. The spherical treadmill was constructed following the design of Dombeck et al. 2007[255]. Briefly, a 3D spherical Styrofoam ball was supported by air, and motion was tracked using two computer mouse sensors positioned roughly +/- 45 degrees from center along the equator of the ball. All motion sensor displacement data was acquired at 100 Hz on a separate computer and synthesized using a custom Python script. Motion sensor displacement data were then sent to the image acquisition computer

to be accumulated using a modified ViRMEn MATLAB script. The timing of each motion sensor displacement data point was also recorded using the OmniPlex system (PLEXON Inc.) to synchronize movement data with optical voltage recordings.

In order to determine the mouse movement speed, ball movement was first calibrated. The ball was pinned on the two sides and rotated vertically to calibrate sensor displacement.

All mice were habituated on the spherical treadmill for at least three days, at least 20 minutes per day, prior to image acquisition. During optical imaging, mice were imaged while freely navigating the spherical treadmill. Each FOV was recorded for at least 36 seconds total. In some fields of view, we performed multiple trials, and each trial was at least 12 seconds in duration with an inter-trial interval of at least 30 seconds in duration.

3.14.9 Local field potential recording

Local field potentials were recorded using an OmniPlex system (PLEXON Inc.) at a 1 kHz sampling rate. To synchronize optical recordings with LFP recordings, the camera sent out a TTL pulse to the OmniPlex system at the onset of imaging and after each acquired frame.

3.14.10 Motion correction

In **Figure 3.7, Figure 3.10,** and **Figure 3.11**, motion correction was performed with a custom Python script. For each FOV, if multiple video imaging files were collected for the

same FOV, we started with the first imaging file to ensure speedy data processing (a single video file contains a series of images). We first generated the reference image by averaging across all images within the file. We then performed a series of image processing procedures to enhance the contrast of the reference image and every image in the file to facilitate motion correction. We first removed 10% of the pixels along all edges of an image to remove any camera induced artifact. We then applied a high-pass filter (Python scipy package, ndimage.gaussian_filter, sigma=50) to remove low frequency components within the images. To enhance the boundary of high intensity areas, we identified the boundary as the difference between two low pass filtered images (sigma=2 and 1). We then enhanced the boundary by adding 100 times the boundary back to the low pass filtered image (sigma=2). We then limited the intensity range of the processed images within one standard deviation above and below the average intensity of the image, by setting the pixels with intensity higher than mean+std as mean+std, and the pixels with intensity lower than mean-std as zeroes. Finally, to counter any potential bleaching over time, we normalized the intensity of each image by shifting the mean intensity to zero and divided intensity values by the standard deviation of all pixel intensities in that image. After image processing, we calculated the displacement of each image, by identifying the max cross-correlation coefficient between each image and the reference image, and then corrected motion by shifting the displacement in the original, unenhanced image sequence. If the same FOV was imaged over an extended period of time, where multiple files were acquired, we motion-corrected subsequent files by aligning them to the first file, so that the same ROIs from the same FOV could be applied across the entire imaging session. Specifically, we

first refined the reference frame by generating the mean intensity projection image from the motion-corrected first imaging file. The refined reference image was then used to motion-correct all files of the same FOV, including the first file, using the same procedure described above. The motion-corrected, original, unenhanced image sequences, were then used for subsequent manual ROI segmentation, and further analysis.

3.14.11 ROI identification

We imported the image files (motion-corrected as above, if necessary) into Fiji/ImageJ or NIS Elements and manually segmented ROIs by examining the time-series images to identify the area with clear neuron outlines and/or intensity dynamics over time. The optically-recorded voltage traces for each ROI were generated from the motion-corrected image sequences using the "multiple measurement" function and were then used for analyses.

The wide dynamic range (16 bit) of the raw images meant that to select dim as well as bright cells, we had to create max projection and standard deviation images of the entire raw video and stretched their LUTs (look up tables) to enhance visibility. For **Figure 3.11** and **Figure 3.13e–h**, cells were densely packed, so we identified and tracked ROIs semi-manually across image sequences without performing motion correction. We first visually inspected all image sequences and identified those with minimal motion and with an SNR greater than ~2 for further analysis. We then performed an iterative ROI-selection procedure to identify ROIs that best fit each cell. Specifically, we started by manually

selecting ROIs from the max projection image of the entire image sequence. The image sequence was then visually inspected to identify frames whose cells exhibited shifts of more than three pixels from the defined ROI. We then used these frames to separate the image sequence into multiple time intervals, and obtained a new set of max projection images to identify new ROIs within these time intervals for these cells. This procedure was repeated iteratively until the ROI represented the cell across all image frames in their corresponding time intervals without the cell moving out of the ROI. Thus, with this procedure, we created multiple ROIs representing the same cell across different frames. For each cell, we extracted traces for every ROI during its corresponding time interval, and stitched the baseline-normalized traces for the same cell(s) in time. The fluorescence traces of each cell were then detrended for further analysis. See **Figure 3.16** for an example of raw and processed traces for two cells in the same FOV.

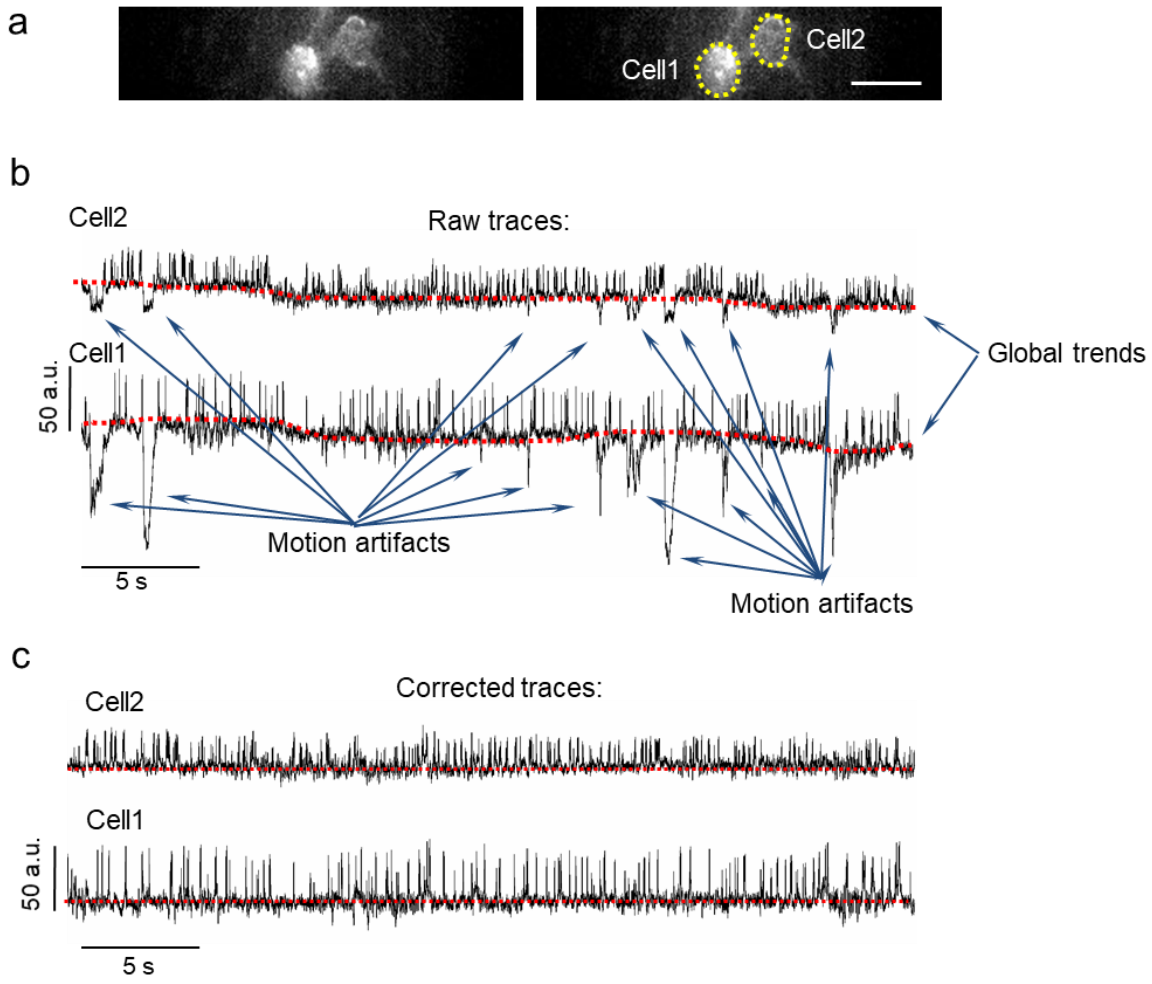

Figure 3.16. Processing of raw optical voltage traces to remove motion artifacts and global trends. Raw voltage traces were processed to remove motion artifacts and global trends. Motion resulted in sharp coordinated changes in fluorescence intensity across all static regions of interest for a given field of view. In addition, global trends in baseline fluorescence were observed due to slow photobleaching or slight drift in focus. (**b**) Here, we present raw voltage traces for two cells imaged in the same field of view (as seen in **a**). Both traces demonstrate collateral shifts in fluorescence for both traces as well as common global trend in the baseline shift. (**c**) The motion artifacts in **b** were removed to yield corrected traces.

3.14.12 Hippocampal spike detection

Spikes were associated with a rapid increase in intensity, followed by a rapid decrease. In contrast, occasional motion artifacts were usually associated with a decrease in intensity as a neuron moved out of the ROI. To facilitate spike detection, we first removed motion

artifacts. For each time point of the fluorescence intensity trace for each ROI, we calculated the change in intensity from that of the prior time point (I_{change}). We then defined noise as the time points where instantaneous I_{change} were three standard deviations below the mean value of I_{change} across the entire trace. We excluded any time points where the I_{change} of the previous time point was more than one standard deviation above the average I_{change}, because this might have indicated a spike. These noise time points and their following three time points (since we found that motion artifacts are typically >4ms) were then considered motion artifacts, and removed from further analysis. We then recalculated the standard deviation of the I_{change}, excluding the data points of motion artifact. The peaks of spikes were then identified as time points with the following two criteria: 1) the intensity change of the time point combined with that of its preceding time point was more than three standard deviations above the average I_{change}, and 2) the intensity change over the next two time points was less than two standard deviations below the average I_{change}.

3.14.13 Hippocampal spike phase calculation

Hippocampal spike-phase analysis was performed on 16 neurons from 7 FOVs from 4 mice. For each FOV, we analyzed data collected over 10 trials (~60 seconds total), where animals experienced an eye puff in each trial as described above in **Section 3.14.8.2**. To calculate the phase of spikes at theta frequency (4–10 Hz), we first band-pass filtered both the optical voltage trace and the simultaneously recorded LFP at theta frequency (eegfilt, EEGLAB toolbox). The peaks of theta oscillation power were then identified with the findspike function in MATLAB. For each spike, we obtained the phase of the spike by

calculating the timing of each spike relative to the period of that oscillation cycle in degrees. We averaged the phases of all spikes from the same neuron as the average phase of a given neuron.

3.14.14 Analysis for pair-wise coherence between hippocampal neurons and LFPs

The coherence analysis was performed on 9 FOVs that contained multiple neurons from 4 mice. Each FOV contained imaging data over a period of 6–36 seconds. For each FOV, we first re-sampled the LFP at the acquisition rate of the optical imaging. We then divided the optical voltage traces and LFPs into segments of 1000 data points. We then calculated the averaged coherence, at theta frequency (4–10 Hz), with the functions in the Chronux toolbox (optical voltage trace to optical voltage trace or LFP: coherencyc, and spike to spike: coherencypt) with tapers=[10 19], fpass=[4 10] and trialave=1. To compare V_{mo}-V_{mo} coherence vs. V_{mo}-LFP coherence across nine FOVs, we averaged the coherence of neurons in the same FOV to obtain the mean coherence of that FOV, and then performed statistical tests across FOVs using the individual FOV's mean coherences. To understand the relationships between pairs of coherence, we used the MATLAB function, fitlm, to perform a linear regression between coherent pairs and obtain the p-value and r^2 value.

To estimate background fluorescence crosstalk, we calculated pair-wise coherence and correlation between background donut areas surrounding a neuron. To select background donut areas, we excluded the edges (5%) of each FOV, since the edge may be missing for a particular image frame when image frames were shifted during motion correction. The

background donut of a neuron was determined as the area 3–10um from the neuron boundary, excluding any pixels within 10 um of the boundary of another neuron. One neuron was excluded from this analysis due to dense labelling where we could not identify its donut area. Fluorescence traces of the background donut area were then processed as that for neurons, and their pair-wise coherence and Pearson correlations were calculated.

3.14.15 Striatum, motor cortex, and visual cortex spike detection

After motion correction, we first identified large fluorescence increases using a threshold of 4 standard deviations above the baseline. The baseline was manually selected as a period of >500ms without spiking or drifting due to z-plane shifting or photobleaching. From these large fluorescence increases, we selected those with shorter than 4 ms rise times and 4 ms decay times as spikes.

3.14.16 Firing rate comparison of striatal neurons during high versus low speed movement

Animals' movement data was first interpolated to the voltage imaging frame rate with MATLAB function interp1, and then smoothed using a 1.5Hz low pass Butterworth filter to remove any motion sensor artifact. We calculated the average movement speed at 0.5-second intervals and defined low speed periods as intervals where the average speed was ≤5cm/s and high speed periods as intervals where the average speed was ≥10cm/s. The firing rates during these high and low motion periods were compared, and a two-sided Wilcoxon rank sum test was used to determine significance between these periods.

3.14.17 Signal to noise ratio (SNR) calculation for in vivo photostability evaluation over imaging duration in striatum and hippocampus

We defined noise as the standard deviation of the fluorescence intensity across the entire trial period. For each neuron, we first calculated the SNR for each action potential by dividing the intensity change observed during an action potential by the noise, and then calculated the average SNRs across all spikes detected in a trial as the corresponding SNR for the trial. For the striatum dataset, only neurons imaged over at least 5 consecutive trials were analyzed. For the hippocampus dataset, all neurons were analyzed.

3.14.18 Detrending

All optically-recorded SomArchon traces reported in the manuscript (except those in **Figure 3.11a,b**) were corrected for photobleaching or focus shift by subtracting baseline fluorescence traces that were low-pass filtered and fit to a double or single exponential function.

3.14.19 Histology

Mice were transcardially perfused with PBS followed by 4% paraformaldehyde. The brain was gently extracted from the skull and post-fixed in 4% paraformaldehyde for 1–4 hours at room temperature or overnight at +4^{o}C. Fixed brains were transferred to a 30% sucrose-PBS solution and rotated 24–48 hours at 4C for cryoprotection. Cryoprotected brains were frozen in OCT in a dry ice bath and sliced (coronal) to 50μm thickness using a cryostat.

Glial and microglial antibody staining were performed with anti-GFAP[254] (1:250, Clone N206/A8, Neuromab) and anti-Iba1[256] (1:500, 019-19741, Wako Chemicals) primary antibodies, followed by Alexa Fluor 568 (1:1000, Goat anti-Mouse IgG (H+L) Cross-Adsorbed Secondary Antibody, A11004, InVitrogen) and 633 secondary antibodies (1:1000, Goat anti-Rabbit IgG (H+L) Cross-Adsorbed Secondary Antibody, A21070, InVitrogen). All antibodies were used according to the protocols that have been validated by suppliers. Slice imaging was performed using an inverted Nikon Eclipse Ti microscope equipped with a spinning disk sCSUW1 confocal scanner unit (Yokogawa, Tokyo, Japan), 488, 561, and 642 nm solid state lasers, 525/25 nm, 579/34 nm, and 664LP emission filters, a 20× NA0.75 air objective lens (Nikon), and a 4.2 PLUS Zyla camera (Andor), controlled by NIS-Elements AR software. Acquired images were contrast-enhanced to improve visualization.

3.14.20 Brain temperature measurements

Under general anesthesia, a craniotomy ~3mm in diameter was made to expose the brain surface, with a small notch on the posterior edge to accommodate the insertion of a temperature probe (Physitemp, IT-1E) coupled to a Thermocouple DAQ (DATAQ Instruments, Model DI-245). An imaging window, identical to those used in all imaging experiments, was positioned on the craniotomy. Kwik sil adhesive was applied around the edges of the imaging window to hold it in place, but not around the craniotomy notch to allow insertion of the temperature probe. Dental cement was then gently applied to affix the imaging window to the skull and to mount an aluminum headbar. Once recovered from

anesthesia, mice were head fixed awake and the temperature probe was inserted under the imaging window above the brain surface, through the craniotomy notch. The 637 nm laser was directed through the 40x objective under identical conditions to those used while imaging (75–95mW laser power), and brain temperature was recorded. We noted a temperature increase of 1.88±0.80°C (mean±standard deviation, n = 3 mice) over the 12 second illumination period commonly used in our experiments. These changes are similar to, or smaller than, changes commonly seen with two-photon imaging, optogenetics, and the making of craniotomies for neural imaging[257-261].

3.14.21 Sample size

No statistical methods were used to estimate sample size for animal studies throughout this study. We did not perform a power analysis, since our goal was to create a new technology; in the reference Dell et. al. 2002[262], as recommended by the NIH, "In experiments based on the success or failure of a desired goal, the number of animals required is difficult to estimate...". As noted in the aforementioned paper, "The number of animals required is usually estimated by experience instead of by any formal statistical calculation, although the procedures will be terminated [when the goal is achieved]." These numbers reflect our past experience in developing neurotechnologies.

3.14.22 Data exclusions

Voltage imaging datasets with significant motion or where no spikes were detected were excluded from analysis. Significant motion was defined as a shift of more than 20 μm in any direction. In **Figure 3.1i,j,k** data points that corresponded to overlapping neurites were excluded. Data exclusion criteria were not pre-established.

3.14.23 Replication

All attempts at replication were successful.

3.14.24 Randomization and blinding

There were no treatment conditions to compare in this study. All recording sessions were randomly performed with different voltage sensors or in different brain regions. On recording days, cultured cells or brain slices expressing specific sensors were known. On *in vivo* recording days, mouse conditions were known. Voltage trace extraction and subsequent analysis were performed with the investigators unaware of specific mouse conditions. For analysis of movement modulation of striatal neuron spiking, a computer algorithm was used to identify periods with different movement parameters. For analysis of spike-phase relationships, or subthreshold membrane voltage relationships, a computer algorithm was used across all conditions. For histology, sections were selected and images were taken from slides by a researcher not aware of the conditions or antibody used. Cells

were also counted and quantified from these sections by a researcher blinded to the experimental conditions or antibody used.

3.14.25 Code availability

Computer codes used to generate results for this study are available at https://github.com/HanLabBU/somarchon-imaging.

3.14.26 Data availability

The data that support the findings of this study are available from the corresponding author upon reasonable request; raw data essential to the work is available online at nature.com[202]. Sequences of the reported proteins are available at Genbank at the following accession codes: SomArchon, MN091368; SomArchon-P2A-CoChR-$K_V2.1_{motif}$, MN091369.

4 MEMBRANE VOLTAGE DELTA OSCILLATIONS ORGANIZE STRIATAL NEURON SPIKE TIMING AND NEURAL SYNCHRONY DURING LOCOMOTION

4.1 Summary

Oscillatory activities in local field potentials (LFPs) capture synchronized population neural dynamics. In the cortical-basal ganglia circuit, LFP oscillations at delta (~1–4Hz) and beta (~10–30Hz) frequency bands have been linked to specific aspects of movement, and pathological exaggeration of oscillations at beta frequencies in particular is considered a biomarker for Parkinson's disease. However, it remains unclear how the striatum, a major nucleated basal ganglion structure, supports network oscillations. We performed simultaneous optical membrane voltage imaging of individual neurons and conventional LFP recordings in the dorsal striatum of mice during locomotion. We report prominent delta oscillations in striatal LFPs and in the subthreshold membrane potentials (Vm) of a large fraction of neurons, particularly in striatal cholinergic interneurons. These Vm delta oscillations organize spike timing and Vm and LFP beta oscillations. Furthermore, we found that delta-rhythmic neurons were selectively modulated by movement speed and movement transitions, and that delta-rhythmic cholinergic neurons in particular were associated with LFP delta and gamma oscillations during high movement. Thus, subthreshold voltage dynamics in individual striatal neurons support delta oscillations across the cortical-basal ganglia motor circuits and play a critical role in temporal patterning during locomotion.

4.2 Introduction

Oscillatory activities in local field potentials (LFPs) capture synchronized extracellular current. In the cortical-basal ganglia-thalamic circuit, LFP oscillations at delta (~1–4Hz) and beta (~10–35Hz) frequency are broadly linked to locomotor behavior, and exaggerated beta oscillations in particular are considered a functional biomarker for Parkinson's disease[48,66,68-74,76-79,263-267]. While prominent in layered cortical structures, LFP oscillations in the striatum, the largest input nucleus of the basal ganglia, are generally weak due to the lack of apparent spatial dipole configurations in this nucleated structure[79,268,269]. Nonetheless, transient fluctuations in striatal LFP beta oscillation power have been related to different aspects of motor behavior[48,76-79] and pathological exaggeration of beta oscillations is generally thought to interfere with the execution of movement plans[66,68-74]. While beta oscillations are generally thought to arise from local neuron interactions, they are coordinated throughout cortical-basal ganglia-thalamic motor circuits by cortical and thalamic delta oscillations[263-267]. Recently, basal ganglia delta oscillations were shown to be augmented upon dopamine depletion, further highlighting the link between delta and beta oscillations[54,267,270-274]. Additionally, striatal LFP delta oscillations have been shown to organize striatal gamma (50-80Hz) and high frequency (150Hz+) oscillations in freely moving rats[263].

To understand how LFP oscillations influence neural circuit functions, *in vivo* studies have largely focused on examining the temporal relationships of spikes relative to LFP features. Spiny projection neurons (SPNs), the principal striatal neuron subtype, exhibit very low,

near zero firing rates and little rhythmicity during resting brain states, but can support high firing rates[47,48] and be driven to spike at specific phases of LFP oscillations in more excited states[53,54]. These distinct excitability states observed in SPNs are generally attributed to a variation in resting membrane potentials, with the "up" state corresponding to a more depolarized condition, and the "down" state to a more hyperpolarized condition. These "up" and "down" states have been broadly observed in brain slices and in anesthetized animals, with state transitions often coupled to slow-wave delta oscillations (~1Hz) originating from cortico-thalamic coordination[49-54,267]. For example, intracellular studies in anesthetized animals demonstrated that SPN spiking is directly phase-locked to cortical delta[53,70,275] and beta[53,70,276] oscillations. Under dopamine depleted conditions, these relationships, however, become even more complex, with some studies reporting a diminished SPN spike-phase relationships with LFP beta oscillations[277], while others report the opposite in specific GPe-projecting SPN subtypes[70,275,278]. Overall, these studies demonstrate that cortical-basal ganglia-thalamic LFP delta and beta oscillations modulate SPN spike timing, even though the exact relationship varies across studies, likely due to the intrinsic noisy nature of spike generation subject to modulation by different network states.

Interneurons, despite composing a small proportion of striatal neurons, are important regulators of local neural networks. Among various striatal interneuron subtypes, cholinergic interneurons (ChIs) have been better characterized due to their unique tonic firing rate and broad spike waveforms, which allow for relative ease of identification using

extracellular recording techniques[58,61]. While ChIs in the ventral striatum exhibit stereotypic pauses in firing in response to reward[31,58], ChIs in the dorsal striatum have been found to modulate their activities during movement[59,62-64]. In addition, ChIs have been suggested to promote coordination between SPNs, and transient elevation of striatal cholinergic tone increases LFP beta and gamma oscillations leading to movement inhibition[59,65-67]. ChI spiking has also been shown to be phase-locked to cortical delta and gamma oscillations under normal conditions[53,276], and striatal beta oscillations in Parkinsonian monkey models[277]. These studies, along with pharmacological studies directly activating acetylcholine receptors[66,67] and computational modeling[279] support a prominent role of ChIs in regulating striatal network dynamics and in contributing to striatal LFP oscillations.

Because action potentials are comparatively transient and sparse, synaptic currents are theorized to dominate LFP signals. Under this framework, synchronized synaptic inputs could thus produce subthreshold membrane potential (Vm) oscillations in individual neurons and influence spike timing[80-83]. Detailed characterization in brain slices has demonstrated that the Vm of individual striatal neurons supports a range of oscillations that organize spike timing, and some neuron subtypes tend to oscillate at specific frequency ranges, a phenomenon known as resonance[92-94]. ChIs, for example, exhibit delta frequency resonance, with ChI spiking phase-locked to delta oscillations, whereas low-threshold spiking interneurons and fast-spiking interneurons exhibit resonance at beta and gamma frequencies respectively[92-94]. On the other hand, SPNs do not have a frequency preference

or resonance, but instead tune Vm dynamics to inputs[92]. Given that action potential generation critically depends on membrane potential, Vm thus provides an important measure for understanding spike timing, and how network level LFP oscillations organize individual neuron spiking. However, until recently, analysis of intracellular Vm has been difficult in behaving mice, and it remains largely unclear how different neuron subtypes with distinct biophysical properties support oscillation dynamics that promote circuit interactions during behavior.

To understand how network oscillations organize spike timing via subthreshold Vm, we performed simultaneous voltage imaging of individual striatal neurons and striatal LFPs in mice during locomotion. Optical membrane voltage imaging was performed on ChIs and putative SPNs using the genetically-encoded voltage indicator, SomArchon[202]. We detected prominent Vm delta oscillations in both cell types, with most ChIs and a subset of SPNs exhibiting spiking activity coupled to these Vm delta rhythms. Spikes in these neurons, which we termed "delta-rhythmic" neurons were phase-locked to both Vm and LFP delta oscillations, and were also accompanied by increased Vm and LFP beta power. Furthermore, delta-rhythmic neurons fired preferentially during high-speed movement and around movement transitions. Interestingly, during high-speed movement, while delta-rhythmic ChI spiking was associated with increased LFP delta and gamma oscillations, delta-rhythmic SPN spiking was accompanied by decreased LFP beta and gamma power. Together, these results demonstrate that the Vm delta oscillations in individual striatal neurons support cortical-basal ganglion-thalamic circuit level delta oscillations, and delta

oscillations in different striatal subtypes differentially organize spike timing and higher frequency oscillations during locomotion.

4.3 Optical voltage imaging captures distinct spike timing in striatal projection neurons and cholinergic interneurons during locomotion

To measure membrane voltage from individual striatal neurons and local field potentials (LFPs) during locomotion (**Figure 4.2A**), we implanted custom imaging windows coupled with an infusion cannula and an LFP electrode over the dorsal striatum (see **Section 4.10.1.1**), and virally transduced spiny projection neurons (SPNs) and cholinergic interneurons (ChIs) with the genetically encoded voltage indicator SomArchon[202] (**Figure 4.2B**). Since a majority of striatal neurons are SPNs[280,281], we infused AAV-syn-SomArchon-GFP into the striatum to transduce neurons non-selectively (n = 7 mice). Histological quantification confirmed that 84.5 ± 7.2% (n = 34 FOVs from 17 brain slices in 4 mice) of transduced neurons were positive for DARPP-32, a protein specific to SPNs (**Figure 4.1**). SomArchon voltage imaging of ChIs was performed by either infusing Cre-dependent AAV-FLEX-SomArchon-GFP into Chat-Cre mice to selectively express SomArchon in ChIs (n = 5 mice) or using tdTomato fluorescence to identify ChIs in ChAT-tdT mice infused with AAV-syn-SomArchon-GFP (n = 3 mice).

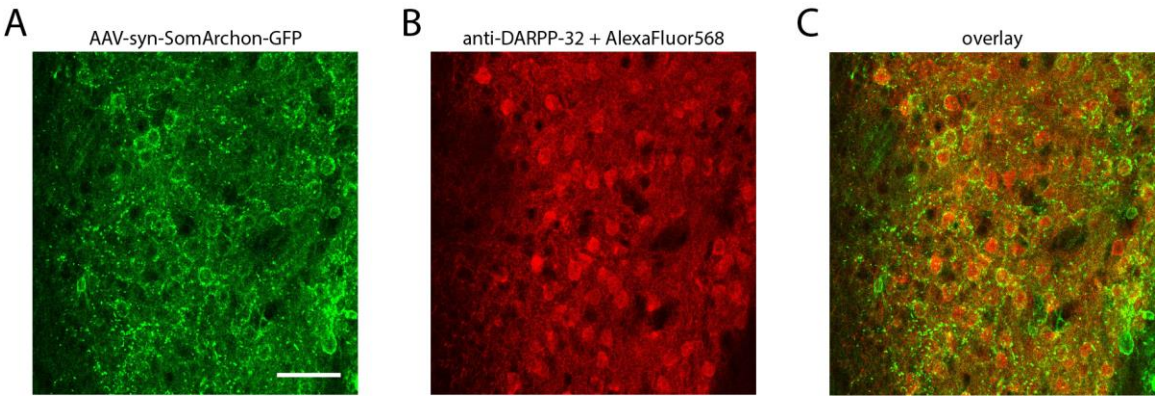

Figure 4.1. Neurons expressing syn-SomArchon can be classified as putative SPNs. (A) GFP fluorescence (λ_{ex}=488nm) from brain slice of mouse injected with AAV-syn-SomArchon. **(B)** AlexaFluor568 fluorescence (λ_{ex}=561nm) from same brain slice as **A** after staining with SPN-specific anti-DARPP-32 primary antibody and AlexaFluor568 secondary antibody. **(C)** Overlay of **A** and **B** demonstrating significant overlap between SomArchon-labeled population and antibody-labeled SPN+ population. Scale bar is 50μm.

SPN and ChI membrane voltage traces and LFPs were obtained as mice ran spontaneously on a spherical treadmill (**Figure 4.2A**). Although striatal ChIs are thought to be tonically active neurons (TANs)[56,282-284], we noticed that many ChIs instead exhibited delta-rhythmic (1–4Hz) spike bursting accompanied by large subthreshold Vm modulations (**Figure 4.2C,D, Figure 4.3A,B**). To illustrate this, we calculated the inter-spike interval (ISI) distribution and return map for an example ChI (**Figure 4.2D**). The neuron had a first ISI peak at about 5–50ms and a second peak at about 400–700ms, which is in the delta frequency range (1–4Hz). In contrast, spiking patterns in SPNs were more mixed, containing delta-rhythmic bursting cells (**Figure 4.3C–D**) as well as non-delta regular spiking neurons (**Figure 4.2E,F**). The ISI distribution and return map of a more regularly-firing SPN neuron (**Figure 4.2F**) exhibited a unimodal distribution peaking in the range of 40–70ms (near-normal distribution on a log-scale).

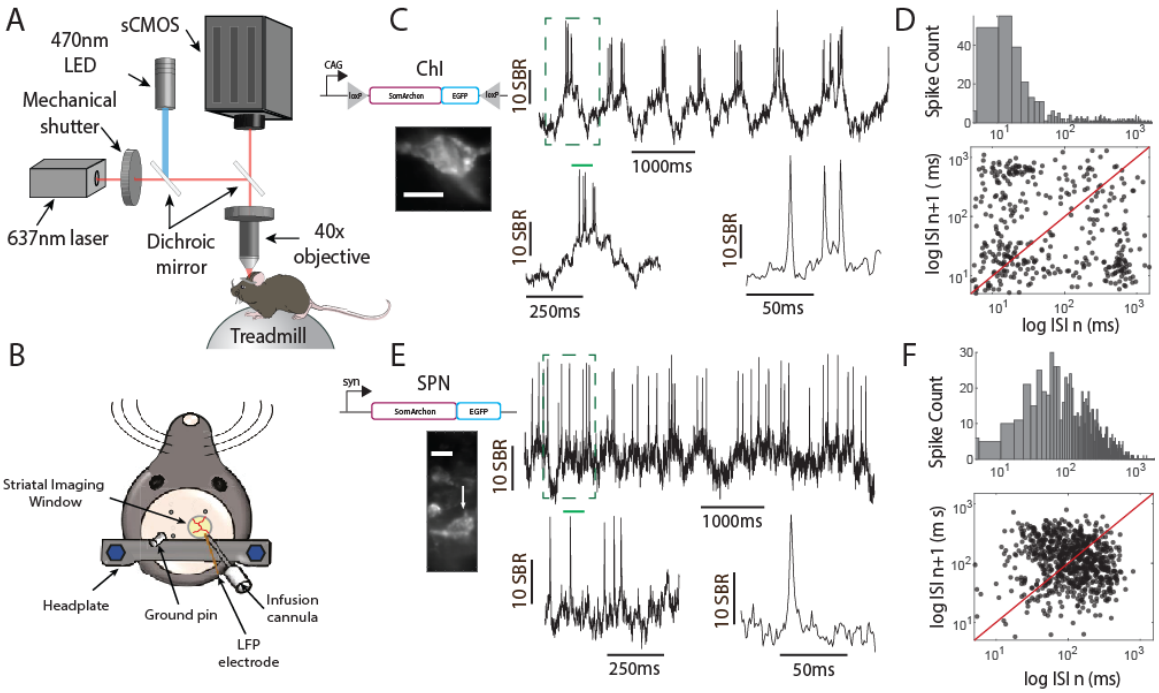

Figure 4.2. Membrane voltage imaging of ChIs and putative SPNs in behaving mice. (A) Illustration of the SomArchon voltage imaging setup in awake behaving mice. **(B)** Illustration of the animal preparation depicting the striatal window access, infusion cannula, electrode and ground pin, and headplate. **(C)** An example SomArchon fluorescence recording at 826Hz is shown from a striatal neuron using the Cre-dependent FLEX promoter in ChAT-Cre animals (ChI). *Left*, the schematic genomic sequence is shown of CAG-FLEX-SomArchon. *Below*, the SomArchon time-averaged field of view is shown. *Right*, a 6 seconds long SomArchon trace is shown of the example ChI. The dashed green box indicates the zoom-in version below. The green line in the left zoom-in version indicates the second zoom-in to the right. **(D)** *Above*, the inter-spike interval (ISI) distribution of the example ChI is shown (log scale). *Below*, the return map (ISI n vs ISI n+1) of the example ChI is shown (log scale). **(E)** Same as **C**, but for an example neuron recorded with SomArchon using the syn promotor, which are putative SPNs, with the example neuron indicated by an arrow. **(F)** Same as **D**, but for the example SPN recorded in **E**. Scale bars are 15μm.

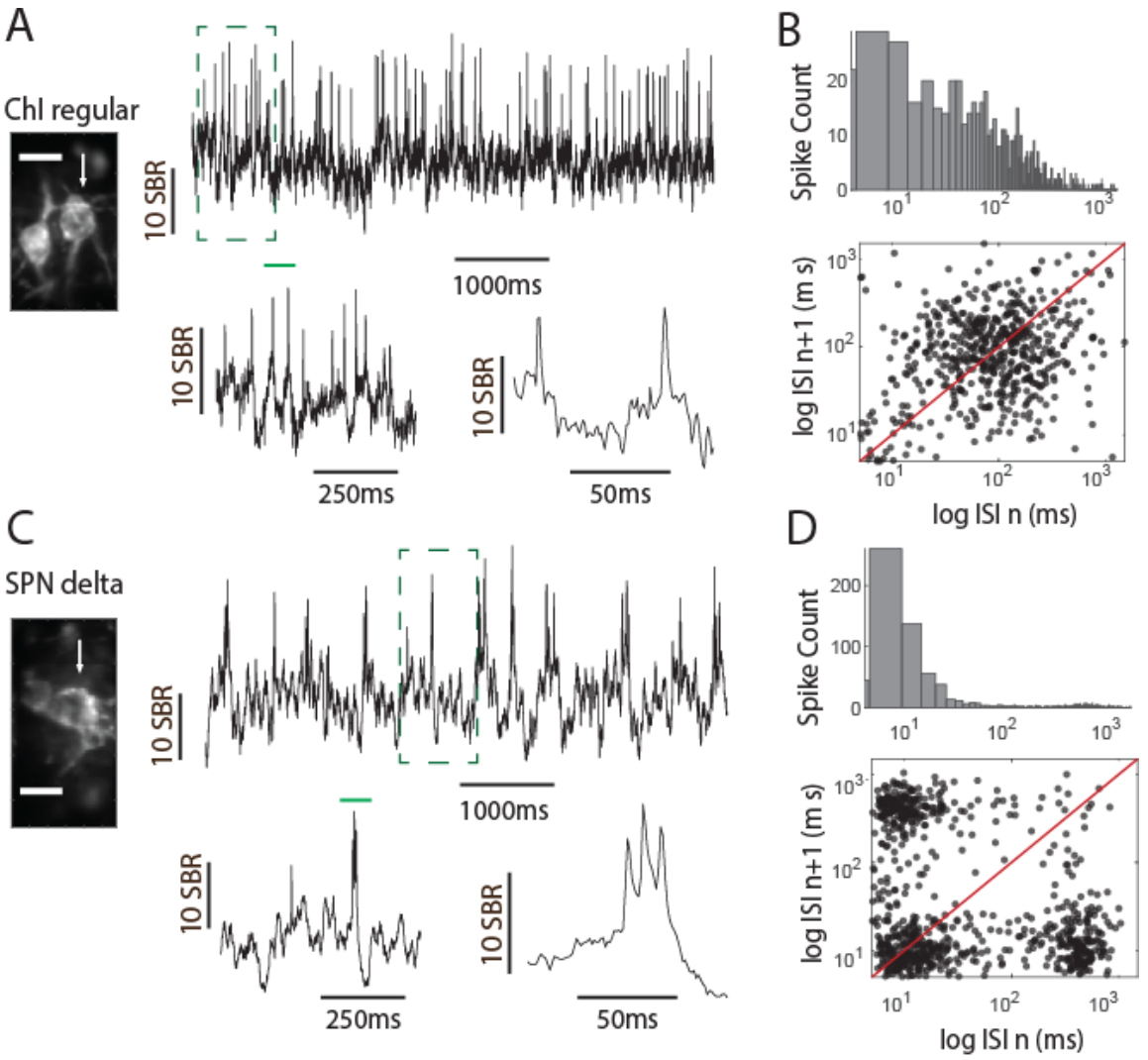

Figure 4.3. Example of regularly spiking ChI and delta rhythmic SPN. **(A)** An example SomArchon fluorescence recording at 826Hz is shown from a striatal neuron using the Cre-dependent FLEX-promotor in ChAT-Cre animals (ChI). *Left*, the SomArchon time-averaged field of view is shown with the example neuron indicated by an arrow. *Right*, a 6 seconds long SomArchon trace is shown of the example ChI. The dashed green box indicates the zoom-in version below. The green line in the left zoom-in version indicates the second zoom-in to the right. **(B)** *Above*, the inter spike interval (ISI) distribution of the example ChI is shown (log scale). *Below*, the return map (ISI n vs ISI n+1) of the example ChI is shown (log scale). **(C)** Same as **A**, but for an example neuron recorded with SomArchon using the syn promotor (putative SPN). **(D)** Same as **B**, but for the example neuron shown in **C**. Scale bars are 15μm.

4.4 Most ChIs and a subset of SPNs exhibit prominent subthreshold membrane potential delta oscillations that coordinate spike timing

To quantify the different ISI profiles from ChIs and putative SPNs as a population, we plotted each neuron's ISI as a function of two ISI ratios. The first ISI ratio captures the delta rhythmicity ($ISI_{300–700ms}$ normalized to $ISI_{80–200ms}$) and the second ISI ratio captures the burstiness ($ISI_{10–40ms}$ normalized to $ISI_{80–200ms}$). We found that manually characterized ISI delta-rhythmic neurons could be well separated by the first ISI ratio (**Figure 4.4A**). Using ISI-based thresholding, we grouped ChIs and SPNs either as being delta-rhythmic or non-delta-rhythmic ('non-delta'). Delta-rhythmic neurons were very common in the ChI population (**Figure 4.4B,C**) with 81% probability of a ChI being identified as a member of this group. In contrast, delta-rhythmic neurons were less common in the SPN population with only 36% probability. Similar ISI analysis as in **Figure 4.2D,F** performed across neuron populations, revealed a similar structure in the ISI distribution and return map with a secondary peak around delta frequency (2–3Hz) in delta bursting neurons (**Figure 4.4E,F**). In contrast, non-delta neurons exhibited unimodal distributions (**Figure 4.4G,H**).

Spike timing critically depends on subthreshold membrane voltage dynamics. To understand how the subthreshold dynamics of individual neurons relate to spike timing, we calculated the Vm of each neuron by removing identified spikes from the recorded SomArchon voltage trace. Interestingly, the most prominent Vm dynamics we observed were slow delta oscillations (1–4Hz), which often occurred concurrently with spikes in delta-rhythmic spiking neurons (**Figure 4.4I,J**), which were not observed in other neurons

(**Figure 4.4K,L)**. To quantify this, we computed the time-averaged Vm wavelet power of delta-bursting neurons versus non-delta neurons. We found that delta-rhythmic neurons have significantly higher Vm delta power than non-delta neurons (**Figure 4.4M**), for both ChI and SPN populations (**Figure 4.4N; Figure 4.5**).

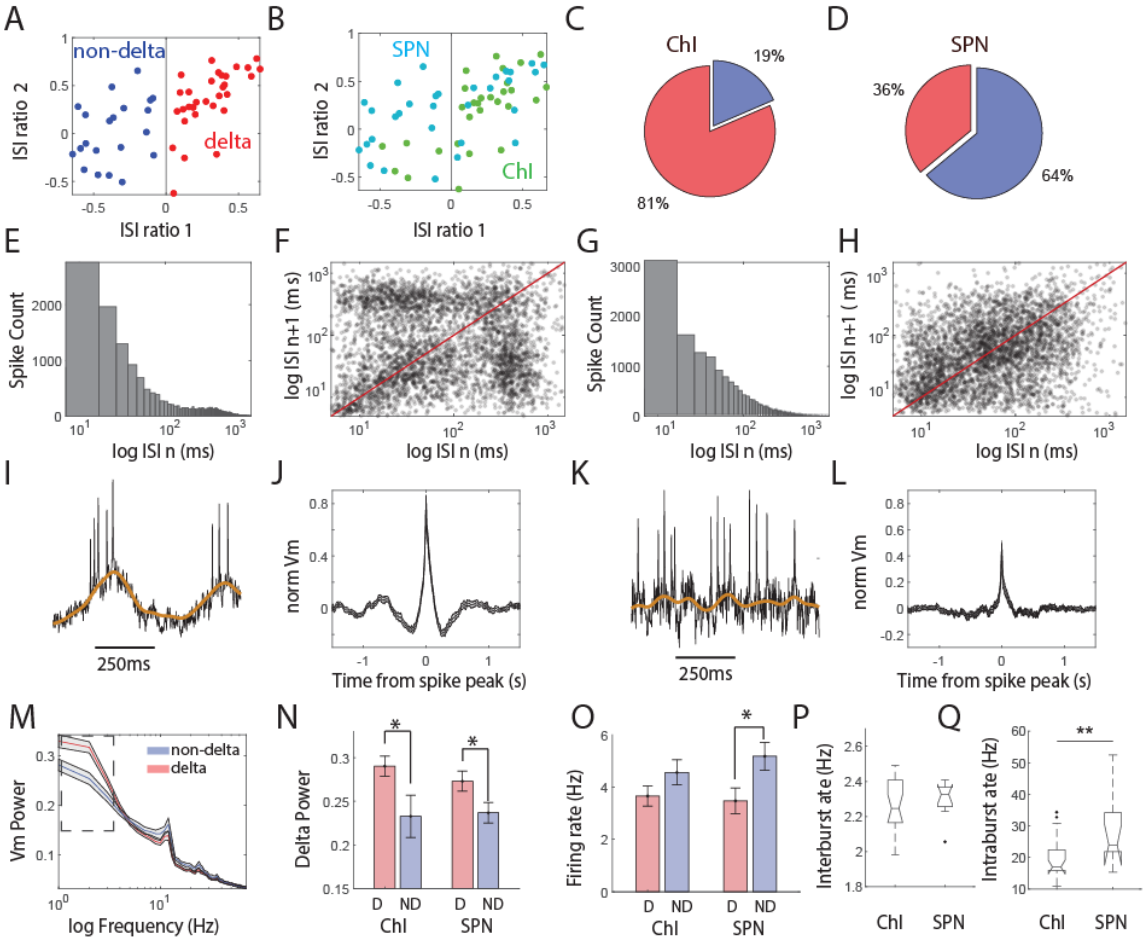

Figure 4.4. A subset of striatal neurons, particularly ChIs, exhibit strong delta-rhythmic Vm and spiking. (A) ISI ratio map with x-axis as the ISI ratio between 300–700ms and 80–200ms and y-axis as the ISI ratio between 10–40ms and 80–200ms. Blue are the ISI identified "non-delta" neurons and red are the ISI identified "delta-rhythmic" neurons. **(B)** ISI ratio map as in **A**, but color labeling SPN (blue) and ChI (green). **(C)**. Pie chart reflecting the probability of a ChI being identified as delta-rhythmic or non-delta rhythmic. **(D)** Pie chart reflecting the probability of an SPN being identified as delta-rhythmic or non-delta rhythmic. **(E)** The inter spike interval (ISI) distribution of all delta-rhythmic neurons (log scale). **(F)** The ISI return map (ISI n vs ISI n+1) of all delta- rhythmic neurons (log scale). **(G)** The ISI distribution of all non-delta neurons (log scale). **(H)** The ISI return map (ISI n vs ISI n+1) of all non-delta neurons (log scale). **(I)** Illustrative

SomArchon trace and smoothed Vm (orange) of a delta rhythmic spiking neuron. **(J)** Population spike-triggered averaged Vm for neurons with delta-rhythmic spiking. **(K)** Illustrative SomArchon trace and smoothed Vm (orange) of a non-delta spiking neuron. **(L)** Population spike-triggered averaged Vm for neurons with non-delta spiking. **(M)** Vm spectral power for all delta-identified neurons (red) and non-delta neurons (blue). **(N)** Quantification of delta power (1-4Hz) for delta-rhythmic and non-delta ChIs and SPNs (all independent t-test, ChI D vs ND: p=0.047, df=25, SPN D vs ND: p=0.006, df=23). **(O)** Mean firing rate quantification for delta-rhythmic and non-delta ChIs and SPNs (all independent t-test, ChI D vs ND: p=0.29, df=25, SPN D vs ND: p=0.046, df= 23). **(P)** Mean delta inter-burst firing frequency for delta-rhythmic ChIs and SPNs (independent t-test, ChI D vs SPN D: p=0.57, df=29). **(Q)** Mean delta intra-burst firing frequency for delta-rhythmic ChIs and SPNs (independent t-test, ChI D vs SPN D: p=0.007, df=29).

The firing rate of ChIs and SPNs as a population were not significantly different (**Figure 4.6**). However, delta-rhythmic ChIs and SPNs had significantly lower firing rates than non-delta neurons (**Figure 4.6**), with non-delta rhythmic neurons having firing rates around ~4.5–5Hz, while delta-rhythmic neurons had firing rates of ~3.5Hz (**Figure 4.4O**). For both ChIs and SPNs, delta-bursting neurons had inter-burst firing rates at delta frequency (ChIs: 2.28 ± 0.034 Hz, SPNs: 2.27 ± 0.039 Hz; **Figure 4.4P**) as expected, and intra-burst firing rates around beta frequency (ChIs: 21 ± 1.5 Hz, SPNs: 27.3 ± 3.57 Hz; **Figure 4.4Q**).

Taken together, these results demonstrate that striatal neurons, including most ChIs and a subset of SPNs, exhibit prominent Vm delta oscillations, suggesting that delta oscillations are a prominent feature of the basal ganglia neural circuit.

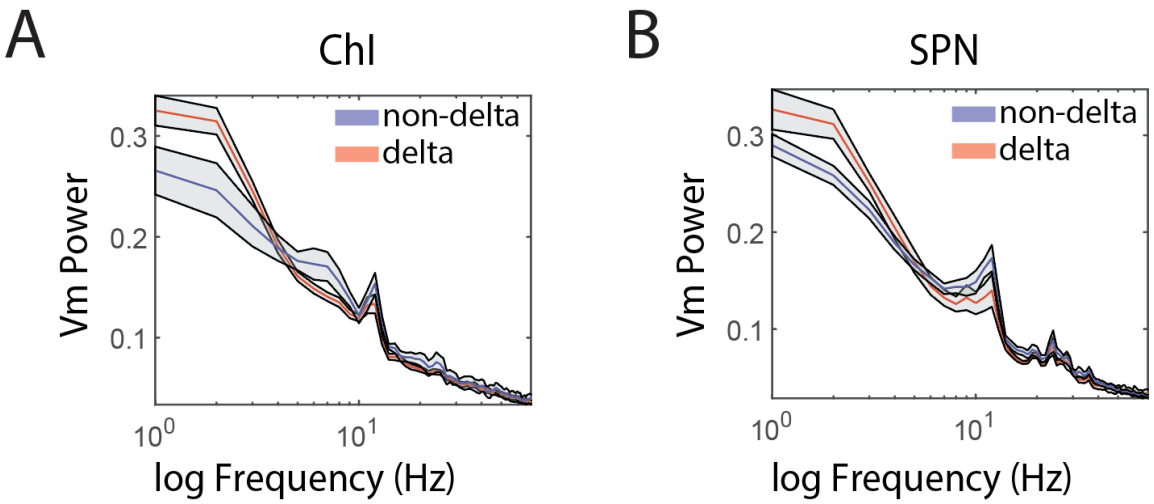

Figure 4.5. Subthreshold Vm power of delta-rhythmic and non-delta-rhythmic neurons for ChI and SPN populations. (A) Vm spectral power for all ChI delta-rhythmic neurons (red, n=22) and ChI non-delta rhythmic neurons (blue, n=5). **(B)** Vm spectral power for all SPN delta-rhythmic neurons (red, n=9) and SPN non-delta rhythmic neurons (blue, n=16).

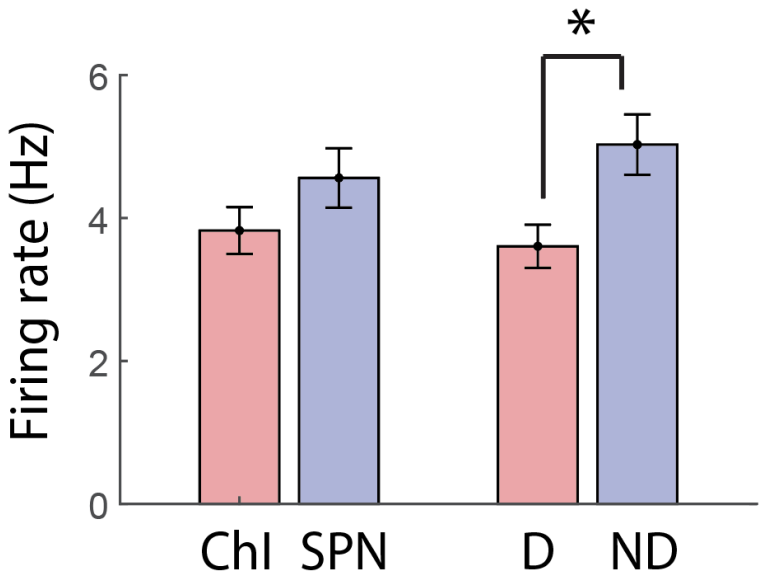

Figure 4.6. Firing rate comparison as a function of cell type and delta rhythmicity. Population mean firing rate between ChIs and SPNs (*left*) were not significantly different (independent t-test, p=0.16, df=50). Population mean firing rate between delta rhythmic neurons and non-delta rhythmic neurons (*right*) were significantly different (independent t-test, p=0.007, df=50).

4.5 Vm delta oscillations organize spike timing and Vm oscillations at beta-gamma frequencies

To further investigate how the delta oscillations we observed relate to spiking output and higher frequency oscillations, we first aligned spiking events to Vm and LFP traces, respectively (**Figure 4.7A,D**) and calculated the strength of spike-phase locking relative to Vm (**Figure 4.7B**) and LFP (**Figure 4.7E**). For both ChIs and SPNs, the strength of spike-Vm and spike-LFP phase locking at delta frequency was significantly higher for delta-rhythmic neurons than for non-delta-rhythmic neurons (**Figure 4.7C,F**).

We then performed wavelet power analysis relative to spike times (**Figure 4.7G**) and found that spikes were coupled to Vm beta-band power in delta-rhythmic neurons for both ChI and SPN populations (**Figure 4.7H,I,K; Figure 4.8A,B**) but not in non-delta rhythmic neurons (**Figure 4.7J,K; Figure 4.8C**). Most strikingly, we found that spikes in delta-rhythmic neurons, but not non-delta rhythmic neurons (**Figure 4.7M**), were coupled to increases in LFP beta power (**Figure 4.7L**) for both ChIs and SPNs (**Figure 4.7N; Figure 4.8D–F**). These results demonstrate that Vm delta frequency oscillations organize beta frequency spike synchronization at the single neuron Vm level and among a sufficient neuron population that produce detectable changes in the LFP.

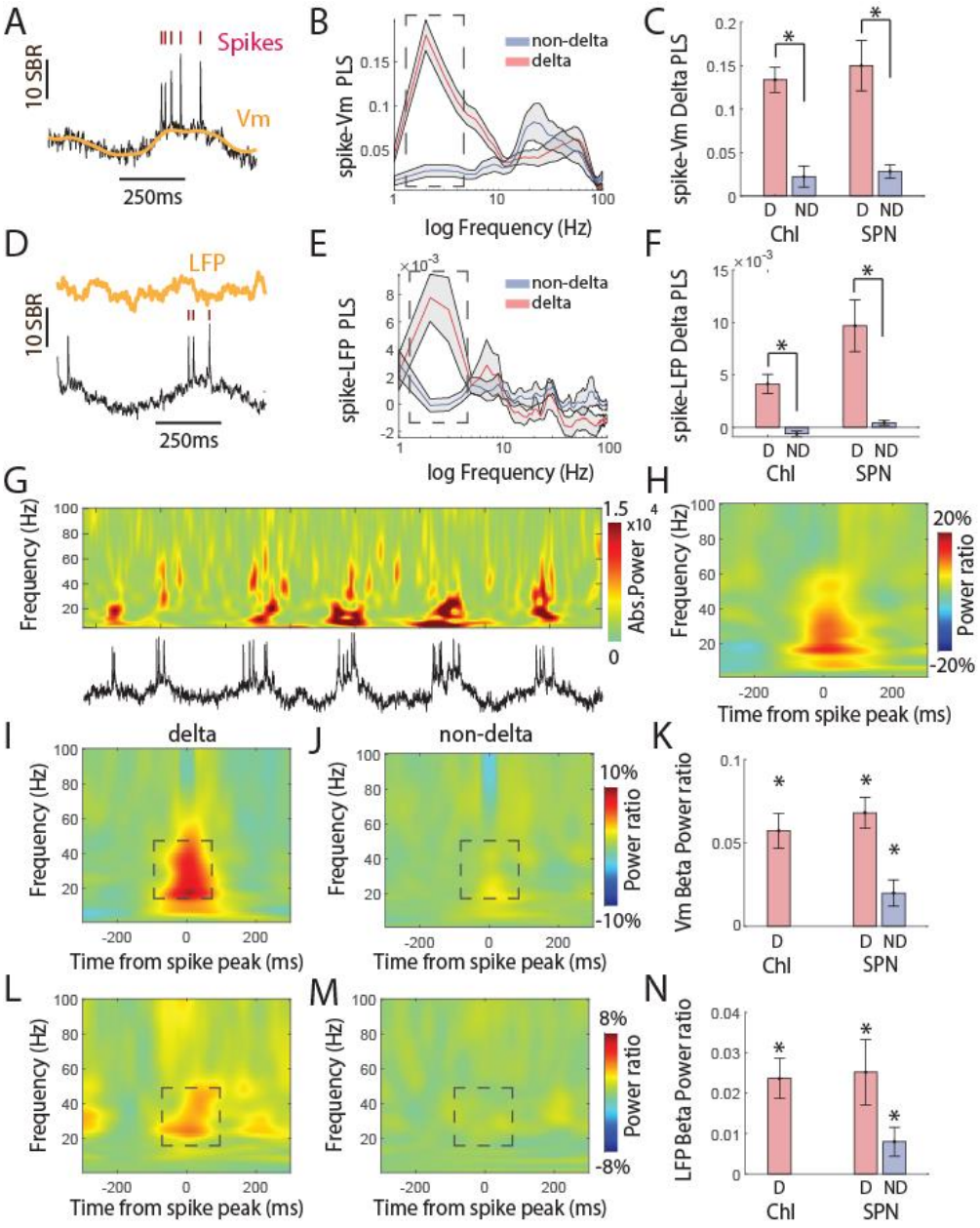

Figure 4.7. Subthreshold delta rhythms structure spike output and beta-gamma power. (A) Example SomArchon trace of a striatal neuron with spike times indicated by red ticks. Orange is the Vm trace. **(B)** Phase-locking strength (PLS) of spikes to Vm across frequencies for either delta-rhythmic (red) or non-delta neurons (blue). Shaded regions are SEM. **(C)** Quantification of the spike-Vm PLS in the delta range (2–4Hz) between delta-identified neurons (red) and regular-identified neurons (blue) for ChIs (*left*) and SPNs (*right*) separately (all independent t-test, ChI D vs ND: p=0.01, df=25, SPN D vs ND: p=9.06e-7, df= 23). **(D)** Example SomArchon trace of a striatal neuron with spike times indicated by red ticks. Orange is the LFP trace. **(E)** PLS of spikes to LFP across frequencies for either delta-rhythmic neuron (red) or non-delta (blue). Shaded regions are SEM. **(F)** Quantification of the spike-LFP PLS in the delta range between delta-rhythmic (red)

and non-delta neurons (blue) for ChIs (*left*) and SPNs (*right*) separately (all independent t-test, ChI D vs ND: p=0.039, df=25, SPN D vs ND: p=6.39e-5, df= 23). **(G)** Example SomArchon trace of a delta-rhythmic striatal neuron with the corresponding Vm wavelet power spectrum shown above. **(H)** Spike-triggered averaged Vm wavelet spectral power ratio of the example neuron in **G**. Vm power is normalized relative to pre-spike period (-200 to -100ms). **(I,J)** Population spike-triggered averaged Vm wavelet spectral power ratio for **(I)** delta-rhythmic (n=29) and **(J)** non-delta rhythmic neurons (n = 16). **(K)** Quantification of the spike-triggered Vm wavelet power ratio in the beta-gamma range (20–40Hz) between delta-rhythmic neurons (red) and non-delta neurons (blue) for ChI (*left*) and SPN (*right*) neurons separately (all one-sample t-test, ChI D: p=5.08e-5, df=20, SPN D: p=1.91e-4, df= 8; SPN ND: p=0.006, df=15). **(L,M)** Population spike-triggered averaged LFP wavelet spectral power ratio for delta-rhythmic (n=31) and **(M)** non-delta-rhythmic neurons (n=21). **(N)** Quantification of the spike-triggered LFP wavelet power ratio in the beta-gamma range (20–40Hz) between delta-rhythmic neurons (red) and non-delta-rhythmic neurons (blue) for ChI (*left*) and SPN (*right*) neurons separately (all one-sample t-test, ChI D: p=1.5e-4, df=20, SPN D: p=0.0142, df=8; SPN ND: p=0.04, df=15).

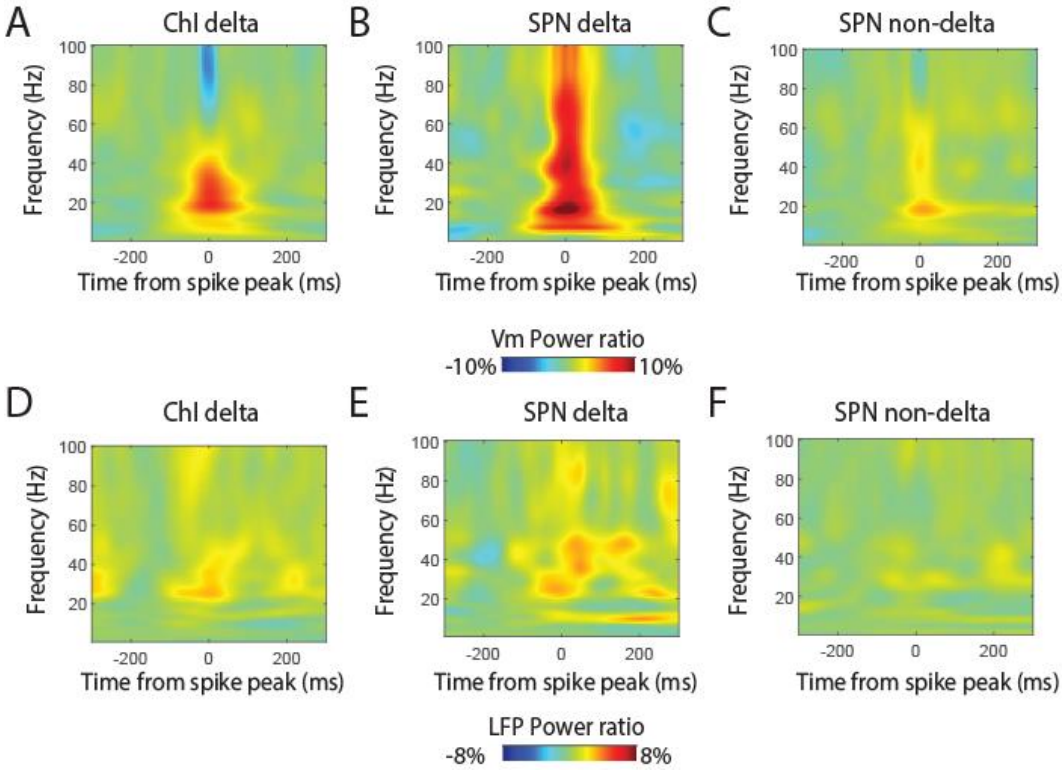

Figure 4.8. Spike-triggered Vm and LFP power as a function of cell type and delta rhythmicity. (A–C) Spike-triggered Vm power (relative to pre-spike period -200 to -100ms) separated as a function of cell type and delta rhythmicity. **(A)** ChI delta-rhythmic neurons (n=21). **(B)** SPN delta-rhythmic neurons (n=9). **(C)** SPN non-delta-rhythmic neurons (n=16). **(D–F)** Spike-triggered LFP power (relative to pre-spike period -200ms to -100ms) separated as a function of cell type and delta rhythmicity. **(D)** ChI delta-rhythmic spiking neurons (n=21). **(E)** SPN delta-rhythmic spiking neurons (n=9). **(F)** SPN non-delta-rhythmic neurons (n=16).

4.6 Delta-rhythmic striatal neurons drive locomotion-related spiking

Finally, we investigated how animal movement, as a state change, drives striatal neuron spiking activity and LFP dynamics. We segregated recording periods into high-speed movement bouts (defined as mouse speed ≥ 5 cm/s; green) and low-speed movement bouts (mouse speed < 5cm/s; pink), with movement onset and offset points (light blue) defined as transitions between these periods (**Figure 4.10A**). We first assessed separately ChI and SPN firing rate modulations with locomotion. We found that a significant proportion of SPNs (12/25) increased their firing rate during high-speed bouts compared to low speed bouts, while 7/25 decreased their firing rate, and another 6/25 remained unchanged, consistent with previous electrophysiology studies of individual striatal neurons[227,228,242] and calcium imaging analysis[59] (**Figure 4.9B**) . In contrast, about half of ChIs (14/27) were insensitive to movement speed, while 11/27 ChIs increased their firing during high-speed bouts compared to low-speed bouts, and only 2/27 decreased their firing rate (**Figure 4.9A**). As populations, ChIs, but not SPNs increased their firing rates with movement (**Figure 4.9**; $p = 0.0042$ and $p = 0.091$ for ChIs and SPNs, respectively). We then compared the average spike rate of individual delta-rhythmic vs. non-delta rhythmic across ChIs and SPNs during low versus high-speed movement bouts. We found that nearly half of delta-rhythmic neurons (14/31) had higher firing rates during high-speed bouts than low-speed bouts, while another 14/31 were insensitive to movement speed, and only 3/31 decreased their firing rate with movement (**Figure 4.10B**). Non-delta rhythmic spiking neurons, on the other hand, had a more even distribution, with 43% of neurons increasing their firing rate during high-speed movement (9/21) while 29% decreased their firing rate

or remained unmodulated with movement speed (n = 6/21 for each group; **Figure 4.10C**). As populations, both delta-rhythmic neurons and non-delta rhythmic neurons generally increased their firing rate with movement (**Figure 4.10B–D**; p = 0.019 and p = 0.042 for delt-rhythmic and non-delta rhythmic neurons, respectively).

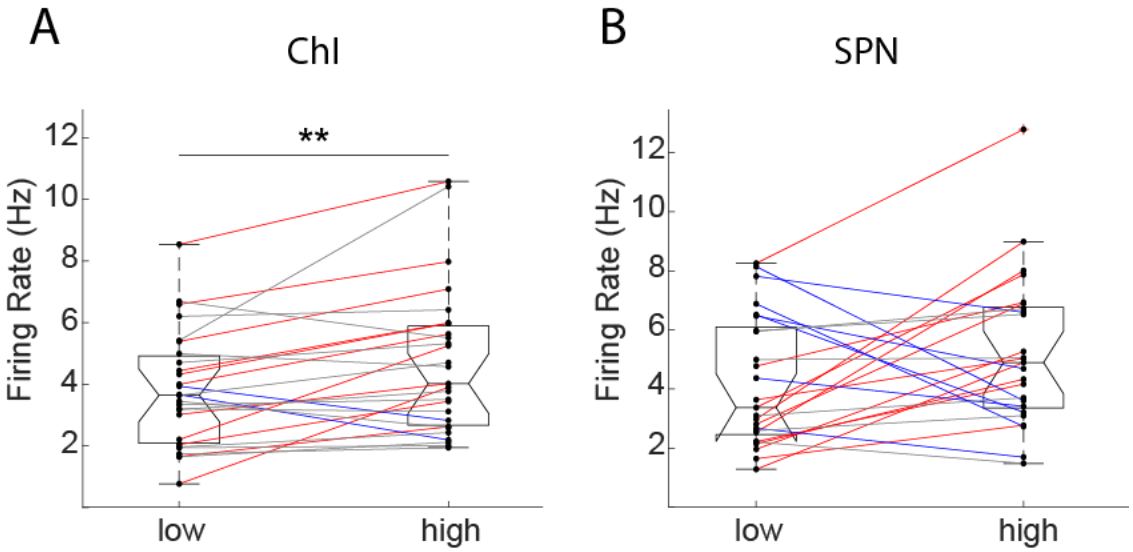

Figure 4.9. ChIs but not SPNs increase their mean firing rate between low and high locomotion periods. (A) Mean firing rates for low and high locomotion periods for ChI neurons. Red are neurons with significantly increasing firing rates from low to high locomotion, whereas blue have significantly decreasing firing rates, and gray neurons' firing rates remained unchanged. Overall, the population of ChIs significantly increased their firing rate with locomotion (n = 27; p=0.0042, df =26). **(B)** Same as **A**, but for SPNs. Overall, the SPN population did not modulate its firing rate with locomotion (n = 25; p=0.091, df =24).

As previous calcium imaging studies have suggested that ChIs and SPNs respond differently during different phase of locomotion[59,64], we next investigated the subsets of delta-rhythmic and non-delta-rhythmic populations pertaining to SPNs and ChIs specifically at movement onset versus offset. Due to the low number of non-delta rhythmic ChIs and limited number of motion transitions, this group is not analyzed separately. We found that delta-rhythmic neurons as a population (**Figure 4.10F**), and when divided by

ChIs (**Figure 4.11A**) and SPNs (**Figure 4.11B**), significantly increased their firing rates about 50–200ms after movement onset, with slight timing differences between the three groups (all delta-rhythmic: increased 50–150ms post onset, delta-rhythmic ChIs: increased 50–100 ms post onset, delta-rhythmic SPNs: increased 50–200ms post onset). An example delta-rhythmic ChI responsive to movement onset is shown in **Figure 4.10E**. Non-delta-rhythmic neurons, in contrast, showed only a small increase in firing rate prior to movement onset (**Figure 4.10G**) and non-delta-rhythmic SPNs, in particular, did not show major locomotion onset-related firing rate modulations (**Figure 4.11C**). Neither ChI nor SPN firing rates changed significantly around movement offset (**Figure 4.11D–F**). These results provide direct evidence that delta-rhythmic neurons, both ChIs and SPNs, contribute more to locomotion-dependent state transitions than do non-delta rhythmic neurons.

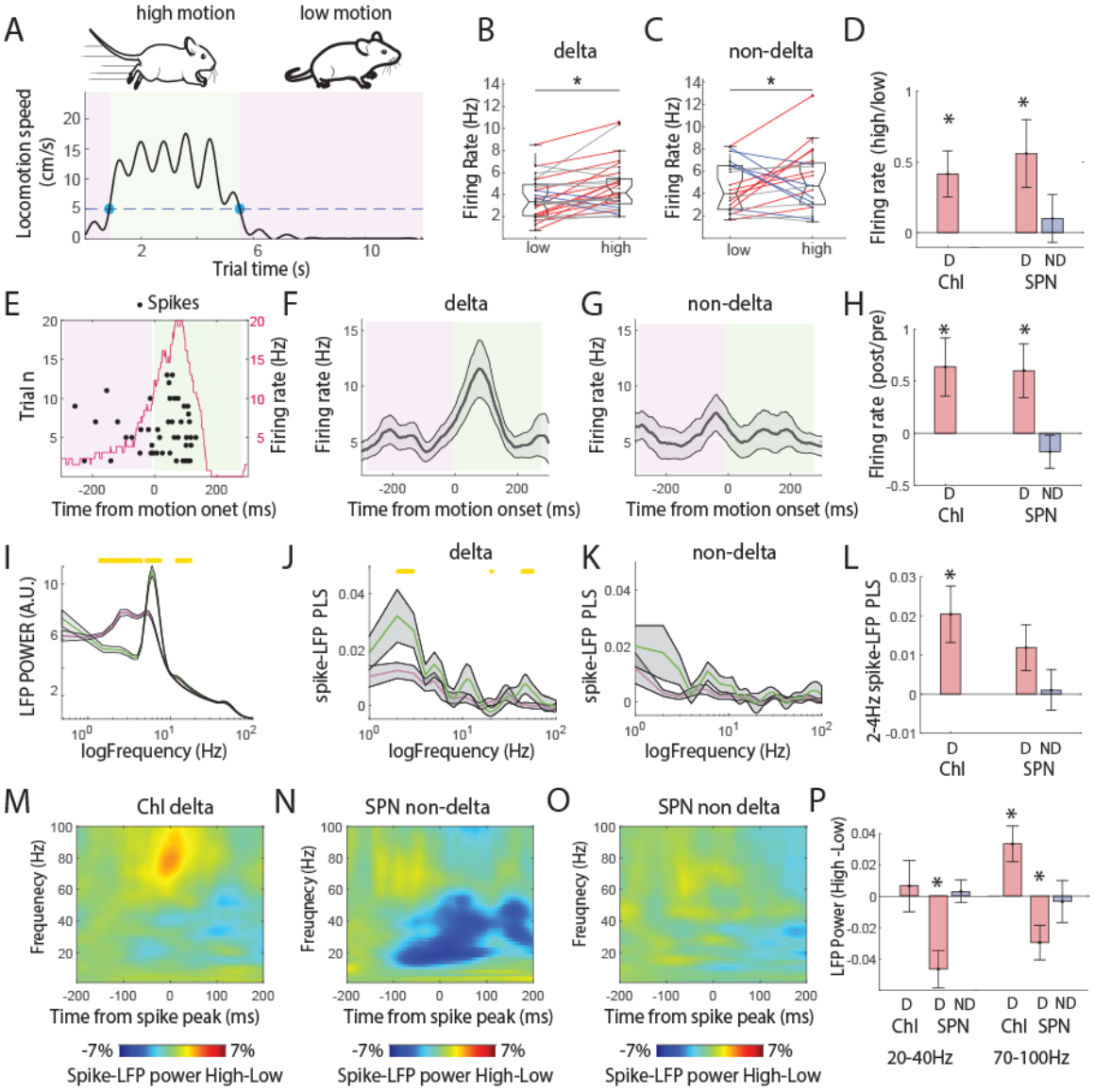

Figure 4.10. Locomotion-dependent firing rate and beta-gamma modulations are specifically related to delta-rhythmic striatal neurons. (A) Example trial showing locomotion speed while animal is running on a pinned ball (black line). The dashed blue line reflects the threshold (5cm/s) used to classify periods of low (pink) and high (green) animal locomotion. Periods had to be at least 500ms long. Light blue dots represent the onset or offset time points of high locomotion periods. **(B)** Mean firing rates for low and high locomotion periods for delta-rhythmic neurons. Red are neurons with significantly increasing firing rates from low to high locomotion, whereas blue have significantly decreasing firing rates, and gray neurons' firing rates remained unchanged. Overall, delta rhythmic neurons significantly increased their firing rate with locomotion (p=0.019, df=30). **(C)** Same as **B**, but for non-delta-rhythmic neurons. As a population, non-delta rhythmic neurons also significantly changed their firing rate with locomotion (p=0.042, df=20). **(D)** Quantification of low vs high locomotion firing rates for delta-rhythmic and non-delta-rhythmic neurons separated

by ChIs and SPNs. ChI non-delta neurons are not shown due to the low number of neurons and motion onsets (all one-sample t-test, ChI D: p=0.019, df=21, SPN D: p=0.048, df=8; SPN ND: p=0.56, df=15). **(E)** Motion onset-triggered firing raster plot (onset of low-to-high locomotion period) of an example ChI neuron. Black points are spike times. Red line is the firing rate averaged over all triggered time windows. **(F,G)** Population motion onset-triggered firing rate plot for **(F)** delta-rhythmic neurons and **(G)** non-delta neurons. Shaded area is SEM. **(H)** Quantification of motion onset related firing rate ratio comparing post-onset (20 to 150ms) vs pre-onset (-150 to -20ms) for delta-rhythmic and non-delta neurons separated by ChIs and SPNs (all one-sample t-test, ChI D: p=0.022, df=20, SPN D: p=0.046, df=8; SPN ND: p=0.79, df=15). **(I)** LFP power separated by low (pink) and high (green) locomotion. **(J)** Spike-LFP phase locking strength (PLS) separated by low (pink) and high (green) locomotion periods for delta-rhythmic neurons. Yellow lines reflect significance ($p < 0.05$) estimated based on shuffling procedure. **(K)** Same as **J**, but for non-delta-rhythmic neurons. **(L)** Quantification of the spike-Vm PLS difference in the delta range (2-4Hz) between low and high locomotion periods for delta-rhythmic neurons (red) and non-delta neurons (blue); separated by ChIs and SPNs (all one-sample t-test, ChI D: p=0.01, df=20, SPN D: p=0.0756, df=8; SPN ND: p=0.19, df=15). **(M–O)** Population spike-triggered averaged LFP wavelet spectral power ratio difference between low and high locomotion periods for (**M**) ChI delta-rhythmic neurons, **(N)** SPN delta-rhythmic neurons, and **(O)** SPN non-delta-rhythmic neurons. **(P)** Quantification of the difference in spike-triggered LFP power ratio between low and high locomotion periods for delta-rhythmic neurons (red) and non-delta-rhythmic neurons (blue) separated by ChIs and SPNs. *Left*, quantifications for power ratio at spike time and pre-spike period (-200 to -100ms) in the beta-gamma range (20-40Hz, all one-sample t-test, ChI D: p=0.9, df=20, SPN D: p=0.009, df=8; SPN ND: p=0.65, df=15) and *right*, in the high gamma range (70-100Hz, all one-sample t-test, ChI D: p=0.012, df=20, SPN D: p=0.054, df=8; SPN ND: p=0.51, df=15).

4.7 Delta-rhythmic spike-LFP locking increases with locomotion

Given that we have found delta-rhythmic spiking neurons exhibit stronger phase locking strength (PLS) to Vm and LFP delta oscillations (**Figure 4.7B,E**), we studied whether the spike-LFP delta PLS exhibited locomotion-dependent effects. We did not analyze spike-Vm PLS or Vm power during high movement periods, due to the concern that subthreshold Vm measurements could be affected by micromotion-induced small fluctuations in optically-acquired fluorescence. We found that overall striatal LFP power at delta frequency (1–4Hz) was elevated during low movement conditions, while a narrow theta band (6–8Hz) and 10–11Hz oscillation was elevated during high movement (**Figure**

4.10I). There was not an obvious 2–3Hz delta peak in the LFP during either low or high locomotion periods, as one would expect based on the overall Vm power spectra from delta rhythmic spiking neurons discussed previously (**Figure 4.4M**). Despite the dominant peak in the theta range of LFP power during high movement, the spike-LFP PLS at delta, not theta, frequency was significantly increased during high movement for delta-rhythmic neurons (**Figure 4.10J**) and for delta-rhythmic ChIs specifically (**Figure 4.10L)**. However, non-delta rhythmic SPN neurons exhibited no significant increase in spike-LFP delta PLS during high motion periods (**Figure 4.10K,L**). This implies that Vm delta oscillations, specifically in ChI neurons, may be driving delta oscillations in LFP, which is consistent with the extensive arborization networks of ChIs that may support synchronized synaptic currents within the striatum during ChI spiking, leading to prominent striatal LFP oscillations.

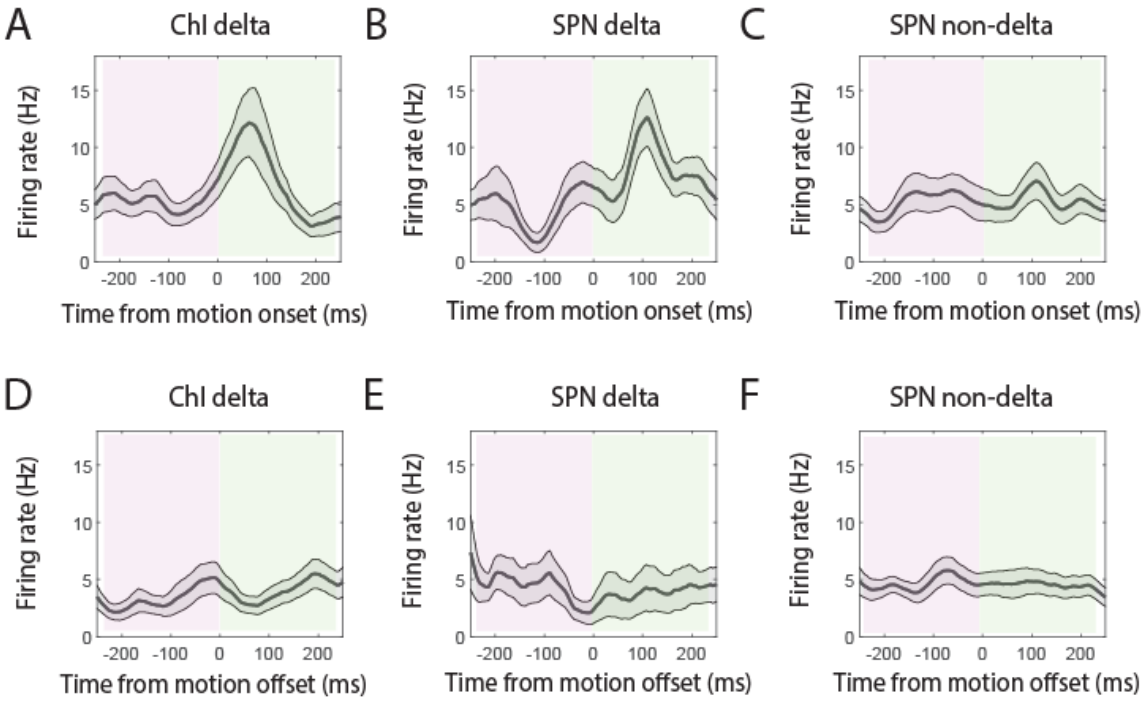

Figure 4.11. Locomotion onset- and offset-triggered firing rates by cell type and delta rhythmicity. (A–C) Population motion onset-triggered firing rate plot for **(A)** delta-rhythmic ChIs (n=21), **(B)** delta-rhythmic SPNs (n = 9), and **(C)** non-delta-rhythmic SPNs (n = 16). **(D–F)** Population motion offset-triggered firing rate plot for **(D)** delta-rhythmic ChIs (n = 21), **(E)** delta-rhythmic SPNs (n = 9), and **(F)** non-delta-rhythmic SPNs (n = 16). Shaded area is SEM.

4.8 Delta-rhythmic neurons exhibit locomotion-dependent spike-triggered LFP beta-gamma power modulations

Next, we investigated the spike-triggered LFP power during low and high locomotion periods separately. When aligned to delta-rhythmic ChI spikes, there was a significant increase in LFP high gamma power (70–100Hz), but not beta power, during high movement, as compared to low movement (**Figure 4.10M,P; Figure 4.12A,D**). In contrast, around delta-rhythmic SPN spikes, we observed a significant decrease in both beta (20–40Hz) and high gamma power (70–100Hz), which started 100ms before the spike and lasted up to 200ms after (**Figure 4.10N,P; Figure 4.12B,E**). This is consistent with

previous studies that have shown decreases in LFP beta power during high movement conditions or linked to SPN spiking[66,69,285,286]. No significant locomotion-modulated differences in LFP oscillations were detected around spikes of non-delta SPNs (**Figure 4.10O,P; Figure 4.12C,F**).

In total, these results highlight a prominent role of Vm delta oscillations, specifically in ChIs, to coordinate cortical-basal ganglia circuits during locomotion. In particular, these delta-rhythmic neurons' spiking dynamics are associated with movement transitions, and uniquely drive movement-associated differences in Vm and LFP power. These results corroborate the hypothesis that LFP oscillations are driven by coordinated synaptic input via Vm dynamics, rather than by just spiking activity and reveals a key mechanism for oscillatory behavior in the nucleated striatum.

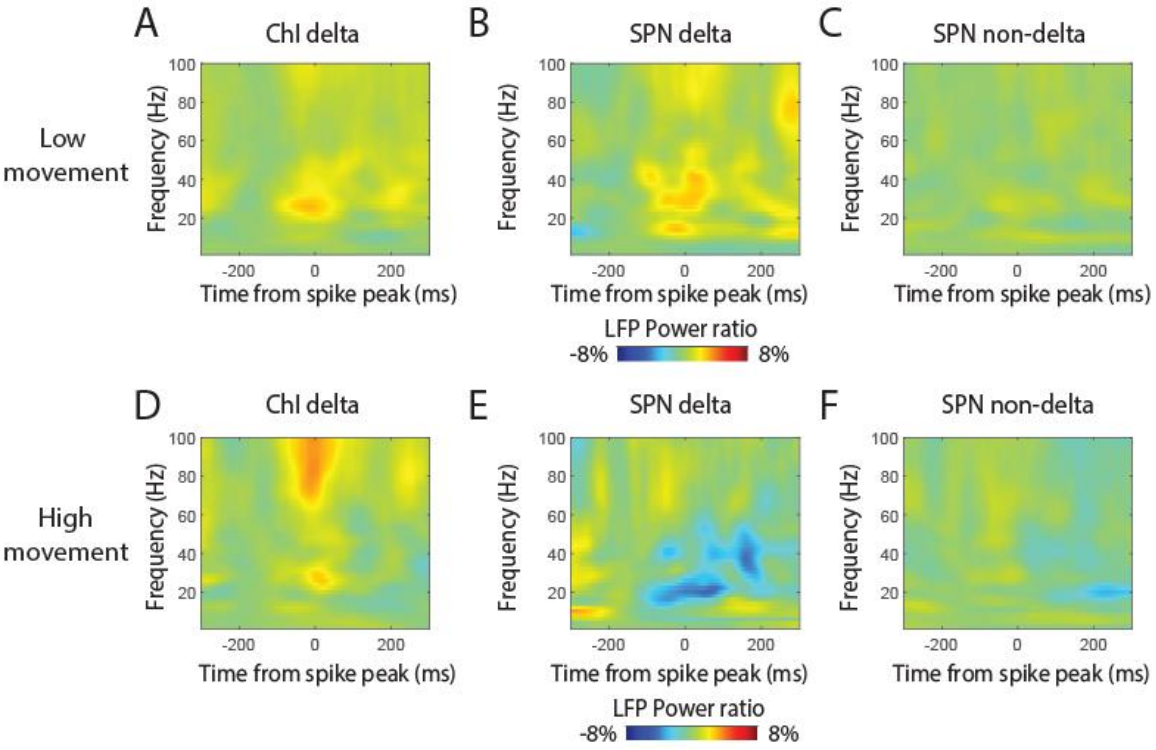

Figure 4.12. Spike-triggered LFP power modulations during low and high locomotion periods. (A–C) Population spike-triggered averaged LFP wavelet spectral power ratio during low locomotion periods (<5cm/s) for **(A)** ChI delta-rhythmic neurons (n = 21), **(B)** SPN delta-rhythmic neurons (n = 9), and **(C)** SPN non-delta-rhythmic neurons (n = 16). **(D–F)** Population spike-triggered averaged LFP wavelet spectral power ratio during high locomotion period (>5cm/s) for **(D)** ChI delta-rhythmic neurons (n = 21), **(E)** SPN delta-rhythmic neurons (n = 9), and **(F)** SPN non-delta-rhythmic neurons (n = 16).

4.9 Discussion

Local field potential (LFP) oscillations at delta and beta frequencies across the cortical-basal ganglia circuits have been broadly linked to motor behavior and pathology[48,66,68-74,76-79]. However, it remains largely unclear how the striatum, the largest basal ganglia nucleus, supports circuit coordination via oscillations. Here, we performed voltage imaging of individual putative spiny projection neurons (SPNs) and cholinergic interneurons (ChIs), recording both spikes and subthreshold membrane voltage (Vm),

simultaneously with striatal LFP during voluntary movement.

We found that a majority of ChIs and a subset of SPNs exhibit prominent Vm delta oscillations (1-4Hz) that organize spike timing. Spikes in these delta-rhythmic neurons displayed beta rhythmicity (~10–35Hz), and the occurrence of spikes was associated with increases in both Vm and LFP beta oscillation power, in addition to spike-phase locking to Vm and LFP delta frequencies. In the context of movement, delta-rhythmic neurons fired preferentially during high-speed movement and around movement transitions, while the remaining non-delta-rhythmic neurons did not modulate their spike rate. During high-speed movement, spikes in delta-rhythmic ChIs in particular showed increased phase locking to LFP delta and gamma oscillations. As increases in LFP gamma power are typically associated with increased neural activity, the LFP beta-gamma oscillations associated with ChI spiking are consistent with the idea that ChIs can drive striatal neuron synchronization through their extensive arborizations[59]. In contrast, spikes in delta-rhythmic SPNs during locomotion were associated with decreases in LFP beta and gamma power, consistent with the general role of beta oscillations in inhibiting movement[65-67,69-71,287]. Together, our results demonstrate that subthreshold membrane voltage delta oscillations in individual striatal neurons organize spike timing and higher frequency beta and gamma oscillations, and play a critical role in temporal patterning during locomotion.

In both delta-rhythmic SPNs and ChIs, we found that Vm delta oscillations organize Vm beta oscillations and spike timing. While SPNs have been broadly shown to have intrinsic

up and down states in brain slices and in anesthetized animals, ChIs, are not known to exhibit these dynamics, instead known for their tonic firing rates[58,61,288]. The delta oscillations we observed in individual SPNs during locomotion may share some of the same biophysical mechanisms as the up and down states observed in brain slices and in anesthetized animals[49-54,267]. However, the coupling of these oscillations to movement suggests that the SPN delta oscillations observed here are distinct from those observed in brain slices or under anesthesia, and capture a unique striatal network state during locomotion. The fact that ChI Vm delta oscillations are also tightly linked to movement provides further support that delta oscillations are a general network feature shared across multiple striatal cell types during locomotion.

ChIs are thought to be tonically active neurons that exhibit pacemaker behavior in the absence of synaptic inputs and receive substantia nigra dopaminergic, and cortical and thalamic glutamatergic inputs[289-293]. We found prominent ChI Vm oscillations at delta frequencies, which organize Vm beta oscillations and spiking. Additionally, we found that ChI spikes were associated with Vm and LFP gamma oscillations during movement. As gamma oscillations are thought to be driven by increased neural activity, rhythmic ChI spiking could drive synchronized cholinergic activation of striatal neurons that express various cholinergic receptors. For example, striatal parvalbumin neurons express nicotinic acetylcholine receptors (AchRs)[294-296], while SPNs differentially express muscarinic AchRs[58,297,298]. In addition, previous studies have demonstrated that ChI activation promotes SPN synchronization and movement completion[59]. In total, these studies are

consistent with prominent LFP beta-gamma oscillations we found associated with ChI spiking. In contrast to ChIs, SPNs primarily project out of the striatum, consistent with the observation that their activation is not associated with any prominent LFP gamma oscillations. Instead, delta-rhythmic SPN spiking was accompanied with a reduction in LFP beta oscillations during movement, corroborating existing relationships between LFP beta and movement inhibition[65,66,299-301].

Our results highlight the unique contribution of ChIs to organize striatal circuit dynamics, particularly in delta and beta-gamma frequencies, which support cortical-basal ganglia circuit interactions. Furthermore, this study demonstrates the prominent role of subthreshold delta oscillations to organize neural synchronization and support striatal participation during locomotion.

4.10 Methods

4.10.1 Mouse surgery

All animal experiments were performed in accordance with the National Institute of Health Guide for Laboratory Animals and approved by the Boston University Institutional Animal Care and Use and Biosafety Committees. Adult male and female C57BL/6 mice (Charles River Laboratories, Inc.) or ChAT-Cre mice (ChAT-cre; Tg(Chat-cre)GM24Gsat/Mmucd, MMRRC_017269-UCD, NIH MMRRC), or ChAT-tdT mice (crossed between ChAT-Cre and the tdT mouse line: B6.Cg-*Gt(ROSA)26Sor*$^{tm14(CAG-tdTomato)Hze}$/J from The Jackson Laboratory), 10–22 weeks at the start of the study, were used for all experiments.

4.10.1.1 Striatum imaging window implantation

Striatal window surgeries were performed similar to those described previously[11,29]. Custom imaging windows consisted of a stainless-steel cannula (OD: 3.17mm, ID: 2.36mm, 1 or 2mm height, AmazonSupply, B004TUE45E) with a circular coverslip (#0, OD: 3mm, Deckgläser Cover Glasses, Warner Instruments Inc., 64-0726 (CS-3R-0)) adhered to the bottom using a UV curable glue (Norland Products Inc., Norland Optical Adhesive 60, P/N 6001). We glued a virus infusion cannula (26G, PlasticsOne Inc., C135GS-4/SPC), and an LFP electrode made of stainless-steel wire (Diameter: 130µm, PlasticsOne Inc., 005SW-30S, 7N003736501F) to the side of the imaging window using super glue (Henkel Corp., Loctite 414 and Loctite 713). The LFP electrode protruded from the bottom of the imaging window by about 200µm.

A craniotomy ~3mm in diameter was made over the striatum (AP: +0.5, ML: -1.8). A small notch was made on the posterior edge of the craniotomy to accommodate the infusion cannula and LFP recording electrode. The overlying cortex was gently aspirated using the corpus callosum as a depth landmark. The corpus callosum was then carefully thinned to expose the dorsal striatum. The imaging window was positioned in the craniotomy, and Kwik sil adhesive (World Precision Instruments LLC, KWIK-SIL) was applied around the edges of the imaging window to hold it in place and to prevent any dental cement from touching the brain. Three small screws (J.I. Morris Co., F000CE094) were screwed into the skull to further anchor the imaging window to the skull, and a small ground pin was inserted into the posterior part of the brain near the lambda suture as a ground reference for

LFP recordings. Dental cement was then gently applied to affix the imaging window to the exposed skull, and to mount an aluminum headbar posterior to the imaging window. See **Figure 4.2B** for diagram of window placement.

AAV virus injection occurred either one week prior to window implantation surgery, or through the virus infusion cannula after window implantation surgery. All AAV was produced by the University of North Carolina Chapel Hill Vector Core. AAV-Syn-SomArchon (5.9e12 genome copies (GC)/ml) or AAV-CAG-FLEX-SomArchon (6.3e12 GC/ml) was injected into the dorsal striatum (AP:+0.5, ML:-1.8, DV:-2.2, 1uL virus). Viral injection occurred at 50–100nL/min. In mice where AAV was injected during surgery, AAVs were infused with a 10uL syringe (NANOFIL, World Precision Instruments LLC) fitted with a 33-gauge needle (World Precision Instruments LLC, NF33BL) and controlled by a microinfusion pump (World Precision Instruments LLC, UltraMicroPump3–4). Other mice were infused with AAVs through an internal infusion cannula (33G, PlasticsOne Inc., C315IS-4/SPC) connected to a microinfusion pump (World Precision Instruments LLC, UltraMicroPump3–4) approximately one week after the window implantation surgery. In both cases, the internal infusion cannula or syringe was left in place for 10 minutes following injection to facilitate viral spread. Mice were awake and head-fixed throughout the injection period.

All mice were treated with buprenex for 48 hours following surgery or with sustained release (SR) buprenorphine at the beginning of surgery and single-housed to prevent any

damage to the headbar or window implant.

4.10.2 SomArchon voltage imaging

All optical recordings were acquired on a custom widefield fluorescence microscope equipped with a Hamamatsu ORCA Fusion Digital CMOS camera (Hamamatsu Photonics K.K., C14440-20UP), 10x NA0.25 LMPlanFI air objective (Olympus Corp.), 40x NA0.8 LUMPlanFI/IR water immersion objective (Olympus Corp.), 470 nm LED (ThorLabs Inc., M470L3), a 140 mW near-infrared 637 nm laser (Coherent Obis 637-140X), a green filter set with a 470/25 nm bandpass excitation filter, a 495 nm dichroic, and a 525/50 nm bandpass emission filter, and a near infrared filter set with a 635 nm laser dichroic filter, and a 664 nm long pass emission filter. The near-infrared laser illuminated a circular area of ~60–80 μm in diameter, with an FOV size of 40–60 μm x 60–80 μm under the 40x objective. A mechanical shutter (Newport Corporation, model 76995) was positioned in the laser path to control the timing of illumination over the imaging window. The GFP fluorescence of the SomArchon-GFP fusion protein was first acquired in the green channel (λ_{ex}=470 nm) at 1024x1024 pixels with 2x2 binning to capture cell morphology. SomArchon optical voltage recordings were then performed in the near infrared channel (λ_{ex}=637 nm) with 2x2 binning. Optical recordings were acquired at ~826 Hz with HCImage Live (Hamamatsu Photonics K.K.). HC Image Live data were stored as DCAM image files (DCIMG), and analyzed offline in Fiji/ImageJ and MATLAB (MathWorks Inc.). To synchronize optical recordings with LFP recordings, the camera sent out a TTL pulse to the OmniPlex system (PLEXON Inc.) at the onset of imaging and after each

acquired frame.

4.10.2.1 Head-fixed voluntary movement experiments

All voluntary movement experiments were performed while awake, head-fixed mice were freely navigating a spherical pinned treadmill. The spherical treadmill was constructed following Dombeck et al. 2007[255]. Briefly, a 3D spherical Styrofoam ball was supported by a 2mm metal rod to restrict free movement to forward or backward motion only (no rotational movement). Movement was tracked using two computer mouse sensors positioned roughly ± 75 degrees from center along the equator of the ball. In order to determine the mouse movement speed, the pinned ball was rotated vertically to calibrate sensor displacement. All motion sensor displacement data was acquired at 20 Hz on an Arduino Teensy board and synthesized using a custom Matlab script. The timing of each motion sensor displacement data point was also recorded using the OmniPlex system (PLEXON Inc.) for offline synchronization with optical voltage recordings.

All mice were habituated on the pinned spherical treadmill for at least three days, at least 20 minutes per day, prior to image acquisition. During optical imaging, mice were imaged while freely navigating the spherical treadmill. Each FOV was recorded for at least 24 seconds total, with most FOVs being recorded for 120 seconds. In all FOVs, we performed multiple imaging sessions (“trials”). Each trial was 12 seconds in duration with an inter-trial interval of at least 30 seconds in duration to avoid photobleaching.

4.10.3 Local field potential recording

LFPs were recorded using OmniPlex (PLEXON Inc.) at a 1 kHz sampling rate. To synchronize voltage imaging and LFP recordings during offline data analysis, the OmniPlex system also recorded TTL pulses that were sent by the sCMOS camera at the onset of each image frame.

4.10.4 Voltage imaging data motion correction & ROI identification

Motion correction was performed with a custom MATLAB script. SomArchon fluorescence images were first motion corrected using a pairwise rigid motion correction algorithm as described previously[302]. Briefly, the displacement of each image was computed by identifying the max cross-correlation coefficient between each image and the reference image. Our recordings consisted of multiple 12-second-long trials. Each video file corresponding to one trial was first concatenated into a multi-trial data matrix, after which the motion correction algorithm was applied. Since the laser illumination area was about 60–80μm in diameter, a rectangular window large enough to cover the entire neuron across all frames was selected manually for motion correction. The window selection was chosen to avoid dark regions of the image and to include regions that had distinguishable cell-like contrasts to facilitate comparison with the reference image. Each trial was first motion corrected individually. We then corrected image shifts across trials by referencing all trials to the first trial. The motion-corrected image sequences were then used for subsequent manual ROI neuron identification using the drawPolygon function in MATLAB. SomArchon fluorescence traces for each ROI were then extracted from the

motion-corrected image sequences. The optically-recorded voltage traces for each ROI were generated from these motion-corrected image sequences and were used for subsequent analyses.

4.10.5 SomArchon fluorescence detrending and spike detection

All optically-recorded SomArchon traces reported in the manuscript were corrected for photobleaching by subtracting the smoothed trace using the MATLAB function fastsmooth(). Spike detection was performed similar to described previously in Xiao et al[32]. To estimate baseline fluorescence, we first averaged the fluorescence trace using a moving window of ±100 frames to obtain the "Smoothed Trace" (SmT). We then removed potential spike contributions to the baseline by replacing fluorescence values above the SmT with the corresponding SmT values, which resulted in a spike-removed trace including only the subthreshold baseline fluctuation. To identify spikes, SomArchon fluorescence traces were high-pass filtered (>120Hz), and spikes were identified as fluorescence increases greater than 4 standard deviations above baseline subthreshold fluctuations.

4.10.6 Subthreshold membrane voltage (Vm) traces

To obtain subthreshold membrane voltage (Vm) traces, we removed three data points around the peak of each detected spike from the non-filtered SomArchon dF/F trace and interpolated the missing data points using the surrounding data points (n = +/-3 points).

4.10.7 Signal to baseline ratio (SBR)

To calculate SBR, we first determined the spike amplitude by calculating the difference between the lowest and peak spike fluorescence value within three data points prior to the spike. We then divided the spike amplitude by the standard deviation of the Vm across the entire recording duration.

4.10.8 SomArchon voltage imaging, LFP, and animal locomotion data alignment

Voltage imaging data, LFP data, and animal locomotion data were aligned to the camera start trigger (first frame) of each trial and interpolated to a frame rate of 1kHz to match that of the LFP recordings. Subsequent analyses were performed on these aligned and interpolated data.

4.10.9 Definition of movement periods and transition points

Animals' movement data was first smoothed using a 1.5Hz low pass Butterworth filter to remove any motion sensor artifact. We defined low movement periods as intervals where the speed was continuously ≤5cm/s for at least 500ms and high movement periods as intervals where the speed was continuously ≥5cm/s for at least 500ms. A movement transition was defined as the point at which a pre-defined low movement period and high movement period intersect, where a low-to-high transition (or "onset") was identified by a high-speed period directly following a low-speed period, and vice versa for a high-to-low transition (or "offset") where a low-speed period directly followed a high-speed period.

See **Figure 4.10A** for an example movement trace with movement periods and transition points identified. In **Figure 4.9** and **Figure 4.10B,C**, the firing rates during these low and high movement periods were compared. For each neuron, we calculated the average spike rate per second in low-speed periods (total spikes/number of low-speed frames x1000) and the average spike rate per second in high speed periods across trials. The difference between the average spike rates in low and high-speed periods was used as the metric. To determine if the neuron was responsive to sustained periods of locomotion, we built a basal distribution of the differences using shuffling. We randomly chose the same number of frames as the total low-speed frames in each trial and calculated the spike rate across these randomly selected frames and finally took an average across trials for every neuron. This was repeated to calculate the average spike rate in random high-speed periods as well. The difference between these random spike rates was calculated and this procedure was repeated 1000 times. If the observed difference for a neuron was beyond 97.5^{th} percentile of the distribution, then the neuron exhibits a significantly increased response to sustained periods of locomotion. On the other hand, if the observed difference was less than 2.5^{th} percentile of the distribution, the neuron shows significantly decreased response to high-speed periods compared to low speed periods.

4.10.10 Inter-spike interval calculation

Inter-spike intervals (ISIs) were calculated as the time between identified spikes in ms. For a given spike, we computed the time difference between the previous spike (ISI n) and with the following spike (ISI n+1). The two-dimensional space of ISI n and ISI+1 represent the

so called ISI return map. Plotting the ISI return map, on a logarithmic scale, helped to visualize the bursty and delta-rhythmic spiking patterns of many neurons, particularly striatal ChI neurons.

4.10.11 Neuron classification based on ISI profile

We observed neurons had distinct ISI structures. Particularly, a subset of neurons exhibited strong delta-rhythmic (2–3Hz) spiking patterns. Other neurons had more regular spiking patterns. We also observed other spiking patterns, including theta bursting neurons (5–8Hz) and fast-spiking neurons, but due to their low number, they were not analyzed separately. All neurons that did not exhibit a clear delta-rhythmic spiking component constituted the non-delta group. To capture the different types of single neuron ISI curves systematically, we computed two ISI ratios (A-B/A+B) defined as: the number of spikes with ISIs of 300–700ms divided by the number of spikes with ISIs of 80–200ms (ISI ratio 1), or the number of spikes with ISIs of 10–40ms divided by the number of spikes with ISIs of 80–200ms (ISI ratio 2). The first ratio captured neurons with prominent ISI delta peaks, whereas the second ratio is a measure of burstiness. We found that neurons that were manually classified as having delta rhythmic ISIs could be well separated from other neurons using the ISI ratio 1. We thus defined neurons as delta-rhythmic spiking patterns which had a ISI ratio 1 of at least 0 or more. Most delta-rhythmic neurons spiked several times per cycle, however a few neurons only had one spike per cycle.

4.10.12 Spike-phase locking strength (PLS)

To quantify how consistent spikes occurred relative to the oscillation phase, we calculated the phase-locking value (PLV[303]) defined as:

$$PLV(f) = \left|\frac{1}{N}\right| \sum_{N} e^{i\emptyset(f,n)}$$

where f is frequency and N is the total number of spikes. The phase ϕ was obtained from the complex wavelet spectrum.

Since PLV is not independent of the number of spikes considered and tends to inflate with low numbers of spikes, we only included neurons that had at least 10 spikes for spike-PLV analysis. Further, we adjusted the PLV value using the following equation[304] to account for any potential differences in the number of spikes between groups of neurons, which we term here as phase locking strength (PLS):

$$PLS = \frac{1}{N-1}(PLV(f)^2 xN - 1)$$

where N is the number of spike occurrences and f is frequency.

4.10.13 Spike-triggered Vm and LFP spectrograms

All spectrograms were calculated with the FieldTrip toolbox (https://www.fieldtriptoolbox.org/) for MATLAB using the wavelet method (morlet wavelets). Spectrograms for each neuron were aligned to each spike and the time window 250ms before and after each spike was averaged to create a spike-triggered spectrogram per neuron (as in **Figure 4.7H**). Population spectrograms shown in **Figure 4.7I,J,L,M**,

Figure 4.8, Figure 4.10M–O, and **Figure 4.12** were created by averaging across the spike-triggered spectrograms for delta-rhythmic neurons, non-delta rhythmic neurons, SPN or ChI populations, respectively. For **Figure 4.12**, spectrograms were aligned only to spikes present in low movement or high movement periods, respectively and these spectrograms were subtracted to create those in **Figure 4.10M–O**. Spectrograms were normalized compared to the averaged pre-spike power between -200 to -100ms before the spike. The spectrogram in **Figure 4.7G** was created using the wavelet method on the corresponding spike Vm trace shown. **Figure 4.7K,N** display the power ratio between the time point of spike occurrence and the pre-spike period (-200ms to -100ms before the spike) at beta frequency (20-40Hz). Only neurons with a minimum number of 20 triggered windows were included in the analysis.

4.10.14 Statistics

Unless otherwise specified, all between-group statistics in bar plots (**Figure 4.4N,O, Figure 4.7C,F**) were conducted using a two-sample independent student t-test. For within group statistics (**Figure 4.7K,N** and **Figure 4.10D,H,L,P**), a one-sample student t-test was used. A p-value threshold of $p \leq 0.05$ was used to determine significance. **Figure 4.7K,N** and **Figure 4.10P** are compared to the pre-spike condition -200 to -100ms before the spike. Statistics in **Figure 4.10D,H** are between the low movement and high movement periods or the pre- and post-transition periods, respectively. Neurons that did not meet criteria for sufficient numbers of spikes, low vs. high movement periods, or movement transitions were excluded from relevant statistical analyses.

4.10.15 Spike raster plot

For an example neuron in **Figure 4.10E**, the spike timing was plotted per trial as compared to movement onset. The average spike rate was then calculated across all onsets for the neuron.

4.10.16 Movement onset and offset triggered spike rate

Movement onset and offset transition points were defined as above. For each neuron, average spike rate across one second time windows (500ms before and after each transition) was calculated in 100ms intervals and averaged across all onset or offset transitions per neuron, respectively. Population spike rate plots shown in **Figure 4.10F,G** and **Figure 4.11** were created by averaging across spike rates for the delta-rhythmic, non-delta rhythmic, SPN and ChI populations, respectively. To determine the statistical significance of these movement-triggered spike rates compared to chance, shuffling was used. For each neuron, the same number of points as the number of onset transition points were randomly selected. One second time windows (500ms before and after each transition) around these random transition points were concatenated across all transitions. The windows across neurons were concatenated and an average across these windows was calculated. Then, the average spike rate was calculated as the moving mean over a sliding window of 100 ms. This shuffling was done 1000 times to build a basal distribution of average spike rates. The actual metric from observation was also calculated in the same manner using the identified onset transition points. If the calculated movement triggered spike rate exceeded the 97.5^{th} percentile or was lower than the 2.5^{th} percentile (equivalent

to being beyond 2 standard deviations), then the spike rate was deemed to be significant and the p value was calculated. Significance was determined if a spike rate exceeded ± 2 standard deviations above or below the shuffled chance value.

4.10.17 Data exclusions

Voltage imaging datasets with significant image motion, with no spikes detected, or a median spike SBR of less than 5.5 were excluded from analysis. Significant motion was defined by thresholding the combined rectified X-Y derivative of the image motion. Any motion crossing the threshold of 0.2μm/ms was classified as motion-affected data. Data exclusion criteria were not pre-established.

4.10.18 Histology

Mice were transcardially perfused with PBS followed by 4% paraformaldehyde. The brain was gently extracted from the skull and post-fixed in 4% paraformaldehyde for 1-4 hours at room temperature or overnight at +4^{o}C. Fixed brains were transferred to a 1% polyvinylpyrrolidone (PVP-40), 30% sucrose, 30% ethylene glycol PBS-based solution and stored at 4C[305]. Before slicing, brains were moved to 30% sucrose-PBS solution and rotated 24-48 hours at 4C to allow cryoprotectant solution to diffuse out. Brains were sliced (coronally) to a 50μm thickness using a freezing microtome. Staining of SPNs was performed with primary antibody rabbit anti-DARPP-32 (1:500, Abcam ab40801 [EP720Y]), followed by the secondary antibody AlexaFluor568 (1:500, goat anti-rabbit

IgG, Invitrogen A11011). All antibodies were used according to protocols that have been validated by suppliers. Slice imaging was performed using an Olympus FV3000 scanning confocal microscope equipped with 405, 488, 561, and 640nm solid state diode lasers and a 20× NA0.45 air objective lens (LUCPLFN20X; Olympus), controlled by Fluoview FV31-SW software. Acquired images were analyzed in Fiji/ImageJ.

5 CONCLUSION

5.1 Summary & Significance

In this dissertation, we optimized a high-performance, genetically-encoded voltage sensor in multiple electrically active systems to enable *in vivo* population voltage imaging with single cell-, single spike precision. We also applied this optimized sensor to the striatum to investigate circuits underlying motor behavior and oscillatory activity.

In Chapter 2, we demonstrate that Archon1 can monitor cardiac action potentials in iPSC-derived cardiomyocytes in 2D monolayers and engineered 3D tissues. Our results highlight that Archon1 is capable of robustly reporting action potential dynamics under a variety of conditions, including when exposed to electrical pacing and ion channel inhibitors, and has comparable sensitivity and time resolution to patch-clamp electrophysiology, the current gold standard in the field, while outperforming commonly used voltage-sensitive dyes. The genetically-encoded nature of Archon1 and compatibility with a Cre-recombinase system allowed us to image the same cells weeks post-infection and enabled optical isolation of CMs within a complex 3D tissue environment, which could be translatable to imaging of whole heart slices or cardiac tissue in Cre-transgenic animals. Finally, we were able to measure the membrane potential of multiple cells simultaneously in both 2D culture and 3D tissue environments, highlighting the possibility of population studies while retaining single-cell precision, such as for measurement of conduction velocity and AP propagation, as well as intercellular phase-locking or phase delay.

In Chapter 3, we achieved a longstanding goal in neuroscience: to image membrane voltage across a population of individual neurons in an awake, behaving mammal. Using the somatically-localized variant of Archon1, SomArchon, we could detect both spiking and subthreshold dynamics in multiple brain regions of awake, behaving animals as well as routinely record populations of 15 neurons simultaneously with high spatiotemporal precision. In addition, by genetically fusing SomArchon to the high-performance channelrhodopsin, CoChR, we could perform all-optical electrophysiology, with simultaneous monitoring and control of membrane dynamics. Furthermore, SomArchon outperformed many of the other available next-generation sensors, while being fully genetically encoded and compatible with conventional one-photon microscopy, making it an easily adaptable tool to diverse contexts in neuroscience.

In Chapter 4, we deployed the newly-developed SomArchon to the dorsal striatum and revealed a relationship between subthreshold delta frequency oscillations and their associated spiking, bulk LFP dynamics, and movement. We found that a majority of ChIs and a subset of SPNs demonstrated spike bursting behavior aligned to subthreshold delta frequency oscillations. These delta-rhythmic neurons' spiking was coupled to LFP delta oscillations, as well as higher frequency Vm and LFP beta oscillations, indicating the ability of these neurons to synchronize striatal networks, measurable by LFP dynamics. Finally, we demonstrated that delta-rhythmic neuron spiking is uniquely linked to high movement periods and movement transitions. During high movement, delta-rhythmic ChIs' spiking activity in particular was more locked to LFP delta and gamma rhythms,

suggesting that ChIs may be synchronizing large striatal networks. In total, these results highlight a prominent role of subthreshold delta oscillations to organize spike output and larger-scale LFP dynamics and the unique contribution of ChIs to movement-related oscillation features, unlocking a greater understanding of basal ganglia neural circuitry.

5.2 Future Directions

Through this dissertation, we have demonstrated voltage imaging as a powerful tool for investigating membrane voltage dynamics of electrically active systems. While Archon1 and SomArchon both outperformed many of the leading competitors in the field, there is still room for genetic engineering techniques to improve features such as brightness, SNR, and photostability. As further evolution of GEVIs continues alongside improvements in camera performance, we anticipate that the voltage dynamics of dozens to hundreds of cells will be imageable with simple one-photon optics in the near future.

The genetically encoded nature of these GEVIs additionally make them useful tools for longer duration studies of disease mechanisms, such as detecting arrhythmias or tracking pathological regression of spiking or oscillatory dynamics. In addition, while these studies used AAV-mediated delivery, lentiviral particles could be developed to create stable cell or mouse lines expressing SomArchon for a variety of applications.

Although we did not take advantage of this utility here, as far-red indicators, Archon1 and SomArchon are compatible with green calcium indicators such as GCaMP. These two

molecules could be used together for simultaneous, multicolor imaging of voltage and calcium dynamics, which could answer important questions about the relationship between calcium transients and spiking, as well as enable studies of diseases like Timothy syndrome or heart failure where both voltage dynamics and calcium handling are affected[220-223]. In addition, as we demonstrated, SomArchon can be used in conjunction with blue light-driven optogenetics. Using this feature to further investigate the relationship between striatal neurons, one could precisely control the voltage dynamics of ChIs and monitor the effect on surrounding SPNs, as well as on LFP oscillations and downstream movement.

Furthermore, while we focused on ChIs and SPNs in this work, several other important interneurons exist in the striatum, such as parvalbumin (PV) interneurons or somatostatin (SST) neurons, which may play a role in shaping striatal dynamics. As mentioned in Chapter 1, SPNs are often characterized into two groups (D1s and D2s), which may have different relationships to downstream movement. Future work could also investigate differences between D1- and D2-SPNs and their relationship with ChIs and other interneurons during behavior. Finally, similar voltage imaging analysis could be performed in disease models, such as the 6-OHDA mediated Parkinsonian model, to monitor the dynamics of neurons during different stages of disease progression, as has been previously done in calcium studies[285]. Such work could provide strategies for disease intervention and therapy, as well as open the door for future voltage imaging analysis of a variety of electrical circuits involved in behavioral and pathological paradigms.

6 APPENDIX: SUPPLEMENTARY TABLES FOR CHAPTER 3

6.1 Statistical Tables

Table 6.1. Two-sample Kolmogorov-Smirnov (K-S) tests comparing fluorescence intensity of Archon1 vs. SomArchon at different positions along neurites in cortex, hippocampus, and striatum. Related to Figure 3.1.

Distance along neurite from soma (μm)	**Cortex** p-value	**Hippocampus** p-value	**Striatum** p-value
5	0.0006	0.1543	0.1103
10	0.1451	1.54E-05	0.1672
15	0.0973	0.0007	0.5598
20	1.43E-05	5.83E-05	0.1542
25	3.81E-08	3.74E-06	0.0011
30	1.54E-09	2.53E-07	8.34E-05
35	1.22E-13	6.37E-08	5.48E-07
40	5.06E-15	6.37E-08	5.48E-07
45	3.14E-16	1.16E-08	1.65E-09
50	7.69E-16	1.73E-08	5.48E-07
55	4.91E-18	2.97E-09	1.27E-08
60	6.44E-17	5.89E-11	1.65E-09
65	8.50E-18	1.26E-11	1.65E-09
70	3.83E-17	2.59E-12	8.12E-07
75	3.83E-17	2.59E-12	1.96E-07
80	2.38E-17	2.59E-12	3.80E-08
85	3.30E-16	2.78E-11	6.90E-08
90	1.08E-15	2.78E-11	1.08E-08
95	1.19E-13	1.42E-11	1.30E-07
100	2.75E-12	4.42E-11	4.56E-08

Table 6.2. Two-sided Wilcoxon Rank Sum test for Figure 3.2e between electrical and optical FWHM (full width, half maximum) of SomArchon-expressing neurons in mouse brain slices

FWHM	**Cortex**
p-value	0.0010
Wilcoxon rank sum statistic	131

FWHM	**Hippocampus**
p-value	0.0019
Wilcoxon rank sum statistic	40

FWHM	**Striatum**
p-value	0.0411
Wilcoxon rank sum statistic	26

Table 6.3. Two-sided Wilcoxon Rank Sum test for membrane resistance of SomArchon- vs. Archon1-expressing or non-expressing neurons in mouse brain slices for Figure 3.4a–c

Membrane Resistance	**Cortex**
p-value	0.8026
Wilcoxon rank sum statistic	103

Membrane Resistance	**Hippocampus**
p-value	0.6294
Wilcoxon rank sum statistic	68.5

Membrane Resistance	**Striatum**
p-value	0.7308
Wilcoxon rank sum statistic	52

Table 6.4. Two-sided Wilcoxon Rank Sum test for the membrane capacitance of SomArchon- vs. Archon-expressing or non-expressing neurons in mouse brain slices for Figure 3.4a–c

Membrane Capacitance	**Cortex**
p-value	0.8895
Wilcoxon rank sum statistic	111

Membrane Capacitance	**Hippocampus**
p-value	0.9720
Wilcoxon rank sum statistic	52

Membrane Capacitance	**Striatum**
p-value	0.8357
Wilcoxon rank sum statistic	51

Table 6.5. Two-sided Wilcoxon Rank Sum test for the resting potential of SomArchon- vs. Archon-expressing or non-expressing neurons in mouse brain slices for Figure 3.4a–c

Resting Potential	**Cortex**
p-value	0.8236
Wilcoxon rank sum statistic	103.5

Resting Potential	**Hippocampus**
p-value	0.8880
Wilcoxon rank sum statistic	65.5

Resting Potential	**Striatum**
p-value	0.7751
Wilcoxon rank sum statistic	39.5

Table 6.6. Two-sided Wilcoxon Rank Sum test for the full width half maximum (FWHM) per action potential of SomArchon-expressing vs. non-expressing neurons in mouse brain slices for Figure 3.4b,c.

FWHM	**Hippocampus**
p-value	0.0037
Wilcoxon rank sum statistic	32
FWHM	**Striatum**
p-value	0.0931
Wilcoxon rank sum statistic	28

Table 6.7. Two-sided Wilcoxon Rank Sum test for Figure 3.6c, ΔF/F of SomArchon vs. ASAP3-Kv, Voltron-ST, QuasAr3-s, and paQuasAr3-s in mouse brain slices

ΔF/F	**ASAP3-Kv**
p-value	6.75×10^{-6}
Wilcoxon rank sum statistic	178

ΔF/F	**Voltron-ST**
p-value	9.25×10^{-6}
Wilcoxon rank sum statistic	106

ΔF/F	**QuasAr3-s**
p-value	0.0022
Wilcoxon rank sum statistic	59

ΔF/F	**paQuasAr3-s**
p-value	0.0045
Wilcoxon rank sum statistic	123

Table 6.8. Two-sided Wilcoxon Rank Sum test for Figure 3.6d, SNR tested in mouse brain slices, between SomArchon ASAP3-Kv, Voltron-ST, QuasAr3-s, and paQuasAr3-s

SNR	**ASAP3-Kv**
p-value	0.0029
Wilcoxon rank sum statistic	218

SNR	**Voltron-ST**
p-value	0.1753
Wilcoxon rank sum statistic	173

SNR	**QuasAr3-s**
p-value	$1.07x10^{-4}$
Wilcoxon rank sum statistic	46

SNR	**paQuasAr3-s**
p-value	0.1667
Wilcoxon rank sum statistic	153

Table 6.9. Two-sided Wilcoxon Rank Sum test for Figure 3.10f comparing striatal neurons' firing rate during periods of low speed movement vs. high speed movement

Cell	**p-value**	**Wilcoxon rank sum statistic**	**zval**
1	0.583	698.5	0.5497
2	0.072	451	-1.7989
3	0.043	417.5	-2.0238
4	2.27E-07	3303	-5.176
5	7.23E-05	2359	3.9684
6	0.525	1071	-0.6359
7	0.655	1086	-0.4468
8	0.0012	865.5	-3.228
9	0.815	1084.5	0.2336
10	0.219	1418.5	1.228
11	0.144	1075	-1.4617
12	0.0015	7239	3.1753
13	0.782	1296.5	-0.2768
14	1.32E-04	-3.8227	920.5

Table 6.10. χ^2 test for neurons included in Figure 3.11a–d testing against the null hypothesis of a uniform distribution. DOF is degrees of freedom.

	LFP			V_{mo}		
Cell #	**p-value**	**χ^2 test statistic**	**DOF**	**p-value**	**χ^2 test statistic**	**DOF**
1	1.58E-07	64.925	17	1.10E-07	65.849	17
2	0.0557	27.168	17	6.23E-40	232.946	17
3	0.619	14.670	17	2.23E-29	180.564	17
4	0.00117	40.308	17	4.14E-171	856.475	17
5	0.12	23.983	17	1.67E-49	279.756	17
6	0.51	16.190	17	1.72E-31	191.132	17
7	0.271	20.064	17	3.66E-20	133.677	17
8	0.618	14.688	17	1.11E-04	47.280	17
9	0.643	14.340	17	7.73E-13	94.909	17
10	0.718	13.263	17	3.92E-02	28.526	17
11	0.0263	30.000	17	1.14E-08	71.596	17
12	4.54E-06	56.109	17	1.00E-10	83.263	17
13	2.23E-34	205.508	17	2.40E-165	829.457	17
14	0.0636	26.641	17	5.47E-02	27.237	17
15	2.87E-05	51.073	17	1.46E-22	146.035	17
16	0.891	10.283	17	4.57E-04	43.146	17

Tables 6.11. Repeated measures ANOVA for Figure 3.12.

Striatum Intensity	
p-value	0.023217
F	3.5861

post hoc Tukey's HSD test					
Trial	**1**	**2**	**3**	**4**	**5**
1		0.979088	0.600956	0.515978	0.36467
2	0.979088		0.440704	0.401273	0.214062
3	0.600956	0.440704		0.901844	0.003871
4	0.515978	0.401273	0.901844		0.1066
5	0.36467	0.214062	0.003871	0.1066	

Striatum SNR					
p-value			0.63726		
F			0.64431		
post hoc Tukey's HSD test					
Trial	**1**	**2**	**3**	**4**	**5**
1		0.907207	0.958312	0.999869	0.982537
2	0.907207		0.576767	0.705478	0.617842
3	0.958312	0.576767		0.831883	0.997305
4	0.999869	0.705478	0.831883		0.931505
5	0.982537	0.617842	0.997305	0.931505	

Striatum Firing Rate	
p-value	0.83742
F	0.35511

post hoc Tukey's HSD test					
Trial	**1**	**2**	**3**	**4**	**5**
1		0.055919	0.882805	1	0.98906
2	0.055919		0.999996	0.991153	0.944225
3	0.882805	0.999996		0.996383	0.95811
4	1	0.991153	0.996383		0.804642
5	0.98906	0.944225	0.95811	0.804642	

Hippocampus Intensity	
p-value	3.44E-22
F	21.491

post hoc Tukey's HSD test										
Trial	**1**	**2**	**3**	**4**	**5**	**6**	**7**	**8**	**9**	**10**
1		0.001593	0.04591	0.574795	0.688343	0.999087	1	1	0.93142	0.580117
2	0.001593		0.012262	2.57E-06	9.58E-05	9.54E-05	1.50E-05	0.000104	0.000122	0.000486
3	0.04591	0.012262		0.061443	0.000648	0.001063	8.37E-06	0.000308	0.000151	0.000585
4	0.574795	2.57E-06	0.061443		0.999964	0.923573	0.144261	0.223195	0.053445	0.055324
5	0.688343	9.58E-05	0.000648	0.999964		0.860278	0.004366	0.028524	0.004819	0.009799
6	0.999087	9.54E-05	0.001063	0.923573	0.860278		0.556941	0.270504	0.017902	0.040012
7	1	1.50E-05	8.37E-06	0.144261	0.004366	0.556941		0.95185	0.038815	0.102821
8	1	0.000104	0.000308	0.223195	0.028524	0.270504	0.95185		0.007861	0.14383
9	0.93142	0.000122	0.000151	0.053445	0.004819	0.017902	0.038815	0.007861		0.684809
10	0.580117	0.000486	0.000585	0.055324	0.009799	0.040012	0.102821	0.14383	0.684809	

Hippocampus SNR	
p-value	2.74E-17
F	15.65

post hoc Tukey's HSD test										
Trial	**1**	**2**	**3**	**4**	**5**	**6**	**7**	**8**	**9**	**10**
1		0.000291	0.000278	0.002971	1.02E-05	0.002021	0.000753	0.000878	0.000441	0.000109
2	0.000291		1	0.97404	0.999693	0.999988	0.999997	1	0.999996	0.947458
3	0.000278	1		0.455752	0.999813	1	0.999999	1	0.999994	0.878177
4	0.002971	0.97404	0.455752		0.343328	0.872355	0.453222	0.304404	0.176835	0.179375
5	1.02E-05	0.999693	0.999813	0.343328		1	1	0.999487	1	0.762035
6	0.002021	0.999988	1	0.872355	1		1	1	1	0.981192

7	0.000753	0.999997	0.999999	0.453222	1	1		0.999909	1	0.936697
8	0.000878	1	1	0.304404	0.999487	1	0.999909		0.99915	0.581095
9	0.000441	0.999996	0.999994	0.176835	1	1	1	0.99915		0.584717
10		0.000291	0.000278	0.002971	1.02E-05	0.002021	0.000753	0.000878	0.000441	0.000109

Hippocampus firing rate	
p-value	0.38894
F	1.07

post hoc Tukey's HSD test										
Trial	**1**	**2**	**3**	**4**	**5**	**6**	**7**	**8**	**9**	**10**
1		0.921965	0.944598	0.996829	0.70055	0.907368	0.992801	0.944117	0.959096	0.999999
2	0.921965		0.999999	1	0.994524	1	0.999985	1	1	0.973125
3	0.944598	0.999999		0.999876	0.999961	1	0.995943	0.999998	0.999875	0.896394
4	0.996829	1	0.999876		0.946252	0.99998	1	1	1	0.883532
5	0.70055	0.994524	0.999961	0.946252		0.991271	0.883536	0.986476	0.874771	0.601617
6	0.907368	1	1	0.99998	0.991271		0.995514	0.999999	0.999564	0.940647
7	0.992801	0.999985	0.995943	1	0.883536	0.995514		0.999995	0.999999	0.995133
8	0.944117	1	0.999998	1	0.986476	0.999999	0.999995		0.999999	0.951565
9	0.959096	1	0.999875	1	0.874771	0.999564	0.999999	0.999999		0.936649
10	0.999999	0.973125	0.896394	0.883532	0.601617	0.940647	0.995133	0.951565	0.936649	

Hippocampus spike amplitude	
p-value	9.9361e-07
F	5.7382

post hoc Tukey's HSD test										
Trial	**1**	**2**	**3**	**4**	**5**	**6**	**7**	**8**	**9**	**10**
1		0.28304	0.68783	0.68004	0.99142	1	0.99999	0.99998	0.99643	0.99777
2	0.28304		0.46636	0.99993	0.049266	0.020181	0.00056424	0.00079058	4.7664e-05	0.973
3	0.68783	0.46636		0.98407	0.41356	0.071376	0.0015959	0.0010367	4.797e-05	0.99967
4	0.68004	0.99993	0.98407		0.031141	0.022343	0.0013281	0.00019081	2.2154e-05	0.9435
5	0.99142	0.049266	0.41356	0.031141		0.51441	0.019361	0.0057928	0.0012401	1
6	1	0.020181	0.071376	0.022343	0.51441		0.11384	0.05668	0.061031	0.98715
7	0.99999	0.00056424	0.0015959	0.0013281	0.019361	0.11384		1	0.87884	0.79075
8	0.99998	0.00079058	0.0010367	0.00019081	0.0057928	0.05668	1		0.68336	0.63414
9	0.99643	4.7664e-05	4.797e-05	2.2154e-05	0.0012401	0.061031	0.87884	0.68336		0.4607
10	0.99777	0.973	0.99967	0.9435	1	0.98715	0.79075	0.63414	0.4607	

Hippocampus noise	
p-value	3.1718e-08
F	6.9714

post hoc Tukey's HSD test										
Trial	**1**	**2**	**3**	**4**	**5**	**6**	**7**	**8**	**9**	**10**
1		0.00035545	0.010149	0.0058873	0.0020157	0.022518	0.31433	0.10414	0.098306	0.011564
2	0.00035545		0.46828	0.029797	0.2885	9.255e-05	0.9993	0.090932	0.030078	0.70542
3	0.010149	0.46828		0.99018	0.99993	0.9636	1	0.95964	0.75254	0.39425
4	0.0058873	0.029797	0.99018		0.99932	1	0.99893	1	0.99922	0.22413
5	0.0020157	0.2885	0.99993	0.99932		0.99972	0.99983	0.99927	0.86987	0.18828
6	0.022518	9.255e-05	0.9636	1	0.99972		0.99824	1	0.99486	0.28566
7	0.31433	0.9993	1	0.99893	0.99983	0.99824		0.97896	0.89708	0.60837
8	0.10414	0.090932	0.95964	1	0.99927	1	0.97896		0.99913	0.2488
9	0.098306	0.030078	0.75254	0.99922	0.86987	0.99486	0.89708	0.99913		0.22088
10	0.011564	0.70542	0.39425	0.22413	0.18828	0.28566	0.60837	0.2488	0.22088	

Tables 6.12. One-way ANOVA for Figure 3.14

Note: groups of 50–60 μm and 60–70 μm only contain one data point each and therefore were excluded.

Neuron pairs coherence at theta frequency	
p-value	0.2638
F	1.44

post hoc Tukey's HSD test		
Distance 1 (μm)	**Distance 2 (μm)**	**p-value**
10–20	20–30	0.6252
10–20	30–40	0.2059
10–20	40–50	0.8327
20–30	30–40	0.6801
20–30	40–50	0.9960
30–40	40–50	0.6801

Neuron pairs coherence at gamma frequency	
p-value	0.1338
F	2.1

post hoc Tukey's HSD test		
Distance 1 (μm)	**Distance 2 (μm)**	**p-value**
10–20	20–30	0.9766
10–20	30–40	0.2314
10–20	40–50	0.9997
20–30	30–40	0.2387
20–30	40–50	0.9558
30–40	40–50	0.1978

Neuron pairs correlation	
p-value	0.4351
F	1.00

post hoc Tukey's HSD test		
Distance 1 (μm)	**Distance 2 (μm)**	**p-value**
10–20	20–30	0.7305
10–20	30–40	0.4389
10–20	40–50	0.4670
20–30	30–40	0.8979
20–30	40–50	0.8930
30–40	40–50	0.9997

Donut pairs coherence at theta frequency	
p-value	0.592
F	0.65

post hoc Tukey's HSD test		
Distance 1 (μm)	**Distance 2 (μm)**	**p-value**
10–20	20–30	0.9777
10–20	30–40	0.9855
10–20	40–50	0.8993
20–30	30–40	0.7781
20–30	40–50	0.5735
30–40	40–50	0.9706

Donut pairs coherence at gamma frequency	
p-value	0.1632
F	1.93

post hoc Tukey's HSD test		
Distance 1 (μm)	**Distance 2 (μm)**	**p-value**
10–20	20–30	0.9834
10–20	30–40	0.3051
10–20	40–50	0.4829
20–30	30–40	0.2604
20–30	40–50	0.5048
30–40	40–50	0.9942

Donut pairs correlation	
p-value	0.4086
F	1.02

post hoc Tukey's HSD test		
Distance 1 (μm)	**Distance 2 (μm)**	**p-value**
10–20	20–30	0.9668
10–20	30–40	0.9775
10–20	40–50	0.7918
20–30	30–40	0.6934
20–30	40–50	0.3725
30–40	40–50	0.9121

6.2 Comparison of screened variants and competing next-generation soma-targeted voltage sensors

Table 6.13. Characteristics of screened soma-localized Archon1 variants

Full name of construct	**How far from the soma, approximately, was the fluorescence detected using visual inspection, in this study?**	**Membrane/cytoplasmic localization detected using visual inspection in near-infrared channel, in this study**	**Voltage sensitivity***
Archon1-linker-KA2(1-150)-EGFP	50–100 μm	Cytoplasmic with bright puncta in soma	Non-functional
Archon1-linker-KA2(1-100)-EGFP	50–100 μm	Cytoplasmic with bright puncta in soma	Non-functional
KA2(1-150)-linker-Archon1-EGFP	50–100 μm	Cytoplasmic with bright puncta in soma	Non-functional
Archon1-KGC-EGFP-$Na_V1.2$(II-III)-ER2	80–100 μm	Membrane with significant aggregation in soma	Not measured
Archon1-KGC-EGFP-$Na_V1.6$(II-III)-ER2	30–60 μm	Membrane with no aggregation	12% of ΔF/F per 100 mV voltage step
Archon1-KGC-EGFP-$K_V2.1$-motif-ER2 (SomArchon)	20–40 μm	Membrane with no aggregation	30% of ΔF/F per 100 mV voltage step
Archon1-KGC-EGFP-AnkMB(270)-motif-ER2	>100 μm	Cytoplasmic with bright puncta in soma	Non-functional
Archon1-KGC-EGFP-AnkMB(490)-motif-ER2	>100 μm	Cytoplasmic with bright puncta in soma	Non-functional
Archon1-KGC-EGFP-AnkSB-motif-ER2	>100 μm	Cytoplasmic with bright puncta in soma	Non-functional

Archon1-KGC-EGFP-AnkCt-motif-ER2	50–70 μm	Membrane with minor aggregation in soma	15% of ΔF/F per 100 mV voltage step
Archon1-KGC-EGFP-AnkSR-motif-ER2	40–60 μm	Membrane with minor aggregation in soma	15% of ΔF/F per 100 mV voltage step
Archon1-KGC-EGFP-AnkTail-motif-ER2	>100 μm	Cytoplasmic with bright puncta in soma	Non-functional

*voltage sensitivity was quantified by whole-cell patch clamp in cultured neurons

Table 6.14. Performance of genetically encoded fluorescent voltage sensors in mouse brain tissues and live mice

Sensor	Ex (nm)	Em (nm)	ΔF/F per AP (%)		SNR per AP		On kinetics[a] (ms)	Off kinetics[a] (ms)	Max reported # of simultaneously imaged neurons *in vivo*	Ref
			Slice	*In vivo*	Slice	*In vivo*				
MacQ-Citrine	516	529	-2.5 in neocortical pyramidal neurons, -0.5 in PV interneurons	-1.5 Purkinje neurons	6 in neocortical pyramids, 2 in PV interneurons at 30mW/mm^2, 440Hz camera frame rate	5–10[b] Purkinje neurons at 10mW/mm^2, 190Hz	2.8 (74)/71 measured in HEK cells at 22ºC	5.4 (77)/67 measured in HEK cells at 22ºC	2 (Cerebellar Purkinje neuron dendrites only)	207,306
Ace2N-4AA-mNeon	506	517	-6.5 in cortex L2/3	-3 in cortex L2/3	ND	5–10[b] in visual cortex L2/3 at 25mW/mm^2, 1kHz	0.37 (58)/5.5 measured in HEK cells at 22ºC	0.5 (60)/5.9 measured in HEK cells at 22ºC	2 (L2/3 primary visual cortex)	188
QuasAr2	637	700	15 in hippocampus	nd	8.5 in hippocampal neurons at 8W/mm^2, 1kHz	nd	0.3 (62)/3.2 in HEK cells at 34 ºC	0.3/(73) 4.0 in HEK cells at 34 ºC	nd	181,208
QuasAr3	637	700	14 in cortex L2/3[c]	nd	6.4 in cortical neurons at 1.5W/mm2, 500Hz[c]	nd	1.2 (77)/10 in HEK cells at 34ºC	0.87 (91)/9 in HEK cells at 34ºC	nd	97
paQuasAr3	637	700	23 in cortex L2/3[c]	nd	28 in cortical neurons at 1.5W/mm2, 500Hz[c]	nd	0.9 (57)/15 in HEK cells at 34ºC	0.93 (79)/15 in HEK cells at 34ºC	4 spiking, 6 non-spiking (pyramidal cell layer hippocampus),	97

ASAP3	900-920 (2P)		-10 in L2/3 cortex under 1P at 500Hz[c]; -17 in hippocampus under 2P, -8.3 in cerebellar molecular layer interneurons, -37.3 in striatum under 2P and 1kHz	-9 in cortex L1 and L2/3 under 2P	2.6 in striatum under 2P and 1kHz; 19 in L2/3 cortex at 25mW/mm^2 at 500Hz[c]	nd	0.94 (72)/7.2 measured in HEK cells at 33–35^{o}C	3.8 (76)/16 measured in HEK cells at 33–35^{o}C	1 (primary visual cortex L1 and L2/3), 3 (primary visual cortex L5 apical dendrites)	[207]
Voltron$_{525}$	525	549	-6.5 in L2/3 cortex[c]	~-5-10 in visual cortex and PV interneurons in hippocampus[b], ~-0.5-3 in layer 1 visual cortex interneuron population[b]	27 in L2/3 of cortex at 29mW/mm^2 500 Hz[c]	4.4 at 3–20mW/mm^2 400Hz	0.64 (61)/4.1 neuronal culture temp not reported	0.78 (55)/3.9 neuronal culture at 34^{o}C	46 (primary visual cortex)	[206]
SomArchon	637	700	53 in cortex L2/3; 37 in hippocampus; 26 in striatum;	nd	37 in cortex L2/3 at 1.5W/mm^2, 500Hz; 20 in hippocampus at 1.5W/mm^2, 1kHz 27 in striatum at 1.5W/mm^2 at 1kHz	7 in motor cortex at 1.6W/mm^2, 7 in visual cortex at 1.6W/mm^2, 12 in striatum at 4W/mm^2, 16 in hippocampus at 4W/mm^2	0.61 (88)/8.1[d] neuronal culture at 34^{o}C	1.1 (88)/13[d] neuronal culture at 34^{o}C	18 (CA1 hippocampus)	[202]

Ex – excitation wavelength;
Em – emission wavelength;
nd – not determined;
[a]voltage kinetics evaluated by bi-exponential fitting (in the format fast/slow), where the value in parentheses represents the % of current magnitude in the fast τ component; [b]estimated from traces presented in the indicated paper; [c]data from this study measured for soma localized version of the sensors QuasAr3, paQuasAr3, Voltron$_{525}$, ASAP3, see **Figure 3.6** for details; [d]data from ref[183,202]. Sensors with negative ΔF/F values are negative-going (fluorescence decreases with membrane voltage increases).

6.3 Additional Tables

Table 6.15. Number of manually selected neurons during *in vivo* population imaging in the hippocampus of awake mice

FOV	Neuron #	Spiking Neuron #	Session duration (s)	Acquisition Freq. (Hz)
Mouse1_FOV1	15	8	27	741
Mouse1_FOV2	9	8	27	741
Mouse1_FOV3	18	10	27	741
Mouse1_FOV4	11	9	27	741
Mouse1_FOV5	15	11	27	741
Mouse1_FOV6	18	12	27	741
Mouse1_FOV7	11	6	13.5	741
Mouse2_FOV1	12	8	24.2	826
Mouse2_FOV2	6	4	24.2	826
Mouse2_FOV3	11	9	24.2	826
Mouse2_FOV4	15	9	24.2	826
Mouse2_FOV5	14	7	24.2	826
Mouse2_FOV6	15	6	24.2	826

BIBLIOGRAPHY

1 Wenning, G. K. *et al.* Prevalence of movement disorders in men and women aged 50–89 years (Bruneck Study cohort): a population-based study. *Lancet. Neurology* **4**, 815–820, doi:10.1016/S1474-4422(05)70226-X (2005).

2 Bach, J. P., Ziegler, U., Deuschl, G., Dodel, R. & Doblhammer-Reiter, G. Projected numbers of people with movement disorders in the years 2030 and 2050. *Movement Disorders* **26**, 2286–2290, doi:10.1002/mds.23878 (2011).

3 Kowal, S. L., Dall, T. M., Chakrabarti, R., Storm, M. V. & Jain, A. The current and projected economic burden of Parkinson's disease in the United States. *Movement Disorders* **28**, 311–318, doi:10.1002/mds.25292 (2013).

4 Armstrong, M. J. & Okun, M. S. Diagnosis and Treatment of Parkinson Disease: A Review. *JAMA: The Journal of the American Medical Association* **323**, 548–560, doi:10.1001/jama.2019.22360 (2020).

5 Cloud, L. J. & Jinnah, H. A. Treatment strategies for dystonia. *Expert Opinion on Pharmacotherapy* **11**, 5–15, doi:10.1517/14656560903426171 (2010).

6 Espay, A. J. *et al.* Current Concepts in Diagnosis and Treatment of Functional Neurological Disorders. *JAMA Neurology* **75**, 1132–1141, doi:10.1001/jamaneurol.2018.1264 (2018).

7 Gelauff, J. M., Dreissen, Y. E., Tijssen, M. A. & Stone, J. Treatment of functional motor disorders. *Current Treatment Options in Neurology* **16**, 286, doi:10.1007/s11940-014-0286-5 (2014).

8 Armstrong, M. J. & Okun, M. S. Choosing a Parkinson Disease Treatment. *JAMA: The Journal of the American Medical Association* **323**, 1420, doi:10.1001/jama.2020.1224 (2020).

9 Connolly, B. S. & Lang, A. E. Pharmacological treatment of Parkinson disease: a review. *JAMA: The Journal of the American Medical Association* **311**, 1670–1683, doi:10.1001/jama.2014.3654 (2014).

10 Ehrt, U., Broich, K., Larsen, J. P., Ballard, C. & Aarsland, D. Use of drugs with anticholinergic effect and impact on cognition in Parkinson's disease: a cohort study. *Journal of Neurology, Neurosurgery, & Psychiatry* **81**, 160–165, doi:10.1136/jnnp.2009.186239 (2010).

11 Lees, A. J. Drugs for Parkinson's disease. *Journal of Neurology, Neurosurgery, & Psychiatry* **73**, 607–610 (2002).

12 Olanow, C. W. & Koller, W. C. An algorithm (decision tree) for the management of Parkinson's disease: treatment guidelines. American Academy of Neurology. *Neurology* **50**, S1–57 (1998).

13 Savitt, J. M., Dawson, V. L. & Dawson, T. M. Diagnosis and treatment of Parkinson disease: molecules to medicine. *Journal of Clinical Investigation* **116**, 1744–1754, doi:10.1172/JCI29178 (2006).

14 Bronstein, J. M. *et al.* Deep brain stimulation for Parkinson disease: an expert consensus and review of key issues. *Archives of Neurology* **68**, 165, doi:10.1001/archneurol.2010.260 (2011).

15 Nonnekes, J. *et al.* Unmasking levodopa resistance in Parkinson's disease. *Movement Disorders* **31**, 1602–1609, doi:10.1002/mds.26712 (2016).

16 Thanvi, B. R. & Lo, T. C. Long term motor complications of levodopa: clinical features, mechanisms, and management strategies. *Postgraduate Medical Journal* **80**, 452–458, doi:10.1136/pgmj.2003.013912 (2004).

17 Yamada, H., Momose, T., Okada, M. & Kuroiwa, Y. Anticholinergic drugs: response of parkinsonism not responsive to levodopa. *Journal of Neurology, Neurosurgery, & Psychiatry* **72**, 111–113, doi:10.1136/jnnp.72.1.111 (2002).

18 Lozano, A. M. *et al.* Deep brain stimulation: current challenges and future directions. *Nature Reviews: Neurology* **15**, 148–160, doi:10.1038/s41582-018-0128-2 (2019).

19 Albin, R. L., Young, A. B. & Penney, J. B. The functional anatomy of basal ganglia disorders. *Trends in Neurosciences* **12**, 366–375 (1989).

20 Penney, J. B., Jr. & Young, A. B. Striatal inhomogeneities and basal ganglia function. *Movement Disorders* **1**, 3–15, doi:10.1002/mds.870010102 (1986).

21 Mazzoni, P., Shabbott, B. & Cortes, J. C. Motor control abnormalities in Parkinson's disease. *Cold Spring Harbor Perspectives in Medicine* **2**, a009282, doi:10.1101/cshperspect.a009282 (2012).

22 Pinter, M. M., Helscher, R. J., Nasel, C. O., Riedl, E. & Schnaberth, G. Quantification of motor deficit in Parkinson's disease with a motor performance test series. *Journal of Neural Transmission: Parkinson's Disease and Dementia Section* **4**, 131–141 (1992).

23 DeLong, M. R. & Wichmann, T. Circuits and circuit disorders of the basal ganglia. *Archives of Neurology* **64**, 20–24, doi:10.1001/archneur.64.1.20 (2007).

24 Milardi, D. *et al.* The Cortico-Basal Ganglia-Cerebellar Network: Past, Present and Future Perspectives. *Frontiers in Systems Neuroscience* **13**, 61, doi:10.3389/fnsys.2019.00061 (2019).

25 Graybiel, A. M., Aosaki, T., Flaherty, A. W. & Kimura, M. The basal ganglia and adaptive motor control. *Science* **265**, 1826–1831, doi:10.1126/science.8091209 (1994).

26 Calabresi, P., Picconi, B., Tozzi, A., Ghiglieri, V. & Di Filippo, M. Direct and indirect pathways of basal ganglia: a critical reappraisal. *Nature Neuroscience* **17**, 1022–1030, doi:10.1038/nn.3743 (2014).

27 Simonyan, K. Recent advances in understanding the role of the basal ganglia. *F1000Res* **8**, doi:10.12688/f1000research.16524.1 (2019).

28 Wang, K. S., McClure, J. P., Jr., Alselehdar, S. K. & Kanta, V. Direct and indirect pathways of the basal ganglia: opponents or collaborators? *Frontiers in Neuroanatomy* **9**, 20, doi:10.3389/fnana.2015.00020 (2015).

29 Reig, R. & Silberberg, G. Multisensory integration in the mouse striatum. *Neuron* **83**, 1200–1212, doi:10.1016/j.neuron.2014.07.033 (2014).

30 Hunnicutt, B. J. *et al.* A comprehensive excitatory input map of the striatum reveals novel functional organization. *Elife* **5**, doi:10.7554/eLife.19103 (2016).

31 Atallah, H. E., McCool, A. D., Howe, M. W. & Graybiel, A. M. Neurons in the ventral striatum exhibit cell-type-specific representations of outcome during learning. *Neuron* **82**, 1145–1156, doi:10.1016/j.neuron.2014.04.021 (2014).

32 Daniel, R. & Pollmann, S. A universal role of the ventral striatum in reward-based learning: evidence from human studies. *Neurobiology of Learning & Memory* **114**, 90–100, doi:10.1016/j.nlm.2014.05.002 (2014).

33 Gottfried, J. A. & Haber, S. N. in *Neurobiology of Sensation and Reward Frontiers in Neuroscience* (ed J. A. Gottfried) (2011).

34 Haber, S. N. & Knutson, B. The reward circuit: linking primate anatomy and human imaging. *Neuropsychopharmacology* **35**, 4–26, doi:10.1038/npp.2009.129 (2010).

35 Pan, W. X., Mao, T. & Dudman, J. T. Inputs to the dorsal striatum of the mouse reflect the parallel circuit architecture of the forebrain. *Frontiers in Neuroanatomy* **4**, 147, doi:10.3389/fnana.2010.00147 (2010).

36 Johansson, Y. & Silberberg, G. The Functional Organization of Cortical and Thalamic Inputs onto Five Types of Striatal Neurons Is Determined by Source and Target Cell Identities. *Cell Reports* **30**, 1178–1194 e1173, doi:10.1016/j.celrep.2019.12.095 (2020).

37 Zhang, Y., Larcher, K. M., Misic, B. & Dagher, A. Anatomical and functional organization of the human substantia nigra and its connections. *Elife* **6**, doi:10.7554/eLife.26653 (2017).

38 Michel, P. P., Hirsch, E. C. & Hunot, S. Understanding Dopaminergic Cell Death Pathways in Parkinson Disease. *Neuron* **90**, 675–691, doi:10.1016/j.neuron.2016.03.038 (2016).

39 Naoi, M. & Maruyama, W. Cell death of dopamine neurons in aging and Parkinson's disease. *Mechanisms of Ageing and Development* **111**, 175–188, doi:10.1016/s0047-6374(99)00064-0 (1999).

40 Song, J. & Kim, J. Degeneration of Dopaminergic Neurons Due to Metabolic Alterations and Parkinson's Disease. *Frontiers in Aging Neuroscience* **8**, 65, doi:10.3389/fnagi.2016.00065 (2016).

41 Surmeier, D. J., Guzman, J. N., Sanchez-Padilla, J. & Goldberg, J. A. What causes the death of dopaminergic neurons in Parkinson's disease? *Progress in Brain Research* **183**, 59–77, doi:10.1016/S0079-6123(10)83004-3 (2010).

42 Reinius, B. *et al.* Conditional targeting of medium spiny neurons in the striatal matrix. *Frontiers in Behavioral Neuroscience* **9**, 71, doi:10.3389/fnbeh.2015.00071 (2015).

43 Martel, J. C. & Gatti McArthur, S. Dopamine Receptor Subtypes, Physiology and Pharmacology: New Ligands and Concepts in Schizophrenia. *Frontiers in Pharmacology* **11**, 1003, doi:10.3389/fphar.2020.01003 (2020).

44 Cui, G. *et al.* Concurrent activation of striatal direct and indirect pathways during action initiation. *Nature* **494**, 238–242, doi:10.1038/nature11846 (2013).

45 Tecuapetla, F., Matias, S., Dugue, G. P., Mainen, Z. F. & Costa, R. M. Balanced activity in basal ganglia projection pathways is critical for contraversive movements. *Nature Communications* **5**, 4315, doi:10.1038/ncomms5315 (2014).

46 Barbera, G. *et al.* Spatially Compact Neural Clusters in the Dorsal Striatum Encode Locomotion Relevant Information. *Neuron* **92**, 202–213, doi:10.1016/j.neuron.2016.08.037 (2016).

47 Jaeger, D., Gilman, S. & Aldridge, J. W. Neuronal activity in the striatum and pallidum of primates related to the execution of externally cued reaching movements. *Brain Research* **694**, 111–127 (1995).

48 Courtemanche, R., Fujii, N. & Graybiel, A. M. Synchronous, focally modulated beta-band oscillations characterize local field potential activity in the striatum of awake behaving monkeys. *Journal of Neuroscience* **23**, 11741–11752 (2003).

49 Stern, E. A., Kincaid, A. E. & Wilson, C. J. Spontaneous subthreshold membrane potential fluctuations and action potential variability of rat corticostriatal and striatal neurons in vivo. *Journal of Neurophysiology* **77**, 1697–1715, doi:10.1152/jn.1997.77.4.1697 (1997).

50 Stern, E. A., Jaeger, D. & Wilson, C. J. Membrane potential synchrony of simultaneously recorded striatal spiny neurons in vivo. *Nature* **394**, 475–478, doi:10.1038/28848 (1998).

51 Wickens, J. R. & Wilson, C. J. Regulation of action-potential firing in spiny neurons of the rat neostriatum in vivo. *Journal of Neurophysiology* **79**, 2358–2364, doi:10.1152/jn.1998.79.5.2358 (1998).

52 Wilson, C. J. & Kawaguchi, Y. The origins of two-state spontaneous membrane potential fluctuations of neostriatal spiny neurons. *Journal of Neuroscience* **16**, 2397–2410 (1996).

53 Sharott, A., Doig, N. M., Mallet, N. & Magill, P. J. Relationships between the firing of identified striatal interneurons and spontaneous and driven cortical activities in vivo. *Journal of Neuroscience* **32**, 13221–13236, doi:10.1523/JNEUROSCI.2440-12.2012 (2012).

54 Tseng, K. Y., Kasanetz, F., Kargieman, L., Riquelme, L. A. & Murer, M. G. Cortical slow oscillatory activity is reflected in the membrane potential and spike trains of striatal neurons in rats with chronic nigrostriatal lesions. *Journal of Neuroscience* **21**, 6430–6439 (2001).

55 Faust, T. W., Assous, M., Tepper, J. M. & Koos, T. Neostriatal GABAergic Interneurons Mediate Cholinergic Inhibition of Spiny Projection Neurons. *Journal of Neuroscience* **36**, 9505–9511, doi:10.1523/JNEUROSCI.0466-16.2016 (2016).

56 Mallet, N., Leblois, A., Maurice, N. & Beurrier, C. Striatal Cholinergic Interneurons: How to Elucidate Their Function in Health and Disease. *Frontiers in Pharmacology* **10**, 1488, doi:10.3389/fphar.2019.01488 (2019).

57 Tepper, J. M. *et al.* Heterogeneity and Diversity of Striatal GABAergic Interneurons: Update 2018. *Frontiers in Neuroanatomy* **12**, 91, doi:10.3389/fnana.2018.00091 (2018).

58 Lim, S. A., Kang, U. J. & McGehee, D. S. Striatal cholinergic interneuron regulation and circuit effects. *Frontiers in Synaptic Neuroscience* **6**, 22, doi:10.3389/fnsyn.2014.00022 (2014).

59 Gritton, H. J. *et al.* Unique contributions of parvalbumin and cholinergic interneurons in organizing striatal networks during movement. *Nature Neuroscience*, doi:10.1038/s41593-019-0341-3 (2019).

60 Contant, C., Umbriaco, D., Garcia, S., Watkins, K. C. & Descarries, L. Ultrastructural characterization of the acetylcholine innervation in adult rat neostriatum. *Neuroscience* **71**, 937–947 (1996).

61 Franklin, N. T. & Frank, M. J. A cholinergic feedback circuit to regulate striatal population uncertainty and optimize reinforcement learning. *Elife* **4**, doi:10.7554/eLife.12029 (2015).

62 Benhamou, L., Kehat, O. & Cohen, D. Firing pattern characteristics of tonically active neurons in rat striatum: context dependent or species divergent? *Journal of Neuroscience* **34**, 2299–2304, doi:10.1523/JNEUROSCI.1798-13.2014 (2014).

63 Ding, Y. *et al.* Enhanced striatal cholinergic neuronal activity mediates L-DOPA-induced dyskinesia in parkinsonian mice. *Proceedings of the National Academy of Sciences of the United States of America* **108**, 840–845, doi:10.1073/pnas.1006511108 (2011).

64 Howe, M. *et al.* Coordination of rapid cholinergic and dopaminergic signaling in striatum during spontaneous movement. *Elife* **8**, doi:10.7554/eLife.44903 (2019).

65 Kondabolu, K. *et al.* Striatal cholinergic interneurons generate beta and gamma oscillations in the corticostriatal circuit and produce motor deficits. *Proceedings of the National Academy of Sciences of the United States of America* **113**, E3159–3168, doi:10.1073/pnas.1605658113 (2016).

66 McCarthy, M. M. *et al.* Striatal origin of the pathologic beta oscillations in Parkinson's disease. *Proceedings of the National Academy of Sciences of the United States of America* **108**, 11620–11625, doi:10.1073/pnas.1107748108 (2011).

67 Pittman-Polletta, B. R. *et al.* Striatal cholinergic receptor activation causes a rapid, selective and state-dependent rise in cortico-striatal beta activity. *European Journal of Neuroscience* **48**, 2857–2868, doi:10.1111/ejn.13906 (2018).

68 Avila, I. *et al.* Beta frequency synchronization in basal ganglia output during rest and walk in a hemiparkinsonian rat. *Experimental Neurology* **221**, 307–319, doi:10.1016/j.expneurol.2009.11.016 (2010).

69 Chartove, J. A. K., McCarthy, M. M., Pittman-Polletta, B. R. & Kopell, N. J. A biophysical model of striatal microcircuits suggests gamma and beta oscillations interleaved at delta/theta frequencies mediate periodicity in motor control. *PLoS Computational Biology* **16**, e1007300, doi:10.1371/journal.pcbi.1007300 (2020).

70 Sharott, A., Vinciati, F., Nakamura, K. C. & Magill, P. J. A Population of Indirect Pathway Striatal Projection Neurons Is Selectively Entrained to Parkinsonian Beta Oscillations. *Journal of Neuroscience* **37**, 9977–9998, doi:10.1523/JNEUROSCI.0658-17.2017 (2017).

71 West, T. O. *et al.* Propagation of beta/gamma rhythms in the cortico-basal ganglia circuits of the parkinsonian rat. *Journal of Neurophysiology* **119**, 1608–1628, doi:10.1152/jn.00629.2017 (2018).

72 Delaville, C. *et al.* Oscillatory Activity in Basal Ganglia and Motor Cortex in an Awake Behaving Rodent Model of Parkinson's Disease. *Basal Ganglia* **3**, 221–227, doi:10.1016/j.baga.2013.12.001 (2014).

73 Singh, A. Oscillatory activity in the cortico-basal ganglia-thalamic neural circuits in Parkinson's disease. *European Journal of Neuroscience* **48**, 2869–2878, doi:10.1111/ejn.13853 (2018).

74 Murer, M. G., Tseng, K. Y., Kasanetz, F., Belluscio, M. & Riquelme, L. A. Brain oscillations, medium spiny neurons, and dopamine. *Cellular and Molecular Neurobiology* **22**, 611–632, doi:10.1023/a:1021840504342 (2002).

75 Muller, E. J. & Robinson, P. A. Suppression of Parkinsonian Beta Oscillations by Deep Brain Stimulation: Determination of Effective Protocols. *Frontiers in Computational Neuroscience* **12**, 98, doi:10.3389/fncom.2018.00098 (2018).

76 Feingold, J., Gibson, D. J., DePasquale, B. & Graybiel, A. M. Bursts of beta oscillation differentiate postperformance activity in the striatum and motor cortex of monkeys performing movement tasks. *Proceedings of the National Academy of Sciences of the United States of America* **112**, 13687–13692, doi:10.1073/pnas.1517629112 (2015).

77 Bartolo, R., Prado, L. & Merchant, H. Information processing in the primate basal ganglia during sensory-guided and internally driven rhythmic tapping. *Journal of Neuroscience* **34**, 3910–3923, doi:10.1523/JNEUROSCI.2679-13.2014 (2014).

78 Bartolo, R. & Merchant, H. beta oscillations are linked to the initiation of sensory-cued movement sequences and the internal guidance of regular tapping in the monkey. *Journal of Neuroscience* **35**, 4635–4640, doi:10.1523/JNEUROSCI.4570-14.2015 (2015).

79 Leventhal, D. K. *et al.* Basal ganglia beta oscillations accompany cue utilization. *Neuron* **73**, 523–536, doi:10.1016/j.neuron.2011.11.032 (2012).

80 Okun, M., Naim, A. & Lampl, I. The subthreshold relation between cortical local field potential and neuronal firing unveiled by intracellular recordings in awake rats. *Journal of Neuroscience* **30**, 4440–4448, doi:10.1523/JNEUROSCI.5062-09.2010 (2010).

81 Steriade, M. Impact of network activities on neuronal properties in corticothalamic systems. *Journal of Neurophysiology* **86**, 1–39, doi:10.1152/jn.2001.86.1.1 (2001).

82 Hasenstaub, A. *et al.* Inhibitory postsynaptic potentials carry synchronized frequency information in active cortical networks. *Neuron* **47**, 423–435, doi:10.1016/j.neuron.2005.06.016 (2005).

83 Lampl, I., Reichova, I. & Ferster, D. Synchronous membrane potential fluctuations in neurons of the cat visual cortex. *Neuron* **22**, 361–374 (1999).

84 Andre, V. M., Fisher, Y. E. & Levine, M. S. Altered Balance of Activity in the Striatal Direct and Indirect Pathways in Mouse Models of Huntington's Disease. *Frontiers in Systems Neuroscience* **5**, 46, doi:10.3389/fnsys.2011.00046 (2011).

85 Deschenes, M., Paradis, M., Roy, J. P. & Steriade, M. Electrophysiology of neurons of lateral thalamic nuclei in cat: resting properties and burst discharges. *Journal of Neurophysiology* **51**, 1196–1219, doi:10.1152/jn.1984.51.6.1196 (1984).

86 Kodandaramaiah, S. B., Franzesi, G. T., Chow, B. Y., Boyden, E. S. & Forest, C. R. Automated whole-cell patch-clamp electrophysiology of neurons in vivo. *Nature Methods* **9**, 585–587, doi:10.1038/nmeth.1993 (2012).

87 Li, Y., Evans, M. S. & Faingold, C. L. In vitro electrophysiology of neurons in subnuclei of rat inferior colliculus. *Hearing Research* **121**, 1–10, doi:10.1016/s0378-5955(98)00066-5 (1998).

88 Mitcheson, J. S., Hancox, J. C. & Levi, A. J. Cultured adult cardiac myocytes: future applications, culture methods, morphological and electrophysiological properties. *Cardiovascular Research* **39**, 280–300, doi:10.1016/s0008-6363(98)00128-x (1998).

89 Nuss, H. B. & Marban, E. Electrophysiological properties of neonatal mouse cardiac myocytes in primary culture. *Journal of Physiology* **479 (Pt 2)**, 265–279, doi:10.1113/jphysiol.1994.sp020294 (1994).

90 Rubaiy, H. N. A Short Guide to Electrophysiology and Ion Channels. *Journal of Pharmacy & Pharmaceutical Sciences* **20**, 48–67, doi:10.18433/J32P6R (2017).

91 Wilders, R. Dynamic clamp: a powerful tool in cardiac electrophysiology. *Journal of Physiology* **576**, 349–359, doi:10.1113/jphysiol.2006.115840 (2006).

92 Beatty, J. A., Song, S. C. & Wilson, C. J. Cell-type-specific resonances shape the responses of striatal neurons to synaptic input. *Journal of Neurophysiology* **113**, 688–700, doi:10.1152/jn.00827.2014 (2015).

93 Sciamanna, G. & Wilson, C. J. The ionic mechanism of gamma resonance in rat striatal fast-spiking neurons. *Journal of Neurophysiology* **106**, 2936–2949, doi:10.1152/jn.00280.2011 (2011).

94 Wilson, C. J. The mechanism of intrinsic amplification of hyperpolarizations and spontaneous bursting in striatal cholinergic interneurons. *Neuron* **45**, 575–585, doi:10.1016/j.neuron.2004.12.053 (2005).

95 Noguchi, A., Ikegaya, Y. & Matsumoto, N. In Vivo Whole-Cell Patch-Clamp Methods: Recent Technical Progress and Future Perspectives. *Sensors (Basel)* **21**, doi:10.3390/s21041448 (2021).

96 Segev, A., Garcia-Oscos, F. & Kourrich, S. Whole-cell Patch-clamp Recordings in Brain Slices. *Journal of Visualized Experiments (JoVE)*, doi:10.3791/54024 (2016).

97 Adam, Y. *et al.* Voltage imaging and optogenetics reveal behaviour-dependent changes in hippocampal dynamics. *Nature* **569**, 413–417, doi:10.1038/s41586-019-1166-7 (2019).

98 Kodandaramaiah, S. B., Boyden, E. S. & Forest, C. R. In vivo robotics: the automation of neuroscience and other intact-system biological fields. *Annals of the New York Academy of Sciences* **1305**, 63–71, doi:10.1111/nyas.12171 (2013).

99 Kodandaramaiah, S. B. *et al.* Multi-neuron intracellular recording *in vivo* via interacting autopatching robots. *Elife* **7**, doi:10.7554/eLife.24656 (2018).

100 Cogan, S. F. Neural stimulation and recording electrodes. *Annual Review of Biomedical Engineering* **10**, 275–309, doi:10.1146/annurev.bioeng.10.061807.160518 (2008).

101 Hubel, D. H. Tungsten Microelectrode for Recording from Single Units. *Science* **125**, 549–550, doi:10.1126/science.125.3247.549 (1957).

102 Barth, B. B., Huang, H. I., Hammer, G. E. & Shen, X. Opportunities and Challenges for Single-Unit Recordings from Enteric Neurons in Awake Animals. *Micromachines (Basel)* **9**, doi:10.3390/mi9090428 (2018).

103 Kajikawa, Y. & Schroeder, C. E. How local is the local field potential? *Neuron* **72**, 847–858, doi:10.1016/j.neuron.2011.09.029 (2011).

104 Keller, C. J., Chen, C., Lado, F. A. & Khodakhah, K. The Limited Utility of Multiunit Data in Differentiating Neuronal Population Activity. *PLoS One* **11**, e0153154, doi:10.1371/journal.pone.0153154 (2016).

105 Super, H. & Roelfsema, P. R. Chronic multiunit recordings in behaving animals: advantages and limitations. *Progress in Brain Research* **147**, 263–282, doi:10.1016/S0079-6123(04)47020-4 (2005).

106 Herreras, O. Local Field Potentials: Myths and Misunderstandings. *Frontiers in Neural Circuits* **10**, 101, doi:10.3389/fncir.2016.00101 (2016).

107 Foffani, G. *et al.* 300-Hz subthalamic oscillations in Parkinson's disease. *Brain* **126**, 2153–2163, doi:10.1093/brain/awg229 (2003).

108 Priori, A., Foffani, G., Rossi, L. & Marceglia, S. Adaptive deep brain stimulation (aDBS) controlled by local field potential oscillations. *Experimental Neurology* **245**, 77–86, doi:10.1016/j.expneurol.2012.09.013 (2013).

109 Ray, N. J. *et al.* Local field potential beta activity in the subthalamic nucleus of patients with Parkinson's disease is associated with improvements in bradykinesia after dopamine and deep brain stimulation. *Experimental Neurology* **213**, 108–113, doi:10.1016/j.expneurol.2008.05.008 (2008).

110 Little, S. & Brown, P. What brain signals are suitable for feedback control of deep brain stimulation in Parkinson's disease? *Annals of the New York Academy of Sciences* **1265**, 9–24, doi:10.1111/j.1749-6632.2012.06650.x (2012).

111 Lopez-Azcarate, J. *et al.* Coupling between beta and high-frequency activity in the human subthalamic nucleus may be a pathophysiological mechanism in Parkinson's disease. *Journal of Neuroscience* **30**, 6667–6677, doi:10.1523/JNEUROSCI.5459-09.2010 (2010).

112 Ozkurt, T. E. *et al.* High frequency oscillations in the subthalamic nucleus: a neurophysiological marker of the motor state in Parkinson's disease. *Experimental Neurology* **229**, 324–331, doi:10.1016/j.expneurol.2011.02.015 (2011).

113 Borst, J. G. & Sakmann, B. Calcium current during a single action potential in a large presynaptic terminal of the rat brainstem. *Journal of Physiology* **506 (Pt 1)**, 143–157, doi:10.1111/j.1469-7793.1998.143bx.x (1998).

114 Borst, J. G. & Helmchen, F. Calcium influx during an action potential. *Methods in Enzymology* **293**, 352–371, doi:10.1016/s0076-6879(98)93023-3 (1998).

115 Fearnley, C. J., Roderick, H. L. & Bootman, M. D. Calcium signaling in cardiac myocytes. *Cold Spring Harbor Perspectives in Biology* **3**, a004242, doi:10.1101/cshperspect.a004242 (2011).

116 Grantham, C. J. & Cannell, M. B. Ca2+ influx during the cardiac action potential in guinea pig ventricular myocytes. *Circulation Research* **79**, 194–200, doi:10.1161/01.res.79.2.194 (1996).

117 Iosub, R., Avitabile, D., Grant, L., Tsaneva-Atanasova, K. & Kennedy, H. J. Calcium-Induced calcium release during action potential firing in developing inner hair cells. *Biophysical Journal* **108**, 1003–1012, doi:10.1016/j.bpj.2014.11.3489 (2015).

118 Scarnati, M. S., Clarke, S. G., Pang, Z. P. & Paradiso, K. G. Presynaptic Calcium Channel Open Probability and Changes in Calcium Influx Throughout the Action Potential Determined Using AP-Waveforms. *Frontiers in Synaptic Neuroscience* **12**, 17, doi:10.3389/fnsyn.2020.00017 (2020).

119 Schneidereit, D., Vass, H., Reischl, B., Allen, R. J. & Friedrich, O. Calcium Sensitive Fluorescent Dyes Fluo-4 and Fura Red under Pressure: Behaviour of Fluorescence and Buffer Properties under Hydrostatic Pressures up to 200 MPa. *PLoS One* **11**, e0164509, doi:10.1371/journal.pone.0164509 (2016).

120 Cecchetto, C., Vassanelli, S. & Kuhn, B. Simultaneous Two-Photon Voltage or Calcium Imaging and Multi-Channel Local Field Potential Recordings in Barrel Cortex of Awake and Anesthetized Mice. *Frontiers in Neuroscience* **15**, 741279, doi:10.3389/fnins.2021.741279 (2021).

121 Hoang, H. *et al.* Improved hyperacuity estimation of spike timing from calcium imaging. *Scientific Reports* **10**, 17844, doi:10.1038/s41598-020-74672-y (2020).

122 Oh, J., Lee, C. & Kaang, B. K. Imaging and analysis of genetically encoded calcium indicators linking neural circuits and behaviors. *Korean Journal of Physiology & Pharmacology* **23**, 237–249, doi:10.4196/kjpp.2019.23.4.237 (2019).

123 Paredes, R. M., Etzler, J. C., Watts, L. T., Zheng, W. & Lechleiter, J. D. Chemical calcium indicators. *Methods* **46**, 143–151, doi:10.1016/j.ymeth.2008.09.025 (2008).

124 Vanwalleghem, G., Constantin, L. & Scott, E. K. Calcium Imaging and the Curse of Negativity. *Frontiers in Neural Circuits* **14**, 607391, doi:10.3389/fncir.2020.607391 (2020).

125 Abdelfattah, A. S. *et al.* Bright and photostable chemigenetic indicators for extended *in vivo* voltage imaging. *bioRxiv*, 436840, doi:10.1101/436840 (2018).

126 Kulkarni, R. U. & Miller, E. W. Voltage Imaging: Pitfalls and Potential. *Biochemistry* **56**, 5171–5177, doi:10.1021/acs.biochem.7b00490 (2017).

127 Sepehri Rad, M. *et al.* Voltage and Calcium Imaging of Brain Activity. *Biophysical Journal* **113**, 2160–2167, doi:10.1016/j.bpj.2017.09.040 (2017).

128 Augustine, G. J., Santamaria, F. & Tanaka, K. Local calcium signaling in neurons. *Neuron* **40**, 331–346, doi:10.1016/s0896-6273(03)00639-1 (2003).

129 Brini, M., Cali, T., Ottolini, D. & Carafoli, E. Neuronal calcium signaling: function and dysfunction. *Cellular and Molecular Life Sciences* **71**, 2787–2814, doi:10.1007/s00018-013-1550-7 (2014).

130 Carafoli, E. & Krebs, J. Why Calcium? How Calcium Became the Best Communicator. *Journal of Biological Chemistry* **291**, 20849–20857, doi:10.1074/jbc.R116.735894 (2016).

131 Endo, M. Calcium ion as a second messenger with special reference to excitation-contraction coupling. *Journal of Pharmacological Sciences* **100**, 519–524, doi:10.1254/jphs.cpj06004x (2006).

132 Hofer, A. M. & Lefkimmiatis, K. Extracellular calcium and cAMP: second messengers as "third messengers"? *Physiology (Bethesda, Md.)* **22**, 320–327, doi:10.1152/physiol.00019.2007 (2007).

133 Kawamoto, E. M., Vivar, C. & Camandola, S. Physiology and pathology of calcium signaling in the brain. *Frontiers in Pharmacology* **3**, 61, doi:10.3389/fphar.2012.00061 (2012).

134 Alford, R. *et al.* Toxicity of organic fluorophores used in molecular imaging: literature review. *Molecular Imaging* **8**, 341–354 (2009).

135 Herron, T. J., Lee, P. & Jalife, J. Optical imaging of voltage and calcium in cardiac cells & tissues. *Circulation Research* **110**, 609–623, doi:10.1161/CIRCRESAHA.111.247494 (2012).

136 Jensen, E. C. Use of fluorescent probes: their effect on cell biology and limitations. *Anatomical Record* **295**, 2031–2036, doi:10.1002/ar.22602 (2012).

137 Robson, A. L. *et al.* Advantages and Limitations of Current Imaging Techniques for Characterizing Liposome Morphology. *Frontiers in Pharmacology* **9**, 80, doi:10.3389/fphar.2018.00080 (2018).

138 Ma, H. *et al.* Wide-field in vivo neocortical calcium dye imaging using a convection-enhanced loading technique combined with simultaneous multiwavelength imaging of voltage-sensitive dyes and hemodynamic signals. *Neurophotonics* **1**, 015003, doi:10.1117/1.NPh.1.1.015003 (2014).

139 Stosiek, C., Garaschuk, O., Holthoff, K. & Konnerth, A. In vivo two-photon calcium imaging of neuronal networks. *Proceedings of the National Academy of Sciences of the United States of America* **100**, 7319–7324, doi:10.1073/pnas.1232232100 (2003).

140 McKenzie, M., Lim, S. C. & Duchen, M. R. Simultaneous Measurement of Mitochondrial Calcium and Mitochondrial Membrane Potential in Live Cells by Fluorescent Microscopy. *Journal of Visual Experiments (JoVE)*, doi:10.3791/55166 (2017).

141 Davidson, S. M. & Duchen, M. R. Imaging mitochondrial calcium signalling with fluorescent probes and single or two photon confocal microscopy. *Methods in Molecular Biology* **810**, 219–234, doi:10.1007/978-1-61779-382-0_14 (2012).

142 Nakai, J., Ohkura, M. & Imoto, K. A high signal-to-noise Ca(2+) probe composed of a single green fluorescent protein. *Nature Biotechnology* **19**, 137–141, doi:10.1038/84397 (2001).

143 Chisholm, K. I., Khovanov, N., Lopes, D. M., La Russa, F. & McMahon, S. B. Large Scale In Vivo Recording of Sensory Neuron Activity with GCaMP6. *eNeuro* **5**, doi:10.1523/ENEURO.0417-17.2018 (2018).

144 Jercog, P., Rogerson, T. & Schnitzer, M. J. Large-Scale Fluorescence Calcium-Imaging Methods for Studies of Long-Term Memory in Behaving Mammals. *Cold Spring Harbor Perspectives in Biology* **8**, doi:10.1101/cshperspect.a021824 (2016).

145 Wekselblatt, J. B., Flister, E. D., Piscopo, D. M. & Niell, C. M. Large-scale imaging of cortical dynamics during sensory perception and behavior. *Journal of Neurophysiology* **115**, 2852–2866, doi:10.1152/jn.01056.2015 (2016).

146 Chen, J. L., Andermann, M. L., Keck, T., Xu, N. L. & Ziv, Y. Imaging neuronal populations in behaving rodents: paradigms for studying neural circuits underlying behavior in the mammalian cortex. *Journal of Neuroscience* **33**, 17631–17640, doi:10.1523/JNEUROSCI.3255-13.2013 (2013).

147 Mohammed, A. I. *et al.* An integrative approach for analyzing hundreds of neurons in task performing mice using wide-field calcium imaging. *Scientific Reports* **6**, 20986, doi:10.1038/srep20986 (2016).

148 Bers, D. M. Calcium cycling and signaling in cardiac myocytes. *Annual Review of Physiology* **70**, 23–49, doi:10.1146/annurev.physiol.70.113006.100455 (2008).

149 Kaestner, L. *et al.* Genetically Encoded Voltage Indicators in Circulation Research. *International Journal of Molecular Sciences* **16**, 21626–21642, doi:10.3390/ijms160921626 (2015).

150 Tallini, Y. N. *et al.* Imaging cellular signals in the heart in vivo: Cardiac expression of the high-signal Ca2+ indicator GCaMP2. *Proceedings of the National Academy of Sciences of the United States of America* **103**, 4753–4758, doi:10.1073/pnas.0509378103 (2006).

151 Eisner, D. A., Caldwell, J. L., Kistamas, K. & Trafford, A. W. Calcium and Excitation-Contraction Coupling in the Heart. *Circulation Research* **121**, 181–195, doi:10.1161/CIRCRESAHA.117.310230 (2017).

152 Bers, D. M. Cardiac excitation-contraction coupling. *Nature* **415**, 198–205, doi:10.1038/415198a (2002).

153 Hobai, I. A. & O'Rourke, B. Decreased sarcoplasmic reticulum calcium content is responsible for defective excitation-contraction coupling in canine heart failure. *Circulation* **103**, 1577–1584, doi:10.1161/01.cir.103.11.1577 (2001).

154 Ye, L., Haroon, M. A., Salinas, A. & Paukert, M. Comparison of GCaMP3 and GCaMP6f for studying astrocyte Ca2+ dynamics in the awake mouse brain. *PLoS One* **12**, e0181113, doi:10.1371/journal.pone.0181113 (2017).

155 Zhong, C. & Schleifenbaum, J. Genetically Encoded Calcium Indicators: A New Tool in Renal Hypertension Research. *Frontiers in Medicine* **6**, 128, doi:10.3389/fmed.2019.00128 (2019).

156 Song, L. *et al.* Dual optical recordings for action potentials and calcium handling in induced pluripotent stem cell models of cardiac arrhythmias using genetically encoded fluorescent indicators. *Stem Cells Translational Medicine* **4**, 468–475, doi:10.5966/sctm.2014-0245 (2015).

157 Peng, S., Lacerda, A. E., Kirsch, G. E., Brown, A. M. & Bruening-Wright, A. The action potential and comparative pharmacology of stem cell-derived human cardiomyocytes. *Journal of Pharmacological and Toxicological Methods* **61**, 277–286, doi:10.1016/j.vascn.2010.01.014 (2010).

158 Sanguinetti, M. C. & Jurkiewicz, N. K. Delayed rectifier outward K+ current is composed of two currents in guinea pig atrial cells. *American Journal of Physiology* **260**, H393–399, doi:10.1152/ajpheart.1991.260.2.H393 (1991).

159 Sanguinetti, M. C., Jurkiewicz, N. K., Scott, A. & Siegl, P. K. Isoproterenol antagonizes prolongation of refractory period by the class III antiarrhythmic agent E-4031 in guinea pig myocytes. Mechanism of action. *Circulation Research* **68**, 77–84, doi:10.1161/01.res.68.1.77 (1991).

160 Olivari, M. T. *et al.* Treatment of hypertension with nifedipine, a calcium antagonistic agent. *Circulation* **59**, 1056–1062, doi:10.1161/01.cir.59.5.1056 (1979).

161 Leyton-Mange, J. S. & Milan, D. J. Pluripotent stem cells as a platform for cardiac arrhythmia drug screening. *Current Treatment Options in Cardiovascular Medicine* **16**, 334, doi:10.1007/s11936-014-0334-1 (2014).

162 Leyton-Mange, J. S. *et al.* Rapid cellular phenotyping of human pluripotent stem cell-derived cardiomyocytes using a genetically encoded fluorescent voltage sensor. *Stem Cell Reports* **2**, 163–170, doi:10.1016/j.stemcr.2014.01.003 (2014).

163 Shaheen, N. *et al.* Human Induced Pluripotent Stem Cell-Derived Cardiac Cell Sheets Expressing Genetically Encoded Voltage Indicator for Pharmacological and Arrhythmia Studies. *Stem Cell Reports* **10**, 1879–1894, doi:10.1016/j.stemcr.2018.04.006 (2018).

164 Shinnawi, R. *et al.* Monitoring Human-Induced Pluripotent Stem Cell-Derived Cardiomyocytes with Genetically Encoded Calcium and Voltage Fluorescent Reporters. *Stem Cell Reports* **5**, 582–596, doi:10.1016/j.stemcr.2015.08.009 (2015).

165 Fiebelkorn, I. C. & Kastner, S. Spike Timing in the Attention Network Predicts Behavioral Outcome Prior to Target Selection. *Neuron* **109**, 177–188 e174, doi:10.1016/j.neuron.2020.09.039 (2021).

166 Klink, P. C. Some spikes are more informative than others. *Journal of Neuroscience* **28**, 4844–4845, doi:10.1523/JNEUROSCI.1036-08.2008 (2008).

167 Mrakic-Sposta, S. *et al.* Extracellular spike microrecordings from the subthalamic area in Parkinson's disease. *Journal of Clinical Neuroscience* **15**, 559–567, doi:10.1016/j.jocn.2007.02.091 (2008).

168 Kuhn, B., Fromherz, P. & Denk, W. High sensitivity of Stark-shift voltage-sensing dyes by one- or two-photon excitation near the red spectral edge. *Biophysical Journal* **87**, 631–639, doi:10.1529/biophysj.104.040477 (2004).

169 Kuhn, B. & Roome, C. J. Primer to Voltage Imaging With ANNINE Dyes and Two-Photon Microscopy. *Frontiers in Cellular Neuroscience* **13**, 321, doi:10.3389/fncel.2019.00321 (2019).

170 Salama, G. & Morad, M. Merocyanine 540 as an optical probe of transmembrane electrical activity in the heart. *Science* **191**, 485–487, doi:10.1126/science.191.4226.485 (1976).

171 Entcheva, E. & Bien, H. Macroscopic optical mapping of excitation in cardiac cell networks with ultra-high spatiotemporal resolution. *Progress in Biophysics & Molecular Biology* **92**, 232–257, doi:10.1016/j.pbiomolbio.2005.10.003 (2006).

172 Panakova, D., Werdich, A. A. & Macrae, C. A. Wnt11 patterns a myocardial electrical gradient through regulation of the L-type Ca(2+) channel. *Nature* **466**, 874–878, doi:10.1038/nature09249 (2010).

173 Hortigon-Vinagre, M. P. *et al.* The Use of Ratiometric Fluorescence Measurements of the Voltage Sensitive Dye Di-4-ANEPPS to Examine Action Potential Characteristics and Drug Effects on Human Induced Pluripotent Stem Cell-Derived Cardiomyocytes. *Toxicological Sciences* **154**, 320–331, doi:10.1093/toxsci/kfw171 (2016).

174 Salama, G. *et al.* Properties of new, long-wavelength, voltage-sensitive dyes in the heart. *Journal of Membrane Biology* **208**, 125–140, doi:10.1007/s00232-005-0826-8 (2005).

175 Hou, J. H., Kralj, J. M., Douglass, A. D., Engert, F. & Cohen, A. E. Simultaneous mapping of membrane voltage and calcium in zebrafish heart in vivo reveals chamber-specific developmental transitions in ionic currents. *Frontiers in Physiology* **5**, 344, doi:10.3389/fphys.2014.00344 (2014).

176 Fiala, T. *et al.* Chemical Targeting of Voltage Sensitive Dyes to Specific Cells and Molecules in the Brain. *Journal of the American Chemical Society* **142**, 9285–9301, doi:10.1021/jacs.0c00861 (2020).

177 Tang, Q. *et al.* In Vivo Mesoscopic Voltage-Sensitive Dye Imaging of Brain Activation. *Scientific Reports* **6**, 25269, doi:10.1038/srep25269 (2016).

178 Tang, Q. *et al.* In vivo voltage-sensitive dye imaging of mouse cortical activity with mesoscopic optical tomography. *Neurophotonics* **7**, 041402, doi:10.1117/1.NPh.7.4.041402 (2020).

179 Dorgans, K., Kuhn, B. & Uusisaari, M. Y. Imaging Subthreshold Voltage Oscillation With Cellular Resolution in the Inferior Olive in vitro. *Frontiers in Cellular Neuroscience* **14**, 607843, doi:10.3389/fncel.2020.607843 (2020).

180 Newton, T. H. *et al.* In silico voltage-sensitive dye imaging reveals the emergent dynamics of cortical populations. *Nature Communications* **12**, 3630, doi:10.1038/s41467-021-23901-7 (2021).

181 Hochbaum, D. R. *et al.* All-optical electrophysiology in mammalian neurons using engineered microbial rhodopsins. *Nature Methods* **11**, 825–833, doi:10.1038/nmeth.3000 (2014).

182 Flytzanis, N. C. *et al.* Archaerhodopsin variants with enhanced voltage-sensitive fluorescence in mammalian and Caenorhabditis elegans neurons. *Nature Communications* **5**, 4894, doi:10.1038/ncomms5894 (2014).

183 Piatkevich, K. D. *et al.* Publisher Correction: A robotic multidimensional directed evolution approach applied to fluorescent voltage reporters. *Nature Chemical Biology* **14**, 901, doi:10.1038/s41589-018-0023-6 (2018).

184 Jin, L. *et al.* Single action potentials and subthreshold electrical events imaged in neurons with a fluorescent protein voltage probe. *Neuron* **75**, 779–785, doi:10.1016/j.neuron.2012.06.040 (2012).

185 St-Pierre, F. *et al.* High-fidelity optical reporting of neuronal electrical activity with an ultrafast fluorescent voltage sensor. *Nature Neuroscience* **17**, 884–889, doi:10.1038/nn.3709 (2014).

186 Gong, Y., Wagner, M. J., Zhong Li, J. & Schnitzer, M. J. Imaging neural spiking in brain tissue using FRET-opsin protein voltage sensors. *Nature Communications* **5**, 3674, doi:10.1038/ncomms4674 (2014).

187 Zou, P. *et al.* Bright and fast multicoloured voltage reporters via electrochromic FRET. *Nature Communications* **5**, 4625, doi:10.1038/ncomms5625 (2014).

188 Gong, Y. *et al.* High-speed recording of neural spikes in awake mice and flies with a fluorescent voltage sensor. *Science* **350**, 1361–1366, doi:10.1126/science.aab0810 (2015).

189 Chamberland, S. *et al.* Fast two-photon imaging of subcellular voltage dynamics in neuronal tissue with genetically encoded indicators. *Elife* **6**, doi:10.7554/eLife.25690 (2017).

190 Chang Liao, M. L. *et al.* Sensing Cardiac Electrical Activity With a Cardiac Myocyte-Targeted Optogenetic Voltage Indicator. *Circulation Research* **117**, 401–412, doi:10.1161/CIRCRESAHA.117.306143 (2015).

191 van Opbergen, C. J. M. *et al.* Optogenetic sensors in the zebrafish heart: a novel in vivo electrophysiological tool to study cardiac arrhythmogenesis. *Theranostics* **8**, 4750–4764, doi:10.7150/thno.26108 (2018).

192 Mutoh, H. *et al.* Spectrally-resolved response properties of the three most advanced FRET based fluorescent protein voltage probes. *PLoS One* **4**, e4555, doi:10.1371/journal.pone.0004555 (2009).

193 Tsutsui, H., Higashijima, S., Miyawaki, A. & Okamura, Y. Visualizing voltage dynamics in zebrafish heart. *Journal of Physiology* **588**, 2017–2021, doi:10.1113/jphysiol.2010.189126 (2010).

194 Borden, P. Y. *et al.* Erratum: Genetically expressed voltage sensor ArcLight for imaging large scale cortical activity in the anesthetized and awake mouse (erratum). *Neurophotonics* **4**, 039801, doi:10.1117/1.NPh.4.3.039801 (2017).

195 Cao, G. *et al.* Genetically targeted optical electrophysiology in intact neural circuits. *Cell* **154**, 904–913, doi:10.1016/j.cell.2013.07.027 (2013).

196 Lee, S. *et al.* Improving a genetically encoded voltage indicator by modifying the cytoplasmic charge composition. *Scientific Reports* **7**, 8286, doi:10.1038/s41598-017-08731-2 (2017).

197 Storace, D. *et al.* Toward Better Genetically Encoded Sensors of Membrane Potential. *Trends in Neurosciences* **39**, 277–289, doi:10.1016/j.tins.2016.02.005 (2016).

198 Nakajima, R., Jung, A., Yoon, B. J. & Baker, B. J. Optogenetic Monitoring of Synaptic Activity with Genetically Encoded Voltage Indicators. *Frontiers in Synaptic Neuroscience* **8**, 22, doi:10.3389/fnsyn.2016.00022 (2016).

199 Lundby, A., Mutoh, H., Dimitrov, D., Akemann, W. & Knopfel, T. Engineering of a genetically encodable fluorescent voltage sensor exploiting fast Ci-VSP voltage-sensing movements. *PLoS One* **3**, e2514, doi:10.1371/journal.pone.0002514 (2008).

200 Azimi Hashemi, N. *et al.* Rhodopsin-based voltage imaging tools for use in muscles and neurons of Caenorhabditis elegans. *Proceedings of the National Academy of Sciences of the United States of America* **116**, 17051–17060, doi:10.1073/pnas.1902443116 (2019).

201 Wang, D., Zhang, Z., Chanda, B. & Jackson, M. B. Improved probes for hybrid voltage sensor imaging. *Biophysical Journal* **99**, 2355–2365, doi:10.1016/j.bpj.2010.07.037 (2010).

202 Piatkevich, K. D. *et al.* Population imaging of neural activity in awake behaving mice. *Nature*, doi:10.1038/s41586-019-1641-1 (2019).

203 Shroff, S. N. *et al.* Voltage Imaging of Cardiac Cells and Tissue Using the Genetically Encoded Voltage Sensor Archon1. *iScience* **23**, 100974, doi:10.1016/j.isci.2020.100974 (2020).

204 Fan, L. Z. *et al.* All-Optical Electrophysiology Reveals the Role of Lateral Inhibition in Sensory Processing in Cortical Layer 1. *Cell* **180**, 521–535 e518, doi:10.1016/j.cell.2020.01.001 (2020).

205 Xiao, S. *et al.* Large-scale voltage imaging in behaving mice using targeted illumination. *iScience* **24**, 103263, doi:10.1016/j.isci.2021.103263 (2021).

206 Abdelfattah, A. S. *et al.* Bright and photostable chemigenetic indicators for extended in vivo voltage imaging. *Science* **365**, 699–704, doi:10.1126/science.aav6416 (2019).

207 Villette, V. *et al.* Ultrafast Two-Photon Imaging of a High-Gain Voltage Indicator in Awake Behaving Mice. *Cell* **179**, 1590–1608 e1523, doi:10.1016/j.cell.2019.11.004 (2019).

208 Lou, S. *et al.* Genetically Targeted All-Optical Electrophysiology with a Transgenic Cre-Dependent Optopatch Mouse. *Journal of Neuroscience* **36**, 11059–11073, doi:10.1523/JNEUROSCI.1582-16.2016 (2016).

209 Johnston, C. M., Krafft, A. J., Russe, M. F. & Rog-Zielinska, E. A. A new look at the heart-novel imaging techniques. *Herzschrittmachertherapie + Elektrophysiologie* **29**, 14–23, doi:10.1007/s00399-017-0546-7 (2018).

210 Ma, J. *et al.* High purity human-induced pluripotent stem cell-derived cardiomyocytes: electrophysiological properties of action potentials and ionic currents. *The American Journal of Physiology. Heart & Circulation Physiology* **301**, H2006–2017, doi:10.1152/ajpheart.00694.2011 (2011).

211 Faivre, J. F., Forest, M. C., Gout, B. & Bril, A. Electrophysiological characterization of BRL-32872 in canine Purkinje fiber and ventricular muscle. Effect on early after-depolarizations and repolarization dispersion. *European Journal of Pharmacology* **383**, 215–222, doi:10.1016/s0014-2999(99)00614-7 (1999).

212 Maddah, M. *et al.* A non-invasive platform for functional characterization of stem-cell-derived cardiomyocytes with applications in cardiotoxicity testing. *Stem Cell Reports* **4**, 621–631, doi:10.1016/j.stemcr.2015.02.007 (2015).

213 Scheel, O. *et al.* Action potential characterization of human induced pluripotent stem cell-derived cardiomyocytes using automated patch-clamp technology. *Assay and Drug Development Technologies* **12**, 457–469, doi:10.1089/adt.2014.601 (2014).

214 Ronaldson-Bouchard, K. *et al.* Advanced maturation of human cardiac tissue grown from pluripotent stem cells. *Nature* **556**, 239–243, doi:10.1038/s41586-018-0016-3 (2018).

215 Nunes, S. S. *et al.* Biowire: a platform for maturation of human pluripotent stem cell-derived cardiomyocytes. *Nature Methods* **10**, 781–787, doi:10.1038/nmeth.2524 (2013).

216 Tu, C., Chao, B. S. & Wu, J. C. Strategies for Improving the Maturity of Human Induced Pluripotent Stem Cell-Derived Cardiomyocytes. *Circulation Research* **123**, 512–514, doi:10.1161/CIRCRESAHA.118.313472 (2018).

217 Zimmermann, W. H. *et al.* Tissue engineering of a differentiated cardiac muscle construct. *Circulation Research* **90**, 223–230, doi:10.1161/hh0202.103644 (2002).

218 Stern, J. A. *et al.* A Small Molecule Inhibitor of Sarcomere Contractility Acutely Relieves Left Ventricular Outflow Tract Obstruction in Feline Hypertrophic Cardiomyopathy. *PLoS One* **11**, e0168407, doi:10.1371/journal.pone.0168407 (2016).

219 Dempsey, G. T. *et al.* Cardiotoxicity screening with simultaneous optogenetic pacing, voltage imaging and calcium imaging. *Journal of Pharmacological & Toxicological Methods* **81**, 240–250, doi:10.1016/j.vascn.2016.05.003 (2016).

220 Splawski, I. *et al.* Severe arrhythmia disorder caused by cardiac L-type calcium channel mutations. *Proceedings of the National Academy of Sciences of the United States of America* **102**, 8089–8096; discussion 8086–8088, doi:10.1073/pnas.0502506102 (2005).

221 Gwathmey, J. K. *et al.* Abnormal intracellular calcium handling in myocardium from patients with end-stage heart failure. *Circulation Research* **61**, 70–76, doi:10.1161/01.res.61.1.70 (1987).

222 Beuckelmann, D. J., Nabauer, M. & Erdmann, E. Intracellular calcium handling in isolated ventricular myocytes from patients with terminal heart failure. *Circulation* **85**, 1046–1055, doi:10.1161/01.cir.85.3.1046 (1992).

223 Kaab, S. *et al.* Ionic mechanism of action potential prolongation in ventricular myocytes from dogs with pacing-induced heart failure. *Circulation Research* **78**, 262–273, doi:10.1161/01.res.78.2.262 (1996).

224 Boudou, T. *et al.* A microfabricated platform to measure and manipulate the mechanics of engineered cardiac microtissues. *Tissue Engineering Part A* **18**, 910–919, doi:10.1089/ten.TEA.2011.0341 (2012).

225 Yazawa, M., Morikawa, K., Song, L.J., Ronaldson-Bouchard, K., Vunjak-Novakovic, G. Electrophysiological recordings of cardiomyocytes isolated from

engineered human cardiac tissues derived from pluripotent stem cells. *Protocol Exchange*, doi:10.1038/protex.2018.030 (2018).

226 Chavarha, M. *et al.* Fast two-photon volumetric imaging of an improved voltage indicator reveals electrical activity in deeply located neurons in the awake brain. *bioRxiv* (2018).

227 Shi, L. H., Luo, F., Woodward, D. J. & Chang, J. Y. Neural responses in multiple basal ganglia regions during spontaneous and treadmill locomotion tasks in rats. *Experimental Brain Research* **157**, 303–314, doi:10.1007/s00221-004-1844-y (2004).

228 Jin, X., Tecuapetla, F. & Costa, R. M. Basal ganglia subcircuits distinctively encode the parsing and concatenation of action sequences. *Nature Neuroscience* **17**, 423–430, doi:10.1038/nn.3632 (2014).

229 Buzsaki, G. Large-scale recording of neuronal ensembles. *Nature Neuroscience* **7**, 446–451, doi:10.1038/nn1233 (2004).

230 Wu, C., Ivanova, E., Zhang, Y. & Pan, Z. H. rAAV-mediated subcellular targeting of optogenetic tools in retinal ganglion cells in vivo. *PLoS One* **8**, e66332, doi:10.1371/journal.pone.0066332 (2013).

231 Baker, C. A., Elyada, Y. M., Parra, A. & Bolton, M. M. L. Cellular resolution circuit mapping with temporal-focused excitation of soma-targeted channelrhodopsin. *eLife* **5**, 1–15, doi:10.7554/eLife.14193 (2016).

232 Shemesh, O. A. *et al.* Temporally precise single-cell-resolution optogenetics. *Nature Neuroscience* **20**, doi:10.1038/s41593-017-0018-8 (2017).

233 Daigle, T. L. *et al.* A Suite of Transgenic Driver and Reporter Mouse Lines with Enhanced Brain-Cell-Type Targeting and Functionality. *Cell*, doi:10.1016/j.cell.2018.06.035 (2018).

234 Klaus, A. *et al.* The Spatiotemporal Organization of the Striatum Encodes Action Space. *Neuron* **96**, 949, doi:10.1016/j.neuron.2017.10.031 (2017).

235 Garrido, Â. *et al.* Identi ® cation of an axonal determinant in the C-terminus of the sodium channel $Na_v1.2$. *EMBO Journal* **20** (2001).

236 Garrido, J. J. *et al.* A targeting motif involved in sodium channel clustering at the axonal initial segment. *Science* **300**, 2091–2094, doi:10.1126/science.1085167 (2003).

237 Wu, C., Ivanova, E., Cui, J., Lu, Q. & Pan, Z. H. Action Potential Generation at an Axon Initial Segment-Like Process in the Axonless Retinal AII Amacrine Cell. *Journal of Neuroscience*, doi:10.1523/JNEUROSCI.1861-11.2011 (2011).

238 Greenberg, K. P., Pham, A. & Werblin, F. S. Differential Targeting of Optical Neuromodulators to Ganglion Cell Soma and Dendrites Allows Dynamic Control of Center-Surround Antagonism. *Neuron* **69**, 713–720, doi:10.1016/j.neuron.2011.01.024 (2011).

239 Zhang, X. & Bennett, V. Restriction of 480/270-kD ankyrin(G) to axon proximal segments requires multiple ankyrin(G)-specific domains. *Journal of Cell Biology* **142**, 1571–1581, doi:10.1083/jcb.142.6.1571 (1998).

240 Boyden, E. A history of optogenetics: the development of tools for controlling brain circuits with light. *F1000 Biology Reports* **3**, 1–12, doi:10.3410/B3-11 (2011).

241 Klapoetke, N. C. *et al.* Addendum: independent optical excitation of distinct neural populations. *Nature Methods* **11**, 972 (2014).

242 Kravitz, A. V. & Kreitzer, A. C. Striatal mechanisms underlying movement, reinforcement, and punishment. *Physiology (Bethesda, Md.)* **27**, 167–177, doi:10.1152/physiol.00004.2012 (2012).

243 Koós, T. & Tepper, J. M. Inhibitory control of neostriatal projection neurons by GABAergic interneurons. *Nature Neuroscience* **2**, 467–472, doi:10.1038/8138 (1999).

244 Zhou, F. M., Wilson, C. J. & Dani, J. A. Cholinergic interneuron characteristics and nicotinic properties in the striatum. *Journal of Neurobiology* **53**, 590–605, doi:10.1002/neu.10150 (2002).

245 Harvey, C. D., Collman, F., Dombeck, D. A. & Tank, D. W. Intracellular dynamics of hippocampal place cells during virtual navigation. *Nature* **461**, 941–946, doi:10.1038/nature08499 (2009).

246 Royer, S. *et al.* Control of timing, rate and bursts of hippocampal place cells by dendritic and somatic inhibition. *Nature Neuroscience* **15**, 769–775, doi:10.1038/nn.3077 (2012).

247 Bittner, K. C. *et al.* Conjunctive input processing drives feature selectivity in hippocampal CA1 neurons. *Nature Neuroscience* **18**, 1133–1142, doi:10.1038/nn.4062 (2015).

248 Wilson, M. A. & McNaughton, B. L. Dynamics of the hippocampal ensemble code for space. *Science* **261**, 1055–1058, doi:10.1126/science.8351520 (1993).

249 Knierim, J. J., Kudrimoti, H. S. & McNaughton, B. L. Interactions Between Idiothetic Cues and External Landmarks in the Control of Place Cells and Head Direction Cells. *Journal of Neurophysiology* **80**, 425–446, doi:10.1152/jn.1998.80.1.425 (1998).

250 Eichenbaum, H., Wiener, S. I., Shapiro, M. L. & Cohen, N. J. The organization of spatial coding in the hippocampus: a study of neural ensemble activity. *The Journal of Neuroscience* **9**, 2764–2775 (1989).

251 Deadwyler, S. a., Bunn, T. & Hampson, R. E. Hippocampal ensemble activity during spatial delayed-nonmatch-to-sample performance in rats. *The Journal of Neuroscience* **16**, 354–372, doi:10.1523/JNEUROSCI.16-01-00354.1996 (1996).

252 Singer, A. C. *et al.* Mesoscale-duration activated states gate spiking in response to fast rises in membrane voltage in the awake brain. *Journal of Neurophysiology* **118**, 1270–1291, doi:10.1152/jn.00116.2017 (2017).

253 Adam, Y. *et al.* All-optical electrophysiology reveals brain-state dependent changes in hippocampal subthreshold dynamics and excitability. *bioRxiv*, doi:10.1101/281618 (2018).

254 Hansen, K. R. *et al.* Mild Blast Injury Produces Acute Changes in Basal Intracellular Calcium Levels and Activity Patterns in Mouse Hippocampal Neurons. *Journal of Neurotrauma* **35**, 1523–1536, doi:10.1089/neu.2017.5029 (2018).

255 Dombeck, D. A., Khabbaz, A. N., Collman, F., Adelman, T. L. & Tank, D. W. Imaging Large-Scale Neural Activity with Cellular Resolution in Awake, Mobile Mice. *Neuron* **56**, 43–57, doi:10.1016/j.neuron.2007.08.003 (2007).

256 Fields, I. E. *et al.* Noninvasive Deep Brain Stimulation via Temporally Article Noninvasive Deep Brain Stimulation via Temporally Interfering Electric Fields. *Cell* **169**, 1029–1041.e1016, doi:10.1016/j.cell.2017.05.024.

257 Kalmbach, A. S. & Waters, J. Brain surface temperature under a craniotomy. *Journal of Neurophysiology* **108**, 3138–3146, doi:10.1152/jn.00557.2012 (2012).

258 Christie, I. N. *et al.* fMRI response to blue light delivery in the naive brain: implications for combined optogenetic fMRI studies. *NeuroImage* **66**, 634–641, doi:10.1016/j.neuroimage.2012.10.074 (2013).

259 Stujenske, J. M., Spellman, T. & Gordon, J. A. Modeling the Spatiotemporal Dynamics of Light and Heat Propagation for In Vivo Optogenetics. *Cell Reports* **12**, 525–534, doi:10.1016/j.celrep.2015.06.036 (2015).

260 Podgorski, K. & Ranganathan, G. Brain heating induced by near-infrared lasers during multiphoton microscopy. *Journal of Neurophysiology* **116**, 1012–1023, doi:10.1152/jn.00275.2016 (2016).

261 Arias-Gil, G., Ohl, F. W., Takagaki, K. & Lippert, M. T. Measurement, modeling, and prediction of temperature rise due to optogenetic brain stimulation. *Neurophotonics* **3**, 045007, doi:10.1117/1.NPh.3.4.045007 (2016).

262 Dell, R. B., Holleran, S. & Ramakrishnan, R. Sample size determination. *ILAR Journal* **43**, 207–213, doi:10.1093/ilar.43.4.207 (2002).

263 Lopez-Azcarate, J. *et al.* Delta-mediated cross-frequency coupling organizes oscillatory activity across the rat cortico-basal ganglia network. *Frontiers in Neural Circuits* **7**, 155, doi:10.3389/fncir.2013.00155 (2013).

264 Arnal, L. H., Doelling, K. B. & Poeppel, D. Delta-Beta Coupled Oscillations Underlie Temporal Prediction Accuracy. *Cerebral Cortex* **25**, 3077–3085, doi:10.1093/cercor/bhu103 (2015).

265 Hamel-Thibault, A., Thenault, F., Whittingstall, K. & Bernier, P. M. Delta-Band Oscillations in Motor Regions Predict Hand Selection for Reaching. *Cerebral Cortex* **28**, 574–584, doi:10.1093/cercor/bhw392 (2018).

266 Saleh, M., Reimer, J., Penn, R., Ojakangas, C. L. & Hatsopoulos, N. G. Fast and slow oscillations in human primary motor cortex predict oncoming behaviorally relevant cues. *Neuron* **65**, 461–471, doi:10.1016/j.neuron.2010.02.001 (2010).

267 Magnusson, J. L. & Leventhal, D. K. Revisiting the "Paradox of Stereotaxic Surgery": Insights Into Basal Ganglia-Thalamic Interactions. *Frontiers in Systems Neuroscience* **15**, 725876, doi:10.3389/fnsys.2021.725876 (2021).

268 Foffani, G., Bianchi, A. M., Baselli, G. & Priori, A. Movement-related frequency modulation of beta oscillatory activity in the human subthalamic nucleus. *Journal of Physiology* **568**, 699–711, doi:10.1113/jphysiol.2005.089722 (2005).

269 Murthy, V. N. & Fetz, E. E. Coherent 25- to 35-Hz oscillations in the sensorimotor cortex of awake behaving monkeys. *Proceedings of the National Academy of Sciences of the United States of America* **89**, 5670–5674 (1992).

270 Belluscio, M. A., Kasanetz, F., Riquelme, L. A. & Murer, M. G. Spreading of slow cortical rhythms to the basal ganglia output nuclei in rats with nigrostriatal lesions. *European Journal of Neuroscience* **17**, 1046–1052, doi:10.1046/j.1460-9568.2003.02543.x (2003).

271 Tseng, K. Y. *et al.* Subthalamic nucleus lesions reduce low frequency oscillatory firing of substantia nigra pars reticulata neurons in a rat model of Parkinson's disease. *Brain Research* **904**, 93–103, doi:10.1016/s0006-8993(01)02489-1 (2001).

272 Hu, X. F. *et al.* Amplitude of low-frequency oscillations in Parkinson's disease: a 2-year longitudinal resting-state functional magnetic resonance imaging study. *Chinese Medical Journal (Engl.)* **128**, 593–601, doi:10.4103/0366-6999.151652 (2015).

273 Parr-Brownlie, L. C., Poloskey, S. L., Bergstrom, D. A. & Walters, J. R. Parafascicular thalamic nucleus activity in a rat model of Parkinson's disease.

Experimental Neurology **217**, 269–281, doi:10.1016/j.expneurol.2009.02.010 (2009).

274 Sharma, A., Vidaurre, D., Vesper, J., Schnitzler, A. & Florin, E. Differential dopaminergic modulation of spontaneous cortico-subthalamic activity in Parkinson's disease. *Elife* **10**, doi:10.7554/eLife.66057 (2021).

275 Walters, J. R., Hu, D., Itoga, C. A., Parr-Brownlie, L. C. & Bergstrom, D. A. Phase relationships support a role for coordinated activity in the indirect pathway in organizing slow oscillations in basal ganglia output after loss of dopamine. *Neuroscience* **144**, 762–776, doi:10.1016/j.neuroscience.2006.10.006 (2007).

276 Sharott, A. *et al.* Different subtypes of striatal neurons are selectively modulated by cortical oscillations. *Journal of Neuroscience* **29**, 4571–4585, doi:10.1523/JNEUROSCI.5097-08.2009 (2009).

277 Deffains, M. *et al.* Subthalamic, not striatal, activity correlates with basal ganglia downstream activity in normal and parkinsonian monkeys. *Elife* **5**, doi:10.7554/eLife.16443e16443 [pii] (2016).

278 Mallet, N., Ballion, B., Le Moine, C. & Gonon, F. Cortical inputs and GABA interneurons imbalance projection neurons in the striatum of parkinsonian rats. *Journal of Neuroscience* **26**, 3875–3884, doi:26/14/3875 [pii]10.1523/JNEUROSCI.4439-05.2006 (2006).

279 Yang, Y. *et al.* Theta-gamma coupling emerges from spatially heterogeneous cholinergic neuromodulation. *PLoS Computational Biology* **17**, e1009235, doi:10.1371/journal.pcbi.1009235 (2021).

280 Graveland, G. A. & DiFiglia, M. The frequency and distribution of medium-sized neurons with indented nuclei in the primate and rodent neostriatum. *Brain Research* **327**, 307–311, doi:10.1016/0006-8993(85)91524-0 (1985).

281 Ren, K. *et al.* Striatal Distribution and Cytoarchitecture of Dopamine Receptor Subtype 1 and 2: Evidence from Double-Labeling Transgenic Mice. *Frontiers in Neural Circuits* **11**, 57, doi:10.3389/fncir.2017.00057 (2017).

282 Aosaki, T., Kimura, M. & Graybiel, A. M. Temporal and spatial characteristics of tonically active neurons of the primate's striatum. *Journal of Neurophysiology* **73**, 1234–1252, doi:10.1152/jn.1995.73.3.1234 (1995).

283 Aosaki, T. *et al.* Responses of tonically active neurons in the primate's striatum undergo systematic changes during behavioral sensorimotor conditioning. *Journal of Neuroscience* **14**, 3969–3984 (1994).

284 Kim, T. *et al.* The Functional Role of Striatal Cholinergic Interneurons in Reinforcement Learning From Computational Perspective. *Frontiers in Neural Circuits* **13**, 10, doi:10.3389/fncir.2019.00010 (2019).

285 Zemel, D. *et al.* Dopamine depletion selectively disrupts interactions between striatal neuron subtypes and LFP oscillations. *Cell Reports* **38**, 110265, doi:10.1016/j.celrep.2021.110265 (2022).

286 Khanna, P. & Carmena, J. M. Beta band oscillations in motor cortex reflect neural population signals that delay movement onset. *Elife* **6**, doi:10.7554/eLife.24573 (2017).

287 Moenne-Loccoz, C. *et al.* Cortico-Striatal Oscillations Are Correlated to Motor Activity Levels in Both Physiological and Parkinsonian Conditions. *Frontiers in Systems Neuroscience* **14**, 56, doi:10.3389/fnsys.2020.00056 (2020).

288 Wilson, C. J., Chang, H. T. & Kitai, S. T. Firing patterns and synaptic potentials of identified giant aspiny interneurons in the rat neostriatum. *Journal of Neuroscience* **10**, 508–519 (1990).

289 Guo, Q. *et al.* Whole-brain mapping of inputs to projection neurons and cholinergic interneurons in the dorsal striatum. *PLoS One* **10**, e0123381, doi:10.1371/journal.pone.0123381 (2015).

290 Klug, J. R. *et al.* Differential inputs to striatal cholinergic and parvalbumin interneurons imply functional distinctions. *Elife* **7**, doi:10.7554/eLife.35657 (2018).

291 Kubota, Y. *et al.* Neostriatal cholinergic neurons receive direct synaptic inputs from dopaminergic axons. *Brain Research* **413**, 179–184, doi:10.1016/0006-8993(87)90167-3 (1987).

292 Lapper, S. R. & Bolam, J. P. Input from the frontal cortex and the parafascicular nucleus to cholinergic interneurons in the dorsal striatum of the rat. *Neuroscience* **51**, 533–545, doi:10.1016/0306-4522(92)90293-b (1992).

293 Meredith, G. E. & Wouterlood, F. G. Hippocampal and midline thalamic fibers and terminals in relation to the choline acetyltransferase-immunoreactive neurons in nucleus accumbens of the rat: a light and electron microscopic study. *Journal of Comparative Neurology* **296**, 204–221, doi:10.1002/cne.902960203 (1990).

294 Demars, M. P. & Morishita, H. Cortical parvalbumin and somatostatin GABA neurons express distinct endogenous modulators of nicotinic acetylcholine receptors. *Molecular Brain* **7**, 75, doi:10.1186/s13041-014-0075-9 (2014).

295 Krenz, I. *et al.* Parvalbumin-containing interneurons of the human cerebral cortex express nicotinic acetylcholine receptor proteins. *Journal of Chemical Neuroanatomy* **21**, 239–246, doi:10.1016/s0891-0618(01)00112-0 (2001).

296 Assous, M. Striatal cholinergic transmission. Focus on nicotinic receptors' influence in striatal circuits. *European Journal of Neuroscience* **53**, 2421–2442, doi:10.1111/ejn.15135 (2021).

297 Bernard, V., Somogyi, P. & Bolam, J. P. Cellular, subcellular, and subsynaptic distribution of AMPA-type glutamate receptor subunits in the neostriatum of the rat. *Journal of Neuroscience* **17**, 819–833 (1997).

298 Yan, Z., Flores-Hernandez, J. & Surmeier, D. J. Coordinated expression of muscarinic receptor messenger RNAs in striatal medium spiny neurons. *Neuroscience* **103**, 1017–1024 (2001).

299 Joundi, R. A., Jenkinson, N., Brittain, J. S., Aziz, T. Z. & Brown, P. Driving oscillatory activity in the human cortex enhances motor performance. *Current Biology* **22**, 403–407, doi:10.1016/j.cub.2012.01.024 (2012).

300 Pogosyan, A., Gaynor, L. D., Eusebio, A. & Brown, P. Boosting cortical activity at Beta-band frequencies slows movement in humans. *Current Biology* **19**, 1637–1641, doi:10.1016/j.cub.2009.07.074 (2009).

301 Prokic, E. J., Stanford, I. M., Woodhall, G. L., Williams, A. C. & Hall, S. D. Bradykinesia Is Driven by Cumulative Beta Power During Continuous Movement and Alleviated by Gabaergic Modulation in Parkinson's Disease. *Frontiers in Neurology* **10**, 1298, doi:10.3389/fneur.2019.01298 (2019).

302 Pnevmatikakis, E. A. & Giovannucci, A. NoRMCorre: An online algorithm for piecewise rigid motion correction of calcium imaging data. *Journal of Neuroscience Methods* **291**, 83–94, doi:10.1016/j.jneumeth.2017.07.031 (2017).

303 Lachaux, J. P., Rodriguez, E., Martinerie, J. & Varela, F. J. Measuring phase synchrony in brain signals. *Human Brain Mapping* **8**, 194–208, doi:10.1002/(sici)1097-0193(1999)8:4<194::aid-hbm4>3.0.co;2-c (1999).

304 Aydore, S., Pantazis, D. & Leahy, R. M. A note on the phase locking value and its properties. *NeuroImage* **74**, 231–244, doi:10.1016/j.neuroimage.2013.02.008 (2013).

305 Watson, R. E., Jr., Wiegand, S. J., Clough, R. W. & Hoffman, G. E. Use of cryoprotectant to maintain long-term peptide immunoreactivity and tissue morphology. *Peptides* **7**, 155–159, doi:10.1016/0196-9781(86)90076-8 (1986).

306 Chavarha, M. *et al.* Fast two-photon volumetric imaging of an improved voltage indicator reveals electrical activity in deeply located neurons in the awake brain. *bioRxiv*, 445064, doi:10.1101/445064 (2018).

CURRICULUM VITAE